

1

²A SEARCH FOR LONG-LIVED, CHARGED, SUPERSYMMETRIC PARTICLES
³USING IONIZATION WITH THE ATLAS DETECTOR

⁴BRADLEY AXEN

5

September 2016 – Version 0.65



6

⁸ Bradley Axen: *A Search for Long-Lived, Charged, Supersymmetric Particles using*
⁹ *Ionization with the ATLAS Detector*, Subtitle, © September 2016

¹⁰ The dissertation of Bradley Axen, titled *A Search for Long-Lived, Charged, Super-*
¹¹ *symmetric Particles using Ionization with the ATLAS Detector*, is approved:

¹² _____
¹³ Chair _____ Date

¹⁴ _____
¹⁵ _____ Date

¹⁶ _____
¹⁷ _____ Date

¹⁸ University of California, Berkeley

19

Usually a quotation.

20

Dedicated to.

₂₁ ABSTRACT

₂₂ How to write a good abstract:

₂₃ <https://plg.uwaterloo.ca/~migod/research/beck00PSLA.html>

24 PUBLICATIONS

25 Some ideas and figures have appeared previously in the following publications:

26

27 Put your publications from the thesis here. The packages `multibib` or `bibtopic`
28 etc. can be used to handle multiple different bibliographies in your document.

30 ACKNOWLEDGEMENTS

31 Put your acknowledgements here.

32

33 And potentially a second round.

34

³⁵ CONTENTS

³⁶ 1	INTRODUCTION	¹
³⁷ I	THEORETICAL CONTEXT	³
³⁸ 2	STANDARD MODEL	⁴
³⁹ 2.1	Action and the Lagrangian	⁴
⁴⁰ 2.2	Gauge Invariance and Forces	⁵
⁴¹ 2.2.1	$SU(2) \times U(1)$ and the Electroweak Force	⁷
⁴² 2.2.2	$SU(3)$ and the Strong Force	⁷
⁴³ 2.3	Noether's Theorem, Charges, and Matter	⁸
⁴⁴ 2.3.1	Quarks	⁸
⁴⁵ 2.3.2	Leptons	⁹
⁴⁶ 2.3.3	Chirality	¹⁰
⁴⁷ 2.4	Higgs Mechanism and Mass	¹⁰
⁴⁸ 2.5	Phenomenology	¹²
⁴⁹ 2.5.1	Standard Model Calculations	¹²
⁵⁰ 2.5.2	Electroweak Physics	¹³
⁵¹ 2.5.3	Strong Physics	¹⁴
⁵² 2.5.4	Proton-Proton Collisions	¹⁵
⁵³ 2.5.5	Simulation	¹⁵
⁵⁴ 2.6	Limitations	¹⁶
⁵⁵ 2.6.1	Theoretical Concerns	¹⁷
⁵⁶ 2.6.2	Cosmological Observations	¹⁷
⁵⁷ 3	SUPERSYMMETRY	¹⁹
⁵⁸ 3.1	Structure	¹⁹
⁵⁹ 3.2	Motivation	²¹
⁶⁰ 3.3	Simplified Models	²²
⁶¹ 3.4	Long-Lived Particles	²³
⁶² II	EXPERIMENTAL STRUCTURE AND RECONSTRUCTION	²⁵
⁶³ 4	THE LARGE HADRON COLLIDER	²⁶
⁶⁴ 4.1	Injection Chain	²⁷
⁶⁵ 4.2	Design	²⁸
⁶⁶ 4.2.1	Layout	²⁸
⁶⁷ 4.2.2	Magnets	²⁹
⁶⁸ 4.2.3	Radio Frequency Cavities	³⁰
⁶⁹ 4.2.4	Beam	³²
⁷⁰ 4.3	Luminosity Parameters	³²
⁷¹ 4.4	Delivered Luminosity	³⁴
⁷² 5	THE ATLAS DETECTOR	³⁶
⁷³ 5.1	Coordinate System	³⁸
⁷⁴ 5.2	Magnetic Field	³⁹
⁷⁵ 5.3	Inner Detector	⁴¹

76	5.3.1	Pixel Detector	44
77	5.3.2	Semiconductor Tracker	46
78	5.3.3	Transition Radiation Tracker	48
79	5.4	Calorimetry	48
80	5.4.1	Electromagnetic Calorimeter	50
81	5.4.2	Hadronic Calorimeters	51
82	5.5	Muon Spectrometer	53
83	5.5.1	Monitored Drift Tube	55
84	5.5.2	Resistive Plate Chamber	56
85	5.5.3	Cathode Strip Chamber	56
86	5.5.4	Thin Gap Chamber	56
87	5.6	Trigger	58
88	6	EVENT RECONSTRUCTION	61
89	6.1	Charged Particles	61
90	6.1.1	Pixel Neural Network	64
91	6.1.2	Pixel dE/dx	65
92	6.1.3	Vertex Reconstruction	66
93	6.2	Electrons and Photons	67
94	6.2.1	Photon Identification	68
95	6.2.2	Electron Identification	68
96	6.3	Muons	69
97	6.3.1	Muon Identification	69
98	6.4	Jets	70
99	6.4.1	Topological Clustering	70
100	6.4.2	Jet Algorithms	71
101	6.4.3	Jet Energy Scale	72
102	6.5	Missing Transverse Energy	73
103	III	CALORIMETER RESPONSE	75
104	7	RESPONSE MEASUREMENT WITH SINGLE HADRONS	76
105	7.1	Dataset and Simulation	77
106	7.1.1	Data Samples	77
107	7.1.2	Simulated Samples	77
108	7.1.3	Event Selection	77
109	7.2	Inclusive Hadron Response	78
110	7.2.1	E/p Distribution	78
111	7.2.2	Zero Fraction	79
112	7.2.3	Neutral Background Subtraction	81
113	7.2.4	Corrected Response	82
114	7.2.5	Additional Studies	84
115	7.3	Identified Particle Response	87
116	7.3.1	Decay Reconstruction	88
117	7.3.2	Identified Response	89
118	7.3.3	Additional Species in Simulation	91
119	7.4	Summary	91
120	8	JET ENERGY RESPONSE AND UNCERTAINTY	93

121	8.1	Motivation	93
122	8.2	Uncertainty Estimate	93
123	8.3	Summary	96
124	IV	SEARCH FOR LONG-LIVED PARTICLES	99
125	9	LONG-LIVED PARTICLES IN ATLAS	100
126	9.1	Event Topology	100
127	9.1.1	Detector Interactions	101
128	9.1.2	Lifetime Dependence	103
129	9.2	Simulation	106
130	10	EVENT SELECTION	109
131	10.1	Trigger	110
132	10.2	Kinematics and Isolation	111
133	10.3	Particle Species Rejection	115
134	10.4	Ionization	119
135	10.4.1	Mass Estimation	119
136	10.5	Event Selection	121
137	11	BACKGROUND ESTIMATION	123
138	11.1	Background Sources	123
139	11.2	Prediction Method	124
140	11.3	Validation	125
141	11.3.1	Closure in Simulation	125
142	11.3.2	Validation Region in Data	126
143	11.4	Expected Background	127
144	12	SYSTEMATIC UNCERTAINTIES	129
145	12.1	Background Estimate	129
146	12.1.1	Analytic Description of dE/dx	130
147	12.1.2	Muon Fraction	130
148	12.1.3	IBL Corrections	130
149	12.1.4	Normalization	130
150	12.2	Signal Yield	131
151	12.2.1	initial state radiation (ISR) Modeling	131
152	12.2.2	Pileup Reweighting	131
153	12.2.3	Trigger Efficiency Reweighting	132
154	12.2.4	Missing Transverse Momentum Scale	133
155	12.2.5	Momentum Parametrization	133
156	12.2.6	Ionization Requirement	134
157	12.2.7	Electron and Jet Rejection	134
158	12.2.8	Muon Veto	134
159	12.2.9	Luminosity	135
160	12.2.10	Signal Cross Section	135
161	13	RESULTS	137
162	13.1	Cross Section Limits	137
163	13.2	Mass Limits	140
164	14	SUMMARY AND OUTLOOK	144

165	V APPENDIX	146
166	A EXPANDED R-HADRON YIELDS AND LIMITS	147
167	BIBLIOGRAPHY	153

168 LIST OF FIGURES

169	Figure 1	A Feynman diagram representing the interaction of the A field with a generic fermion, f	7
170	Figure 2	The particle content of the SM , including the names, masses, spins, and charges of each of the particles.	9
171	Figure 3	A feynman diagram for photon propagation including a loop of electrons.	13
172	Figure 4	An approximation of the running of the coupling con- stants in the Standard Model (SM) up to the Planck scale [1].	13
173	Figure 5	The Feynman diagrams representing the decays of the W and Z bosons to fermions. Here f indicates a generic fermion, \bar{f} its antiparticle, and f' the partner of that fermion in the same generation.	14
174	Figure 6	The parton distribution functions (PDFs) for proton- proton collisions at $Q^2 = 10 \text{ GeV}^2$ and $Q^2 = 10^4$ GeV^2 . Each shows the fraction of particles which carry a fraction x of the total proton energy at the specified scale [3]. The distribution for gluons is scaled by 0.1 to fit within the axis range.	16
175	Figure 7	The distribution of velocities of stars as a function of the radius from the center of the galaxy. The contrib- utions to the velocity from the various components of matter in the galaxy are shown [7].	18
176	Figure 8	An approximation of the running of the coupling con- stants in the Minimal Supersymmetric Model (MSSM) up to the Planck scale [1].	22
177	Figure 9	The decay of a gluino to quarks and an LSP , which pre- cedes through a squark.	23
178	Figure 10	The four collision points and corresponding experi- ments of the Large Hadron Collider (LHC). The image includes the location of the nearby city of Geneva as well as the border of France and Switzerland.	27
179	Figure 11	The cumulative luminosity over time delivered to the ATLAS experiment from high energy proton-proton collisions since 2011. The energies of the collisions are listed for each of the data-taking periods. The fig- ure shows the delivered luminosity as of the conclu- sion of data collection in 2016.	28

207	Figure 12	The accelerator complex that builds up to the full design energies at the LHC . The protons are passed in order to Linac 2, the PSB , the PS , the SPS and then the LHC	29
208			
209			
210			
211	Figure 13	A schematic of the layout of the LHC , not to scale. The arched and straight sections are illustrated at the bottom of the schematic, and all four crossing sites are indicated with their respective experiments.	30
212			
213			
214			
215	Figure 14	A cross section of the the cryodipole magnets which bend the flight path of protons around the circumference of the LHC . The diagram includes both the superconducting coils which produce the magnetic field and the structural elements which keep the magnets precisely aligned.	31
216			
217			
218			
219			
220			
221	Figure 15	The arrangement of four radiofrequency (RF) cavities within a cryomodule.	31
222			
223	Figure 16	The cumulative luminosity versus time delivered to ATLAS (green), recorded by ATLAS (yellow), and certified to be good quality data (blue) during stable beams for pp collisions at 13 TeV in 2015.	34
224			
225			
226			
227	Figure 17	The luminosity-weighted distribution of the mean number of interactions per crossing for the 2015 pp collision data at 13 TeV.	35
228			
229			
230	Figure 18	A cut-away schematic of the layout of the ATLAS detector. Each of the major subsystems is indicated.	37
231			
232	Figure 19	A cross-sectional slice of the ATLAS experiment which illustrates how the various SM particles interact with the detector systems.	37
233			
234			
235	Figure 20	The layout of the four superconducting magnets in the ATLAS detector.	40
236			
237	Figure 21	A quarter section of the ATLAS inner detector which shows the layout of each of the subdetectors in detail. The lower panel shows an enlarged view of the pixel detector. Example trajectories for a particle with $\eta = 1.0, 1.5, 2.0, 2.5$ are shown. The Insertible B-Layer (IBL), which was added after the original detector commissioning, is not shown.	42
238			
239			
240			
241			
242			
243			
244	Figure 22	A computer generated three-dimensional view of the inner detector along the line of the beam axis. The subdetectors and their positions are labeled.	43
245			
246			
247	Figure 23	An alternative computer generated three-dimensional view of the inner detector transverse to the beam axis. The subdetectors and their positions are labeled.	43
248			
249			

250	Figure 24	The integrated radiation lengths traversed by a particle at the exit of the ID envelope (outside of the Transition Radiation Tracker (TRT) after 108.2 cm), including the services and thermal enclosures. The distribution is shown as a function of $ \eta $ and averaged over ϕ . The breakdown indicates the contributions of individual sub-detectors, including services in their active volume.	44
251			
252			
253			
254			
255			
256			
257	Figure 25	A cut away image of the outer three layers of the pixel detector.	45
258			
259	Figure 26	An image of the insertion of the IBL into the current pixel detector.	46
260			
261	Figure 27	A three-dimensional computer-generated image of the geometry of the IBL with a view (a) mostly transverse to the beam pipe (b) mostly parallel to the beam pipe.	47
262			
263			
264	Figure 28	An expanded view of the geometry of the silicon microstrip (SCT) double layers in the barrel region.	47
265			
266	Figure 29		49
267	Figure 30	The depth of (a) the electromagnetic barrel calorimeter in radiation lengths and of (b) all calorimeters in interaction lengths as a function of pseudorapidity.	50
268			
269			
270	Figure 31	A schematic of the liquid argon (LAr) calorimeter in the barrel region, highlighting the accordion structure.	50
271			
272	Figure 32	A schematic of a hadronic tile module which shows the alternating layers of steel and plastic scintillator.	52
273			
274	Figure 33	The segmentation in depth and η of the tile-calorimeter modules in the central (left) and extended (right) barrels.	52
275			
276	Figure 34	A cut-away diagram of the muon systems on ATLAS.	53
277	Figure 35	A quarter view of the muon spectrometer which highlights the layout of each of the detecting elements. The BOL, BML, BIL, EOL, EML, and EIL are all Monitored Drift Tube (MDT) elements, where the acronyms encode their positions.	54
278			
279			
280			
281			
282	Figure 36	A schematic of the cross-section of the muon spectrometer in the barrel region.	54
283			
284	Figure 37	A schematic of a single MDT chamber, which shows the multilayers of drift tubes as well as the alignment system.	55
285			
286			
287	Figure 38	A schematic of the Cathode Strip Chamber (CSC) end-cap, showing the overlapping arrangement of the eight large and eight small chambers.	57
288			
289			
290	Figure 39	A schematic of the Thin Gap Chamber (TGC) doublet and triplet layers.	57
291			
292	Figure 40	The Level 1 (L1) Trigger rate broken down into the types of triggers as a function of the luminosity block for the 2015 data collection period.	59
293			
294			

295	Figure 41	The HLT Trigger rate broken down into the types of triggers as a function of the luminosity block for the 2015 data collection period.	60
296			
297			
298	Figure 42	An illustration of the perigee representation of track parameters for an example track. The charge is not directly shown, but is indicated by the direction of curvature of the track [23].	62
299			
300			
301			
302	Figure 43	The x and y locations of the hits generated in a simulated $t\bar{t}$ event in the inner detector. The hits which belong to tracks formed using the inside-out algorithm are highlighted in red, while the hits which belong to tracks formed using the outside-in algorithm are circled in black. This figure does not include hits in the IBL.	63
303			
304			
305			
306			
307			
308			
309	Figure 44	The tracking reconstruction efficiency as a function of (a) η and (b) p_T [24].	64
310			
311	Figure 45	Examples of the clusters formed in a single layer of the pixel detector for (a) a single isolated particle, (b) two nearly-overlapping particles, and (c) a particle which emits a δ -ray [25].	65
312			
313			
314			
315	Figure 46	The vertex reconstruction efficiency as a function of the number of associated tracks [27].	67
316			
317	Figure 47	The total, fractional jet energy scale (JES) uncertainties estimated for 2015 data as a function of jet p_T	73
318			
319	Figure 48	The E/p distribution and ratio of simulation to data for isolated tracks with (a) $ \eta < 0.6$ and $1.2 < p/\text{GeV} < 1.8$ and (b) $ \eta < 0.6$ and $2.2 < p/\text{GeV} < 2.8$	79
320			
321			
322	Figure 49	The fraction of tracks as a function (a, b) of momentum, (c, d) of interaction lengths with $E \leq 0$ for tracks with positive (on the left) and negative (on the right) charge.	80
323			
324			
325			
326	Figure 50	An illustration (a) of the geometry of energy deposits in the calorimeter. The red energy deposits come from the charged particle targeted for measurement, while the blue energy deposits are from nearby neutral particles and must be subtracted. The same diagram (b) for the neutral-background selection, described in Section 7.2.3.	81
327			
328			
329			
330			
331			
332			
333	Figure 51	$\langle E/p \rangle_{\text{BG}}$ as a function of the track momentum for tracks with (a) $ \eta < 0.6$, (b) $0.6 < \eta < 1.1$, and as a function of the track pseudorapidity for tracks with (c) $1.2 < p/\text{GeV} < 1.8$, (d) $1.8 < p/\text{GeV} < 2.2$	82
334			
335			
336			
337	Figure 52	$\langle E/p \rangle_{\text{COR}}$ as a function of track momentum, for tracks with (a) $ \eta < 0.6$, (b) $0.6 < \eta < 1.1$, (c) $1.8 < \eta < 1.9$, and (d) $1.9 < \eta < 2.3$	83
338			
339			

340	Figure 53	$\langle E/p \rangle_{\text{COR}}$ calculated using LCW-calibrated topological clusters as a function of track momentum for tracks with (a) zero or more associated topological clusters or (b) one or more associated topological clusters.	84
341			
342			
343			
344	Figure 54	Comparison of the $\langle E/p \rangle_{\text{COR}}$ for tracks with (a) less than and (b) greater than 20 hits in the TRT.	85
345			
346	Figure 55	Comparison of the $\langle E/p \rangle_{\text{COR}}$ for (a) positive and (b) negative tracks as a function of track momentum for tracks with $ \eta < 0.6$	86
347			
348			
349	Figure 56	Comparison of the E/p distributions for (a) positive and (b) negative tracks with $0.8 < p/\text{GeV} < 1.2$ and $ \eta < 0.6$, in simulation with the FTFP_BERT and QGSP_BERT physics lists.	86
350			
351			
352			
353	Figure 57	Comparison of the response of the hadronic calorimeter as a function of track momentum (a) at the EM-scale and (b) after the LCW calibration.	87
354			
355			
356	Figure 58	Comparison of the response of the EM calorimeter as a function of track momentum (a) at the EM-scale and (b) with the LCW calibration.	87
357			
358			
359	Figure 59	The reconstructed mass peaks of (a) K_S^0 , (b) Λ , and (c) $\bar{\Lambda}$ candidates.	88
360			
361	Figure 60	The E/p distribution for isolated (a) π^+ , (b) π^- , (c) proton, and (d) anti-proton tracks.	89
362			
363	Figure 61	The fraction of tracks with $E \leq 0$ for identified (a) π^+ and π^- , and (b) proton and anti-proton tracks	90
364			
365	Figure 62	The difference in $\langle E/p \rangle$ between (a) π^+ and π^- (b) p and π^+ , and (c) \bar{p} and π^-	91
366			
367	Figure 63	$\langle E/p \rangle_{\text{COR}}$ as a function of track momentum for (a) π^+ tracks and (b) π^- tracks.	92
368			
369	Figure 64	The ratio of the calorimeter response to single particles of various species to the calorimeter response to π^+ with the physics list FTFP_BERT.	92
370			
371			
372	Figure 65	The spectra of true particles inside anti- k_t , $R = 0.4$ jets with (a) $90 < p_T/\text{GeV} < 100$, (b) $400 < p_T/\text{GeV} < 500$, and (c) $1800 < p_T/\text{GeV} < 2300$	94
373			
374			
375	Figure 66	The JES response uncertainty contributions, as well as the total JES uncertainty, as a function of jet p_T for (a) $ \eta < 0.6$ and (b) $0.6 < \eta < 1.1$	97
376			
377			
378	Figure 67	The correlations between bins of average reconstructed jet momentum as a function of jet p_T and $ \eta $ for jets in the central region of the detector.	98
379			
380			
381	Figure 68	The processes which contribute to gluino pair production in the proton proton collisions, where the quarks and gluons are proton constituents.	101
382			
383			
384	Figure 69	The generated p_T and β distributions for R-Hadrons with $M = 1600 \text{ GeV}$	101
385			

386	Figure 70	A schematic diagram of an R-Hadron event with a life-time around 0.01 ns. The diagram includes one charged R-Hadron (solid blue), one neutral R-Hadron (dashed blue), Lightest Supersymmetric Particles (LSPs) (dashed green) and charged hadrons (solid orange). The pixel detector, calorimeters, and muon system are illustrated but not to scale.	104
387			
388			
389			
390			
391			
392			
393	Figure 71	Schematic diagram of an R-Hadron event with a life-time around 5 ns, where the masses of the R-Hadron and LSP are nearly degenerate. The diagram includes charged R-Hadrons (solid blue), neutral R-Hadrons (dashed blue), LSPs (dashed green) and charged hadrons (solid orange). The pixel detector, calorimeters, and muon system are illustrated but not to scale.	105
394			
395			
396			
397			
398			
399			
400	Figure 72	Schematic diagram of an R-Hadron event with a life-time around 5 ns, where the masses of the R-Hadron and LSP are not degenerate. The diagram includes charged R-Hadrons (solid blue), neutral R-Hadrons (dashed blue), LSPs (dashed green) and charged hadrons (solid orange). The pixel detector, calorimeters, and muon system are illustrated but not to scale.	106
401			
402			
403			
404			
405			
406			
407	Figure 73	A schematic diagram of an R-Hadron event with a life-time around 20 ns. The diagram includes one charged R-Hadron (solid blue), one neutral R-Hadron (dashed blue), LSPs (dashed green) and charged hadrons (solid orange). The pixel detector, calorimeters, and muon system are illustrated but not to scale.	107
408			
409			
410			
411			
412			
413	Figure 74	A schematic diagram of a very long-lived (VLL) R-Hadron event. The diagram includes one charged R-Hadron (solid blue) and one neutral R-Hadron (dashed blue). The pixel detector, calorimeters, and muon system are illustrated but not to scale.	108
414			
415			
416			
417			
418	Figure 75	The distribution of (a) E_T^{miss} and (b) Calorimeter E_T^{miss} for simulated signal events before the trigger requirement. The final bin includes all events above the axis range.	111
419			
420			
421			
422	Figure 76	The distribution of E_T^{miss} for data and simulated signal events, after the trigger requirement. The final bin includes all events above the axis range.	112
423			
424			
425	Figure 77	The trigger efficiency for the HLT_xe70 trigger requirement as a function of (a) E_T^{miss} and (b) Calorimeter E_T^{miss} for simulated signal events.	113
426			
427			
428	Figure 78	The dependence of dE/dx on N_{split} in data after basic track hit requirements have been applied.	114
429			

430	Figure 79	The distribution of dE/dx with various selections applied in data and simulated signal events. The final bin includes all tracks above the axis range.	114
431			
432			
433	Figure 80	The distribution of track momentum for data and simulated signal events, after previous selection requirements have been applied. The final bin includes all tracks above the axis range.	115
434			
435			
436			
437	Figure 81	The distribution of M_T for data and simulated signal events, after previous selection requirements have been applied. The final bin includes all tracks above the axis range.	116
438			
439			
440			
441	Figure 82	The distribution of summed tracked momentum within a cone of $\Delta R < 0.25$ around the candidate track for data and simulated signal events, after previous selection requirements have been applied. The final bin includes all tracks above the axis range.	117
442			
443			
444			
445			
446	Figure 83	The normalized, two-dimensional distribution of E/p and f_{EM} for simulated (a) 1200 GeV VLL R-Hadron, and (b) 1200 GeV, 10 ns R-Hadron, (c) $Z \rightarrow ee$, and (d) $Z \rightarrow \tau\tau$ events.	118
447			
448			
449			
450	Figure 84	Two-dimensional distribution of dE/dx versus charge signed momentum (qp) for minimum-bias tracks. The fitted distributions of the most probable values for pions, kaons and protons are superimposed.	120
451			
452			
453			
454	Figure 85	The distribution of mass estimated using dE/dx for simulated VLL R-Hadrons with masses between 1000 and 1600 GeV.	120
455			
456			
457	Figure 86	The acceptance \times efficiency as a function of R-Hadron (a) mass and (b) lifetime. (a) shows all of the combinations of mass and lifetime considered in this search, and (b) highlights the lifetime dependence for 1000 GeV and 1600 GeV R-Hadrons.	122
458			
459			
460			
461			
462	Figure 87	The distribution of (a) dE/dx and (b) momentum for tracks in data and simulated signal after requiring the event level selection and the track selection on p_T , hits, and N_{split} . Each sub-figure shows the normalized distributions for tracks classified as hadrons, electrons, and muons in data and R-Hadrons in the simulated signal.	124
463			
464			
465			
466			
467			
468			
469	Figure 88	The distribution of $M_{dE/dx}$ (a) before and (b) after the ionization requirement for tracks in simulated W boson decays and for the randomly generated background estimate.	126
470			
471			
472			

473	Figure 89	The distribution of $M_{dE/dx}$ (a) before and (b) after the ionization requirement for tracks in the validation region and for the randomly generated background estimate.	127
474			
475			
476			
477	Figure 90	The trigger efficiency for the HLT_xe70 trigger requirement as a function of Calorimeter E_T^{miss} for simulated data events with a W boson selection. Simulated signal events and simulated W boson events are also included.	132
478			
479			
480			
481			
482	Figure 91	The efficiency of the muon veto for R-hadrons of two different masses, as a function of $\frac{1}{\beta}$ for simulated R-Hadron tracks.	135
483			
484			
485	Figure 92	The average reconstructed MDT β distribution for $Z \rightarrow \mu\mu$ events in which one of the muons has a late arrival time in the MDT, for both data and simulation. A gaussian fit is superimposed.	136
486			
487			
488			
489	Figure 93	The observed mass distribution of events in data and the generated background distribution in (a) the VLL and (b) the long-lived (LL) signal region. A few example simulated signal distributions are superimposed.	138
490			
491			
492			
493	Figure 94	The observed and expected cross section limits as a function of mass for the VLL simulated signal. The predicted cross section values for the corresponding signals are also shown.	140
494			
495			
496			
497	Figure 95	The observed and expected cross section limits as a function of mass for each generated lifetime. The predicted cross section values for the corresponding signals are also shown. An example of Run 1 cross section limits and predicted cross sections are shown in (d) for comparison.	141
498			
499			
500			
501			
502			
503	Figure 96	The excluded range of masses as a function of gluino lifetime. The expected lower limit (LL), with its experimental $\pm 1\sigma$ band, is given with respect to the nominal theoretical cross section. The observed 95% LL obtained at $\sqrt{s} = 8$ TeV [86] is also shown for comparison.	143
504			
505			
506			
507			
508	Figure 97	The constraints on the gluino mass as a function of lifetime for a split-supersymmetry model with the gluino R-Hadrons decaying into a gluon or light quarks and a neutralino with mass of 100 GeV. The solid lines indicate the observed limits, while the dashed lines indicate the expected limits. The area below the curves is excluded. The dots represent results for which the particle is assumed to be prompt or VLL. This curve representing this analysis is shown in orange.	145
509			
510			
511			
512			
513			
514			
515			

517 LIST OF TABLES

518 Table 1	The particles in the SM and their corresponding superpartners in the MSSM	20
519		
520 Table 2	The design parameters of the LHC beam that determines the energy of collisions and the luminosity, for both the injection of protons, at the nominal circulation, and during the 2015 data-taking period.	33
521		
522		
523		
524 Table 3	The performance goals for each of the subsystems of the ATLAS detector. The $ \eta $ coverage specifies the range where the subsystem needs to be able to provide measurements with the specified resolution. The resolutions include a p_T or E dependence that is added in quadrature with a p_T/E independent piece.	38
525		
526		
527		
528		
529		
530 Table 4	A summary of the parameters of each of the three magnet systems on ATLAS.	40
531		
532 Table 5	A summary of the parameters of the inner detector and each of the subdetectors [16].	45
533		
534 Table 6	A subset of the trigger menu for the 2015 data collection with $L = 5 \times 10^{33} \text{ cm}^{-2} \text{ s}^{-1}$. Both the L1 and high level trigger (HLT) selection requirements and their trigger rates are shown measured at the specified luminosity are shown. The typical offline selections represent a typical set of offline requirements imposed after the trigger in an analysis.	59
535		
536		
537		
538		
539		
540		
541 Table 7	The dominant sources of corrections and systematic uncertainties in the JES estimation technique, including typical values for the correcting shift (Δ) and the associated uncertainty (σ).	95
542		
543		
544		
545 Table 8	The radial distances of each of the subdetectors and example arrival times for an R-Hadron with $\eta = 0$ and the specified β	102
546		
547		
548 Table 9	The expected number of events at each level of the selection for LL 1600 GeV, 10 ns R-Hadrons, along with the number of events observed in data, for 3.2 fb^{-1} . The simulated yields are shown with statistical uncertainties only. The total efficiency \times acceptance is also shown for the signal and the rejection factor relative to initial track requirement is shown for data.	121
549		
550		
551		
552		
553		
554		
555 Table 10	The expected number of background events within each of the mass windows for the stable and metastable signal regions.	128
556		
557		

558	Table 11	A summary of the sources of systematic uncertainty for the data-driven background in the signal region. If the uncertainty depends on the mass, the maximum values are reported.	129
559			
560			
561			
562	Table 12	A summary of the sources of systematic uncertainty for the simulated signal yield. The uncertainty depends on the mass and lifetime, and the maximum negative and positive values are reported in the table.	131
563			
564			
565			
566	Table 13	Example of the contributing systematic variations to the total systematic for the E_T^{miss} Scale, as measured in a 1200 GeV, VLL R-Hadron signal sample.	133
567			
568			
569	Table 14	The estimated number of background events and the number of observed events in data for the specified selection regions prior to the requirement on mass. The background estimates show statistical and systematic uncertainties.	137
570			
571			
572			
573			
574	Table 15	The left and right extremum of the mass window for each generated mass point with a 10 ns lifetime.	138
575			
576	Table 16	The left and right extremum of the mass window used for each generated VLL mass point.	138
577			
578	Table 17	The expected number of signal events, the expected number of background events, and the observed number of events in data with their respective statistical errors within the respective mass window for each generated VLL mass point	139
579			
580			
581			
582			
583	Table 18	The expected number of signal events, the expected number of background events, and the observed number of events in data with their respective statistical errors within the respective mass window for each generated mass point with a lifetime of 10 ns.	139
584			
585			
586			
587			
588	Table 19	The observed and expected 95% CL lower limit on mass for gluino R-Hadrons for each considered lifetime.	142
589			
590	Table 20	The left and right extremum of the mass window for each generated mass point with a 50 ns lifetime.	147
591			
592	Table 21	The left and right extremum of the mass window for each generated mass point with a 30 ns lifetime.	147
593			
594	Table 22	The left and right extremum of the mass window for each generated mass point with a 10 ns lifetime.	148
595			
596	Table 23	The left and right extremum of the mass window used for each generated mass point with a lifetime of 3 ns.	148
597			
598	Table 24	The left and right extremum of the mass window used for each mass point with a lifetime of 1 ns.	148
599			
600	Table 25	The left and right extremum of the mass window for each generated mass point with a lifetime of 0.4 ns.	149
601			
602	Table 26	The left and right extremum of the mass window used for each generated stable mass point.	149
603			

604	Table 27	The expected number of signal events, the expected number of background events, and the observed number of events in data with their respective statistical errors within the respective mass window for each generated mass point with a lifetime of 50 ns.	149
605			
606			
607			
608			
609	Table 28	The expected number of signal events, the expected number of background events, and the observed number of events in data with their respective statistical errors within the respective mass window for each generated mass point with a lifetime of 30 ns.	150
610			
611			
612			
613			
614	Table 29	The expected number of signal events, the expected number of background events, and the observed number of events in data with their respective statistical errors within the respective mass window for each generated mass point with a lifetime of 10 ns.	150
615			
616			
617			
618			
619	Table 30	The expected number of signal events, the expected number of background events, and the observed number of events in data with their respective statistical errors within the respective mass window for each generated mass point with a lifetime of 3 ns.	151
620			
621			
622			
623			
624	Table 31	The expected number of signal events, the expected number of background events, and the observed number of events in data with their respective statistical errors within the respective mass window for each generated mass point with a lifetime of 1 ns.	151
625			
626			
627			
628			
629	Table 32	The expected number of signal events, the expected number of background events, and the observed number of events in data with their respective statistical errors within the respective mass window for each generated mass point with a lifetime of p4 ns.	152
630			
631			
632			
633			
634	Table 33	The expected number of signal events, the expected number of background events, and the observed number of events in data with their respective statistical errors within the respective mass window for each generated stable mass point	152
635			
636			
637			
638			

639 ACRONYMS

- 640 SM Standard Model
641 CERN European Organization for Nuclear Research
642 SUSY Supersymmetry
643 MSSM Minimal Supersymmetric Model
644 cMSSM Constrained MSSM
645 pMSSM Phenomenological MSSM
646 LSP Lightest Supersymmetric Particle
647 LHC Large Hadron Collider
648 ATLAS A Toroidal LHC ApparatuS
649 CMS Compact Muon Solenoid
650 ALICE A Large Ion Collider Experiment
651 LHCb Large Hadron Collider beauty experiment
652 LEP the Large Electron Positron collider
653 PS Proton Synchrotron
654 PSB Proton Synchrotron Booster
655 SPS Super Proton Synchrotron
656 SCT silicon microstrip
657 TRT Transition Radiation Tracker
658 LAr liquid argon
659 EM electromagnetic
660 RPC Resistive Plate Chamber
661 TGC Thin Gap Chamber
662 MDT Monitored Drift Tube
663 CSC Cathode Strip Chamber
664 ToT time over threshold
665 RoI Region of Interest

- 666 LCW local cluster weighted
667 MIP minimally ionizing particle
668 IP impact parameter
669 EPJC European Physical Journal C
670 JES jet energy scale
671 LLP Long-Lived Particle
672 LL long-lived
673 VLL very long-lived
674 CR Control Region
675 NLO next-to-leading order
676 NLL next-to-leading logarithmic
677 PDF parton distribution function
678 ISR initial state radiation
679 RMS root mean square
680 IBL Insertible B-Layer
681 CP Combined Performance
682 MDT Monitored Drift Tube
683 RF radiofrequency
684 L1 Level 1
685 HLT high level trigger
686 QCD quantum chromodynamics
687 BSM Beyond the Standard Model

688

689 INTRODUCTION

690 As of 2012, with the discovery of the Higgs boson, the [SM](#) provides a complete
691 and validated description of the interactions of fundamental particles. It de-
692 scribes a remarkable range of phenomena given its simple foundation, and has
693 been successful in explaining high energy physics in all experiments yet per-
694 formed. However, it is clear that the picture is incomplete: without a description
695 of gravity or an explanation for dark matter, an extension is necessary to de-
696 scribe new physics at higher energies. These deficiencies motivate a wide range
697 of experiments that search for new physics. The [LHC](#) provides the highest en-
698 ergy approach, seeking to discover unobserved particles or interactions in high
699 energy proton collisions.

700 The experiments at the [LHC](#) have searched for a variety of new phenomena
701 in the years since collisions began in 2010. A major focus of these searches has
702 been on Supersymmetry ([SUSY](#)), an extension to the [SM](#) which has the potential
703 to ameliorate many of its shortfalls. None of the searches have found evidence of
704 new physics, and between them they have begun to rule out a number of models
705 that would predict new particles at the TeV scale. This motivates searches for
706 more exotic signals that may have been missed, using analysis techniques tuned
707 specifically for those signals.

708 This dissertation presents a search for Long-Lived Particles ([LLPs](#)) using the
709 13 TeV collisions collected during 2015 at the [LHC](#). Charged [LLPs](#) are predicted
710 to exist in a subset of [SUSY](#) models, and have dramatically different detector sig-
711 natures than both [SM](#) processes and other [SUSY](#) models. This search focuses on
712 isolating that unique signature using ionization measurements in the ATLAS de-
713 tector.

714 Part I provides the theoretical context and motivation for a search for new
715 physics in high energy collisions. Chapter 2 outlines the basic framework of the
716 [SM](#) and describes its particles and interactions. It also discusses the limitations of
717 the [SM](#) that motivate the existence of new physics. Chapter 3 discusses a possible
718 solution to the shortcomings of the [SM](#), the theory of Supersymmetry, and the
719 ways that it can generate [LLP](#).

720 Part II discusses the structure of the accelerator complex that provides col-
721 lisions as well as the experiment that measures them. Chapter 4 summarizes
722 the design and performance of the [LHC](#) and the features of the proton-proton
723 collisions it produces. Chapter 5 then discusses the components of the ATLAS
724 detector and how they can be used to measure the particles produced in [LHC](#) col-
725 lisions. Chapter 6 describes the algorithms used to reconstruct physics particles
726 and processes from the electronic signals in the detector.

727 Part III presents a measurement of calorimeter response, an important compo-
728 nent of event reconstruction used in many physics analyses. Chapter 7 describes
729 a direct, in situ measurement of calorimeter response using isolated hadrons, and

730 investigates the modeling of that response in simulation. Chapter 8 uses those
731 measurements to construct a correction for the energy of jets in simulation, the
732 JES, and to estimate an uncertainty for that correction.

733 Part IV details the search for LLPs. It begins with a discussion of the simulation
734 of LLPs in ATLAS, focusing on the detector signatures and how they vary with
735 the properties of those particles in Chapter 9. Then Chapter 10 discusses the
736 strategy of the search and the requirements used to select LLPs and to reject SM
737 backgrounds. Chapter 11 explains a method for predicting the background from
738 SM processes, and shows a validation of the technique. Chapter 12 describes the
739 systematic uncertainties on both the selection efficiency for signal events and
740 the background method. The results of the search are presented in Chapter 13.
741 Chapter 14 concludes with a summary of the search and its context in the com-
742 bined search for LLP, as well as an outlook for future searches.

743

PART I

744

THEORETICAL CONTEXT

745

746

747 STANDARD MODEL

748 The **SM** of particle physics seeks to explain the symmetries and interactions of
 749 fundamental particles. The **SM** provides predictions in particle physics for inter-
 750 actions up to the Planck scale (10^{19} GeV). It has been tested by several genera-
 751 tions of experiments and has been remarkably successful; no significant devia-
 752 tions from its predictions have been found.

753 The theory itself is a quantum field theory grown from an underlying sym-
 754 metry, $SU(3) \times SU(2) \times U(1)$, that generates all of the interactions consis-
 755 tent with experimental observations¹. These interactions are referred to as the
 756 Strong, Weak, and Electromagnetic forces. Each postulated symmetry necessi-
 757 tates the existence of an associated conserved charge, which appear as properties
 758 of the observed particles in nature.

759 Although this model has been very predictive, the theory is incomplete; for
 760 example, it is not able to describe gravity or astronomically observed dark mat-
 761 ter. These limitations suggest a need for an extension or new theory to describe
 762 physics at higher energies.

763 2.1 ACTION AND THE LAGRANGIAN

Originally, both action and the Lagrangian were constructed for an integral reformulation of the laws of classical mechanics, which is a purely mathematical step: any differential equation can be re-expressed in terms of an integral equation. The Lagrangian, \mathcal{L} , is classically given by the difference of kinetic energy and potential energy. The Lagrangian is defined this way so that the action, \mathcal{S} , given by

$$\mathcal{S}[\mathbf{q}(t)] = \int_{t_1}^{t_2} \mathcal{L}(\mathbf{q}, \dot{\mathbf{q}}, t) dt \quad (1)$$

764 returns the classical equations of motion when one requires it to be stationary
 765 in the path, $\mathbf{q}(t)$. This formulation of classical mechanics is extremely useful in
 766 calculations, and generalizes beautifully to cover all types of physics.

767 In particular, with the development of quantum mechanics in the twentieth
 768 century, the concepts of action and the Lagrangian were found to generalize to
 769 more complicated physics for which the classical laws do not hold. Quantum
 770 mechanics and quantum field theory can be constructed from the action, using
 771 the path integral formulation, by assuming that a particle undergoes all possible
 772 paths $\mathbf{q}(t)$ with an imaginary phase given by $e^{i\mathcal{S}[\mathbf{q}(t)]/\hbar}$. This reduces to classical
 773 mechanics in the limit as \hbar goes to zero, as all paths for which the action is not
 774 stationary interfere with each other so as to cancel their contributions. Because

¹ excluding gravity

775 the wavefunction of a particle can be completely determined through the action
 776 and the action depends only on the Lagrangian, the Lagrangian itself is sufficient
 777 to describe the physics governing the particle.

778 So, in both classical and quantum mechanics, the Lagrangian of a system con-
 779 tains everything there is to know about the system, apart from initial conditions.
 780 Thus, the most natural way to express that a system has a certain symmetry is to
 781 require that the Lagrangian is invariant under a corresponding symmetry trans-
 782 formation. This makes the Lagrangian the central piece of the discussion of
 783 gauge invariance; the mathematical representation of gauge invariance is that a
 784 gauge transformation on the appropriate components of the Lagrangian returns
 785 an identical Lagrangian. That is,

$$\mathcal{L}(\psi, D^\mu) = \mathcal{L}(U\psi, D'^\mu) \quad (2)$$

786 where ψ is the wavefunction and D^μ is the derivative operator, both of which
 787 may transform under a symmetry operation. There are a number of immedi-
 788 ate and surprisingly powerful consequences of requiring that the Lagrangian is
 789 invariant under a symmetry operation.

790 2.2 GAUGE INVARIANCE AND FORCES

791 The simplest possible relativistic, quantum Lagrangian for matter particles is the
 792 free Dirac Lagrangian, which describes a relativistic fermion in a vacuum.

$$\mathcal{L} = i\bar{\psi}\not{d}\psi - m\bar{\psi}\psi \quad (3)$$

793 A fermion denotes a particle with spin-1/2, and the kinematic term ($i\bar{\psi}\not{d}\psi$) is
 794 chosen to correctly describe the free propagation of a fermionic particle with
 795 mass m . This equation is invariant under a global $U(1)$ transformation, that is
 796 changing ψ by a complex phase has no effect. The derivative operator commutes
 797 with a constant phase factor, and wherever ψ appears its complex conjugate also
 798 appears so as to cancel out the change of phase. However, the Lagrangian as writ-
 799 ten is not invariant under the local $U(1)$ symmetry postulated for the SM, which
 800 can be written as $U = e^{i\alpha(x)}$. The piece of the Lagrangian involving a derivative
 801 will return an extra term that will break the invariance of the Lagrangian under
 802 this transformation:

$$\begin{aligned} \mathcal{L}' &= i(\bar{\psi}U^\dagger)\not{d}(U\psi) - m(\bar{\psi}U^\dagger)(U\psi) \\ &= i(\bar{\psi}U^\dagger)U(\not{d} - \gamma^\mu\partial_\mu\alpha(x))\psi - m(\bar{\psi}U^\dagger)(U\psi) \\ &= i\bar{\psi}\not{d}\psi - m\bar{\psi}\psi - i\gamma^\mu\partial_\mu\alpha(x)\bar{\psi}\psi \\ &= \mathcal{L} - i\gamma^\mu\partial_\mu\alpha(x)\bar{\psi}\psi \\ &\neq \mathcal{L} \end{aligned}$$

803 So, in order to enforce the required symmetry, the typical approach is to con-
 804 struct a covariant derivative, that is to add a term to the derivative operator

so that the unwanted term in \mathcal{L}' is exactly canceled. A generic form for such a derivative is given by

$$D^\mu = \partial^\mu - iqA^\mu$$

where at this point A^μ is an arbitrary field that transforms under the $U(1)$ operator and q is a scaling factor. Adding this component to the above Lagrangian gives

$$\mathcal{L}' = i(\bar{\psi}U^\dagger)U(\not{d} - \gamma^\mu\partial_\mu\alpha(x) - iq\gamma^\mu A'_\mu)\psi - m(\psi U^\dagger)(U\psi) \quad (4)$$

$$\mathcal{L}' = \mathcal{L} + \gamma^\mu(-i\partial_\mu\alpha(x) - iqA'_\mu + iqA_\mu)\bar{\psi}\psi \quad (5)$$

and because the transformation of A^μ is unspecified, $\mathcal{L} = \mathcal{L}'$ whenever

$$A'_\mu = A_\mu - \frac{1}{q}\partial_\mu\alpha(x)$$

The above procedure demonstrated that beginning with the Lagrangian for a free fermion and imposing a local $U(1)$ symmetry required the existence of a vector field A^μ , and specified its transformation under the $U(1)$ gauge group. The additional term in the derivative can be expanded to form a completely separate term in the Lagrangian,

$$\mathcal{L} = i\bar{\psi}\not{d}\psi - m\bar{\psi}\psi - (q\bar{\psi}\gamma^\mu\psi)A^\mu \quad (6)$$

and in this form it is clear that the A^μ term has the exact form of the electromagnetic interaction. That is, this is the Lagrangian which reproduces the relativistic form of Maxwell's equations for a particle interacting with an electromagnetic field. It is natural to also introduce a term to the Lagrangian at this point to describe the free propagation of the vector A field, where the propagation of a vector field has the form of

$$-\frac{1}{16\pi}F^{\mu\nu}F_{\mu\nu} \quad \text{with} \quad F_{\mu\nu} = \partial_\mu A_\nu - \partial_\nu A_\mu \quad (7)$$

This then also describes the electromagnetic interactions in a vacuum and the propagation of a photon. This component of the Lagrangian could also potentially include a mass term, but such a term would not be gauge invariant and so must be excluded. The photon is an example of a gauge boson, a spin-1 particle required to exist by a gauge symmetry of the Lagrangian and one that corresponds to a force. In summary, requiring the $U(1)$ symmetry was enough to recover all of electromagnetism and to predict the existence of a photon in the SM.

The interaction term that was placed into the Lagrangian by this procedure can be conveniently summarized with Feynman diagrams, which diagrammatically represent a transition from an initial state to a final state. The contribution

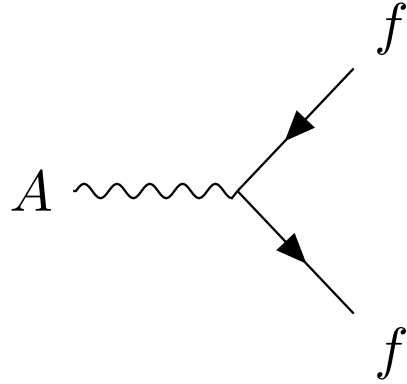


Figure 1: A Feynman diagram representing the interaction of the A field with a generic fermion, f .

of all diagrams that start with the same initial state and end with the same final state must be summed, but more complicated diagrams can be built by linking together the simplest versions. A diagram that corresponds to the above term, $(q\bar{\psi}\gamma^\mu\psi)A^\mu$, is shown in Figure 1, for an interaction with a generic fermion.

2.2.1 $SU(2) \times U(1)$ AND THE ELECTROWEAK FORCE

The full picture of the electroweak section of the SM is more complicated than the simplified explanation of the electromagnetic piece described above. In practice, it is necessary to consider the entire $SU(2) \times U(1)$ symmetry together, but the procedure is the same. Enforcing the symmetry on the Lagrangian requires the introduction of a covariant derivative, this time with four total distinct terms, one for each of the generators of $SU(2) \times U(1)$. The result is a series of terms in the Lagrangian which describe the interaction of a fermion with four vector (spin-1) fields, the W_1 , W_2 , W_3 , and B fields. These fields can mix in the quantum sense, and linear combinations form the W^+ , W^- , Z , and A fields that are considered actual particles in the SM².

2.2.2 $SU(3)$ AND THE STRONG FORCE

The same procedure can be applied starting with the $SU(3)$ symmetry requirement, where eight additional fields must be introduced, one for each of the generators of $SU(3)$. The resulting Lagrangian describes quantum chromodynamics (QCD) and predicts the existence of eight massless gauge bosons known collectively as gluons. The complexity of the interactions of those eight gluons leads to surprising phenomena, discussed in Section 2.5.3.

² These states are the actual particles because they are mass eigenstates, but the full explanation of this will have to wait for the discussion of the Higgs mechanism in Section 2.4.

855 2.3 NOETHER'S THEOREM, CHARGES, AND MATTER

856 Another direct consequence of the symmetries stipulated in the SM are a series
857 of conserved quantities, Noether charges, named after the mathematician and
858 physicist Emmy Noether. The charges arise as a direct consequence of Noether's
859 theorem, which can be informally stated as

860 *For every symmetry of the Lagrangian, there exists a corresponding phys-
861 ical quantity whose value is conserved in time.*

862 Or, stated another way, symmetries of the Lagrangian mathematically require
863 the conservation of specific quantities taken from the Lagrangian. This rela-
864 tionship can also be thought of as operating in the other direction, the exis-
865 tence of a conserved charge can be shown to generate the symmetry in the La-
866 grangian. This theorem is actually quite striking in a somewhat unexpected re-
867 lation between simple geometric symmetries and physically observable conser-
868 vation laws. For example, the theorem connects the translation invariance of
869 the Lagrangian in space to the conservation of momentum and the translation
870 invariance in time to the conservation of energy.

871 In the context of the SM, the required symmetries of $U(1) \times SU(2) \times SU(3)$
872 correspond to the charges that are considered properties of all elementary par-
873 ticles. The most familiar of these properties is the electric charge, Q, which is
874 one of the conserved quantities of $SU(2) \times U(1)$. The remaining pieces of
875 $SU(2) \times U(1)$ correspond to weak isospin, T and T_3 , where T has only non-
876 negative values and T_3 can be positive and negative. T is the magnitude of the
877 full three vector of weak isospin, T, and T_3 is the projection along the third com-
878 ponent that is the other conserved quantity derived from $SU(2) \times U(1)$. The
879 $SU(3)$ symmetry is generated by the three colors of QCD, red, green, and blue,
880 each with a corresponding opposite color, anti-red, anti-green, and anti-blue.
881 The color charges are also conserved in the SM.

882 The matter in the observable universe consists of a collection of particles which
883 carry these charges, in addition to spin and mass. The matter particles are all
884 fermions: particles with spin-1/2. All of the fermions belong to one of two
885 groups, quarks and leptons, and one of three generations. Each of the genera-
886 tions have the same quantum numbers and charges but significantly different
887 masses; the particles in higher generations have increasing mass. Quarks are dis-
888 tinguished from leptons in that they carry color charge, in addition to electric
889 charge and weak isospin. The particles in the SM are summarized in Figure 2,
890 and the matter particles are the twelve types of fermions displayed on the left
891 side of the graphic.

892 2.3.1 QUARKS

893 The three generations of quarks each consist of a quark with electric charge +2/3
894 and one with charge -1/3. They are called up and down, charm and strange,
895 and top and bottom respectively, and these are referred to as the quark flavors.
896 Although Figure 2 only shows these six flavors, there is a unique particle for each

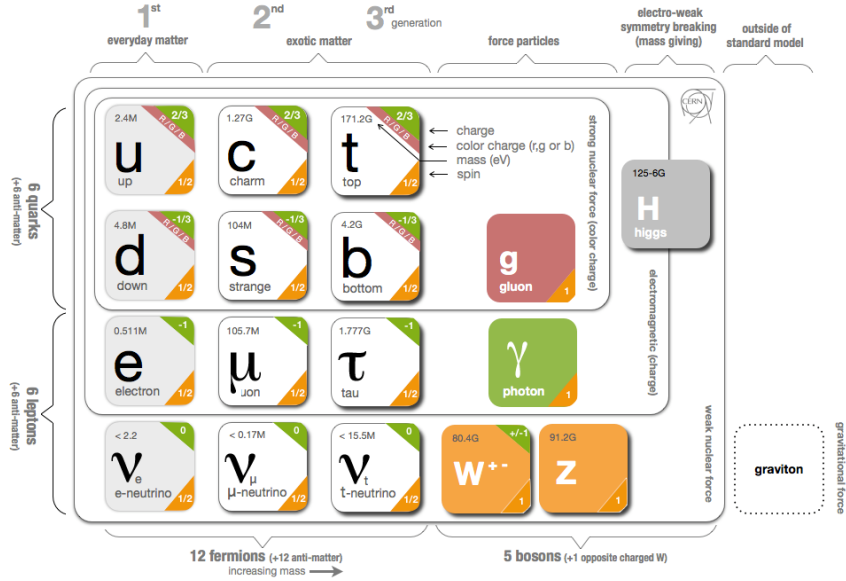


Figure 2: The particle content of the SM, including the names, masses, spins, and charges of each of the particles.

combination of the three colors and flavor. And each quark has an anti-particle with the opposite electric charge values.

However, individual quarks are never observed in nature, but instead form color-neutral bound states. This is a consequence of interaction of gluons with color charge called confinement, discussed in Section 2.5.3. One way to form a color neutral combination is a bound state of three quarks with three different color charges, called a baryon. Baryons are the most common type of quark configuration in conventional matter, and include protons and neutrons. The other common configuration is a bound state of a quark and an anti-quark, called a meson, where the two quarks have opposite colors. Although there is no direct conservation law resulting from the symmetries of the SM Lagrangian, an accidental symmetry results in the approximate conservation of baryon number, B , where baryons have $B = 1$ and mesons have $B = 0$. That is, no interactions have been observed which directly alter baryon number.

2.3.2 LEPTONS

The remaining fermions, the leptons, do not carry color charge. Each generation contains an electrically charged lepton, the electron, muon, and tau, and an electrically neutral lepton called a neutrino. For the charged leptons, the flavors are mass eigenstates, with the masses listed in Figure 2. The flavors of the neutrinos, on the other hand, are not mass eigenstates: their propagation in quantum superpositions of flavor states leads to oscillations between different flavors. The absolute masses of the neutrinos are not currently known, but the phenomenon

of oscillations shows that they have three different mass values. Another accidental symmetry leads to an approximate conservation of lepton number L , the difference in the number of leptons and anti-leptons; again there are no interactions present in the SM which directly alter lepton number.

2.3.3 CHIRALITY

All of the fermions described above have two possible values of the magnitude of weak isospin, T , either 0 or 1/2. The fermions with $T = 0$ are called right-handed, while those with $T = 1/2$ are called left-handed. Because T is the charge corresponding to the weak force, right-handed particles do not interact with the weak gauge bosons in the same way that neutral particles do not interact with photons. For left-handed fermions, each of the quark and lepton generations have one particle with $T_3 = -1/2$ and one with $T_3 = +1/2$. The neutrinos have $T_3 = +1/2$, while the charged leptons have $T_3 = -1/2$. Similarly, the positively charged quarks have $T_3 = +1/2$ and the negatively charged quarks have $T_3 = -1/2$. Because the right-handed neutrinos would have no charge of any type, it is not clear if they exist at all.

2.4 HIGGS MECHANISM AND MASS

The description of the electroweak forces above left out an important part of the observed nature of the electroweak force. Many physical experiments observed phenomena corresponding to the interaction of the weak bosons that were best explained if they had significant masses. But as mentioned before, massive bosons would break the gauge invariance of the Lagrangian. A large mass for the W and Z bosons is necessary to explain the relative weakness of their interactions compared to the electromagnetic field. The Lagrangian's discussed above did not include a mass term for the gauge bosons, and in fact such a term would not be allowed by the requirement of gauge invariance. This was a significant problem for the SM, and the symmetry of the electroweak sector would have to be broken in order to allow for non zero masses for some of the gauge bosons.

One mechanism to allow for this symmetry breaking is the Higgs mechanism, which posits the existence of an additional scalar field. It begins with a $SU(2) \times U(1)$ invariant Lagrangian of the form

$$\mathcal{L} = |D_\mu \phi|^2 - \frac{1}{2}\mu^2\phi^+\phi - \frac{1}{4}\lambda(\phi^+\phi)^2 \quad (8)$$

where ϕ is the new scalar field with two components and, importantly, μ^2 is negative. This leads to a minimum value of the field at a non-zero value of ϕ , specifically where

$$\langle\phi\rangle = \frac{1}{\sqrt{2}} \begin{pmatrix} 0 \\ v \end{pmatrix} \quad \text{with} \quad v = \frac{2\mu^2}{\lambda} \quad (9)$$

954 Expanding the original Lagrangian about its expectation value in terms of the
 955 perturbation H ,

$$\langle \phi \rangle = \frac{1}{\sqrt{2}} \begin{pmatrix} 0 \\ v + H \end{pmatrix} \quad (10)$$

956 gives potential terms in the Lagrangian like

$$\mathcal{L}_H = -\frac{1}{2} m_H^2 H^2 - \sqrt{\frac{\lambda}{2}} m_H H^3 - \frac{1}{4} \lambda H^4 \quad (11)$$

957 where $m_H = \sqrt{2}\mu$. The form of this Lagrangian shows that the non-zero ex-
 958 pectation value of the ϕ field has introduced a massive scalar field H with self
 959 interaction terms. It has an additional important consequence on the description
 960 of the gauge bosons, through the expansion of the term involving the covariant
 961 derivative:

$$|D_\mu \phi|^2 \supset \frac{1}{8} (g^2 (W_{1\mu} W_1^\mu + W_{2\mu} W_2^\mu) + (g' B_\mu - g W_3 \mu)^2) \quad (12)$$

962 where the W_i and B fields are the original $SU(2) \times U(1)$ gauge fields men-
 963 tioned previously. The above equation can be rearranged using linear combi-
 964 nations of the fields to form mass terms for the gauge bosons, and the mass eigen-
 965 states are exactly the W^\pm , Z , and A fields. Only the A field, corresponding to the
 966 photon, results in a zero mass, and the remaining three particles have non-zero
 967 mass values. Because the previously introduced Lagrangian, written in terms of
 968 ϕ , was clearly gauge invariant, this resulting configuration must also be gauge
 969 invariant.

970 This is the Higgs mechanism, where the introduction of a gauge invariant
 971 scalar field with a non-zero expectation value can generate masses for the gauge
 972 bosons without violating the underlying symmetries. The particle that is associ-
 973 ated with the perturbations of this field, H , is called the Higgs boson, and is said
 974 to generate the masses of the remaining bosons because the vacuum expectation
 975 value introduces mass-like terms for each of the bosons. The resulting masses
 976 are listed in Figure 2. Because this mechanism was so successful in describing
 977 the observed properties of the W and Z bosons, it has been considered part of
 978 the SM for decades, although the actual Higgs boson was only recently observed
 979 in 2012, fully confirming the theory.

980 The Higgs mechanism is also responsible for generating the masses of the
 981 fermions. The original mass terms that were listed in the Lagrangian for fermions
 982 are replaced with Yukawa coupling terms, which introduce interactions between
 983 the ϕ field and the fermions. Like with the gauge bosons, the non-zero expec-
 984 tation value of the field yields mass terms, and the expansion about that value
 985 introduces interaction terms between the fermions and the Higgs boson. The
 986 masses are different between each fermion because each has a different Yukawa
 987 coupling, which results in the masses listed in Figure 2.

988 2.5 PHENOMENOLOGY

989 The SM Lagrangian described above contains all of the information necessary
 990 to describe particle physics through the path integral formulation. However, a
 991 tremendous amount of complexity emerges from that description because of the
 992 diverse allowed interactions between the ensemble of particles in the SM. A qual-
 993 itative understanding of the phenomenology produced by those interactions is
 994 immensely helpful in understanding the analysis of particle physics.

995 2.5.1 STANDARD MODEL CALCULATIONS

The terms in the Lagrangian describing interactions of particles can be used to evaluate cross sections or decay widths through perturbation theory. The feynman diagrams corresponding to those interactions provide a convenient tool to calculate those values, as each diagram encodes a transition amplitude between the initial and final state according to feynman rules. The transition amplitude includes a phase space component to account for the initial and final momenta, and an addition matrix element which describes the interaction from the SM. The complex amplitude for each process with the same initial and final state must be summed, and then the cross section or decay width is calculated as the square of the amplitude integrated over all valid final state momenta. For example, the decay rate for a particle of mass m_A to two final state particles with momenta \mathbf{p}_i and \mathbf{p}_j is given by

$$\Gamma = \int \frac{d^3 p_i d^3 p_j}{(2\pi)^6 4E_i E_j} (2\pi)^4 \delta^{(4)}(\mathbf{p}_A - \mathbf{p}_i - \mathbf{p}_j) |\mathcal{M}|^2$$

996 where the prefactor is the phase space term, the delta function enforces conser-
 997 vation of four-momentum, and \mathcal{M} is the matrix element. The matrix element
 998 includes dimensionless constant terms that describe the strength of the interac-
 999 tion, called coupling constants: α for the photon, α_W for the weak bosons, and
 1000 α_s for the gluons.

1001 The sum over all diagrams with the same initial and final state leads to im-
 1002 portant consequences in the SM. Most process have a small number of leading
 1003 order diagrams, where leading order indicates the diagram with the fewest fac-
 1004 tors of the coupling constants. When the coupling constants are less than unity,
 1005 the diagrams of higher order have diminishing contributions. This is called the
 1006 perturbative regime, and allows for approximate calculations by using a set or-
 1007 der, referred to as LO! (LO!), next-to-leading order (NLO), and so on. A coupling
 1008 constant greater than unity results in a non-perturbative regime, and requires
 1009 other calculation techniques.

1010 However, even in a perturbative theory, the sum over all diagrams in the ampli-
 1011 tude includes loop diagrams; for example any photon line in a feynman diagram
 1012 can be replaced with the line in Figure 3 and still form a vaild interaction. These
 1013 and other types of loop diagrams introduce divergent contributions to SM pro-
 1014 cesses, which would seem to make the theory inconsistent. The solution to this
 1015 problem is to absorb those contributions into the coupling constants and charges

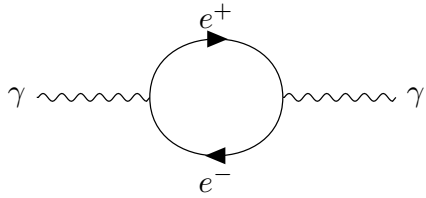


Figure 3: A feynman diagram for photon propagation including a loop of electrons.

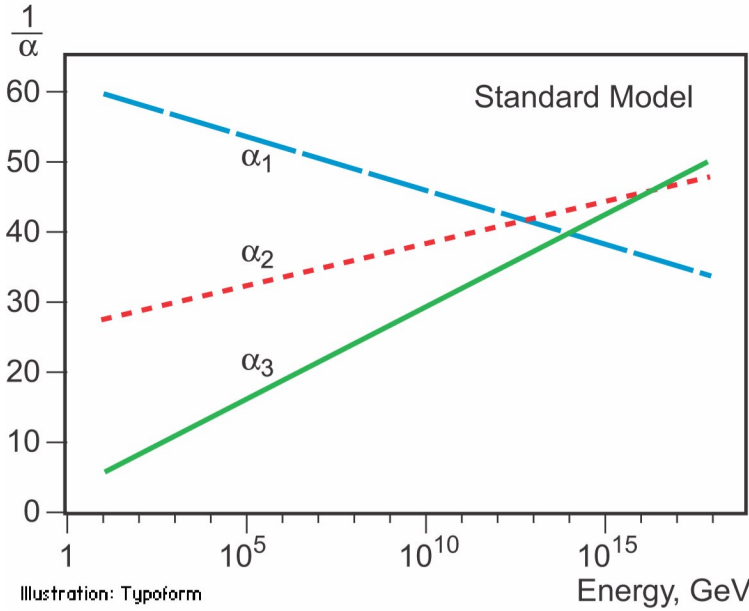


Figure 4: An approximation of the running of the coupling constants in the SM up to the Planck scale [1].

in the Lagrangian, so that the combination of the bare value and the loop contributions gives the correct physical observables. This process is called renormalization, and a theory where the divergences can be consistently absorbed into the definition of the constants in the Lagrangian is called renormalizable.

Setting the renormalized coupling constants requires a measurement at a specific energy scale, and at exactly that scale the contributions of the loop diagrams are precisely cancelled. At a different energy, however, the loop diagram contribution changes, and can be thought of as a difference in the coupling constant. The renormalization procedure thus predicts a variation of the coupling constants with the scale of the interaction, and specifies how they change with energy. The energy dependence is called the running of the coupling constants, and the effect on the three couplings in the SM is shown in Figure 4.

2.5.2 ELECTROWEAK PHYSICS

The masses of the W and Z bosons result in significantly different processes for the weak fields than the electromagnetic field, despite their interactions being similar before symmetry breaking. The massless photon is stable, and can

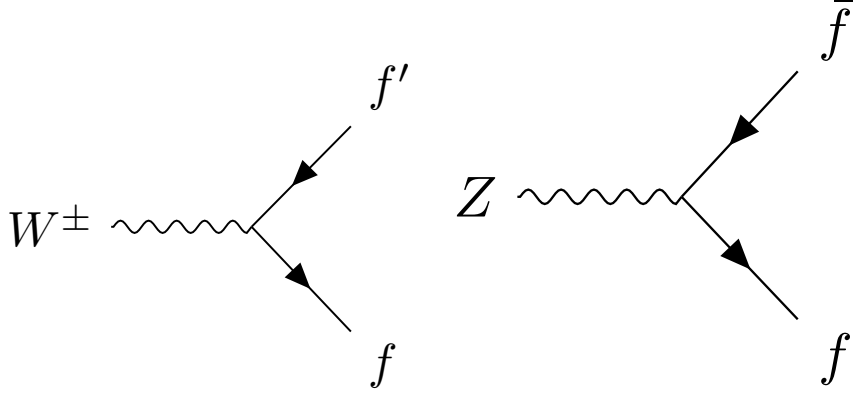


Figure 5: The Feynman diagrams representing the decays of the W and Z bosons to fermions. Here f indicates a generic fermion, \bar{f} its antiparticle, and f' the partner of that fermion in the same generation.

propagate in a vacuum, resulting in the familiar long range interactions of electromagnetism. The W and Z bosons, however, are unstable, as they have large enough masses to decay to fermions, such as the decays shown in Figure 5. For this reason, photons can be observed directly, while the other bosons are sufficiently short-lived (with lifetimes around 10^{-25} s) that they can only be measured from their decay products.

Because the electroweak bosons interact with both quarks and leptons, they are responsible for the production of leptons in proton-proton collisions. Z bosons and photons produce pairs of opposite sign, same flavor leptons. W bosons, on the other hand, produce a single lepton and the corresponding neutrino. The electroweak bosons also decay to hadrons by producing pairs of quarks, as shown in Figure 5. The Z boson decays to hadrons with a branching ratio of 69.9%, to neutrinos with 20.0%, and to charged leptons 10.1% of the time [2]. The W boson decays to hadrons with a branching ratio of 67.6% and to leptons 32.4% [2].

2.5.3 STRONG PHYSICS

The phenomenology of the strong sector differs significantly from the weak sector because the gluons are massless but color charged. Because of this, gluons can interact with each other, and contributions from multiple gluon interactions lead to a significant growth in the strength of the field at low energies. The dependence of the field strength on the energy scale is described by renormalization, and in QCD the coupling is only small at high energies. Below approximately 1 GeV, the strength of those interactions results in confinement: the interactions are so strong that when quark-antiquark pairs separate, the fields between them generate additional quarks to form color neutral bound states. Above around the GeV scale, the interactions of quarks become perturbative, similar to the electroweak fields; this phenomenon is known as asymptotic freedom.

At lower energies, however, the strength of the strong interaction is so significant that the interactions of color-charged particles create additional particles until they form neutral bound-states. This process is known as hadronization, and explains why no quarks are observed isolated in nature: they all form bound states of hadrons like protons, neutrons, and pions. The hadronization process can produce a significant number of particles, so that a single energetic quark recoiling against another quark can generate a cascade of dozens of hadrons. Because of the initial boost of such an energetic configuration, the resulting hadrons are collimated, and conical spray of particles often referred to as a jet.

2.5.4 PROTON-PROTON COLLISIONS

Proton-proton collisions are a convenient way to generate high energy interactions to probe the SM and to search for new physics. At the energies that will be discussed in this analysis, the substructure of the protons is very important to the description of the resulting interactions. At lowest order, protons are composed of two up quarks and one down quark, but this description is incomplete. The actual bound state includes a chaotic sea of additional gluons and $q\bar{q}$ pairs, each of which carries a variable fraction of the proton's energy. When a proton-proton collision takes place, it is these constituents that interact with each other, resulting in a highly variable collision energy even when the proton-proton energy is consistent.

The fraction of the energy carried by each constituent varies moment to moment, but can be modelled probabilistically by PDFs. These are difficult to predict theoretically, as the QCD calculations are non-perturbative, and instead are measured in hard-scattering experiments. They are usually represented by how often a given type of particle carries a fraction x of the total proton energy. Those fractions change significantly with the scale of the interaction, Q ; the PDFs of proton-proton collisions at both $Q^2 = 10 \text{ GeV}^2$ and $Q^2 = 10^4 \text{ GeV}^2$ are shown in Figure 6.

2.5.5 SIMULATION

Although the SM provides the necessary components to model the proton-proton collisions at the LHC, the complexity of the processes make direct predictions difficult. The LHC experiments rely on simulations that break down the collisions and resulting detector interactions into several steps in order to predict expected SM and even Beyond the Standard Model (BSM) events. The simulation begins with a selection of two proton constituents to collide from the PDFs described in Section 2.5.4, which fully specify the particle types and their momenta. The initial momenta are then fed into an event generator, which calculates the cross section and predicts the final momentum using the matrix element formulation described in Section 2.5.1. This analysis uses both the Pythia 6.4.27 [4] and MG5_aMC@NLO [5] generators in simulated events. The next step calculates additional processes that occur during the primary interaction, including hadronization, fragmentation, and initial state radiation. The result of this intial event

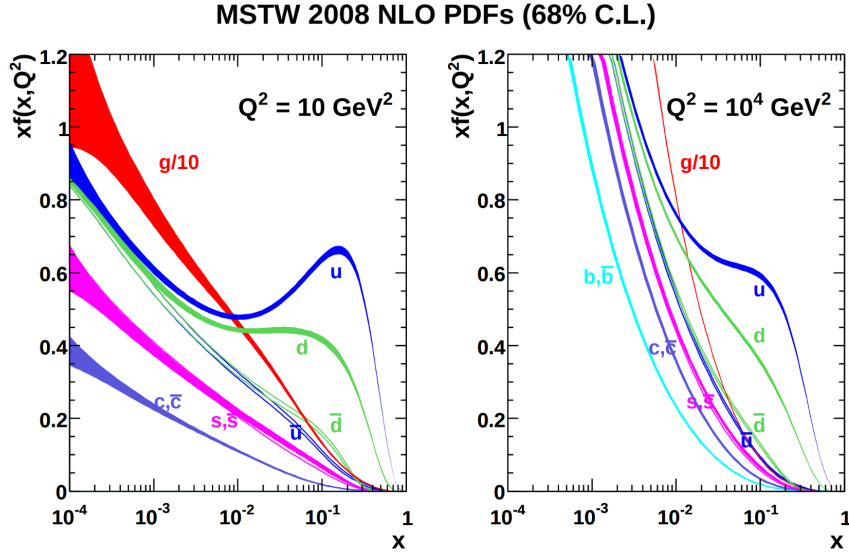


Figure 6: The PDFs for proton-proton collisions at $Q^2 = 10 \text{ GeV}^2$ and $Q^2 = 10^4 \text{ GeV}^2$. Each shows the fraction of particles which carry a fraction x of the total proton energy at the specified scale [3]. The distribution for gluons is scaled by 0.1 to fit within the axis range.

1100 generation is a series of particles and momentum that were produced in the col-
 1101 lision. These initial particle states are recorded for simulation studies, and are
 1102 often referred to as truth.

1103 These particles must then be propagated through a simulated detector geo-
 1104 metry, where the signal they produce in the detector models can be modeled.
 1105 Geant4 [6] provides a toolbox that describes the propagation of particles in the
 1106 magnetic field as well as their interactions with the detector material. It also sim-
 1107 ulates secondary interactions where additional particles may be produced, such
 1108 as a photon interacting with the detector material and converting to two elec-
 1109 trons. Each particle is tracked until its energy is lost or it exits the volume of the
 1110 detector, and the signals it generates in the active regions of the detector simula-
 1111 tion are recorded. Those signal are then converted into the expected electronic
 1112 outputs of the detector in a process called digitization. The result of this step has
 1113 precisely the same format as collected data, so that both can be fed into the same
 1114 reconstruction algorithms for analysis.

1115 2.6 LIMITATIONS

1116 Despite the great success of the relatively simple SM in describing such a broad
 1117 range of emergent phenomena, it is clear that the picture it presents of the in-
 1118 teractions of fundamental particles is incomplete. The SM contains concerning
 1119 coincidences that suggest a more ordered underlying substructure that is not ex-
 1120 pressed in the current form. It also fails to explain a number of cosmological
 1121 measurements of the nature of matter in the universe. These limitations suggest

1122 the need for new, **BSM** physics that would provide a more complete description
 1123 at higher energies.

1124 2.6.1 THEORETICAL CONCERNS

1125 There have been no successful integrations of the **SM**'s description of the elec-
 1126 troweak and strong forces with the description of gravity, and it is still unclear
 1127 how to account for the effects of gravity at the Planck scale of approximately 10^{19}
 1128 GeV, where its interactions are as strong as the remaining forces. The Planck
 1129 scale is an important cutoff for the **SM**, as it is clear that the **SM** must break down
 1130 somewhere between the current highest energy tests of the **SM**, around 1 TeV,
 1131 and the Planck scale.

1132 One example of this is the Higgs mass, which is determined by a sum of its
 1133 bare mass and the interactions in the vacuum with all massive particles. As there
 1134 must be new physics at the Planck scale to describe gravity, some of those cor-
 1135 rections would include contributions at a scale seventeen orders of magnitude
 1136 above the mass of the Higgs. Either the bare mass of the Higgs boson precisely
 1137 cancels those contributions to leave a remainder seventeen orders of magnitudes
 1138 smaller, or a new theory exists at a lower scale the shields the Higgs mass from
 1139 those terms. A theory where such a unlikely cancellation of free parameters oc-
 1140 curs is called fine-tuned, and one that is free from such cancellations is called
 1141 natural. Theories where the mass of the Higgs is natural are usually preferred,
 1142 as they suggest an underlying, coherent structure. The enormous difference in
 1143 scales between the weak scale (including the Higgs mass), and the Planck scale,
 1144 is often referred to as the hierarchy problem.

1145 There is also a compelling argument that the $SU(3) \times SU(2) \times U(1)$ gauge
 1146 structure of the **SM** might originate from a single, unified gauge theory. For ex-
 1147 ample, it is possible to represent that gauge structure as a $SU(5)$ gauge group
 1148 with only a few inconsistencies with the current implementation. This unifica-
 1149 tion is suggested by the scaling of the coupling constants for each of the forces
 1150 under renormalization; they come close to converging to a single value at higher
 1151 energies, as seen in Figure 4. An additional correction to the scaling of the cou-
 1152 pling constants from new physics above the TeV scale could cause them to merge
 1153 into a single value at high energies.

1154 2.6.2 COSMOLOGICAL OBSERVATIONS

1155 The **SM** contains a symmetry in the description of matter and antimatter that is
 1156 not reflected in cosmological observations. The processes of the standard model
 1157 create or remove matter and antimatter in equal amounts, so a universe that be-
 1158 gins with an equal quantity of each should result in a universe with an approxi-
 1159 mate³ balance of matter and antimatter. However, cosmological observations of
 1160 the relative amount of each type clearly show that the directly observable mass
 1161 of the universe is overwhelmingly made of matter. As this difference is largely

3 There are some processes in the standard model which can result in a small imbalance of matter and antimatter, but not at the scale observed cosmologically.

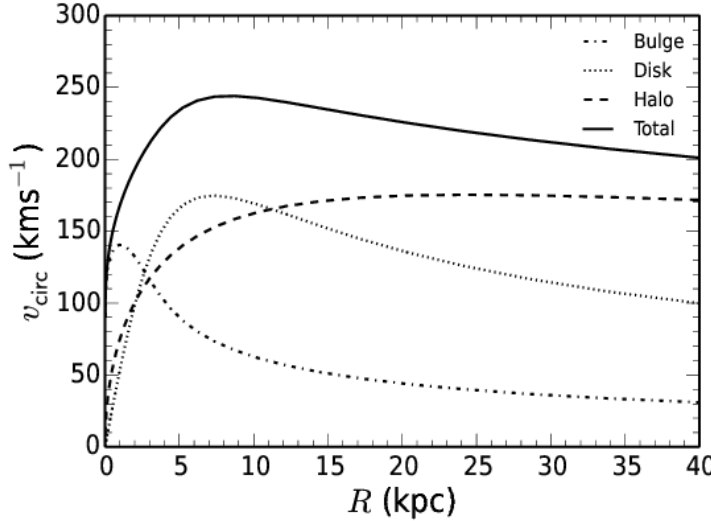


Figure 7: The distribution of velocities of stars as a function of the radius from the center of the galaxy. The contributions to the velocity from the various components of matter in the galaxy are shown [7].

1162 a difference in the generation of baryons and anti-baryons, this discrepancy is
 1163 often referred to as the baryogenesis problem.

1164 A number of astrophysical observations of large scale gravitational interactions
 1165 suggest the presence of a significant amount of non-luminous matter that
 1166 interacts with the normal matter only gravitationally. The first evidence of this
 1167 came from the observation of galactic rotation curves, the velocities of stars as
 1168 a function of the radius from the center of a galaxy. These can be directly pre-
 1169 dicted from the amount of matter contained within the sphere up to the radius of
 1170 the star. An estimate of velocity based only on the luminous matter in the galax-
 1171 ies would predict a dependence that falls off with the radius, but the observed
 1172 curves show a mostly constant distribution of velocities [7], as seen in Figure 7.
 1173 The higher velocities than predicted by the luminous matter can be explained by
 1174 a halo of dark matter that extends significantly outside the galactic disk.

1175 This dark matter accounts for a majority of the matter in the universe, and is
 1176 incompatible with the matter particles predicted by the SM. Many observations
 1177 support its existence, but there have been no direct detections of a particle which
 1178 could account for the large quantity of gravitationally interacting dark matter.
 1179 The SM would have to require a significant extension to include the particles
 1180 needed to explain dark matter and the processes needed to explain the observed
 1181 matter-antimatter asymmetry.

1182

1183 SUPERSYMMETRY

1184 The theory of [SUSY](#) presents an extension to the [SM](#) that solves a number of the
1185 outstanding issues. It is based on another proposed symmetry, one which intro-
1186 duces an equality between the fermionic particles and proposed bosonic partners
1187 and also between bosonic particles and their proposed fermionic partners. The
1188 symmetry is defined by extending spacetime into a superspace, which includes
1189 one dimension that describes a particle's spin: a transformation in this space
1190 moves a fermion with spin-1/2 to a boson with spin-0 or vice-versa. Requiring
1191 the [SM](#) to be symmetrical under these transformations requires the existence of a
1192 bosonic partner for every current matter fermion in the [SM](#) and a fermionic part-
1193 ner for every boson. The partners are called superparticles (sparticles), where
1194 quarks partner with squarks and leptons partner with sleptons, and each boson
1195 has a fermionic partner called a gaugino. The superpartners, in the original form
1196 of the theory, should be identical to the original particle in every way except for
1197 spin; that is they would have the same quantum charges and the same mass.

1198 However, the simplest version of the theory, where the symmetry is unbro-
1199 ken, is incompatible with current observations of physics in a number of sys-
1200 tems. The most striking example comes from the electron, as the superpartner
1201 of an electron would introduce a stable, negatively charged, and bosonic parti-
1202 cle. Such a particle would drastically alter atomic properties by providing a way
1203 to create atoms without the valence structure of electrons that results from the
1204 Pauli exclusion principle for fermions. Various high energy physics measure-
1205 ments have also confirmed the spin of the W and Z bosons, for example, and
1206 a fermionic gaugino has never been produced at those masses. The solution to
1207 this incompatibility with observation is to conjecture that the symmetry exists
1208 but is spontaneously broken, where the masses of the supersymmetric particles
1209 are significantly larger than those of the current [SM](#) particles. Like the sponta-
1210 neous symmetry breaking of the electroweak system, this symmetry breaking
1211 can be accomplished by introducing an additional Higgs mechanism.

1212 3.1 STRUCTURE

1213 There are a number of ways to model the particulars of [SUSY](#), but many of the
1214 resulting phenomena are similar, and a discussion of an example is sufficient
1215 to describe the structure and results of the theory. The [MSSM](#) is one example of
1216 a complete description that includes the necessary symmetry breaking to result
1217 in the different masses between particles and sparticles [8]. It is called minimal
1218 because it is designed to use the simplest possible extension to the [SM](#) that incor-
1219 porates [SUSY](#). However even a minimal version includes a remarkable number of
1220 free parameters, over 100, and the [MSSM](#) is often further constrained to include

Sector	Particles	Sparticles
Baryonic Matter	(u, d)	(\tilde{u}, \tilde{d})
	(c, s)	(\tilde{c}, \tilde{s})
	(t, b)	(\tilde{t}, \tilde{b})
Leptonic Matter	(ν_e, e)	$(\tilde{\nu}_e, \tilde{e})$
	(ν_μ, μ)	$(\tilde{\nu}_m u, \tilde{\mu})$
	(ν_τ, τ)	$(\tilde{\nu}_\tau, \tilde{\tau})$
Higgs	(H_u^+, H_u^0)	$(\tilde{H}_u^+, \tilde{H}_u^0)$
	(H_d^0, H_d^-)	$(\tilde{H}_d^0, \tilde{H}_d^-)$
Strong	g	\tilde{g}
Electroweak	(W^\pm, W^0)	$(\tilde{W}^\pm, \tilde{W}^0)$
	B^0	\tilde{B}^0

Table 1: The particles in the SM and their corresponding superpartners in the MSSM.

fewer parameters in models such as the Phenomenological MSSM ([pMSSM](#)) and the Constrained MSSM ([cMSSM](#)) [9].

The theory includes a sparticle partner for every SM particle, which are listed in Table 1. To then provide the different masses for those sparticles, the MSSM introduces a second Higgs interaction. The resulting scalar field, along with the original Higgs field, generates five total particles, h^0 , the original Higgs boson, A^0 , H^0 , and H^\pm , where the last two are electrically charged. These Higgs bosons can mix with the supersymmetric gauginos to form a series of mass eigenstates. These are usually referred to by the order of their masses, where the neutral gauginos (neutralinos) are labeled $\tilde{\chi}_1^0$, $\tilde{\chi}_2^0$, $\tilde{\chi}_3^0$, and $\tilde{\chi}_4^0$. The charged gauginos (charginos) are similarly labeled $\tilde{\chi}_1^\pm$ and $\tilde{\chi}_2^\pm$. Table 1, lists the gauginos which are direct partners of the original gauge bosons in the SM rather than these resulting mass eigenstates.

In addition to the new particle content, the MSSM introduces new interactions for the gauge bosons and gauginos. All interaction terms are added to the Lagrangian which describe the interaction of a gauge boson or gaugino with a particle or sparticle with the appropriate charge. Such terms include a few interactions which would violate the observed $B - L$ symmetry that prevents proton decay. Either the couplings on these terms must be extremely small to match the experimental limits on those decays, or an additional symmetry must be imposed to exclude the terms. The MSSM and several other SUSY models choose to introduce a new symmetry known as R-parity, where the conserved quantity, P_R is defined as

$$P_R = (-1)^{2s+3(B-L)}$$

with s as the spin of the particle. Sparticles are R-parity odd while SM particles are R-parity even. And by requiring that each term in the supersymmetric Lagrangian conserves R-parity, it is enforced that sparticles are produced in pairs.

1237 The conservation of R-parity removes the $B - L$ violating terms from the La-
 1238 grangian. The remaining terms include all of the interactions of the **SM** where
 1239 two of the particles are replaced with their **SUSY** partners, so that R-parity is con-
 1240 served in the interactions. This also has an important significance in making the
 1241 Lightest Supersymmetric Particle (**LSP**), the $\tilde{\chi}_1^0$, stable, as it cannot decay to only
 1242 **SM** particles without violating the conservation of R-parity. The heavier sparti-
 1243 cles then decay in chains, emitting an **SM** particle in each step, and leave behind
 1244 the **LSP** at the end of the chain.

1245 3.2 MOTIVATION

1246 **SUSY** models, including the **MSSM**, ameliorate many of the issues in the **SM** dis-
 1247 cussed in Section 2.6. **SUSY** is particularly well motivated as a natural extension
 1248 to the **SM** because the simple underlying assumption solves three major, seem-
 1249 ingly unrelated concerns. And these benefits all require that at least some of the
 1250 sparticles exist at the TeV scale, within the reach of modern collider experiments.

1251 The first, a solution to the hierarchy problem, comes as a direct consequence
 1252 of the introduction of massive superpartners for each **SM** particle. The contribu-
 1253 tions to the Higgs mass from the much higher energy Planck scale come from a
 1254 series of loop diagrams in the **SM**, where each massive **SM** particle has a loop con-
 1255 tribution. The introduction of superpartners generates a series of corresponding
 1256 diagrams for correction to the Higgs mass, with opposite sign contributions be-
 1257 cause the superpartners have different spins. Those opposite sign contributions
 1258 cancel the divergences from the original loop diagrams at high energies, leaving
 1259 behind a correction to the Higgs mass that is at the same scale as the masses of the
 1260 superpartners. If the superpartners exist at the TeV scale, then the Higgs mass
 1261 of 125 GeV can be explained without significant fine-tuning, and the theory be-
 1262 comes natural.

1263 **SUSY** also has the potential to precisely enable the unification of the coupling
 1264 constants at high energy. Without supersymmetric contributions, the coupling
 1265 constants come close to a single value near the Planck scale suggesting an un-
 1266 derlying trend, as shown in Figure 4, but they do not exactly merge. With the
 1267 addition of the **MSSM**, they can join almost exactly at a single point, enabling a
 1268 unification into a single gauge theory at high energy, as shown in Figure 8. This
 1269 precise unification, like the naturalness argument, also requires that the masses
 1270 of the superpartners be near the TeV scale.

1271 The presence of R-parity in a **SUSY** model also provides an explanation for
 1272 dark matter. The **LSP**, as discussed in Section 3.1, is a massive, neutral, and stable
 1273 particle as long as R-parity is conserved. In the early universe, when the energy
 1274 density was extremely high, **LSPs** could be spontaneously produced just as often
 1275 as other particles like photons, and would result in a thermal equilibrium. Then,
 1276 as the universe cooled, the average energy would be too low to create additional
 1277 **LSPs**, and they would be left behind and only interact with the remaining matter
 1278 gravitationally, a process called freeze out. Since those particles are stable, they
 1279 would remain indefinitely. With the existence of an **LSP** at around the TeV scale,
 1280 this process can explain the observed amount of dark matter in the universe. A

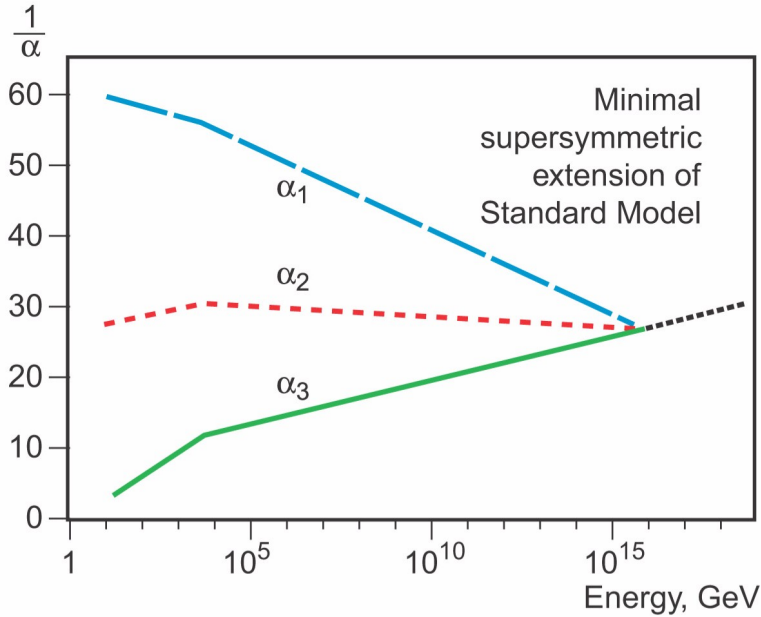


Figure 8: An approximation of the running of the coupling constants in the [MSSM](#) up to the Planck scale [1].

1281 **WIMP!** (**WIMP!**), exactly what is proposed in the [LSP](#), provides the correct interaction
 1282 rate to predict the currently observed ratio of dark matter to baryonic matter.
 1283

1284 Together, this variety of solutions to existing problems provides strong theoretical
 1285 support for the existence of [SUSY](#) near the TeV scale. The [LHC](#) is the first
 1286 collider experiment to be able to probe into TeV scale interactions, providing a
 1287 new opportunity to search for this extension to the [SM](#). A range of models have
 1288 begun to be excluded with masses above 1 TeV [2], leading to a motivation to
 1289 explore a wider variety of models with phenomena that may have been missed
 1290 by the most direct search strategies.

1291 3.3 SIMPLIFIED MODELS

1292 The [MSSM](#) is just one example of a large suite of [SUSY](#) models with similar results.
 1293 Each of those models can have hundreds of individual parameters that ultimately
 1294 determine the masses and interactions of the supersymmetric particles. To avoid
 1295 this complexity in making experimental measurements, the analyses of high en-
 1296 ergy collisions often rely on simplified models. These models focus on a single
 1297 process predicted by a theory, and the observable parameters such as the mass
 1298 of the particles and their lifetimes are controlled directly, rather than tuning the
 1299 hundreds of underlying parameters. This allows straightforward simulation of
 1300 a specific event topology with control over the parameters that most directly
 1301 influence the experimental signatures.

1302 Experimental analyses use these models to search for new physics and to set
 1303 limits on the production rates for a given type of process with working points
 1304 of a few observable parameters. As one example, a simplified model may specify

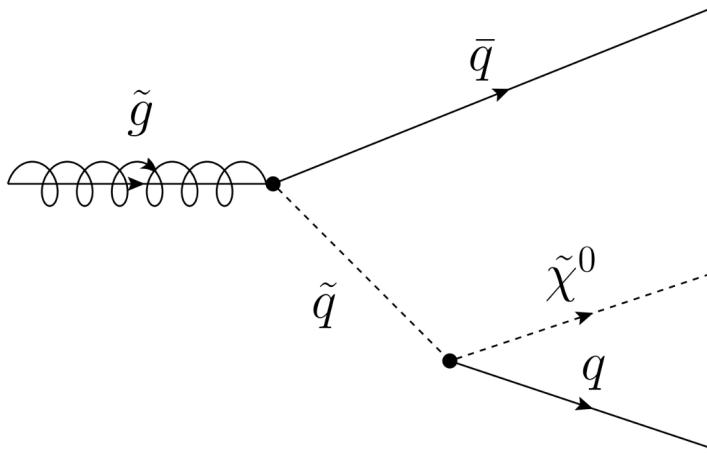


Figure 9: The decay of a gluino to quarks and an LSP, which precedes through a squark.

pair production of gluinos where the free parameters are the mass of the gluino and the types and masses of the particles it can decay into. The small number of parameters allows the phase space to be searched in a grid by simulating events with a few examples for the parameters and interpolating between them. The resulting analysis can set cross sectional limits as a function of the simplified parameters, and this allows for an easy interpretation of the result in a number of SUSY models.

3.4 LONG-LIVED PARTICLES

Some proposed SUSY models can produce LLPs other than just the LSP. The most direct search strategies for SUSY often assume that the various non-stable sparticles decay promptly, rather than propagating through some fraction of the detector. Although the processes involved are very similar, the long-lifetime of the produced particles can lead to very different experimental signatures, and often require separate dedicated searches. It is important to design and execute search strategies for LLPs in order to completely cover possible production of new physics.

There are several ways to generate long lifetimes for the massive SUSY particles, depending on the specific model. In examples like Spread Supersymmetry [10] and Split Supersymmetry [11, 12], the introduction of a split between two mass scales suppresses the decay of gluinos. In these and similar models, the squarks are much heavier than the gluino, where the mass scale of the squarks is roughly 10^6 GeV while the mass scale of the gluinos is roughly 10^3 GeV. The gluino must decay through the production of a virtual squark, as shown in the diagram of Figure 9. The large mass of the squarks in the split models suppresses the decay rate, and can result in lifetimes of the order of 1 ns [10].

Nearly degenerate particles can also result in long lifetimes, again by suppressing decay rates. When a particle must decay to another particle with nearly the same mass, the phase space factor in the decay results in a low decay rate. For

1333 example, a neutron has a lifetime of roughly fifteen minutes because its mass is
1334 so close to the proton. Models which result in a nearly degenerate chargino and
1335 LSP provide a long-lived chargino as well.

1336 Again, because of the wide variety of models which can produce LLPs and the
1337 large number of parameters which determine their masses and lifetimes, the anal-
1338 ysis presented here focuses on simplified models rather than assuming any par-
1339 ticular underlying theory. The models directly specify the decay mode of the
1340 LLPs as well as their masses and lifetimes, using a grid of values. The results of
1341 searches using these simplified models can be interpreted over a very wide range
1342 of models that predict LLPs, even including non-supersymmetric extensions to
1343 the SM.

1344

PART II

1345

EXPERIMENTAL STRUCTURE AND RECONSTRUCTION

1346

1347

1348 THE LARGE HADRON COLLIDER

1349 The LHC, a two-ring superconducting hadron accelerator, provides high energy
1350 proton-proton collisions for several large experiments at European Organiza-
1351 tion for Nuclear Research (CERN) in Geneva, Switzerland [13, 14]. It is the largest,
1352 highest-luminosity, and highest-energy proton collider ever built, and was con-
1353 structed by a collaboration of more than 10,000 scientists and engineers from
1354 the more than 100 countries that contribute to CERN. The original design of
1355 the LHC focused on providing collision energies of up to 14 TeV and generating
1356 enough collisions to reveal physics beyond the SM which is predicted to exist at
1357 higher energy scales.

1358 The LHC was installed in an existing 27 km tunnel at CERN which was orig-
1359 inally designed to house the Large Electron Positron collider (LEP) [15]. This
1360 allows the collider to use existing accelerators at the same complex to provide
1361 the initial acceleration of protons up to 450 GeV before injecting into LHC. The
1362 injected hadrons are accelerated up to as much as 14 TeV while being focused
1363 into two beams traveling in opposite directions. During this process the protons
1364 circulate around the tunnel millions of times, while the beams are intermittently
1365 crossed at the four locations of the experiments to provide collisions. These col-
1366 lision points correspond to the four major LHC experiments: ATLAS, Compact
1367 Muon Solenoid (CMS), Large Hadron Collider beauty experiment (LHCb), and A
1368 Large Ion Collider Experiment (ALICE), and Figure 10 shows the layout of the
1369 experiments both on the surface and below. ATLAS and CMS are both general
1370 purpose, high-luminosity detectors which search for a wide range of new types
1371 of physics [16, 17]. LHCb studies the interactions of b-hadrons to explore the
1372 asymmetry between matter and antimatter [18]. ALICE focuses on the collisions
1373 of lead ions, which the LHC also provides for about one month per year, in order
1374 to study the properties of quark-gluon plasma [19].

1375 During the first five years of continued operation, after the LHC turned on in
1376 2010, the LHC has provided four major data collecting periods. In 2010 the LHC
1377 generated collisions at several energies, starting at 900 GeV. It increased the
1378 energy from 900 GeV to 2.76 TeV and then subsequently to 7 TeV, with a peak
1379 luminosity of $2 \times 10^{32} \text{ cm}^{-2}\text{s}^{-1}$, and a total delivered luminosity of 50 pb^{-1} .
1380 The next run, during 2011, continued the operation at 7 TeV and provided an
1381 additional 5 fb^{-1} with a peak luminosity of $4 \times 10^{33} \text{ cm}^{-2}\text{s}^{-1}$. The energy was
1382 then increased to 8 TeV for the data collection during 2012, which provided 23 fb^{-1}
1383 with a peak luminosity of $7.7 \times 10^{33} \text{ cm}^{-2}\text{s}^{-1}$. After the first long shutdown
1384 for 2013 and 2014, the LHC resumed operation and increased the energy to 13
1385 TeV in 2015, where it delivered 4.2 fb^{-1} with a peak luminosity of $5.5 \times 10^{33} \text{ cm}^{-2}\text{s}^{-1}$.
1386 The LHC is currently providing additional 13 TeV collisions in 2016 with higher
1387 luminosities than during any previous data collection periods. These running
1388 periods are summarized in Figure 11, which shows the total delivered

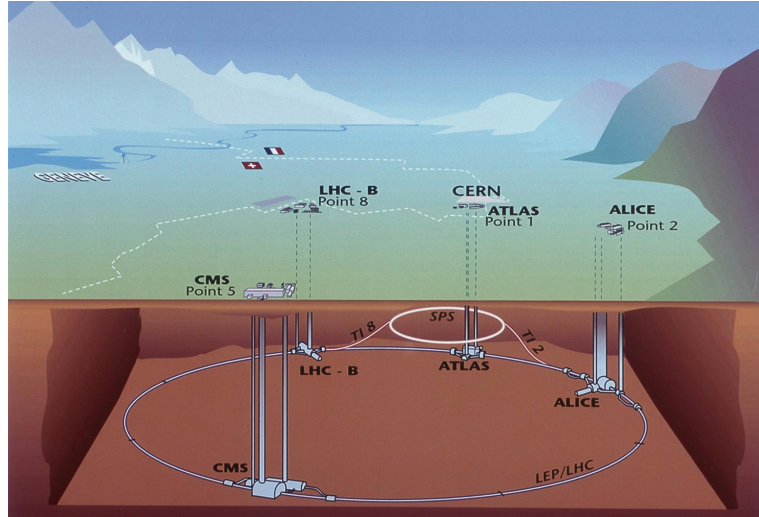


Figure 10: The four collision points and corresponding experiments of the LHC. The image includes the location of the nearby city of Geneva as well as the border of France and Switzerland.

luminosity over time for the ATLAS experiment during each of the four years of data collection since 2011. The full design energy of 14 TeV can only be reached after further magnet training that is scheduled for the long shutdown over 2019-2020.

4.1 INJECTION CHAIN

The LHC takes advantage of the presence of previously built accelerators at CERN to work up to the target energy in consecutive stages. The series of accelerators that feed into the LHC are known collectively as the injection chain, and together with the LHC form the accelerator complex. The full complex is illustrated in Figure 12, which details the complex series required to reach high energy collisions in the LHC experiments.

Protons at the LHC begin as hydrogen atoms in the Linac 2, a linear accelerator which replaced Linac 1 as the primary proton accelerator at CERN in 1978. In Linac 2, the hydrogen atoms are stripped of their electrons by a strong magnetic field, and the resulting protons are accelerated up to 50 MeV by cylindrical conductors charged by radio frequency cavities. The protons are then transferred to the Proton Synchrotron Booster (PSB), which uses a stack of four synchrotron rings to accelerate the protons up to 1.4 GeV. Then the protons are injected into the Proton Synchrotron (PS) which again uses synchrotron rings to bring the energy up to 25 GeV. The intermediate step between Linac 2 and the PS is not directly necessary, as the PS can accelerate protons starting from as low as 50 MeV. The inclusion of the PSB allows the PS to accept a higher intensity of injection and so increases the deliverable luminosity in the LHC. The penultimate stage of acceleration is provided by the Super Proton Synchrotron (SPS), a large synchrotron with a 7 km circumference that was commissioned at CERN

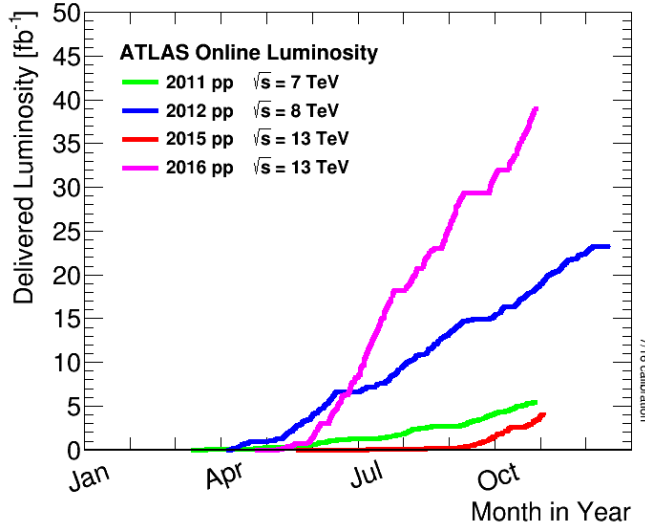


Figure 11: The cumulative luminosity over time delivered to the ATLAS experiment from high energy proton-proton collisions since 2011. The energies of the collisions are listed for each of the data-taking periods. The figure shows the delivered luminosity as of the conclusion of data collection in 2016.

in 1976. During this step the protons increase in energy to 450 GeV, after which they can be directly injected into the [LHC](#).

The final step is the [LHC](#) itself, which receives protons from the [SPS](#) into two separate beam pipes which circulate in opposite directions. The filling process at this steps takes approximately 4 minutes, and the subsequent acceleration to the final energy (6.5 TeV during 2015 and up to 7 TeV by design) takes approximately half an hour. At this point the protons circulate around the circumference tens of thousands of times a second and continue for up to two hours.

4.2 DESIGN

4.2.1 LAYOUT

Many of the aspects of the [LHC](#) design are driven by the use of the existing [LEP](#) tunnel. This tunnel slopes gradually, with a 1.4% decline, with 90% of its length built into molasse rock which is particularly well suited to the application. The circumference is composed of eight 2987 meter arcs and eight 528 meter straight sections which connect them; this configuration is illustrated in Figure 13. The tunnel diameter is 3.7 m throughout its length.

The design energy is directly limited by the size of this tunnel, with its radius of curvature of 2804 m. A significant magnetic field is required to curve the protons around that radius of curvature; the relationship is given by

$$p \simeq 0.3BR \quad (13)$$

where p is the momentum of the particle in GeV, B is the magnetic field in Tesla, and R is the radius of curvature in meters. From the target design energy of

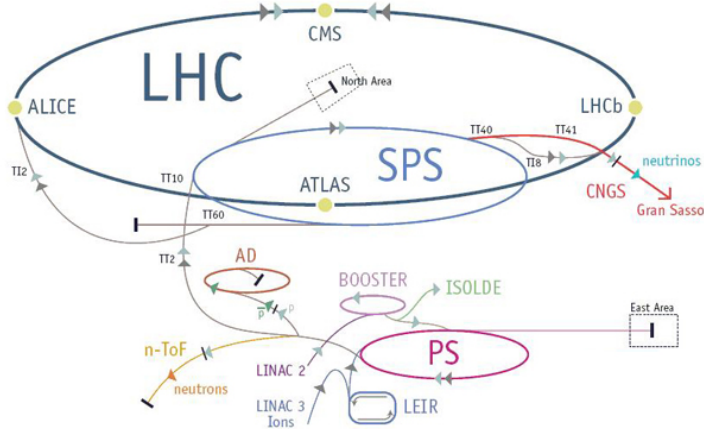


Figure 12: The accelerator complex that builds up to the full design energies at the LHC. The protons are passed in order to Linac 2, the PSB, the PS, the SPS and then the LHC.

1432 14 TeV, or 7 TeV of momentum for protons in each beam, the required mag-
 1433 netic field is 8.33 Tesla. This is too large a field strength to be practical with
 1434 iron electromagnets, because of the enormous power required and the resulting
 1435 requirements for cooling. Because of these constraints, the LHC uses supercon-
 1436 ducting magnets which can maintain that field strength with significantly less
 1437 power consumption.

1438 4.2.2 MAGNETS

1439 The magnets chosen were made of Niobium and Titanium (NbTi) which allow
 1440 for field strengths as high as 10 Tesla when cooled down to 1.9 K. Reaching the
 1441 target temperature of 1.9 K for all of the magnets requires superfluid helium
 1442 and a large cryogenic system along the entire length of the tunnel. During nor-
 1443 mal operation, the LHC uses 120 tonnes of helium within the magnets, and the
 1444 entire system is cooled by eight cryogenic helium refrigerators. The tempera-
 1445 ture increase that occurs during transit from the refrigerator along the beam
 1446 necessitates that the refrigerators cool the helium down to 1.8 K. Any significant
 1447 increase above this temperature range can remove the superconductive proper-
 1448 ties of the magnets, which in turn generates drastically larger heat losses from
 1449 the current within the magnets and causes a rapid rise in temperature called a
 1450 quench.

1451 There are approximately 8000 superconducting magnets distributed around
 1452 the LHC. The 1232 bending magnets, which keep the protons curving along the
 1453 length of the beam, are twin bore cryodipoles, which allow both proton beams
 1454 to be accommodated by one magnet and all of the associated cooling structure.
 1455 Figure 14 shows the cross section of the design for these dipoles. The magnets
 1456 are very large, 16.5 m long with a diameter of 0.57 meters and a total weight of 28
 1457 tonnes. They are slightly curved, with an angle of 5.1 mrad, in order to carefully
 1458 match the beam path. The twin bore accommodates both magnets inside the

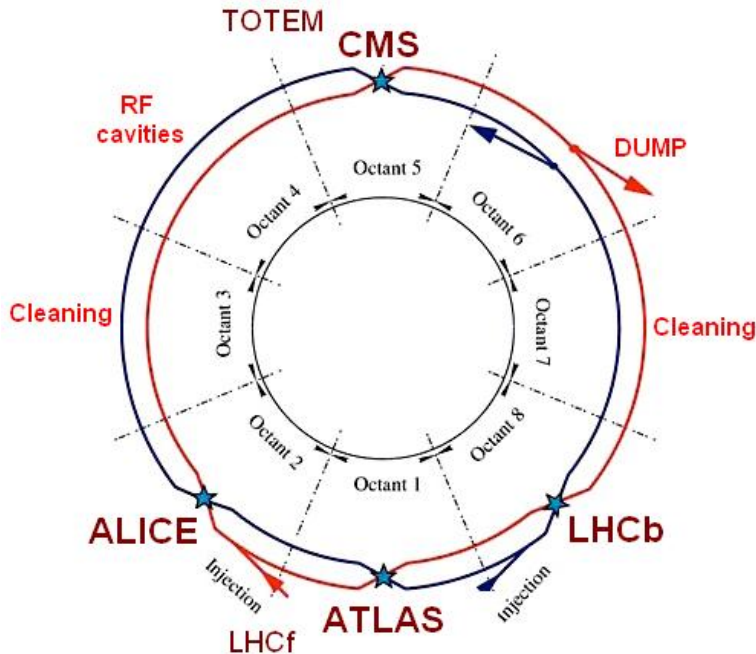


Figure 13: A schematic of the layout of the LHC, not to scale. The arched and straight sections are illustrated at the bottom of the schematic, and all four crossing sites are indicated with their respective experiments.

1459 two 5 cm diameter holes which are surrounded by the superconducting coils.
 1460 The coils require 12 kA of current in order to produce the required magnetic
 1461 field. These coils are comprised of NbTi cable wound in two layers; the wire in
 1462 the inner layer has a diameter of 1.065 mm while the wire in the outer layer has
 1463 a diameter of 0.825 mm.

1464 The large currents in the wires, along with the magnetic field produced, result
 1465 in forces on the magnets which would tend to push them apart with over 10,000
 1466 Newtons per meter. Constraining the magnets requires a significant amount of
 1467 structure including non-magnetic stainless steel collars. Both the presence of
 1468 these electromagnetic forces and the varying thermal contraction coefficient of
 1469 the pieces of the magnet produce significant forces on the cold mass structure.
 1470 The cold mass is carefully engineered to so that these stresses do not significantly
 1471 alter the magnetic field shape, which must be maintained between magnets to a
 1472 precision of approximately 10^{-4} for successful operation.

1473 The remaining 6800 magnets are a variety of quadrupole, sextapole, octopole,
 1474 and single bore dipole magnets. These are used to damp oscillations, correct
 1475 beam trajectories, focus the beams during circulation, and to focus the beams
 1476 before collisions.

1477 4.2.3 RADIO FREQUENCY CAVITIES

1478 Sixteen RF cavities produce the actual acceleration of the proton beam up to the
 1479 design energy. These RF cavities are tuned to operate at 400 MHz, and are pow-
 1480 ered by high-powered electron beams modulated at the same frequency, called

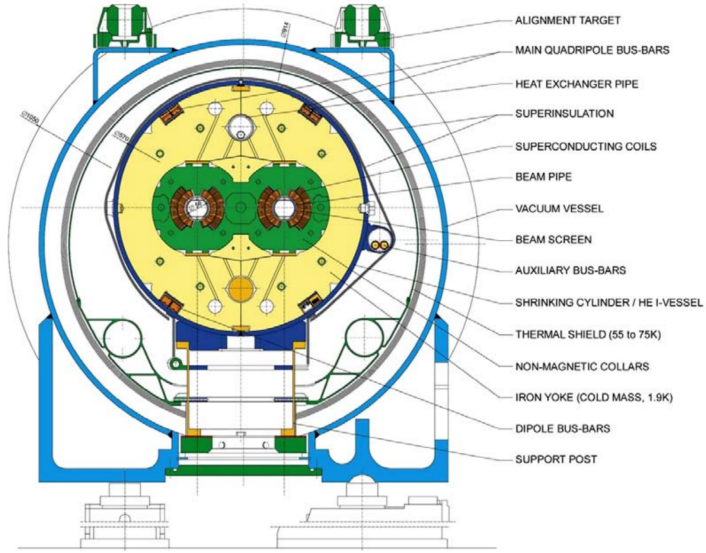


Figure 14: A cross section of the the cryodipole magnets which bend the flight path of protons around the circumference of the LHC. The diagram includes both the superconducting coils which produce the magnetic field and the structural elements which keep the magnets precisely aligned.

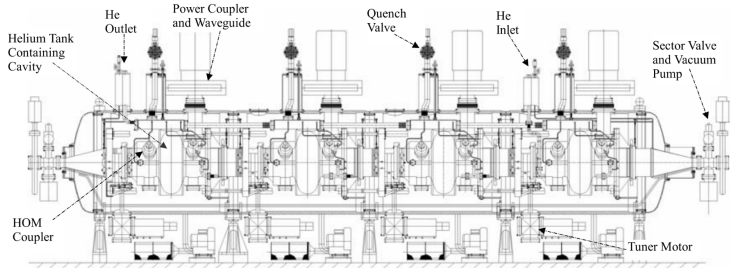


Figure 15: The arrangement of four RF cavities within a cryomodule.

1481 klystrons. The resonance within the cavity with the oscillating electric field
 1482 establishes a voltage differential of 2 MV per cavity. The sixteen cavities are
 1483 split between the two beams, so combined the cavities provide 16 MV per beam,
 1484 which accelerate the protons on each consecutive pass through the cavity. This
 1485 acceleration is also necessary during circulation even after the target energy has
 1486 been reach in order to compensate for losses from synchrotron radiation.

1487 The cavities are arranged in cryomodules which contain four cavities, with
 1488 two cryomodules per beam; this arrangement is illustrated in Figure 15. These
 1489 cryomodules are necessary to maintain the superconducting state of the cavities,
 1490 which are also constructed from niobium. The RF cavities use niobium along
 1491 with copper to allow for low power losses in the superconductors. The copper
 1492 provides a reduced susceptibility to quenching, as it rapidly conducts away heat
 1493 generated by imperfections in the niobium, as well as natural shielding from the
 1494 earth's magnetic field which can interfere with the RF system.

1495 The nature of the radio frequency oscillations tends to group protons together
 1496 into buckets. A proton traveling exactly in phase with the RF oscillations will not
 1497 be displaced at all during a single circulation, and those slightly ahead or behind
 1498 of that phase will slightly decelerate or accelerate, respectively. This produces
 1499 separate clusters of protons which arrive in phase to the cavities every 2.5 ns,
 1500 corresponding to the 400 MHz frequency.

1501 4.2.4 BEAM

1502 The beams of protons circulate within 27 km of 5 cm diameter beam pipe. This
 1503 entire structure is kept under vacuum at 1.9 K to prevent interactions between
 1504 the beam pipe and the magnets as well as to prevent any interactions between the
 1505 circulating protons and gas in the pipe. The vacuum within the pipe establishes
 1506 a pressure as low as 10^{-9} mbar before the protons are introduced.

1507 Because of the very high energies of the circulating protons, synchrotron ra-
 1508 diation is not negligible in the bending regions. The protons are expected to
 1509 radiate 3.9 kW per beam at 14 TeV, with 0.22 W/m, which is enough power to
 1510 heat the liquid helium and cause a quench were it absorbed by the magnets. To
 1511 prevent this, a copper screen is placed within the vacuum tube that absorb the
 1512 emitted photons. This screen is kept between 5 and 20 K by the liquid helium
 1513 cooling system.

1514 4.3 LUMINOSITY PARAMETERS

In addition to the high energy of the collisions, the rate of collisions is extremely important to enabling the discovery of new physics. Many measurements and searches require a large number of events in order to be able to make statistically significant conclusions. The rate of collisions is measured using luminosity, the number of collisions per unit time and unit cross section for the proton-proton collisions. From the beam parameters, luminosity is given by

$$\mathcal{L} = \frac{N_b^2 n_b f_{rev} \gamma}{4\pi\epsilon_n \beta^*} F \quad (14)$$

1515 where N_b is the number of protons per bunch, n_b is the number of bunches col-
 1516 liding, f_{rev} is the frequency of revolution, γ is the Lorentz factor for the protons
 1517 at the circulating energy, ϵ_n is the emittance, β^* is the amplitude function at the
 1518 collision point, and F is a geometric factor that accounts for the crossing angle of
 1519 the beams at the collision point. The emittance measures the average spread of
 1520 particles in both position and momentum space, while the amplitude function is
 1521 a beam parameter which measures how much the beam has been squeezed. To-
 1522 gether ϵ_n and β^* give the size of the beam in the transverse direction, $\sigma = \sqrt{\epsilon \beta^*}$.
 1523 β changes over the length of the beam as the accessory magnets shape the distri-
 1524 bution of protons, but only the value at the point of collisions, β^* , affects the
 1525 luminosity.

1526 The luminosity is maximized to the extent possible by tuning the parameters
 1527 in Equation 14. A number of these are constrained by the design decisions. The

Parameter	Unit	Injection	Nominal	2015
Beam Energy	TeV	0.450	7	6.5
Peak Instantaneous Luminosity	$\text{cm}^{-2}\text{s}^{-1}$	-	10^{34}	5×10^{33}
Bunch Spacing	ns	25	25	25
Number of Filled Bunches	-	2808	2808	2240
Normalized Transverse Emittance	μm	3.75	3.75	-
Frequency	MHz	400.789	400.790	-
RF Voltage/Beam	MV	8	16	-
Stored Energy	MJ	-	362	-
Magnetic Field	T	0.54	8.33	-
Operating Temperature	K	1.9	1.9	1.9

Table 2: The design parameters of the [LHC](#) beam that determines the energy of collisions and the luminosity, for both the injection of protons, at the nominal circulation, and during the 2015 data-taking period.

revolution frequency is determined entirely by the length of the tunnel, as the protons travel at very close to the speed of light. The geometric factor F is determined by the crossing angle of the beams at the collision points, a tunable component of the tunnel design; this angle is already very small at $285 \mu\text{rad}$, which helps to maximize the geometric factor.

The major pieces that can be adjusted are the number of protons per bunch, N_b , the number of bunches in the beam, n_b , and the amplitude function β . Increasing either N_b or n_b increases the amount of energy stored in the beam, which presents a danger if control of the beam is lost. At design specifications, the beam stores 362 MJ, which is enough energy to damage the detectors or accelerator if the beam were to wander out of the beam pipe. So, the luminosity is primarily controlled at the [LHC](#) by adjusting β^* , where lowering β^* increases the luminosity. β^* is tuned to provide the various values of luminosity used at the [LHC](#) which can be raised to as much as $1.4 \times 10^{34} \text{ cm}^{-2}\text{s}^{-1}$.

The nominal bunch structure consists of 3654 bunches, each holding 10^{11} protons, which cross a collision point in 25 ns. These are further subdivided into the buckets mentioned in Section 4.2.3 by the clustering properties of the [RF](#) cavities. In 2015, the bunches are further grouped into trains of 72 bunches which are separated by a gap which would otherwise hold 12 bunches. At nominal operation 2808 of the bunches will actually be filled with protons, while the remainder are left empty to form an abort gap that can be used in case the beam needs to be dumped.

The various beam parameters are summarized in Table 2 for the designed operation. In practice, the beam has operated at lower energies and lower luminosities than the design values for the majority of its lifetime, but the [LHC](#) has begun to operate at full design values during Run 2.

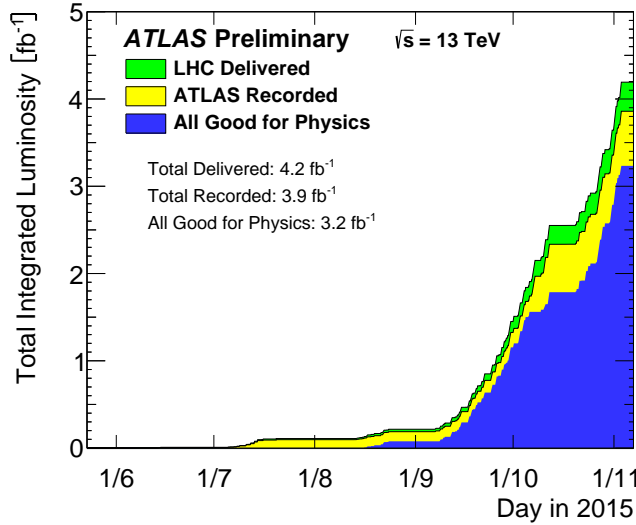


Figure 16: The cumulative luminosity versus time delivered to ATLAS (green), recorded by ATLAS (yellow), and certified to be good quality data (blue) during stable beams for pp collisions at 13 TeV in 2015.

1554 4.4 DELIVERED LUMINOSITY

During the data collection of 2015, the LHC operated at luminosities as large as $5 \times 10^{33} \text{ cm}^{-2} \text{s}^{-1}$. It is convenient to refer to the integrated luminosity, the integral of the instantaneous luminosity, which corresponds directly to the number of delivered events for a given process.

$$N = \sigma \times \int \mathcal{L}(t) dt$$

1555 where σ is the cross section for the process of interest. The integrated luminosity
 1556 over time is shown in Figure 16. This includes the luminosity delivered by the
 1557 LHC as well as the luminosity that was recorded by ATLAS. ATLAS only records
 1558 collisions when the LHC reports that the beam conditions are stable, so some of
 1559 the delivered luminosity is not recorded. The figure also includes the amount of
 1560 luminosity marked as good for physics, which includes additional requirements
 1561 on the operation of the detector during data collection that are necessary for
 1562 precise measurements.

1563 Because the beam circulates and collides bunches of protons, it is possible
 1564 for a single crossing to produce multiple proton-proton collisions. As the in-
 1565 stantaneous luminosity is increased, the average number of collisions generated
 1566 per bunch crossing increases. An event refers to the entire collection of inter-
 1567 actions during a single bunch crossing, while interactions refer to the individ-
 1568 ual proton-proton collisions. The additional interactions produced during each
 1569 bunch crossing are referred to as pileup, which can be more precisely defined
 1570 quantified using the average number of additional proton-proton interactions
 1571 per crossing, often denoted μ . Figure 17 shows the luminosity-weighted distri-
 1572 bution of the mean number of interactions for events collected in 2015. The
 1573 presence of as many as twenty interactions in a single collision provides a sig-

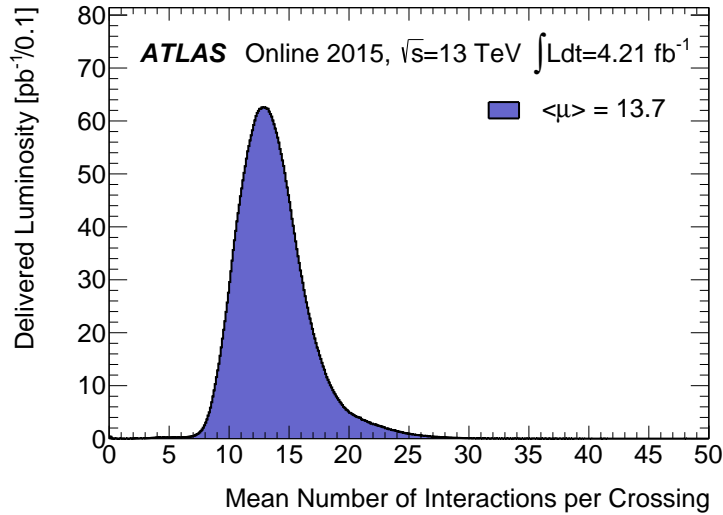


Figure 17: The luminosity-weighted distribution of the mean number of interactions per crossing for the 2015 pp collision data at 13 TeV.

1574 nificant challenge in reconstructing events and isolating the targeted physical
1575 processes.

1576

1577 THE ATLAS DETECTOR

1578 The four major LHC experiments at CERN seek to use the never before matched
1579 energies and luminosities of the new collider to explore the boundaries of par-
1580 ticle physics and to gain insight into the fundamental forces of nature. Two of
1581 these experiments, ATLAS and CMS, are general purpose detectors that seek to
1582 measure a variety of processes in the up to 13 TeV proton-proton collisions that
1583 occur as much as 800 million times per second at the LHC at the design lumi-
1584 nosity of $10^{34} \text{ cm}^{-2}\text{s}^{-1}$. ATLAS employs a hermetic detector design, one which
1585 encloses the particle collisions as completely as possible with detecting elements,
1586 that allows it to study a wide range of physics from SM precision measurements
1587 to searches for new physics in models like SUSY [16].

1588 Accommodating this wide variety of goals is a challenge for the design of the
1589 detector. The wide range of energies involved requires high measurement pre-
1590 cision over several orders of magnitude, and the numerous physics processes
1591 require an ability to measure a variety of particle types. At the time of the con-
1592 struction of ATLAS, the Higgs boson had yet to be discovered, but the diphoton
1593 decay mode was (correctly) expected to be important and necessitated a high
1594 resolution photon measurement. The potential for decays of new heavy gauge
1595 bosons, W' and Z' , required a similarly high momentum resolution for leptons
1596 with momentum up to several TeV. Hadronic decay modes of several possible
1597 new high energy particles could result in very energetic jets, again up to several
1598 TeV, and reconstructing the decay resonances would again require good energy
1599 resolution. Several models, such as SUSY or Extra Dimensions, predict the exis-
1600 tence of particles which would not interact with traditional detecting elements.
1601 However these particles can still be observed in a hermetic detector by accurately
1602 measuring the remaining event constituents to observe an imbalance in energy
1603 called missing energy or E_T^{miss} . Measuring E_T^{miss} implicitly requires a good res-
1604 olution on all SM particles that can be produced. And at the lower end of the
1605 energy spectrum, precision SM measurements would require good resolution of
1606 a variety of particle types at energies as low as a few GeV, so the design needs to
1607 accommodate roughly three orders of magnitude.

1608 This broad spectrum of measurements requires a variety of detector systems
1609 working together to form a cohesive picture of each collision. Two large mag-
1610 net systems produce magnetic fields that provide a curvature to the propagation
1611 of charged particles and allows for precision momentum measurements in the
1612 subdetectors. The inner detector uses a combination of detector technologies
1613 to reconstruct particle trajectories and vertices for charged particles. A variety
1614 of calorimeters measure the energies of hadrons, electrons, and photons over a
1615 large solid angle. A large muon spectrometer identifies muons and uses the sec-
1616 ond magnet system to provide an independent measurement of their momentum

1617 from the inner detector and improve the resolution. The layout of all of these
 1618 systems is shown in Figure 18.

1619 The performance goals needed to achieve the various targeted measurements
 1620 and searches discussed above can be summarized as resolution and coverage re-
 1621 quirements on each of these systems. Those requirements are listed in Table 3.

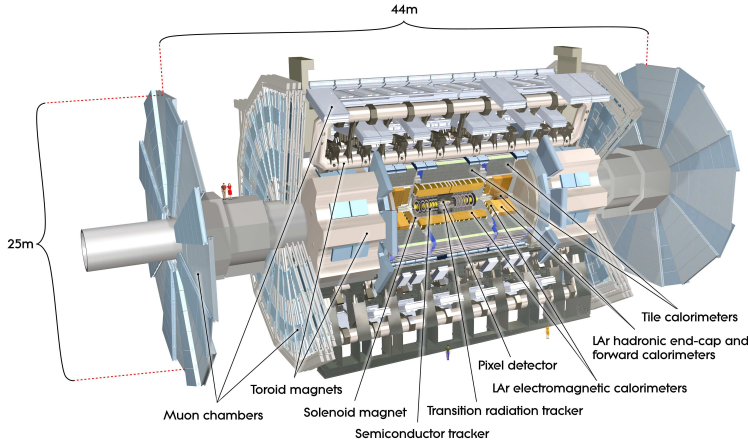


Figure 18: A cut-away schematic of the layout of the ATLAS detector. Each of the major subsystems is indicated.

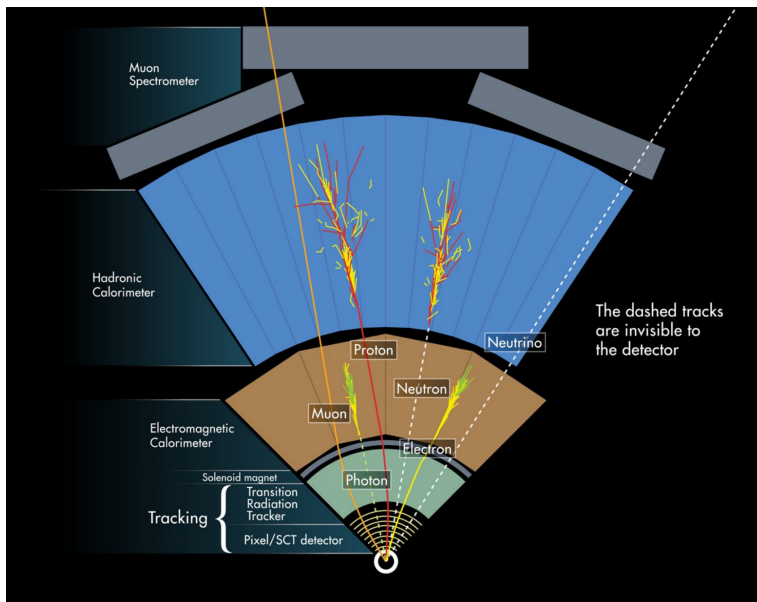


Figure 19: A cross-sectional slice of the ATLAS experiment which illustrates how the various SM particles interact with the detector systems.

1622 Incorporating these various pieces into a single detector is a significant tech-
 1623 nical challenge. The resulting detector has a diameter of 22 m, is 46 m long,
 1624 and weighs 7,000 tons; it is the largest volume particle detector ever constructed.
 1625 The various detector elements need to be constructed and assembled with pre-
 1626 cision as low as micrometers. These systems all need to function well even after
 1627 exposure to the significant radiation dose from the collisions. Designing, con-

Detector Component	Required Resolution	$ \eta $ Coverage	
		Measurement	Trigger
Tracking	$\sigma_{p_T}/p_T = 0.05\% p_T \oplus 1\%$	2.5	-
EM Calorimetry	$\sigma_E/E = 10\%/\sqrt{E} \oplus 0.7\%$	3.2	2.5
Hadronic Calorimetry			
Barrel and Endcap	$\sigma_E/E = 50\%/\sqrt{E} \oplus 3\%$	3.2	3.2
Forward	$\sigma_E/E = 100\%/\sqrt{E} \oplus 10\%$	3.1 – 4.9	3.1 – 4.9
Muon Spectrometer	$\sigma_{p_T}/p_T \leq 10\% \text{ for } p_T \leq 1 \text{ TeV}$	2.7	2.4

Table 3: The performance goals for each of the subsystems of the ATLAS detector. The $|\eta|$ coverage specifies the range where the subsystem needs to be able to provide measurements with the specified resolution. The resolutions include a p_T or E dependence that is added in quadrature with a p_T/E independent piece.

1628 structing, and installing the detector took the combined effort of more than 3000
 1629 scientists from 38 countries over almost two decades.

1630 5.1 COORDINATE SYSTEM

1631 The coordinate system defined for the ATLAS detector is used throughout all of
 1632 the sections of this thesis. The system begins with the choice of a z axis along
 1633 the beamline. The positive z side of the detector is commonly referred to as the
 1634 *A*-side, and the negative z side is referred to as the *C*-side. The $x - y$ plane is
 1635 then the plane transverse to the beam direction, with the x direction defined as
 1636 pointing from the interaction point to the center of the LHC ring and the y direc-
 1637 tion defined as pointing upwards. The nominal interaction point is the origin of
 1638 this system.

1639 It is more convenient in practice to use a cylindrical coordinate system; this
 1640 choice of coordinate system reflects the cylindrical symmetry of the ATLAS de-
 1641 tector. The distance from the beamline is the radius, r' , and the angle from the
 1642 z -axis is θ . The azimuthal angle, ϕ , runs around the z -axis with $\phi = 0$ corre-
 1643 sponding to the x -axis. Many aspects of the detector are independent of this
 1644 coordinate to first order; the detector is symmetric in ϕ . The θ direction is typi-
 1645 cally specified using rapidity or pseudorapidity, where rapidity is defined as

$$y = \frac{1}{2} \ln \frac{E + p_z}{E - p_z} \quad (15)$$

1646 Rapidity is particularly useful to indicate the component along the z direction
 1647 because differences in rapidity are invariant to boosts along the z -direction. A
 1648 similar quantity which depends only the θ is the pseudorapidity,

$$\eta = -\ln \tan \frac{\theta}{2} \quad (16)$$

which approaches rapidity in the limit where the energy is much larger than the particle's mass and is identical for massless particles. It is often useful to refer to differences in solid angle using the pseudorapidity and the azimuthal angle:

$$\Delta R = \sqrt{\Delta\phi^2 + \Delta\eta^2} \quad (17)$$

The pseudorapidity is also invariant to boosts along the z -axis for high momentum particles, and is preferable to rapidity because it does not depend on the specific choice of particle. Pseudorapidity is also preferable to θ because particle production is roughly uniform in equal-width intervals of η up to about $\eta = 5.0$. A particle traveling along the beampipe has $\eta = \infty$ and a particle traveling perpendicular to the beampipe has $\eta = 0$. The extent of the tracker, $|\eta| < 2.5$, corresponds to approximately $0.05\pi < \theta[\text{rad}] < 0.95\pi$ and the extent of the calorimeters, $|\eta| < 4.9$ corresponds to approximately $0.005\pi < \theta[\text{rad}] < 0.995\pi$. Many detector components are broken into multiple subsystems to provide coverage at greater $|\eta|$. The lower $|\eta|$ region is referred to as the barrel, typically with $|\eta| \lesssim 1.4$, and the greater $|\eta|$ region is often referred to as the endcap.

The initial momentum along the z direction of the constituents in a proton-proton collision is unknown in hadron colliders because the constituent momenta vary between collisions (Section 2.5.4). Along the transverse plane, however, the vector sum of momentum will be zero. For this reason, many physical quantities are quantified in terms of their projection onto the transverse plan, such as p_T or E_T . In addition, p_T alone determines the amount of curvature in the magnetic field, and can be measured independently by measuring the curvature of a particle's propagation.

5.2 MAGNETIC FIELD

The magnet system used in ATLAS is designed to provide a substantial magnetic field in the two regions where the trajectory of particles is measured, the inner detector and the muon spectrometer. The magnetic field generates a Lorentz force that curves the trajectory of charged particles, following Equation 13. This allows the precision tracking elements to make high resolutions measurements of p_T . To provide a magnetic field in these regions, ATLAS uses a hybrid system with four separate, superconducting magnets. A single solenoid provides a 2 T axial, uniform magnetic field for the inner detector, while a barrel toroid and two endcap toroids produce a non-uniform magnetic field of 0.5 and 1 T, respectively, for the muon detectors. This geometry is illustrated in Figure 20, and the parameters of the three magnet systems are summarized in Table 4.

The central solenoid uses a single-layer coil with a current of 7.730 kA to generate the 2 T axial field at the center of the magnet. The single-layer coil design enables a minimal amount of material to be used in the solenoid's construction, which is important because the solenoid is placed between the inner detector and the calorimeters. At normal incidence the magnet has only 0.66 radiation lengths worth of material, where one radiation length is the mean distance over

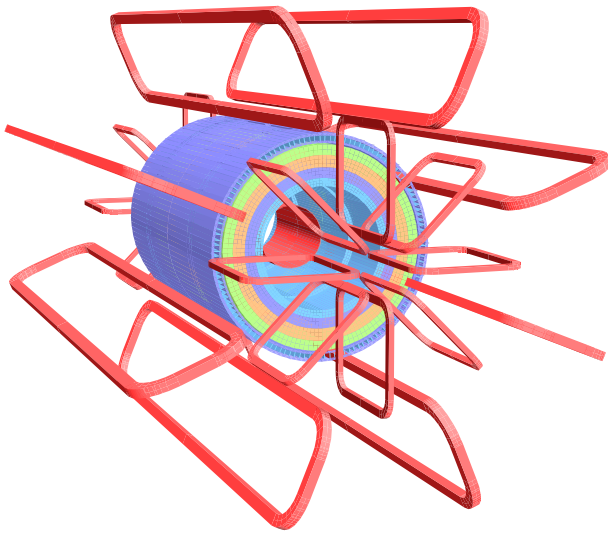


Figure 20: The layout of the four superconducting magnets in the ATLAS detector.

Parameter	Unit	Solenoid	Barrel Toroid	Endcap Toroids
Inner Diameter	m	2.4	9.4	1.7
Outer Diameter	m	2.6	20.1	10.7
Axial Length	m	5.3	25.3	5.0
Weight	tons	5.7	830	239
Conductor Size	mm^2	30×4.25	57×12	41×4.25
Peak Field	T	2.6	3.9	4.1
Heat Load	W	130	990	330
Current	kA	7.7	20.5	20.0
Stored Energy	MJ	38	1080	206

Table 4: A summary of the parameters of each of the three magnet systems on ATLAS.

which a high-energy electron loses all but $1/e$ of its energy through material interactions [2]. The coil is made of a high-strength aluminum stabilized NbTi superconductor which was optimized to achieve a high field with minimal thickness. The axial magnetic field produced by the solenoid bends charged particles in the ϕ direction, following a circular path with a radius specified by Maxwell's equations (see Equation 13).

The barrel toroid consists of eight coils which generate a 0.5 T magnetic field, on average, in the cylindrical region around the calorimeters with an approximately 20 kA current. The coils are separated only by air to reduce the scattering of muons as they propagate through the region. The coils are made of an aluminum stabilized NbTiCu superconductor and each is separately housed in a vacuum and cold chamber. This magnetic configuration produces a field in the ϕ and so curves muons traversing the volume primarily in the η direction.

The endcap toroids follow a similar design to the barrel toroid and produce a 1.0 T magnetic field, on average. Each has eight separate NbTiCu coils, and in this case all eight are housed within a single cold mass. This extra structure is necessary to withstand the Lorentz forces exerted by the magnets. These magnets are rotated 22.5% relative to the barrel toroid to provide a uniform field in the transition between the two systems. The endcap toroids also produce a field in the ϕ direction and curve muons primarily in the η direction.

5.3 INNER DETECTOR

The ATLAS inner detector provides excellent momentum resolution as well as accurate primary and secondary vertex measurements through robust pattern recognition that identifies tracks left by charged particles. These tracks fulfill a number of important roles in the ATLAS measurement system: they measure the momentum of charged particles including electrons and muons, they can identify electrons, they assign particles to different vertices, and they provide a correction to E_T^{miss} measurements from low energy particles. The system has to be accurate enough to separate tracks from dozens of vertices, to resolve each vertex individually, and to measure the p_T of very high momentum tracks which curve very little even in the large magnetic field. This is accomplished by several independent layers of tracking systems. Closest to the interaction point is the very high granularity Pixel detector, including the newly added IBL, which is followed by the SCT layers. These silicon subdetectors both use discrete space-points to reconstruct track patterns. The final layer, the TRT, uses many layers of straw tube elements interleaved with transition radiation material to provide continuous hits in the transverse plane. To provide the desired hermetic coverage, the subdetectors are divided into barrel and endcap geometries. Figure 21 shows the layout of the subdetectors in more detail, and illustrates how tracks at various pseudorapidities can traverse the subdetectors; tracks with $\eta > 1.1$ begin to traverse the endcap subdetectors rather than those in the barrel, and tracks with $\eta > 1.7$ use primarily endcap elements. The IBL was not present during the original commissioning of the inner detector and is not shown in this figure.

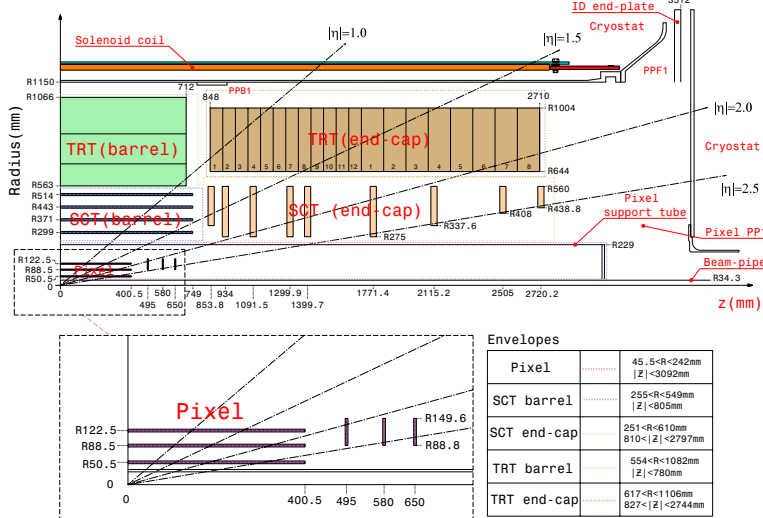


Figure 21: A quarter section of the ATLAS inner detector which shows the layout of each of the subdetectors in detail. The lower panel shows an enlarged view of the pixel detector. Example trajectories for a particle with $\eta = 1.0, 1.5, 2.0, 2.5$ are shown. The IBL, which was added after the original detector commissioning, is not shown.

1734 Figure 22 shows a computer generated three-dimensional view of the inner
 1735 detector along the beam axis, which emphasizes the straw tube structure of the
 1736 TRT as well as the overlapping geometry of the SCT. This figure also includes
 1737 the IBL, which was added during the long shutdown and provides an additional
 1738 measurement layer in the Pixel detector as of the beginning of Run 2. Figure 23
 1739 shows an alternative computer generated three-dimensional view transverse to
 1740 the beam axis which emphasizes the endcap structures of the SCT and TRT.

1741 As the closest system to the interaction point, it is crucial for the inner detector
 1742 to use as little material as possible to avoid scattering of charged particles before
 1743 they reach the remaining subdetectors. The various components, including the
 1744 readout electronics, cooling infrastructure, gas volumes, and support structures,
 1745 were designed to accommodate this need for minimal components. Even with
 1746 these optimizations, the combination of stringent performance requirements
 1747 and the harsh radiation environment in the inner detector requires a significant
 1748 amount of material. This material causes many electrons to lose most of their
 1749 energy before reaching the electromagnetic calorimeter and approximately 40%
 1750 of photons convert into an electron-positron pair while traversing the inner de-
 1751 tector. Figure 24 shows the integrated radiation lengths traversed by a straight
 1752 track in the inner detector as a function of η , grouped by subdetector. There is a
 1753 large increase in the amount of material for support structures around $|\eta| = 1.7$,
 1754 where the inner detector transitions from barrel to endcap.

1755 The inner detector is designed to work as a cohesive unit to provide complete
 1756 tracking information for charged particles. Table 5 summarizes the parameters
 1757 of each of the subdetectors as well as the parameters of the combined inner de-
 1758 tector.

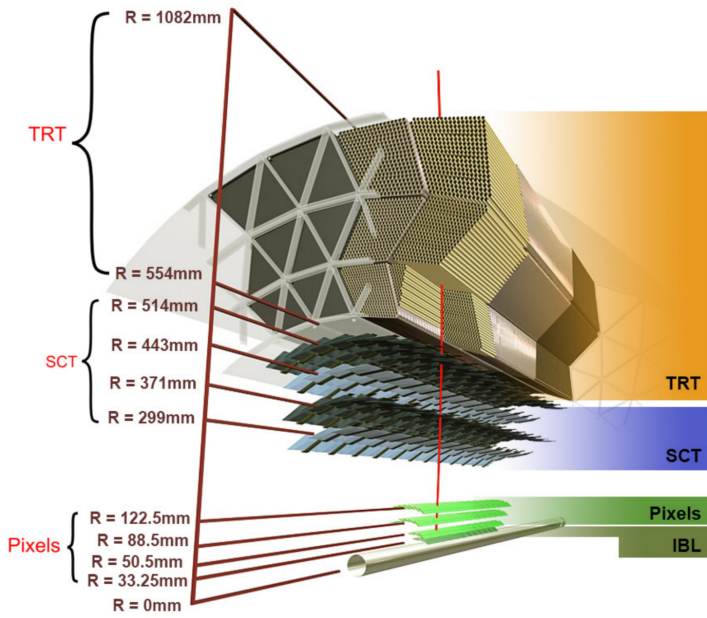


Figure 22: A computer generated three-dimensional view of the inner detector along the line of the beam axis. The subdetectors and their positions are labeled.

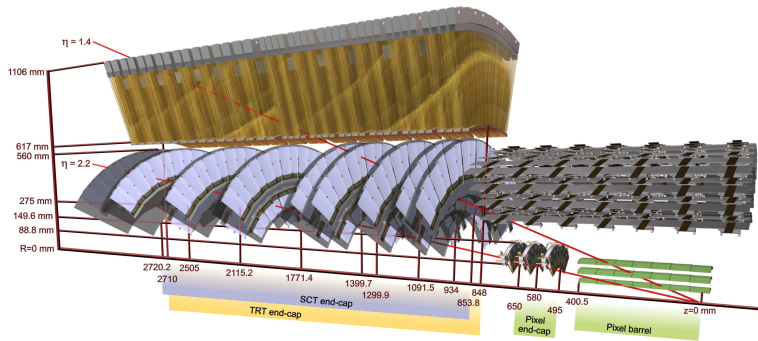


Figure 23: An alternative computer generated three-dimensional view of the inner detector transverse to the beam axis. The subdetectors and their positions are labeled.

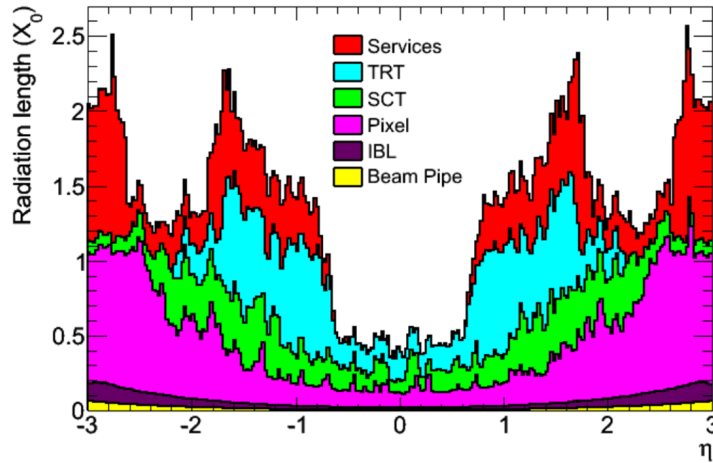


Figure 24: The integrated radiation lengths traversed by a particle at the exit of the ID envelope (outside of the TRT after 108.2 cm), including the services and thermal enclosures. The distribution is shown as a function of $|\eta|$ and averaged over ϕ . The breakdown indicates the contributions of individual sub-detectors, including services in their active volume.

5.3.1 PIXEL DETECTOR

The Pixel detector is the closest detector to the interaction point and therefore is designed to provide high granularity while simultaneously handling a large dose of radiation from collisions. It consists of four layers of silicon pixel modules, each of which provides a precision measurement on the trajectory of any charged particle. In the barrel region, the four layers are located at radial distances of 33 mm, 50.5 mm, 88.5 mm, and 122.5 mm. The three outer layers also include endcap elements, illustrated in Figure 21, which are located at $z = 495$ mm, $z = 580$ mm, and $z = 650$ mm away from the interaction point.

The pixel sensor technology uses a p-n junction of n-type bulk that contains both p⁺ and n⁺ impurities. This combination is crucial in maintaining performance after a significant radiation dose, as the n⁺ implants allow the sensor to continue function after the n-type bulk has been converted to a p-type bulk by the accumulation of radiation. In either configuration, when a charged particle passes through the bulk, it ionizes thousands of electron-hole pairs. The electrons and holes are pulled in opposite directions by the electric field established between the anode and cathode of the junction, which then produces a current that can be measured and recorded by readout electronics.

The size of the pixels in the original three layers are 50 μm x 400 μm in the $r - \phi$ and z directions, respectively. Those pixels are bump-bonded to front-end readout chips, the FE-I3, which contains a total of 2880 pixels per chip. In the three original pixel layers, the chips are grouped into modules composed of 16 chips each with 46,080 pixels per module and a total size of 20 mm x 60 mm x 250 μm . The modules are further arranged into long rectangular structures that run parallel to the beamline called staves. By tiling several staves with an offset of 20°, the stave geometry provides full azimuthal coverage in the barrel

Parameter	Inner Detector	Pixel	SCT	TRT
Inner Radius	3.3 cm	3.3 cm	30 cm	56 cm
$ \eta $ Coverage	-	2.5	2.5	2.0
Cell Width	-	50 μm	80 μm	4 mm
Cell Length	-	400 μm	12 cm	70 cm
Material at $ \eta = 0.0$	0.3 X/X_0			
Material at $ \eta = 1.7$	1.2 X/X_0			
Material at $ \eta = 2.5$	0.5 X/X_0			
Number of Hits	48	4	8	36
Channels	99 M	92 M	6.3 M	350 k

Table 5: A summary of the parameters of the inner detector and each of the subdetectors [16].

region while accommodating the readout and cable systems. The endcap regions are instead arranged into petals and then into wheels. This arrangement can be seen in Figure 25 which shows a computer-generated, cut-away image of the outer three layers of the pixel detector. Together these three layers contain 1744 modules between the barrel and two endcap sections.

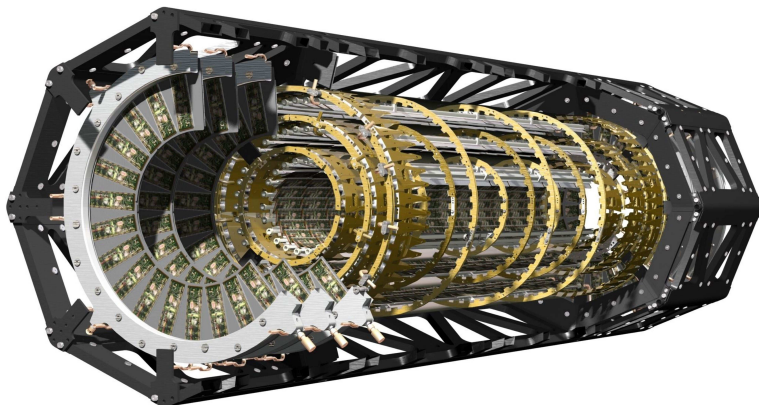


Figure 25: A cut away image of the outer three layers of the pixel detector.

The innermost layer, the IBL, was added during the long shutdown before Run 2, and provides the fourth track measurement. It was inserted directly into the existing pixel detector by removing the existing beam pipe and replacing it with a significantly smaller version. This insertion can be seen in action in Figure 26, which emphasizes the extreme precision required to place the the 70 cm long layer with only 2 mm of clearance. The IBL was commissioned to provide continued tracking robustness and high precision in the higher luminosity environment of Run 2 [20]. The proximity of this layer to the collisions necessitated an even higher granularity and better radiation hardness than the other pixel layers. And the strict space requirements to add an active sensing layer so close to the interaction point required a sensor chip with a much higher active area and a larger overall area per chip. These requirements led to the development of a

1802 new chip type, the FE-I4 (compared to the FE-I3 chips used in the original pixel
 1803 detector) with improved radiation hardness and a larger active area. The **IBL** is
 1804 comprised of 448 of these individual chips arranged in 14 staves, with 26,880
 1805 pixels per chip and a chip size of 18.5 mm x 41.3 mm x 200 μm . The staves,
 1806 like in the other layers of the pixel detector, are offset by 14° to provide full az-
 1807 imithal coverage. This arrangement can be seen in Figure 27, which shows two
 1808 computer-generated images of the **IBL** geometry and includes the some of the
 1809 remaining pixel layers.



Figure 26: An image of the insertion of the **IBL** into the current pixel detector.

1810 5.3.2 SEMICONDUCTOR TRACKER

1811 The **SCT**, the subdetector which immediately surrounds the Pixel detector, pro-
 1812 vides additional discrete measurements of the trajectory of a charged particle.
 1813 Because the **SCT** is further away from the interaction point, the spatial resolution
 1814 does not need to be as high as in the pixel detector, and so the **SCT** uses micro-
 1815 strips instead of pixels. Although pixels provide a more accurate measurement,
 1816 the number of pixels and readout channels required to cover the cylindrical area
 1817 at the radius of the **SCT** layers would be prohibitively complicated and expensive.

1818 Each individual silicon strip sensor contains 768 individual readout strips
 1819 with a total area of 6.36 cm x 6.40 cm and a pitch of 80 μm . Pairs of these sen-
 1820 sors are then bonded together to form a combined strip with a length of 12.8 cm.
 1821 Two of these combined strips are then placed back to back with a relative tilt of
 1822 40 mrad. This geometry is illustrated in an expanded view in Figure 28. The
 1823 purpose of angular offset of the consecutive layers is to allow the strip sensor
 1824 areas to more accurately measure the position of a particle in the z direction by
 1825 comparing the overlap of the two strips which were traversed by a track.

1826 Four of these double layers are placed in the barrel region, with radii of 299
 1827 mm, 371 mm, 443 mm, and 514 mm. Together these layers provide eight addi-
 1828 tional measurements for each track that traverses the central $|\eta|$ region. In the
 1829 endcap region, the layers are arranged in wheels, with the double layers simi-

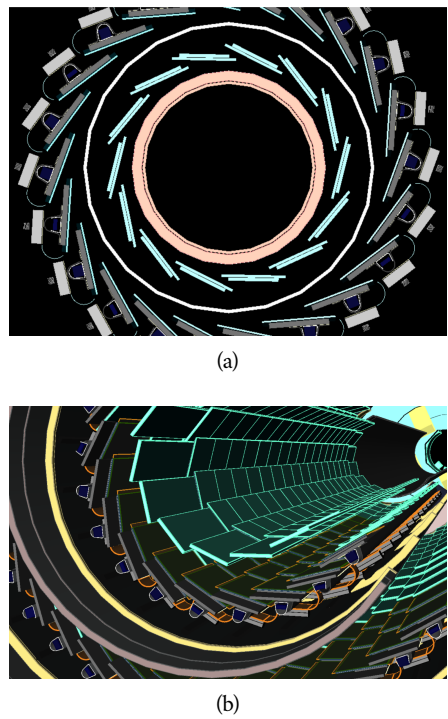


Figure 27: A three-dimensional computer-generated image of the geometry of the **IBL** with a view (a) mostly transverse to the beam pipe (b) mostly parallel to the beam pipe.

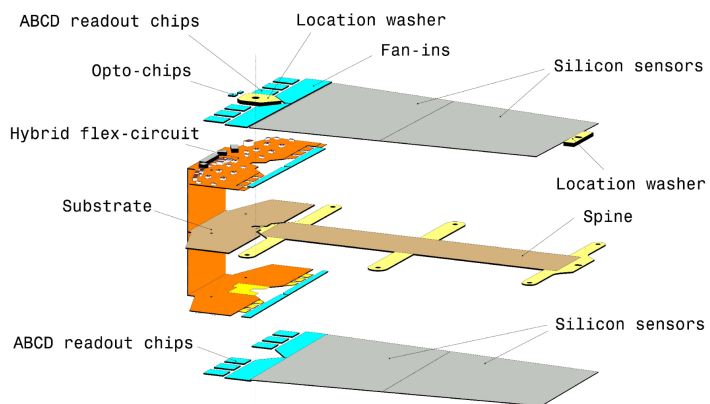


Figure 28: An expanded view of the geometry of the **SCT** double layers in the barrel region.

larly offset to provide improved resolution. With these configurations, the [SCT](#) achieves a spatial resolution of $17\text{ }\mu\text{m}$ in the $r - \phi$ direction and $580\text{ }\mu\text{m}$ in the z direction.

5.3.3 TRANSITION RADIATION TRACKER

The final component of the inner detector, the [TRT](#), provides continuous tracking using straw drift tubes. The tubes are made of Kapton and aluminum with a diameter of 4 mm and are filled with a gas mixture of 70% Xe, 27% CO_2 , and 3% O_2 . At the center of each tube is a gold-plated anode tungsten wire which is $30\text{ }\mu\text{m}$ in diameter. When a charged particle passes through these tubes, it ionizes the gas within. The ions produced drift in the electric field established between the wire and the tube wall, and the large electric field near the wire produces avalanche multiplication and results in an electric current on the wire that is read out by the electronics and provides a track measurement. The time it takes the ionization to drift to the wire can be used to estimate the distance from the wire that the particle passed through the tube; this gives a resolution on the distance of approximately $130\text{ }\mu\text{m}$. Combining several such measurements between consecutive hits in the [TRT](#) tubes allows the trajectory of the particle to be reconstructed with much better resolution than is available in each individual tube.

In addition to the continuous tracking, the detector can use transition radiation produced when a particle passes between the layers to distinguish between electrons and heavier charged particles. The space between the tubes is filled with CO_2 , and so has a different dielectric constant than the gas within the tubes which contains Xe. At the transition between those media, a relativistic particle emits radiation proportional to γ , so inversely proportional to mass at a fixed momentum. The photons produced in this transition then produce an ionization cascade which is significantly larger than the signal for the minimally-ionizing charged particles. To distinguish between these two cases, the [TRT](#) defines two signal thresholds, a low threshold for the typical signal produced by a minimally ionizing particle ([MIP](#)) and a high threshold for the signal produced by transition radiation. A high momentum electron is expected to produce approximately 7 to 10 high threshold hits as it traverses the [TRT](#), and thus these hits provide a way to distinguish electrons from other charged particles.

The [TRT](#) contains 351,000 tubes in total, divided between the barrel and endcap regions. In the barrel region, the tubes are 144 cm long and arranged in 73 layers parallel to the beampipe. In the endcap region, the tubes are 37 cm long and arranged in 160 layers transverse to the beampipe. These configurations can be seen in Figure 22 and Figure 23. With this geometry the [TRT](#) achieves a resolution of $130\text{ }\mu\text{m}$ in the $r - \phi$ direction.

5.4 CALORIMETRY

The combination of calorimeter systems used in ATLAS can measure the energy of electrons, photons, hadrons, and hadronic jets with complete coverage up to

1872 $|\eta| < 4.9$ and across ϕ . Unlike the inner detector, the calorimeters are capable
 1873 of measuring neutral particles. To accomplish precision measurements of these
 1874 particle types, the ATLAS calorimeter system uses four individual calorimeters,
 1875 a LAr electromagnetic calorimeter in the barrel region, a tile hadronic calorime-
 1876 ter in the barrel region, a LAr hadronic endcap calorimeter, and a LAr forward
 1877 calorimeter. Together these provide hermetic coverage for the ATLAS detector.
 1878 The configuration of these calorimeters is illustrated in Figure 29.

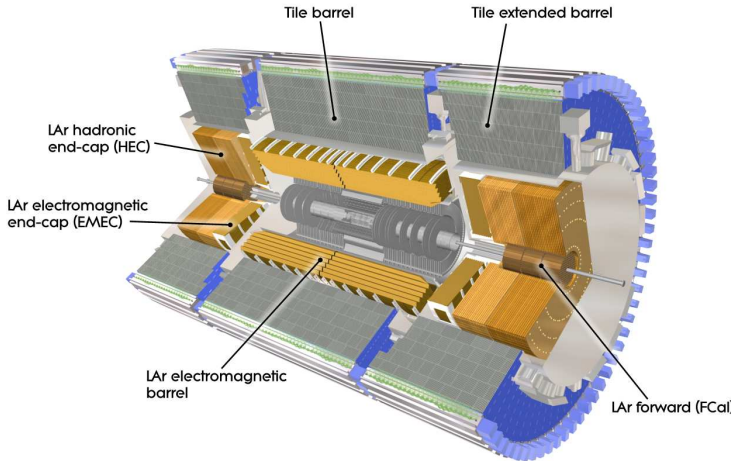


Figure 29

1879 The calorimeters are designed to absorb and measure the energy carried by
 1880 a particle, and completely stop the particle's propagation in the process. This
 1881 requires a significant amount of material to provide interactions. These inter-
 1882 actions then produce secondary particles, which can produce tertiary particles
 1883 in turn, and thus form a cascade of particles called an electromagnetic (EM) or
 1884 hadronic shower, depending on the governing mechanism. Electromagnetic and
 1885 hadronic showers have very different properties and require different technolo-
 1886 gies to measure them accurately. All of the calorimeters in the ATLAS calorime-
 1887 ter system are sampling calorimeters: they use alternating layers of absorbing
 1888 and active material. The dense absorbing layers initiate the showers while the
 1889 active layers measure the energy of the produced particles. A fraction of the en-
 1890 ergy is lost in the inactive layers, so the energy measurement from the active
 1891 layers has to be corrected to estimate the actual energy of the particle.

1892 The EM calorimeter provides around 20 radiation lengths (X_0) while the hadronic
 1893 calorimeter provides around 10 interaction lengths (λ). As mentioned previ-
 1894 ously, radiation lengths measure the distance over which an electromagnetically
 1895 interacting particle loses a characteristic fraction of its energy. Interaction lengths,
 1896 on the other hand, measure the mean distance traveled by a hadronic particle be-
 1897 fore undergoing a nuclear interaction [2]. Figure 30 show the radiation lengths
 1898 in the layers of the EM calorimeter in the barrel region as well as the interaction
 1899 lengths for all calorimeters.

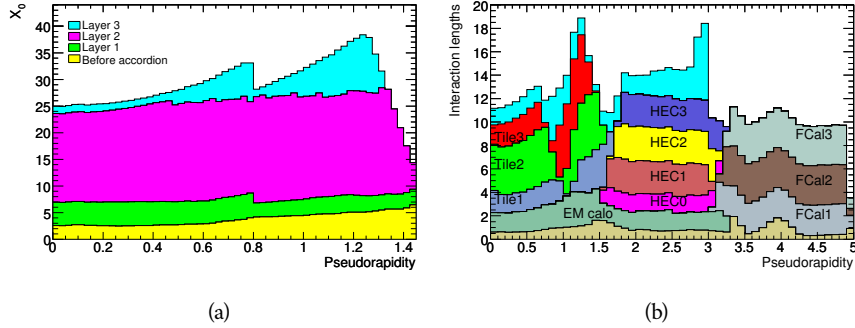


Figure 30: The depth of (a) the electromagnetic barrel calorimeter in radiation lengths and of (b) all calorimeters in interaction lengths as a function of pseudorapidity.

1900 5.4.1 ELECTROMAGNETIC CALORIMETER

1901 The electromagnetic calorimeters use alternating layers of liquid argon and lead
 1902 in an accordion shape. The accordion shape provides complete coverage in the
 1903 ϕ direction while also providing many alternating layers for the a particle to
 1904 pass through. The configuration is detailed in Figure 31. When an electron or
 1905 a photon passes through the lead, it produces an electromagnetic shower. The
 1906 particles produced in those showers then pass into and ionize the liquid argon;
 1907 the ions produced can then be collected by an electrode in the liquid argon layer
 1908 to provide the actual energy measurement.

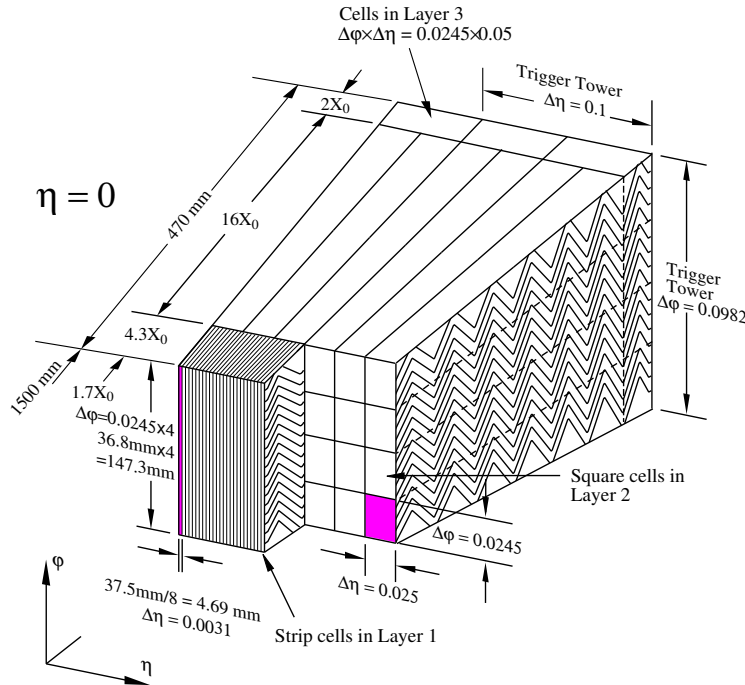


Figure 31: A schematic of the LAr calorimeter in the barrel region, highlighting the accordion structure.

1909 The barrel region is covered by a presampler and three separate sampling lay-
 1910 ers with decreasing segmentation. The presampler is a thin layer of liquid argon
 1911 which measures the energy of any electromagnetic showers which are initiated
 1912 before the particle reaches the calorimeter due to interactions with the detec-
 1913 tor material. The first layer is the strip layer, which has fine segmentation in η
 1914 to enhance the identification of shower shapes and to provide a precise η mea-
 1915 surement for reconstructing photons and electrons. The strip layer has only 4
 1916 radiation lengths worth of material, and has a segmentation of $\Delta\eta = 0.003$ and
 1917 $\Delta\phi = 0.1$. The second layer is also finely segmented, with a segmentation of
 1918 $\Delta\eta = 0.025$ and $\Delta\phi = 0.025$, and a thickness of $16 X_0$. This layer is designed
 1919 to contain an electromagnetic shower and to measure the majority of the energy
 1920 for photons and electrons. The third layer is only $2 X_0$ thick and measures the
 1921 energy of electromagnetic showers which leak out of the second layer, and helps
 1922 to separate electromagnetic showers from hadronic showers. The structure of
 1923 the LAr endcap calorimeter is similar except that the layers are arranged parallel
 1924 to the beampipe to measure energy deposits from high η particles.

1925 5.4.2 HADRONIC CALORIMETERS

1926 The hadronic calorimeters use a few different technologies to satisfy the resolu-
 1927 tion demands in the different areas of the detector, and together they cover the
 1928 region $|\eta| < 2.7$. In the barrel region, for $|\eta| < 1.7$, the hadronic calorimeters
 1929 are constructed of alternating tiles of steel and plastic scintillator. Like in the
 1930 electromagnetic calorimeter, the dense layer initiates a shower (in this case the
 1931 dense layer is the steel and the shower is hadronic) of particles which pass into
 1932 and ionize the following layer. The ionization in the plastic scintillator instead
 1933 produces a light signal proportional to the amount of ionization produced by the
 1934 shower, and this signal is measured using photomultipliers and provides the ac-
 1935 tual energy measurement. The construction of a tile in the calorimeter is shown
 1936 Figure 32, which highlights the alternating layers of steel and scintillator.

1937 This tile calorimeter, as well as the remaining hadronic calorimeters, have a
 1938 much coarser granularity than the electromagnetic calorimeters. The high gran-
 1939 ularity is not needed for an accurate energy measurement, and the hadronic
 1940 calorimeters are not designed to distinguish particle types like the electromag-
 1941 netic calorimeters. The tile granularity is approximately $\Delta\eta = 0.1$ and $\Delta\phi = 0.1$,
 1942 and the segmentation in depth and η is shown in Figure 33.

1943 The remaining hadronic calorimeters all use the same alternating, sampling
 1944 structure but with different active and inactive materials. The hadronic endcap
 1945 calorimeter covers the range of $1.5 < |\eta| < 3.2$ and uses an inactive layer of
 1946 copper and an active layer of liquid argon. The forward calorimeter covers the
 1947 range of $3.1 < |\eta| < 4.9$ and uses a dense matrix of copper and tungsten filled
 1948 with liquid argon. Particles propagating through the sampling layers ionize the
 1949 liquid argon, and the ionization is collected at an electrode to provide a signal.

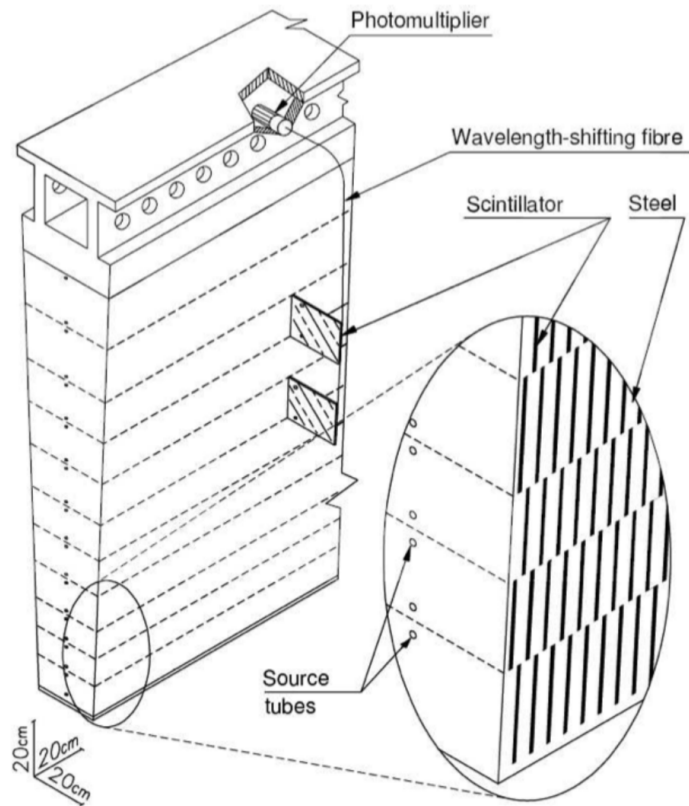


Figure 32: A schematic of a hadronic tile module which shows the alternating layers of steel and plastic scintillator.

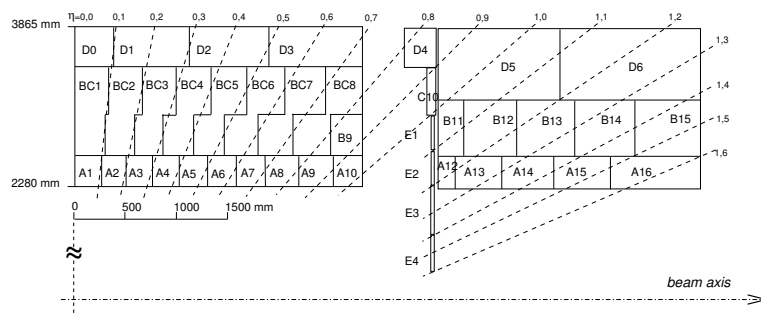


Figure 33: The segmentation in depth and η of the tile-calorimeter modules in the central (left) and extended (right) barrels.

5.5 MUON SPECTROMETER

Among SM particles, only muons and neutrinos consistently pass through the calorimeters. Because the neutrinos are also electrically neutral, there is no feasible option to measure them directly in ATLAS. The muons, on the other hand, are charged and are thus already measured as a track in the inner detector. The muon spectrometer provides a way to consistently identify muon tracks and also a way to provide an additional measurement of their momentum.

The muon spectrometer contains four subdetectors that cover the barrel and endcap regions. In the barrel region, the muon spectrometer uses a combination of Resistive Plate Chambers (RPCs) and MDTs to provide both a coarse, fast measurement for triggering and a precise momentum measurement for offline event reconstruction. Similarly, in the endcap region, the TGCs, MDTs, and CSCs allow for both triggering and precise measurements. The CSCs are used only in the innermost layer of the endcap region between $2.0 < |\eta| < 2.7$ where the particle flux is too large for the MDTs to provide accurate measurements. The overall layout of the muon systems are shown in the cut-away diagram in Figure 34, and Figure 35 shows a precise schematic of the layout of each of the detecting elements. The geometric arrangement shown provides consistent coverage for muons produced up to $|\eta| < 2.7$, and takes full advantage of the bending of the muons in the toroidal magnetic field, described in Section 5.2, to measure their momentum. Figure 36 shows a cross-section of the arrangement of the muon spectrometer in the barrel; the layers are divided into eight small and eight large chambers that are overlapped to provide complete coverage in ϕ .

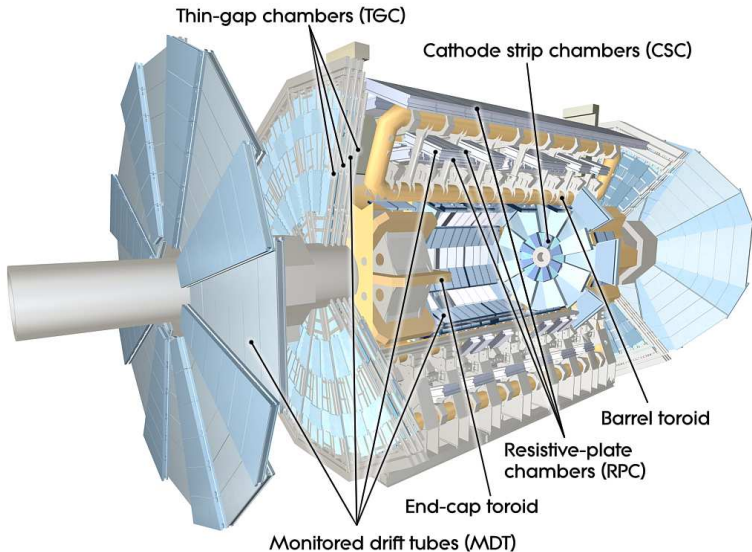


Figure 34: A cut-away diagram of the muon systems on ATLAS.

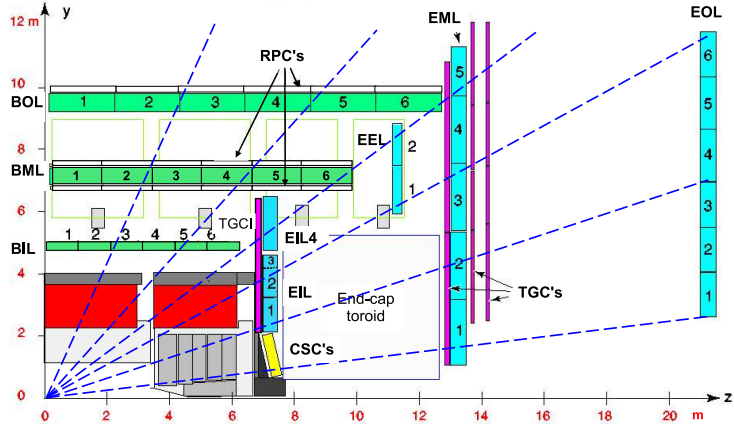


Figure 35: A quarter view of the muon spectrometer which highlights the layout of each of the detecting elements. The BOL, BML, BIL, EOL, EML, and EIL are all MDT elements, where the acronyms encode their positions.

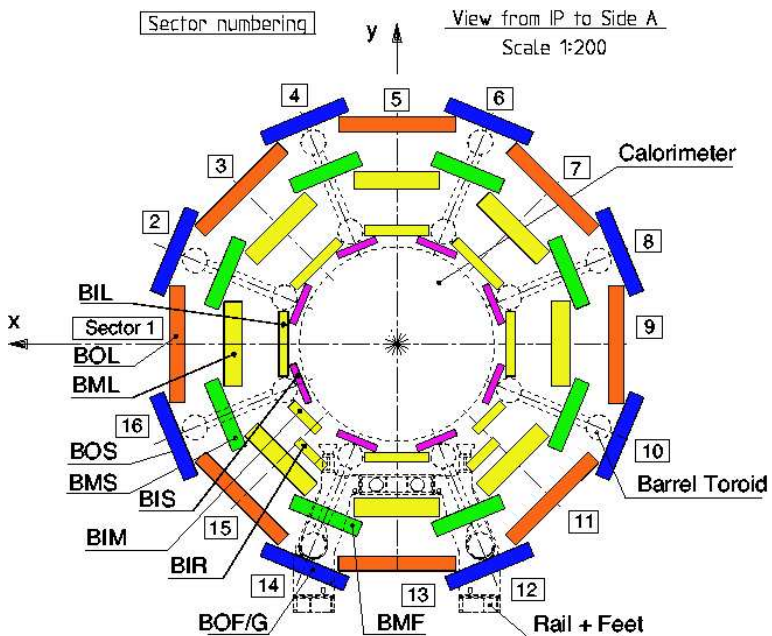


Figure 36: A schematic of the cross-section of the muon spectrometer in the barrel region.

1973 5.5.1 MONITORED DRIFT TUBE

1974 The momentum measurements in the barrel region are provided by three consecutive layers of MDT elements, located at approximately 5 m, 7 m, and 9 m from
 1975 the interaction point. Each of these layers is a composite of two multilayers of
 1976 drift tubes: two layers of three to four layers of tubes, as shown in Figure 37.
 1977 These aluminum tubes are 3 cm in diameter, with lengths between 0.9 and 6.2 m,
 1978 and are filled with a mixture of ArCO₂ kept at 3 bar absolute pressure. A central
 1979 tungsten-rhenium wire with a diameter of 50 μm runs along the length of the
 1980 tube, and is kept at a potential of 3080 V.
 1981

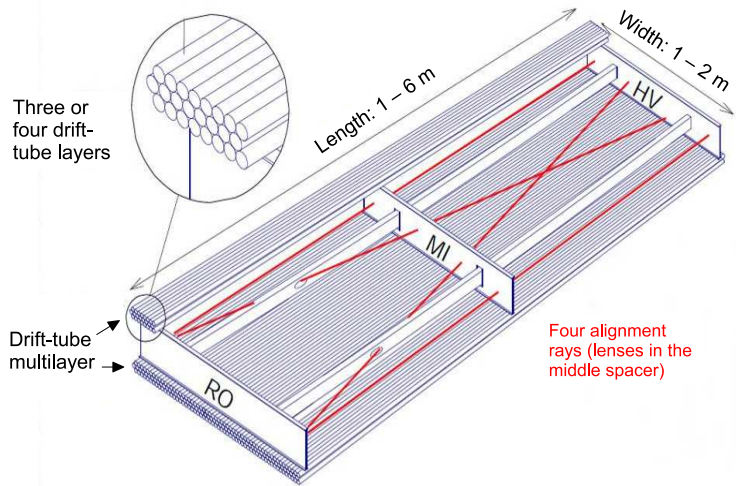


Figure 37: A schematic of a single MDT chamber, which shows the multilayers of drift tubes as well as the alignment system.

1982 A muon traversing these tubes ionizes the gas, and the ionization electrons
 1983 then drift in the electric field toward the central wire. Close to the wire, the
 1984 electric field is strong enough to cause the original ionization electrons to ionize
 1985 additional electrons, producing an avalanche that can be measured as a current
 1986 along the wire. The time of arrival of that current depends on how far the muon
 1987 entered from the wire, and can be used to achieve a position resolution of 80 μm
 1988 in an individual tube. The combination of the measurements in the consecutive
 1989 layers of tubes improves this position resolution to 35 μm transverse to the tubes,
 1990 with a resolution of 1 m along the tube direction.

1991 To achieve a good resolution over the entire length of a muon track, the rel-
 1992 ative positions of the tubes of the muon spectrometer must be known to an ac-
 1993 curacy of 30 μm . This is achieved by an optical laser alignment system placed in
 1994 each of the individual chambers and throughout the cavern. These monitor any
 1995 changes in position or alignment due to effects like gravitational sag, tem-
 1996 perature shifts, and the magnetic field. The configuration of the alignment system
 1997 within an individual chamber is also shown in Figure 36.

1998 5.5.2 RESISTIVE PLATE CHAMBER

2000 The **RPC** is the provides a fast measurement of the ϕ position of muons for trig-
 2001 gering in the barrel region. The system has a lower spatial resolution than the
 2002 **MDTs** but has a faster measurement with a time resolution of just a few tens of
 2003 nanoseconds. There are three **RPCs** layers in the muon spectrometer, two located
 2004 on either side of the central **MDT** layer and one located outside the final **MDT**
 2005 layer, as shown in Figure 35. The **RPCs** consist of two layers of parallel plates
 2006 filled with a gas mixture of $C_2H_2F_4$. A muon passing through these systems ion-
 2007 izes the gas, like in the **MDT**, which causes an avalanche of ionization electrons
 2008 in the electric field maintained between the plates. Metal strips on the outside
 2009 of the chamber capacitively couple to the accumulated charge, and are read out
 to measure the η and ϕ positions of the muon track.

2010 5.5.3 CATHODE STRIP CHAMBER

2011 The majority of the momentum measurements in the endcap region are provided
 2012 by the **MDTs**. In the most forward region of the muon spectrometer, between
 2013 $2.0 < \eta < 2.7$, the particle flux is very high due to contributions from low energy
 2014 photons and neutrons. The **MDT** can only sustain a hit rate of approximately 150
 2015 Hz/cm² because of limitations in the drift times of the gas and the capacity of
 2016 the readout electronics. The **CSCs** were designed to handle higher hit rates, up to
 2017 1000 Hz/cm², and provide the necessary coverage in that high flux region.

2018 The **CSC** consists of several multiwire proportional chambers, where the wires
 2019 are oriented in the radial direction out from the beampipe. There are eight large
 2020 and eight small chambers, arranged to partially overlap in the ϕ direction, as
 2021 shown in Figure 38. Like in the **MDT**, a muon traversing the system produces
 2022 ionization in the gas; here, however, the ionization is collected on a number of
 2023 wires. These wires couple to cathodes on the chambers which are segmented
 2024 into strips in two directions. The relative amount of charge on each of the neigh-
 2025 boring strips can be used to interpolate to the position of the muon in both η
 2026 and ϕ .

2027 5.5.4 THIN GAP CHAMBER

2028 Like in the barrel region, a separate, fast detector is required to provide position
 2029 measurements of muons for trigger in the endcap region. This is provided by
 2030 the **TGC** which consists of seven layers in the middle station of the endcap, two
 2031 doublet layers and one triplet layer, and a single doublet layer in the inner endcap
 2032 station. Figure 39 shows the arrangement of the triple and doublet layers of the
 2033 **TGCs**.

2034 Like the **CSCs**, the **TGCs** are multiwire proportional chambers with a wire-to-
 2035 cathode distance of 1.4 mm and a wire-to-wire distance of 1.8 mm. Readout
 2036 strips on the outside of the chambers run perpendicular to the wires, and couple
 2037 to the charge collected on the wires to provide a position measurement in the η
 2038 direction. The current induced on the wires is also readout to provide a position

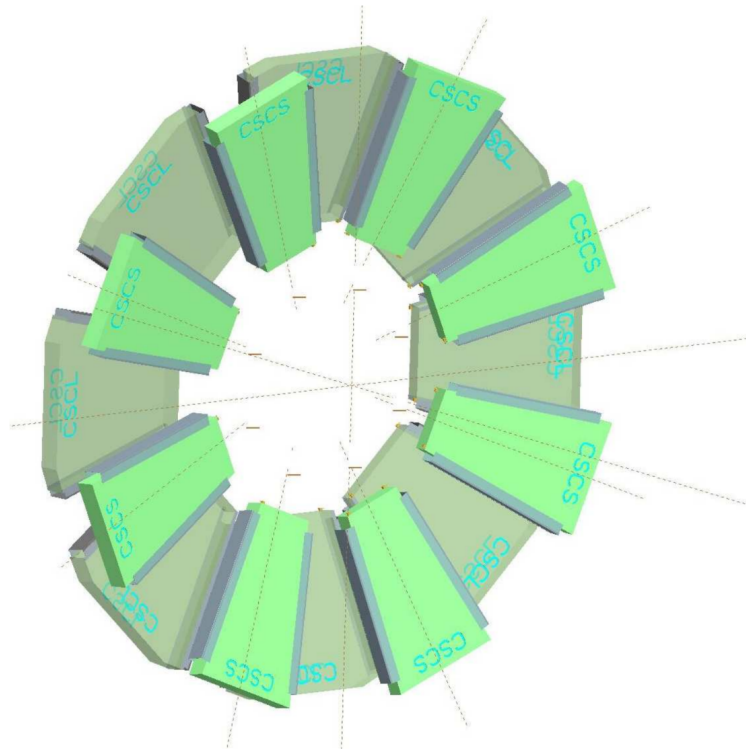


Figure 38: A schematic of the [CSC](#) endcap, showing the overlapping arrangement of the eight large and eight small chambers.

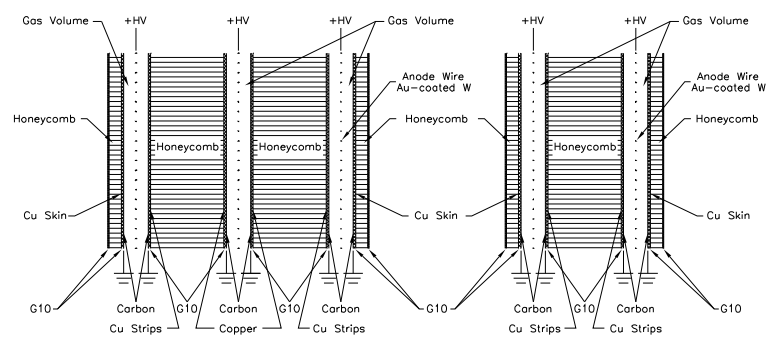


Figure 39: A schematic of the TGC doublet and triplet layers.

2039 measurement in the ϕ direction. The high electric field and small wire-to-wire
 2040 distance give it the required good time resolution to be used for triggering events.

2041 5.6 TRIGGER

2042 It is not possible for the detector and the associated computing systems to record
 2043 the 80 TB of data that the 40 MHz event rate produces every second. Instead, a
 2044 small fraction of these events are selected by the trigger system to be recorded
 2045 and later analyzed. Selecting interesting events at such a high rate poses a sig-
 2046 nificant challenge for the both the detector design and the implementation of a
 2047 trigger decision and data acquisition system. The trigger must balance the time
 2048 needed to decide to keep an event, to avoid losing information, with the filtering
 2049 accuracy to consistently select a full menu of physics events that can be used for
 2050 the wide array of searches and measurements targeted by ATLAS.

2051 The ATLAS trigger system, as of Run 2, consists of two levels of decision mak-
 2052 ing. The first level, referred to as [L1](#), is hardware based and uses inputs from a
 2053 subset of the detector elements to reduce the considered event rate from the
 2054 original 40 MHz down to 100 kHz. The 100 kHz rate is the maximal rate that
 2055 the event information can be transferred from the detector. The [L1](#) trigger deci-
 2056 sions must be made with $2.5 \mu\text{s}$, or else the information stored from the event is
 2057 still available to be read out to the next step. The second, software-based level,
 2058 referred to as the [HLT](#), makes the final decisions on which events to keep for anal-
 2059 ysis and selects a rate of around 1 kHz. The collection of selection criteria used
 2060 to make the [L1](#) decisions feed into subsequent selection criteria in the [HLT](#), and
 2061 the set of these combinations of [L1](#) and [HLT](#) criteria from the trigger menu which
 2062 defines exactly what events are recorded on ATLAS. A subset of the trigger menu
 2063 used for 2015 data collection is shown in Table 6, which summarizes the selec-
 2064 tion requirements at both levels and additionally shows the peak measured rates
 2065 contributed by each.

2066 At [L1](#), the trigger system uses information primarily from the calorimeters and
 2067 muon spectrometer to select high p_T jets, electrons, photons, and muons. The
 2068 electromagnetic calorimeter uses reduced granularity energy measurements as
 2069 well as isolation requirements to select electrons and photons. The hadronic
 2070 calorimeter also uses a combination of reduced granularity energy measurements
 2071 and isolation to select high momentum jets and hadronically decaying tau lep-
 2072 tons. The calorimeters are also used to provide triggers based on missing energy:
 2073 the coarse granularity energy measurements are used to calculate a directional
 2074 sum of energies and to trigger on a significant imbalance. The analysis discussed
 2075 here uses the E_T^{miss} trigger shown in Table 6, with a [L1](#) rate of 0.7 kHz and an [HLT](#)
 2076 rate of 55 Hz.

2077 Only the [RPCs](#) and [TGCs](#) muon subdetectors contribute to the decision at [L1](#),
 2078 and are used to identify high momentum muons. The contributions to the trig-
 2079 gering rate of the various types of [L1](#) triggers are shown in Figure 40. The total
 2080 rate is indicated in black and is lower than the sum of individual rates because
 2081 their is significant overlap between different trigger channels. The majority of
 2082 the rate comes from lepton and photon triggers.

Trigger	Typical offline selection	Trigger Selection		Level-1 Peak Rate (kHz)	HLT Peak Rate (Hz)
		Level-1 (GeV)	HLT (GeV)		
Single leptons	Single iso μ , $p_T > 21$ GeV	15	20	7	130
	Single e , $p_T > 25$ GeV	20	24	18	139
	Single μ , $p_T > 42$ GeV	20	40	5	33
	Single τ , $p_T > 90$ GeV	60	80	2	41
Two leptons	Two μ 's, each $p_T > 11$ GeV	2×10	2×10	0.8	19
	Two μ 's, $p_T > 19, 10$ GeV	15	18, 8	7	18
	Two loose e 's, each $p_T > 15$ GeV	2×10	2×12	10	5
	One e & one μ , $p_T > 10, 26$ GeV	20 (μ)	7, 24	5	1
	One loose e & one μ , $p_T > 19, 15$ GeV	15, 10	17, 14	0.4	2
	Two τ 's, $p_T > 40, 30$ GeV	20, 12	35, 25	2	22
	One τ , one μ , $p_T > 30, 15$ GeV	12, 10 (+jets)	25, 14	0.5	10
	One τ , one e , $p_T > 30, 19$ GeV	12, 15 (+jets)	25, 17	1	3.9
Three leptons	Three loose e 's, $p_T > 19, 11, 11$ GeV	15, 2×7	17, 2×9	3	< 0.1
	Three μ 's, each $p_T > 8$ GeV	3×6	3×6	< 0.1	4
	Three μ 's, $p_T > 19, 2 \times 6$ GeV	15	18, 2×4	7	2
	Two μ 's & one e , $p_T > 2 \times 11, 14$ GeV	2×10 (μ 's)	$2 \times 10, 12$	0.8	0.2
	Two loose e 's & one μ , $p_T > 2 \times 11, 11$ GeV	$2 \times 8, 10$	$2 \times 12, 10$	0.3	< 0.1
One photon	one γ , $p_T > 125$ GeV	22	120	8	20
Two photons	Two loose γ 's, $p_T > 40, 30$ GeV	2×15	35, 25	1.5	12
	Two tight γ 's, $p_T > 25, 25$ GeV	2×15	2×20	1.5	7
Single jet	Jet ($R = 0.4$), $p_T > 400$ GeV	100	360	0.9	18
	Jet ($R = 1.0$), $p_T > 400$ GeV	100	360	0.9	23
E_T^{miss}	$E_T^{\text{miss}} > 180$ GeV	50	70	0.7	55
Multi-jets	Four jets, each $p_T > 95$ GeV	3×40	4×85	0.3	20
	Five jets, each $p_T > 70$ GeV	4×20	5×60	0.4	15
	Six jets, each $p_T > 55$ GeV	4×15	6×45	1.0	12
b -jets	One loose b , $p_T > 235$ GeV	100	225	0.9	35
	Two medium b 's, $p_T > 160, 60$ GeV	100	150, 50	0.9	9
	One b & three jets, each $p_T > 75$ GeV	3×25	4×65	0.9	11
	Two b & two jets, each $p_T > 45$ GeV	3×25	4×35	0.9	9
b -physics	Two μ 's, $p_T > 6, 4$ GeV plus dedicated b -physics selections	6, 4	6, 4	8	52
Total				70	1400

Table 6: A subset of the trigger menu for the 2015 data collection with $L = 5 \times 10^{33} \text{ cm}^{-2} \text{ s}^{-1}$. Both the L1 and HLT selection requirements and their trigger rates are shown measured at the specified luminosity are shown. The typical offline selections represent a typical set of offline requirements imposed after the trigger in an analysis.

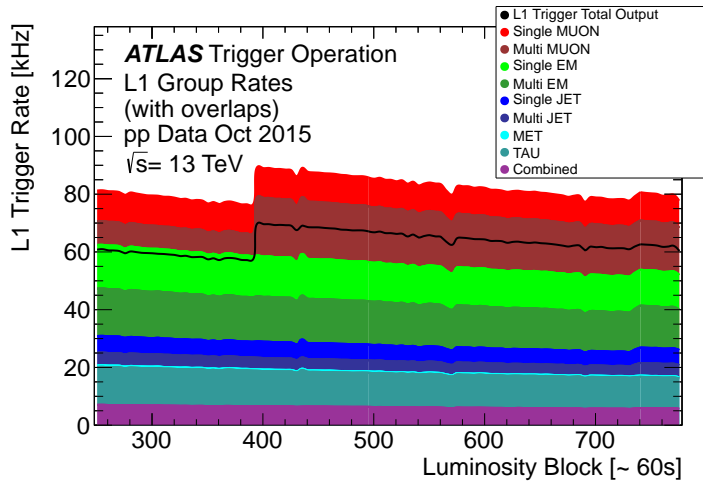


Figure 40: The L1 Trigger rate broken down into the types of triggers as a function of the luminosity block for the 2015 data collection period.

After an event is chosen by the L1 trigger, the detector measurements from the bunch crossing which fired the trigger is read out from the front-end electronics and stored on read-out boards. This inclusive information is necessary to make more the more precise event selections than is possible with the reduced information at L1. The HLT then uses this information with software algorithms to decide whether or not to permanently record the event. The L1 trigger also forwards which decision was made and Region of Interests (RoIs) to the HLT, which allows the HLT to focus on particular algorithms and particular sections of the detector to greatly improve the algorithmic selection speed. The additional information available to the HLT allows it to use full offline reconstruction algorithms (Chapter 6) to implement additional trigger targets, such as identified jets from the decays of b-hadrons. The contributions to the triggering rate of the various types of HLT triggers are shown in Figure 41.

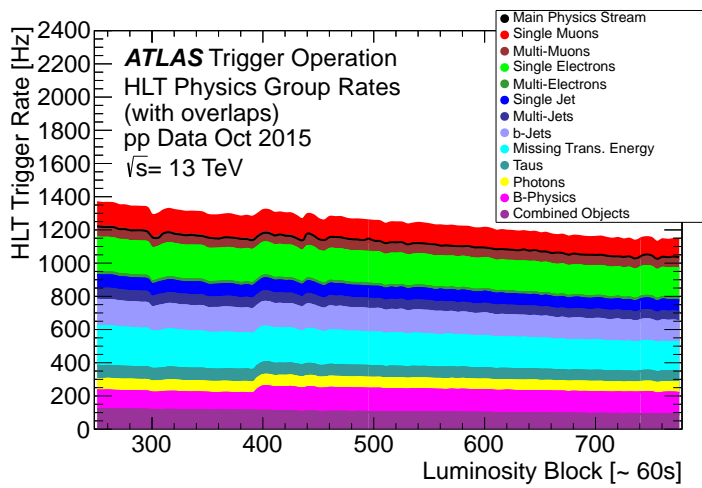


Figure 41: The HLT Trigger rate broken down into the types of triggers as a function of the luminosity block for the 2015 data collection period.

2096

2097 EVENT RECONSTRUCTION

2098 The ATLAS experiment combines measurements in the subdetectors to form a
2099 cohesive picture of each physics event. The majority of particles that traverse
2100 the detector leave behind some combination of ionization hits in the tracking
2101 detectors or energy deposits in the calorimeters, and these measurements can
2102 be used to reconstruct physical quantities like the particle’s energy, momentum,
2103 or trajectory. Even the type of the particle can be distinguished by comparing
2104 the various ways that different species of stable particles interact with the sub-
2105 detectors. Reconstruction is the series of algorithms which take the electronic
2106 outputs of the detector and assigns them into individual physics objects. The
2107 physics objects summarize the properties of particles produced by the collision
2108 or subsequent decays, either for individual isolated particles like leptons, or for
2109 a collection of the cascade of products produced in the decay of an energetic
2110 hadron, called a jet. These are the objects and quantities most often used in anal-
2111 ysis to make measurements of SM processes or to search for new physics.

2112 6.1 CHARGED PARTICLES

2113 As described in Section 5.3, charged particles that traverse the inner detector
2114 leave behind hits in the subdetectors. Each of these hits translates into a position
2115 measurement along the trajectory of that particle, with position resolutions de-
2116 pending on the subdetector that provided the measurement. Track reconstruc-
2117 tion uses these position measurements to collect hits in consecutive layers of
2118 the detector into a trajectory consistent with a particle curving in a magnetic
2119 field [21, 22]. This reconstructed trajectory is called a track. The number of hits
2120 in the inner detector for each event makes a combinatorial method completely
2121 infeasible: the algorithms that form tracks must be significantly more intelligent
2122 so that event reconstruction does not exhaust computing resources.

2123 The first and primary algorithm employed in track reconstruction is called
2124 the inside-out method, which begins with the assumption that the track orig-
2125 inated from the interaction point. Its purpose is to identify primary particles,
2126 those which originate in the proton-proton collisions and with a lifetime long
2127 enough to reach the inner detector. Combinations of three hits are considered
2128 from measurements in the Pixel detector and the SCT, and form the seed for a
2129 track. Specifically, the seeding algorithm looks for a seed using three pixel hits,
2130 two pixel hits and one SCT hit, or three SCT hits. The seed is then extrapolated
2131 forwards and backwards into the Pixel and SCT detectors depending on the seed
2132 location, and hits in each layer are considered to be added to the track using a
2133 combinatorial Kalman filter [22]. After all of the silicon layers have been con-
2134 sidered, tracks are filtered to reduce ambiguities from other nearby tracks or
2135 from combinatorial coincidences. Then the tracks are extended outwards into

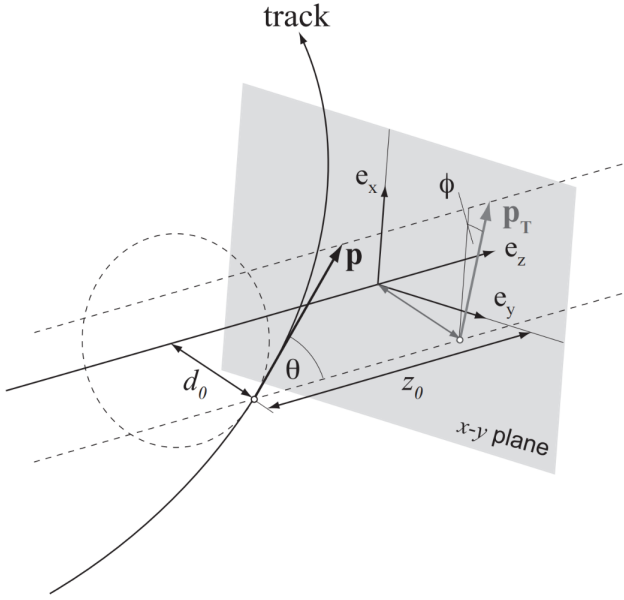


Figure 42: An illustration of the perigee representation of track parameters for an example track. The charge is not directly shown, but is indicated by the direction of curvature of the track [23].

the TRT in the same way. The result of this clustering algorithm is a collection of hits identified to belong to a single track. Once the hits are collected, a fitting algorithm calculates the track parameters which best model the locations of the hits and their resolutions. The fitting uses five parameters, $(d_0, z_0, \phi, \theta, q/p)$, to specify a track in a perigee representation: d_0 and z_0 are the transverse and longitudinal impact parameters at the closest approach to the nominal beam axis, ϕ and θ are the usual angular coordinates, and q/p is the charge divided by the curvature. These parameters are illustrated in Figure 42. Those parameters directly determine the direction and momentum of the particle which produced the track.

This inside-out algorithm is complemented by an outside-in algorithm, which is used to find tracks from secondary particles, those produced in the decays or interactions of the primary particles inside the detector. As the name indicates, the outside-in algorithm begins by seeding tracks in the outermost layers of the inner detector, in the TRT. The seed in this case is formed by a segment in the TRT, and the track is propagated backwards into the SCT before being refitted to use all the included points. Some tracks are found with TRT segments only, which can result from interactions with the detector following the SCT. Figure 43 shows an example of the geometry of tracks formed by both algorithms, where the hits belonging to tracks found using the inside-out algorithm are highlighted in red, and the hits belonging to the tracks found using the outside-in algorithm are circled in black. The figure highlights the presence of a large number of both primary and secondary tracks in a single event, as well as the overall large number of hits present in the inner detector.

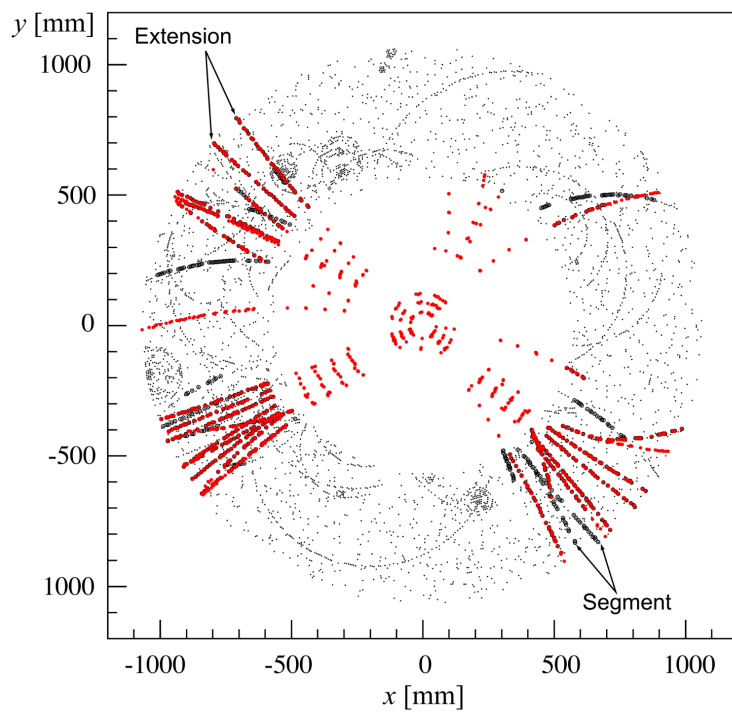


Figure 43: The x and y locations of the hits generated in a simulated $t\bar{t}$ event in the inner detector. The hits which belong to tracks formed using the inside-out algorithm are highlighted in red, while the hits which belong to tracks formed using the outside-in algorithm are circled in black. This figure does not include hits in the IBL.

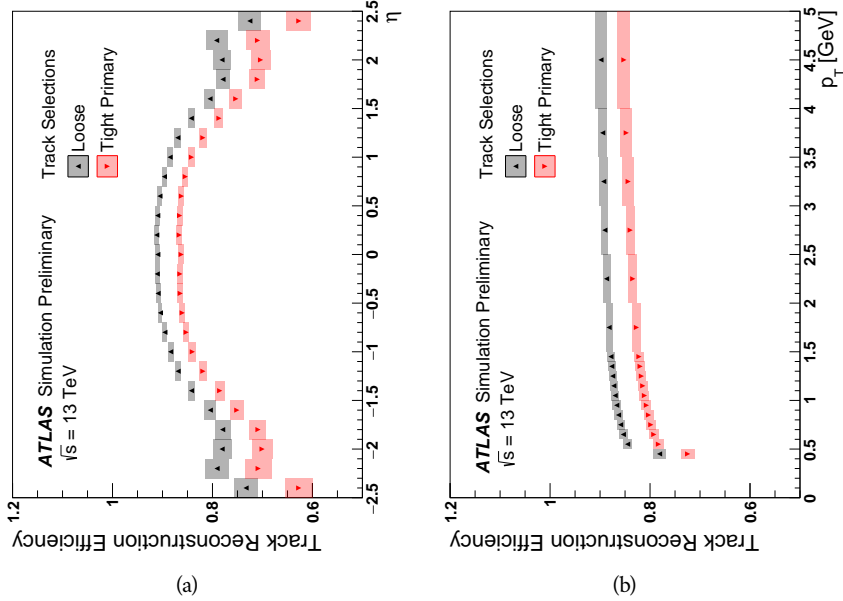


Figure 44: The tracking reconstruction efficiency as a function of (a) η and (b) p_T [24].

The tracks resulting from these algorithms can be contaminated by nearby particles confusing the tracking algorithm in a high luminosity environment. For example, enough hits present in the inner detector can lead to fake tracks from combinations of hits from multiple individual tracks. Therefore, after the tracks are formed and fitted, additional quality requirements are imposed in order to reduce such backgrounds. Most tracking applications require at least seven silicon hits, that is, seven hits between the Pixel detector and SCT. Then the tracks are required to have at most two holes in the Pixel detector, where holes are non-existing but expected measurements in a layer of the subdetector. If the missing hit corresponds to an inactive module, however, it is not counted as a hole but instead as a hit for tracking as the lack of a measurement is expected in that case. With these requirements, the inner detector achieves the reconstruction efficiencies shown in Figure 44 as a function of p_T and η . The efficiency ranges between 80% and 90% for the tight primary selection described above, and is maximized at high p_T and low $|\eta|$.

6.1.1 PIXEL NEURAL NETWORK

The hits in the Pixel detector are not typically confined to a single pixel, but rather the charge is spread over several pixels per layer which are grouped together into clusters. The clustering of these pixels for isolated tracks is relatively straightforward; a connected component analysis identifies groups of neighboring pixels above the readout threshold [25]. Complications can arise in the high occupancy environment where hits from multiple particles can overlap in a single cluster. Figure 45 shows examples of clusters generated by a single isolated

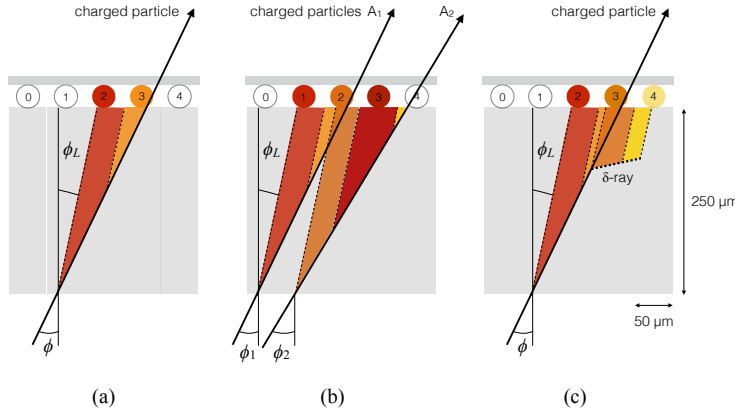


Figure 45: Examples of the clusters formed in a single layer of the pixel detector for (a) a single isolated particle, (b) two nearly-overlapping particles, and (c) a particle which emits a δ -ray [25].

2183 particle, two nearly overlapping particles, and a particle which emits a δ -ray. A
 2184 δ -ray is a secondary electron which is generated with enough energy to escape
 2185 a significant distance away from the original particle and to generate additional
 2186 ionization.

2187 A series of neural-networks analyzes the shape of the clusters to determine
 2188 how many particles produced the cluster and to estimate the positions of each
 2189 of the particles within the cluster. These allow for an identification of clusters
 2190 caused by more than one particle or by a particle that emits a δ -ray. In a high-
 2191 density tracking environment, the multiple position outputs can be used as the
 2192 locations of individual hits to allow reconstruction of tracks which almost over-
 2193 lap and with a much better separation than is possible without the splitting of
 2194 individual clusters.

2195 6.1.2 PIXEL DE/DX

2196 A hit in the Pixel detector corresponds to the voltage generated from ionization
 2197 current rising above a threshold value that is tuned to consistently record the
 2198 passing of MIPs. A larger amount of charge deposited results in a larger voltage,
 2199 and a larger signal remains above the threshold for a longer period of time. The
 2200 time over threshold (ToT) is read out of the Pixel detector, and can be used to
 2201 provide a measurement of the charge deposited in each pixel. The charge mea-
 2202 surements from each of the pixels included in a pixel cluster are summed to form
 2203 one charge measurement per layer of the pixel detector. That charge measure-
 2204 ment, combined with the angle of incidence of the track and the known sizes of
 2205 each detector element, can be converted into a measurement of dE/dx , the ion-
 2206 ization energy deposited per unit distance, measured in $\text{MeVg}^{-1}\text{cm}^2$. The IBL
 2207 only has sixteen available values (4 bits) of ToT to readout, compared to the 256
 2208 available values (8 bits) in the remaining pixel layers. To help alleviate this lack
 2209 of range, the IBL also records if it is in overflow: when the ionization is sufficient

2210 to generate a [ToT](#) above the largest value that can be recorded in the 4 bits. In the
 2211 remaining layers, the charge value is lost if the hit is in overflow; however the
 2212 significantly larger range of values makes this very rare in those layers.

2213 The measurements across multiple layers are combined to form an average
 2214 value of dE/dx for the track as a whole. Depending on where a charged particle
 2215 is produced, it will traverse four Pixel layers and create four clusters on average.
 2216 It can produce as few as two clusters in the Pixel detector if it passes through in-
 2217 active modules, and as many as five if is in a region of the detector where multiple
 2218 modules overlap. To reduce the influence of the typical long Landau tails of the
 2219 distribution of dE/dx deposits [2], the average is calculated as a truncated mean
 2220 of these clusters. The value measured in the [IBL](#) is removed if it is in overflow, as
 2221 the measured value is not reliable in that case. If a track has five measurements
 2222 in the pixel detector, the two highest cluster values are removed. If a track has
 2223 two, three, or four measurements in the pixel detector, only the single highest
 2224 cluster value is removed. The remaining values are averaged to form the pixel
 dE/dx .

2226 6.1.3 VERTEX RECONSTRUCTION

2227 A vertex represents the intersection of multiple tracks and corresponds to the
 2228 location of an interaction. If at least two charged particles result from the in-
 2229 teraction, the intersection of their resulting tracks reveals its position with high
 2230 precision. Vertices are divided into two groups, primary vertices which corre-
 2231 spond to the actual proton-proton collisions, and secondary vertices which cor-
 2232 respond to decays of short-lived particles or interactions with the detector. Pri-
 2233 mary vertices are particularly important, as they can provide a precise location
 2234 for the interaction which generated the observed particles. Understanding that
 2235 location is crucial in understanding the geometry of the event.

2236 Primary vertices are reconstructed by iteratively identifying seeds from recon-
 2237 structed tracks [26]. Each track's extrapolated z position at the beamline forms a
 2238 seed, and nearby tracks are fitted using that position as a point along their trajec-
 2239 tory. The goodness of fit with that vertex is considered for each track, measured
 2240 in χ^2 . The final position of the vertex is determined by a fit to all of the con-
 2241 sidered tracks, where the contribution from each track is weighted according to
 2242 the χ^2 compatibility with that vertex and by the error on its position. Any tracks
 2243 that are displaced by more than 7σ from that vertex are removed from the fit and
 2244 used to seed a new vertex. This procedure is iterated until no additional vertices
 2245 can be found.

2246 This procedure is typically performed twice. The first set of vertices is used
 2247 to fit a profile for the beamspot, which indicates the position of the intersec-
 2248 tion of beams in that particular bunch crossing. The fitted beamspot then pro-
 2249 vides a constraint for the second attempt to locate primary vertices, where both
 2250 the track fitting and seeding of vertices are required to be consistent with in-
 2251 teractions occurring within the beamspot. The vertex reconstruction algorithm
 2252 achieves the efficiency shown in Figure 46, increasing from 83% for vertices with

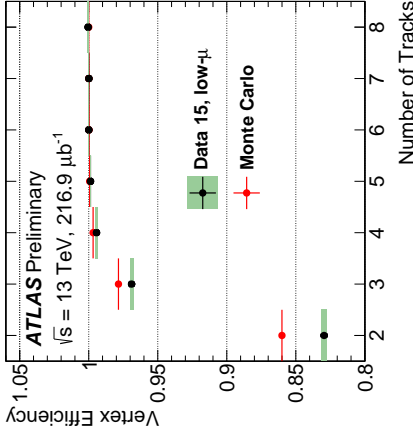


Figure 46: The vertex reconstruction efficiency as a function of the number of associated tracks [27].

two associated tracks and up to nearly 100% for vertices with four or more associated tracks.

6.2 ELECTRONS AND PHOTONS

Electrons are measured as both a charged particle track and energy deposits in the electromagnetic calorimeter. Photons, on the other hand, leave energy deposits in the electromagnetic calorimeter but do not produce a corresponding track. Because the electromagnetic interactions with the calorimeter of both photons and electrons produces more photons and electrons, the behavior in the calorimeter is very similar and there is significant overlap in the reconstruction techniques for each.

The reconstruction of a photon or an electron in the calorimeter is based on clustering algorithms which identify groups of energy deposits [28–30]. For this purpose, the entire electromagnetic calorimeter is subdivided into a grid of 200 by 256 towers in the η and ϕ directions, respectively, where the individual grid units have a size of $\Delta\eta = 0.025$ and $\Delta\phi = 0.025$. These towers correspond to individual cells in the middle, coarsest layer of the EM calorimeter, and in the remaining layers the cells are grouped together cover the same area in $\eta - \phi$ space. The clustering begins by finding seeds with a sliding-window algorithm based on the towers: a window of 3 by 5 towers is formed and translated until the sum of the energy within the window is maximized. If that energy is above 2.5 GeV, then that region becomes a seed. The choice of 2.5 GeV was chosen to compromise between maximizing reconstruction efficiency while minimizing fake electron seeds from electronic noise or soft hadrons from additional interactions. The seeds are rejected if the energy measured in the hadronic calorimeter behind the seed is large, as this typically indicates a hadron rather than an electron or photon.

Next, the inner detector tracks within a cone of $\Delta R = 0.3$ are compared to the location and energy of the seed. Tracks are matched to the cluster if the ex-

2281 trapolation of the track to the energy-weighted center in the middle layer of the
 2282 **EM** calorimeter falls within $\Delta\phi < 0.2$ in the direction of the curvature of the
 2283 track or $\Delta\phi < 0.05$ in the direction opposite of the curvature of the track. If the
 2284 seed matches with a track that originated from a primary vertex, the combina-
 2285 tion of track and electromagnetic cluster is reconstructed as an electron. If the
 2286 seed matches with a track that did not originate from a primary vertex, then the
 2287 electromagnetic cluster is reconstructed as a converted photon. And if there is
 2288 no corresponding track in the inner detector, than the cluster is reconstructed
 2289 as a photon.

2290 After classification, the final clustering of the energy in the **EM** calorimeter
 2291 calorimeter is performed. The classification must be done first, as the expected
 2292 size of the energy deposits in the calorimeter are different for electrons and pho-
 2293 tons. In the barrel region, the final clusters for electrons are formed in rectangles
 2294 of 3 towers in the η -direction and 7 towers in the ϕ -direction. This asymmetric
 2295 window accounts for the curving of the charged particles only in the ϕ direction.
 2296 For photons, the size of the rectangle is 3 towers by 5 towers. In the endcap re-
 2297 gion, all object types are clustered in rectangles of 5 towers by 5 towers, as the
 2298 effect of the magnetic field curvature is less pronounced in this region. The sum
 2299 of the energies in these clusters provide the final energy measurement for the
 2300 electron or photon.

2301 6.2.1 PHOTON IDENTIFICATION

2302 The original requirement for constructing a photon cluster, a significant energy
 2303 deposit in the electromagnetic calorimeter without a corresponding track or en-
 2304 ergy deposits in the hadronic calorimeter, is already effective in identifying pho-
 2305 tons. However, there is a significant background for prompt photon production
 2306 from the decays of pions, $\pi^0 \rightarrow \gamma\gamma$. These can be identified using the shape of
 2307 the cluster in the narrow η granularity in the first layer of the **EM** calorimeter.

2308 6.2.2 ELECTRON IDENTIFICATION

2309 Prompt electrons have a number of backgrounds, such as secondary electrons
 2310 from hadron decays or misidentified hadronic jets, that can be rejected using ad-
 2311 ditional information from the **EM** calorimeter and the inner detector. The most
 2312 basic level of electron identification, referred to as Loose, makes requirements
 2313 on the shower shapes in the high granularity first layer of the **EM** calorimeter
 2314 as well as the quality of the inner detector track. It also requires a good match
 2315 between the track and the calorimeter energy deposits and a small fraction of
 2316 energy in the hadronic calorimeter behind the electromagnetic cluster. ATLAS
 2317 defines several additional working points, including MediumLL and TightLL,
 2318 which provide progressively lower background rates for electrons by imposing
 2319 additionally strict requirements on the above variables as well as new require-
 2320 ments like the impact parameter of the inner detector track or the comparison
 2321 of the cluster energy to the momentum in the inner detector. The LL designates

2322 that the requirement is based on a threshold on the output of a likelihood func-
 2323 tion using the above quantities as an input [29].

2324 6.3 MUONS

2325 Muons produced in ATLAS first traverse the inner detector and leave behind a
 2326 track as described in Section 6.1. The muon then passes through the calorimeter,
 2327 leaving behind a small, characteristic amount of energy, and then passes through
 2328 the muon spectrometer where it produces hits in the MDTs or CSCs. Muon tracks
 2329 are formed from local segments of hits in each layer of the MDTs or CSCs, and
 2330 then the final muon spectrometer track is formed by combining the two local
 2331 segments [31]. When a track is reconstructed in both the inner detector and
 2332 the muon spectrometer, the track is refitted to include the hits in both the inner
 2333 detector and the muon spectrometer, and forms a combined muon.

2334 In a few regions of the detector, a muon may fail to leave behind both a com-
 2335 plete inner detector and muon system track. For a very small fraction of the
 2336 acceptance of the muon system, there is only one layer of muon chambers and a
 2337 global muon system track is not formed. In this case, as long as the track in the
 2338 inner detector exists and geometrically matches to a segment, a segment-tagged
 2339 muon is formed using momentum measurements from the inner detector. In
 2340 the region where the muon system has coverage but the inner detector does not,
 2341 $2.5 < |\eta| < 2.7$, a stand-alone muon is formed which uses only information
 2342 from the muon system. And for muons produced within one of the few holes in
 2343 the muon system, including $|\eta| < 0.1$, the characteristic energy deposits in the
 2344 calorimeter can be used to tag an inner detector track as a calo-tag muon. These
 2345 additional categories are used to achieve high efficiency over a larger range of
 2346 acceptance, but the combined muons are the most reliable.

2347 6.3.1 MUON IDENTIFICATION

2348 The various types of muons are incorporated into three working points: Loose,
 2349 Medium, and Tight, which reflect the increasing muon purity for each of the
 2350 selections definitions. Tight muons include only combined muons with a good
 2351 track fit quality and momentum resolution and at least two hits in a precision
 2352 muon system layer. Medium muons include those in tight as well as combined
 2353 muons with one precision hit and one precision hole, where hole is defined in
 2354 the same way as in Section 6.1. The medium working point also includes stand-
 2355 alone muons with $|\eta| > 2.5$ and at least two hits in precision layers. And finally
 2356 the loose working point includes both medium and tight muons, but additional
 2357 includes segment-tagged and calo-tagged muons in the region $|\eta| < 0.1$. The
 2358 reconstruction efficiencies for muons with $p_T > 20$ GeV range from 91.8% for
 2359 tight muons and up to 98.1% for loose muons [31].

2360 6.4 JETS

2361 A jet does not directly correspond to a physical particle, unlike all of the recon-
 2362 structed objects described above, but instead tries to capture the conical cascade
 2363 of particles produced in the hadronization of a quark or gluon from the proton-
 2364 proton collision. The hadronization process creates a very large number of col-
 2365 limated particles, with a high enough density that individually reconstructing all
 2366 of the produced particles in the calorimeter is not possible within ATLAS. How-
 2367 ever most analyses are interested only in the kinematics of the particle which
 2368 produced the cascade, rather than the individual products. Therefore, jets are
 2369 a useful tool to measure the combined energy and direction of the ensemble of
 2370 products and thus represents the kinematics of the original. Jet algorithms are
 2371 very generic and can be used to group together a number of types of objects to
 2372 form aggregate representations. For example, truth particles in simulation can
 2373 be grouped in truth jets, or tracks from the inner detector can be grouped to-
 2374 gether to form track jets. This section, however, will focus on calorimeter jets
 2375 which take topoclusters of energy deposits in the calorimeter as inputs and pro-
 2376 duce a combined object which represents the energy measured by the calo-
 2377 meter and the location where it was deposited.

2378 6.4.1 TOPOLOGICAL CLUSTERING

2379 Hadrons often deposit their energy into multiple individual cells in both the elec-
 2380 tromagnetic and hadronic calorimeters. The purpose of topological clustering is
 2381 to group cells in all three dimensions into clusters that represent a single energy
 2382 deposit. The procedure must be robust enough to reject noise fluctuations in
 2383 the cell energy measurements that can come from both electronic noise and ad-
 2384 dditional low energy particles produced in pileup activity. The background level
 2385 of calorimeter noise is called σ_{noise} , and is an important component of the topo-
 2386 logical clustering.

2387 The topological clusters are formed in a three step process called the 4-2-0
 2388 threshold scheme, which uses three energy thresholds to build up a cluster from
 2389 cells [32]. First, any cells with a measured energy above $4\sigma_{\text{noise}}$ are identified
 2390 as seed cells. The cells adjacent to the seed cells with a measured energy above
 2391 $2\sigma_{\text{noise}}$ are called secondary cells. All of the cells which are adjacent to a sec-
 2392 ondary cell with $E_{\text{cell}} > 2\sigma_{\text{noise}}$ are also labeled secondary cells. Tertiary cells
 2393 are those immediately adjacent to a seed or secondary cell with a measured en-
 2394 ergy above zero. Adjacency in this sense is defined in three dimensions, cells are
 2395 adjacent if they are neighbors within a layer but also if they have the same $\eta - \phi$
 2396 coordinates but are in adjacent layers or even in an adjacent layer in another
 2397 calorimeter.

2398 From these definitions, clusters are built by resolving the seeds in order of
 2399 significance, the ratio $E_{\text{cell}}/\sigma_{\text{noise}}$. All adjacent secondary cells to the highest
 2400 significance seed are added to that seed's topocluster, and any of those cells which
 2401 would also have qualified as seeds are removed from the list of seeds. Once all
 2402 of the secondary cells have been added, the tertiary cells are then added to that

2403 cluster as well. This procedure is then iterated until no seeds remain, forming
 2404 the first round of topoclusters.

2405 It is also useful to split topoclusters into multiples if local maxima are present
 2406 within the topocluster, as clusters produced by multiple nearby particles can
 2407 merge. The splitting process begins by finding local maxima cells in the middle
 2408 layer of the calorimeters with a minimum energy of 500 MeV and at least four
 2409 neighboring secondary cells. These requirements reduce the likelihood to split
 2410 a cluster due to random fluctuations, as the middle layers provide the most reli-
 2411 able energy measurements. Cells between two local maxima can then be shared
 2412 between two clusters to account for overlapping contributions from two parti-
 2413 cles. The energy sharing is weighted by the energy of each cluster as well as the
 2414 distance of the cell to the centroid of that cluster.

2415 The energies of all the cells in the cluster are then summed together to form
 2416 the energy of that cluster. The energy needs to be corrected for the various losses
 2417 expected in the calorimeter, as described in Section 5.4. The simplest correction,
 2418 scaling the measured energy by the sampling fraction, brings the cluster energies
 2419 to the EM scale. It is called the EM scale because it accurately describes the energy
 2420 of electromagnetic showers.

2421 Another scale is defined to improve accuracy for hadronic processes, the local
 2422 cluster weighted (LCW) scale, that helps to correct for the expected variations in
 2423 hadronic energy deposits. The LCW correction first determines if the shower is
 2424 hadronic or electromagnetic, based on the depth of the shower and the cluster
 2425 energy density. For hadronic showers, the energy is corrected for calorimeter
 2426 non-compensation, an effect which reduces the measured energy of hadronic
 2427 showers because some of the energy goes into invisible processes like the break
 2428 up of nuclei. All clusters are then corrected for energy that may be deposited in
 2429 uninstrumented regions in that cluster’s location in the calorimeter, and they are
 2430 also corrected with an estimate of how much energy falls outside the extent of
 2431 the cluster based on its shape and the deposit type.

2432 6.4.2 JET ALGORITHMS

2433 Using the topological clusters as inputs, a jet algorithm groups them together
 2434 into a collection of adjacent energy deposits that is intended to correspond to
 2435 a single process [33]. Jet algorithms need a few key characteristics to be usable
 2436 for physics analysis. First, the jets produced by the algorithm should have little
 2437 dependence on the addition of soft particles to the event (infrared safety), as a
 2438 negligible addition of energy should not significantly modify the event topology.
 2439 The jets produced by the algorithm should also be collinear safe: a single quark
 2440 replaced by two, parallel quarks with half the original’s momentum should not
 2441 change the resulting jets. This requirement is important as the jets are intended
 2442 to capture only the properties of the aggregate and not those of individual parti-
 2443 cles. And finally the algorithm needs to be sufficiently simple and fast to be used
 2444 for the large rate of collected proton-proton collisions on ATLAS.

2445 The most commonly used algorithm on ATLAS that satisfies these require-
 2446 ments is called the anti- k_t algorithm [34]. The anti- k_t , in brief, relies on itera-

tively combining the input objects that are closest together, where closest is defined by a particular distance metric, $d_{i,j}$, where the index i represents the combination constructed so far and j is an additional object being considered. The combinations stop when the closest remaining object is the beam itself, where the distance to the beam is called $d_{i,B}$. An entire class of algorithms follows this procedure with the following distance metrics

$$d_{i,j} = \min(k_{ti}^{2p}, k_{tj}^{2p}) \frac{\Delta_{ij}^2}{R^2} \quad (18)$$

$$d_{i,B} = k_{ti}^{2p} \quad (19)$$

where $\Delta_{ij} = (y_i - y_j)^2 + (\phi_i - \phi_j)^2$, k_{ti} is the transverse momentum of the object, y is the rapidity, and p is a parameter of the algorithm. Anti- k_t is the particular case where $p = -1$, and is a choice that results in an algorithm that is both infrared and collinear safe.

The algorithm is repeated until there are no input objects remaining, which results in a series of jets. Each jet has a complete four momentum from the combination of its input clusters, where the combinations assume a mass of zero. The jet energies then need to be calibrated to attempt to match the energy of the object which produced the jet.

6.4.3 JET ENERGY SCALE

Though the [LCW](#) scheme attempts to correct the topoclusters to reflect the true deposited energy, the correction does not fully account for energy lost within the calorimeters. Because of these effects, the original reconstructed jet energy does not reflect the true energy of the particle which initiated the jet. Therefore it is necessary to additionally correct the reconstructed jet itself, in addition to the corrections on the inputs. This correction is referred to as the [JES](#), which combines several individual steps of calibration [35].

The first calibration step corrections the direction of the jet to ensure that it points back to the primary vertex. Next, the energy of the jet is corrected for pileup by subtracting the expected contribution from pileup based on the momentum, η , and area of the jet as well as the number of reconstructed vertices and the expected number of interactions per crossing, μ . The largest single correction adjusts the jet energy and pseudorapidity to attempt to match the energy and pseudorapidity of the parton which produced it. This correction is measured in simulation by comparing the reconstructed jet energies to the energy of the truth particle which produced it. However the simulation is not relied on alone to estimate this correction, and an additional step applies an additional energy correction based on in-situ measurements in data. These corrections come from various techniques which measure jet energies indirectly by balancing them with other, well-measured objects. In the central region ($|\eta| < 1.2$), jets are balanced against photons and the leptonic decays of Z bosons and high momentum jets ($p_T > 210$ GeV) are also balanced against multiple smaller jets in multijet events.

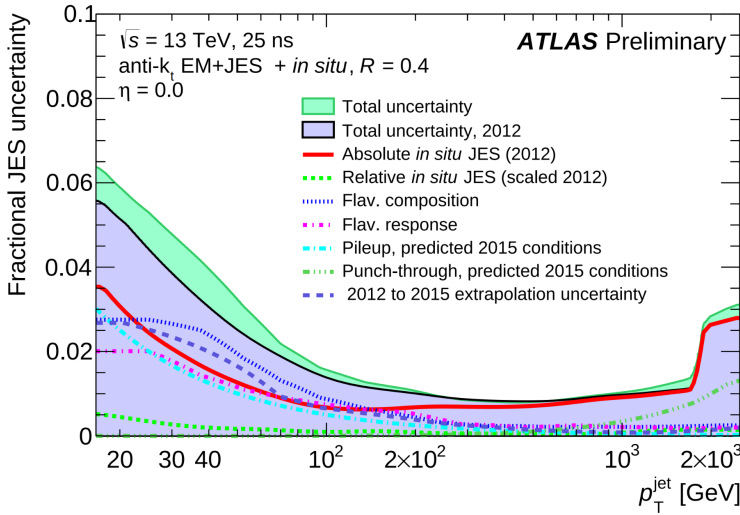


Figure 47: The total, fractional JES uncertainty estimated for 2015 data as a function of jet p_T .

2485 Jets at larger pseudorapidities, above $|\eta| = 1.2$, are calibrated by balancing with
 2486 lower pseudorapidity jets.

2487 These steps introduce a number of systematic uncertainties, referred to as
 2488 the JES uncertainty. The largest of these comes from the in-situ measurements,
 2489 which are statistically limited in measuring high momentum and high pseudora-
 2490 pidity jets. The total, fractional JES uncertainty is shown as a function of p_T in
 2491 Figure 47. The uncertainty falls to a minimum value of just over 1.0% around a
 2492 few hundred GeV, and rises again at high momentum because of the difficulty of
 2493 measuring jet balance in data above 2–3 TeV. The uncertainty is also minimized
 2494 at low $|\eta|$, and grows at large $|\eta|$ again where making in-situ measurements is
 2495 difficult. This technique does not actually provide a measurement of the uncer-
 2496 tainty for the highest energy jets, above 3 TeV, because there are not enough
 2497 measured data events to provide them. An alternative method for deriving the
 2498 JES and JES uncertainty that can be used even for very high p_T jets will be dis-
 2499 cussed in Chapter 8.

2500 6.5 MISSING TRANSVERSE ENERGY

2501 Among stable SM particles, only the neutrino cannot be directly measured in the
 2502 ATLAS detector. Because the neutrino carries neither electric nor color charge,
 2503 it is very unlikely to interact with the tracking detectors or the calorimeters,
 2504 and instead passes through the detector completely unobserved. Some particles
 2505 which have been conjectured to exist, like the LSP in many SUSY models, would
 2506 also have the same behavior. Therefore, it is important for ATLAS to provide
 2507 some way to assess the momentum carried away by a neutral, colorless parti-
 2508 cle. This can be accomplished through a measurement of missing energy in the
 2509 transverse direction, or E_T^{miss} , which quantifies the momentum imbalance of the
 2510 observed particles. From the conservation of momentum and the lack of the

2511 initial momentum in the transverse plane in the proton-proton collisions, any
 2512 imbalance of momentum can be inferred to be carried away by an unmeasured
 2513 particle.

2514 E_T^{miss} is more precisely defined as the magnitude of the vector sum of the
 2515 (p_x, p_y) components of each observed object's momentum. The definition is
 2516 simple, but there can be significant complexity in defining the inputs. As of Run
 2517 2, ATLAS uses a common algorithmic approach to carefully calculate missing en-
 2518 ergy, but each analysis is free to define its own inputs. For the analysis discussed
 2519 throughout this thesis, the missing energy inputs consist of the electrons, pho-
 2520 tons, muons, and jets discussed in the previous sections, in addition to a track-
 2521 based term that accounts for the contribution of low p_T particles (soft term).

2522 To produce the most precise measurement of E_T^{miss} , it is important to use the
 2523 best representation of the momentum of each of the input objects, which can
 2524 often be reconstructed as multiple different types in a single event. For example,
 2525 an electron can be reconstructed separately as an electron (Section 6.2) and a
 2526 jet (Section 6.4), but the electron representation has the highest precision for
 2527 reconstructing the true electron momentum. To ensure no duplications in the
 2528 E_T^{miss} definition, the inputs are collectively considered for overlap removal. Only
 2529 the most precise object type is kept for objects that fall within a cone of $\Delta R < 0.2$
 2530 for pairs of electrons and jets and a cone of $\Delta R < 0.4$ for other pair types.

2531 The fully reconstructed objects do not include all of the energy within the
 2532 events, as some clusters do not enter into a jet and some tracks are not classified
 2533 as electrons or muons. These momentum carried by these objects is accounted
 2534 for in a soft-term, which tallies all of the energy carried by the particles too soft
 2535 to form separate objects. The track soft term uses only tracking information to
 2536 estimate the contribution of soft objects, and does so by vectorially summing the
 2537 momentum of all well-reconstructed tracks with momentum above 400 MeV
 2538 that are not associated to other objects.

2539 All of these contributions together give a single E_T^{miss} value for a given event.
 2540 The direction of that missing energy is taken as opposite the vector sum of all the
 2541 constituents, to correspond to the momentum an invisible particle would have to
 2542 have to make the event balanced. Depending on the context, this missing energy
 2543 can be considered the energy of a neutrino or an LSP, with a large missing energy
 2544 being a common signal criteria for searches for new physics.

2545

PART III

2546

CALORIMETER RESPONSE

2547

2548

2549 RESPONSE MEASUREMENT WITH SINGLE HADRONS

2550 As discussed in Section 6.4, colored particles produced in collisions hadronize
2551 into jets of multiple hadrons. One approach to understanding jet energy mea-
2552 surements in the ATLAS calorimeters is to evaluate the calorimeter response to
2553 those individual hadrons; measurements of individual hadrons can be used to
2554 build up an understanding of the jets that they form. The redundancy of the
2555 momentum provided by the tracking system and the energy provided by the
2556 calorimeter provides an opportunity to study calorimeter response using real
2557 collisions, as described further in Section 7.2.

2558 Calorimeter response includes a number of physical effects that can be ex-
2559 tracted to provide insight into many aspects of jet modeling. First, many charged
2560 hadrons interact with the material of the detector prior to reaching the calorime-
2561 ters and thus do not deposit any energy. Comparing this effect in data and simu-
2562 lation is a powerful tool in validating the interactions of particles with the mate-
2563 rial of the detector and the model of the detector geometry in simulation, see Sec-
2564 tion 7.2.2. The particles which do reach the calorimeter deposit their energy into
2565 several adjacent cells, which are then clustered together. The energy of the clus-
2566 ter is then the total energy deposited by that particle. Comparing the response of
2567 hadrons in data to that of simulated hadrons provides a direct evaluation of the
2568 showering of hadronic particles and the energy deposited by particles in matter
2569 (Section 7.2.4).

2570 The above studies all use an inclusive selection of charged particles, which are
2571 comprised predominantly of pions, kaons, and (anti)protons. It is also possible to
2572 measure the response to various identified particle types separately to evaluate
2573 the simulated interactions of each particle, particularly at low energies where
2574 differences between species are very relevant. Pions and (anti)protons can be
2575 identified through decays of long-lived particles, in particular Λ , $\bar{\Lambda}$, and K_S^0 , and
2576 then used to measure response as described above. This is discussed in detail in
2577 Section 7.3.

2578 The results in this chapter use data collected at 7 and 8 TeV collected in 2010
2579 and 2012, respectively. Both are included as the calorimeter was repaired and
2580 recalibrated between those two data-taking periods. Both sets of data are com-
2581 pared to an updated simulation that includes new physics models provided by
2582 Geant4 [6] and improvements in the detector description [36, 37]. The present
2583 results are published in European Physical Journal C (EPJC) [38] and can be com-
2584 compared to a similar measurement performed in 2009 and 2010 [39], which used
2585 the previous version of the simulation framework [40].

2586 7.1 DATASET AND SIMULATION

2587 7.1.1 DATA SAMPLES

2588 The two datasets used in this chapter are taken from dedicated low-pileup runs
 2589 where the fraction of events with multiple interactions was negligible. These
 2590 datasets are used rather than those containing full-pileup events to facilitate mea-
 2591 surement of isolated hadrons. The 2012 dataset at $\sqrt{s} = 8$ TeV contains 8 mil-
 2592 lion events and corresponds to an integrated luminosity of 0.1 nb^{-1} . The 2010
 2593 dataset at $\sqrt{s} = 7$ TeV contains 3 million events and corresponds to an inte-
 2594 grated luminosity of 3.2 nb^{-1} . The latter dataset was also used for the 2010 re-
 2595 sults [39], but it has since been reanalyzed with an updated reconstruction in-
 2596 cluding the final, best understanding of the detector description for the material
 2597 and alignment from Run 1.

2598 7.1.2 SIMULATED SAMPLES

2599 The two datasets above are compared to simulated single-, double-, and non-
 2600 diffractive events generated with Pythia8 [41] using the A2 configuration of
 2601 hadronization [42] and the MSTW 2008 parton-distribution function set [43,
 2602 44]. The admixture of the single-, double-, and non-diffractive events uses the
 2603 default relative contributions from Pythia8. The conditions and energies for
 2604 the two simulations are chosen so that they match those of the corresponding
 2605 dataset.

2606 To evaluate the interaction of hadrons with detector material, the simulation
 2607 uses two different collections of hadronic physics models, called physics lists, in
 2608 Geant4 9.4 [45]. The first, QGSP_BERT, combines the Bertini intra-nuclear
 2609 cascade [46–48] below 9.9 GeV, a parametrized proton inelastic model from 9.5
 2610 to 25 GeV [49], and a quark-gluon string model above 12 GeV [50–54]. The
 2611 second, FTFP_BERT, combines the Bertini intra-nuclear cascade [46–48] below
 2612 5 GeV and the Fritiof model [55–58] above 4 GeV. In either list, Geant4 en-
 2613 forces a smooth transition between models where multiple models overlap.

2614 7.1.3 EVENT SELECTION

2615 The event selection for this study is minimal, as the only requirement is selecting
 2616 good-quality events with an isolated track. Such events are triggered by requir-
 2617 ing at least two hits in the minimum-bias trigger scintillators. After trigger, each
 2618 event is required to have exactly one reconstructed vertex, and that vertex is re-
 2619 quired to have four or more associated tracks.

2620 The particles which are selected for the response measurements are first iden-
 2621 tified as tracks in the inner detector. The tracks are required to have at least 500
 2622 MeV of transverse momentum. To ensure a reliable momentum measurement,
 2623 these tracks are required to have at least one hit in the pixel detector, six hits in
 2624 the SCT, and small longitudinal and transverse impact parameters with respect
 2625 to the primary vertex [39]. For the majority of the measurements in this chapter,

2626 the track is additionally required to have 20 hits in the TRT, which significantly
 2627 reduces the contribution from tracks which undergo nuclear interactions. This
 2628 requirement and its effect is discussed in more detail in Section 7.2.5. In addition,
 2629 tracks are rejected if there is any other reconstructed track which extrapolates
 2630 to the calorimeter within a cone of $\Delta R = \sqrt{(\Delta\phi)^2 + (\Delta\eta)^2} < 0.4$. This require-
 2631 ment guarantees that the contamination of energy from nearby charged particles
 2632 is negligible [39].

2633 7.2 INCLUSIVE HADRON RESPONSE

2634 The calorimeter response is more precisely defined as the ratio of the measured
 2635 calorimeter energy to the true energy carried by the particle, although this true
 2636 energy is unknown. For charged particles, however, the inner detector provides
 2637 a very precise measurement of momentum (with uncertainty less than 1%) that
 2638 can be used as a proxy for true energy. The ratio of the energy deposited by
 2639 the charged particle in the calorimeter, E , to its momentum measured in the
 2640 inner detector p , forms the calorimeter response measure called E/p . Though
 2641 the distribution of E/p contains a number of physical features, this study focuses
 2642 on the trends in two aggregated quantities: $\langle E/p \rangle$, the average of E/p for the
 2643 selected tracks, and the zero fraction, the fraction of tracks with no associated
 2644 energy in the calorimeter for those tracks.

2645 The calorimeter energy assigned to a track is defined using clusters. The clus-
 2646 ters are formed using a 4–2–0 algorithm [59] that begins with seeds requiring
 2647 at least 4 times the average calorimeter cell noise. The neighboring cells with
 2648 at least twice that noise threshold are then added to the cluster, and all bound-
 2649 ing cells are then added with no requirement. This algorithm minimizes noise
 2650 contributions through its seeding process, and including the bounding cells im-
 2651 proves the energy resolution [60]. The clusters are associated to a given track
 2652 if they fall within a cone of $\Delta R = 0.2$ of the extrapolated position of the track,
 2653 which includes about 90% of the energy on average [39].

2654 7.2.1 E/P DISTRIBUTION

2655 The E/p distributions measured in both data and simulation are shown in Fig-
 2656 ure 48 for two example bins of track momentum and for tracks in the central
 2657 region of the detector. These distributions show several important features of
 2658 the E/p observable. The large content in the bin at $E = 0$ comes from tracks that
 2659 have no associated cluster, which occurs due to interactions with detector mate-
 2660 rial prior to reaching the calorimeter or the energy deposit being insufficiently
 2661 large to generate a seed, and are discussed in Section 7.2.2. The small negative
 2662 tail also comes from tracks that do not deposit any energy in the calorimeter but
 2663 are randomly associated to a cluster with an energy below the noise threshold.
 2664 The long positive tail above 1.0 comes from the contribution of neutral parti-
 2665 cles. Nearby neutral particles deposit (sometimes large) additional energy in the
 2666 calorimeter but do not produce tracks in the inner detector, so they cannot be
 2667 rejected by the track isolation requirement. Additionally the peak and mean of

2668 the distribution falls below 1.0 because of the loss of energy not found within
 2669 the cone as well as the non-compensation of the calorimeter.

2670 The data and simulation share the same features, but the high and low tails
 2671 are significantly different. The simulated events tend to overestimate the con-
 2672 tribution of neutral particles to the long tail, an effect which can be isolated and
 2673 removed as discussed in Section 7.2.3. Additionally, the simulated clusters have
 2674 less noise on average, although this is a small effect on the overall response.

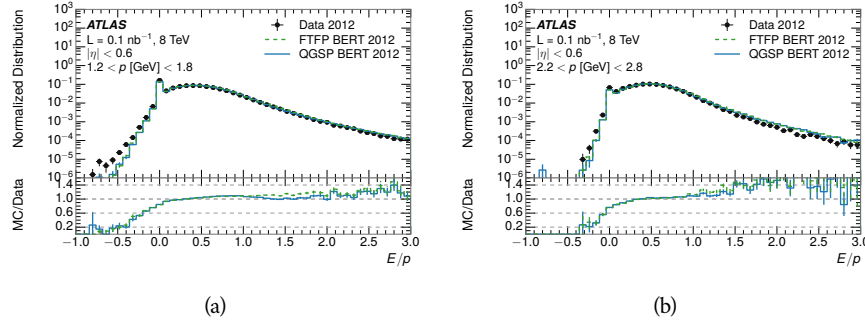


Figure 48: The E/p distribution and ratio of simulation to data for isolated tracks with
 (a) $|\eta| < 0.6$ and $1.2 < p/\text{GeV} < 1.8$ and (b) $|\eta| < 0.6$ and $2.2 < p/\text{GeV} < 2.8$.

2675 7.2.2 ZERO FRACTION

2676 The fraction of particles with no associated clusters, or similarly those with $E \leq$
 2677 0, reflects the modeling of both the detector geometry and hadronic interactions.
 2678 The zero fraction is expected to rise as the amount of material a particle traverses
 2679 increases, while it is expected to decrease as the particle energy increases. This
 2680 dependence can be seen in Figure 49, where the zero fraction in data and simula-
 2681 tion is shown as a function of momentum and the amount of material measured
 2682 in interaction lengths. The trends are similar between 2010 and 2012 and for
 2683 positively and negatively charged particles. The zero fraction decreases with
 2684 energy as expected. The absolute discrepancy in zero fraction between data and
 2685 simulation decreases with momentum from 5% to less than 1%, but this becomes
 2686 more pronounced in the ratio as the zero fraction shrinks quickly with increas-
 2687 ing momentum. The amount of material in the detector increases with η , which
 2688 is used to obtain results for interaction lengths ranging between 0.1 and 0.65 λ .
 2689 As the data and simulation have significant disagreement in the zero fraction
 2690 over a number of interaction lengths, the difference must be primarily from the
 2691 modeling of hadronic interactions with detector material and not just the detec-
 2692 tor geometry. Although two different hadronic interaction models are shown
 2693 in the figure, they have very similar discrepancies to data because both use the
 2694 same description (the BERT model) at low momentum.

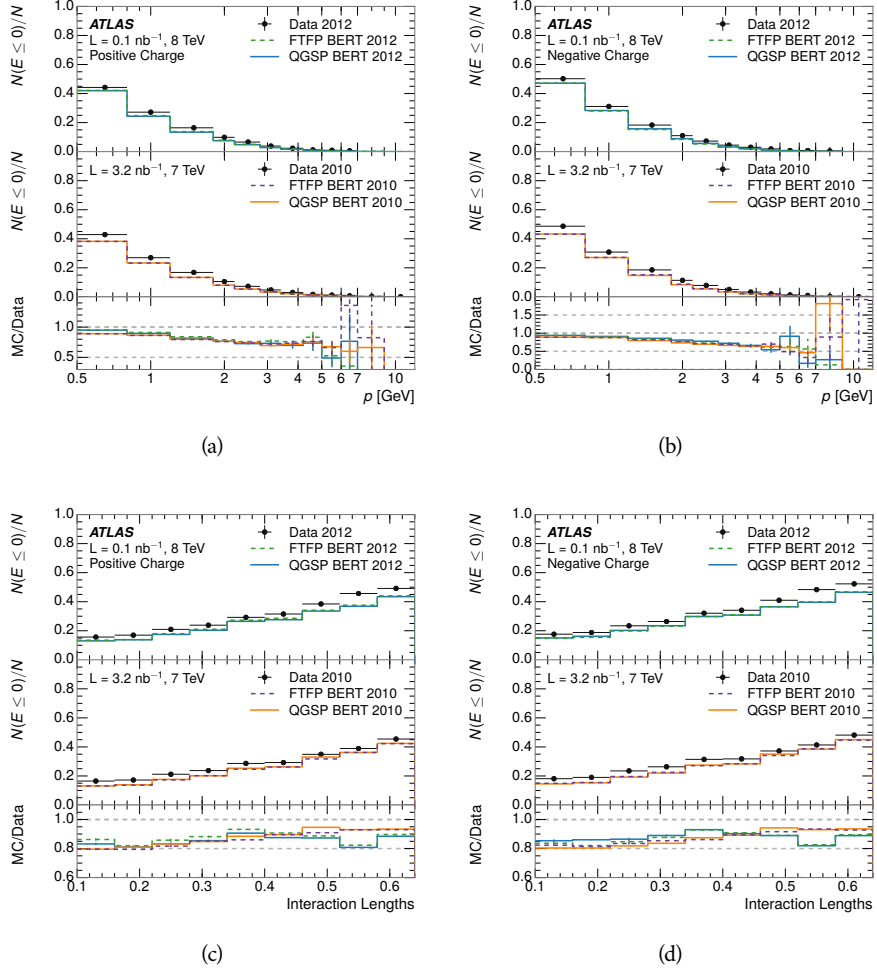


Figure 49: The fraction of tracks as a function (a, b) of momentum, (c, d) of interaction lengths with $E \leq 0$ for tracks with positive (on the left) and negative (on the right) charge.

2695 7.2.3 NEUTRAL BACKGROUND SUBTRACTION

2696 The isolation requirement on hadrons is only effective in removing an energy
 2697 contribution from nearby charged particles. Nearby neutral particles, predomi-
 2698 nantly photons from π^0 decays, also add their energy to the calorimeter clusters,
 2699 but mostly in the electromagnetic calorimeter. The arrangement of energy de-
 2700 posits is shown in Figure 50, which illustrates both energy deposits from the
 2701 hadronic particle and additional deposits from neutral particles. It is possible to
 2702 measure this contribution, on average, using late-showering hadrons that min-
 2703 imally ionize in the electromagnetic calorimeter. Such particles are selected by
 2704 requiring that they deposit less than 1.1 GeV in the EM calorimeter within a
 2705 cone of $\Delta R < 0.1$ around the track. To ensure that these particles are well mea-
 2706 sured, they are additionally required to deposit between 40% and 90% of their
 2707 energy in the hadronic calorimeter within the same cone.

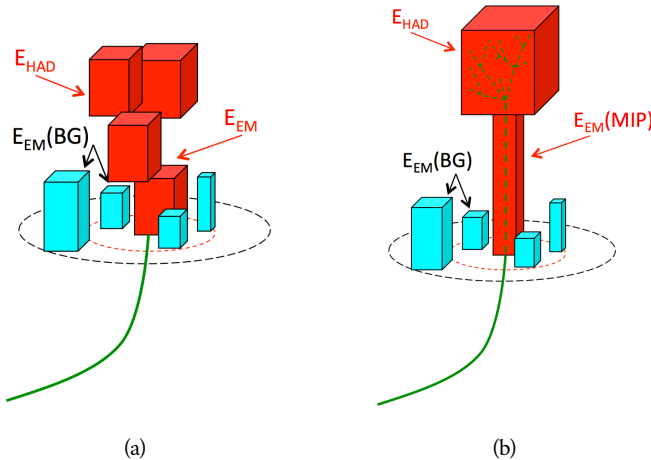


Figure 50: An illustration (a) of the geometry of energy deposits in the calorimeter. The red energy deposits come from the charged particle targeted for measurement, while the blue energy deposits are from nearby neutral particles and must be subtracted. The same diagram (b) for the neutral-background selection, described in Section 7.2.3.

2708 These particles provide a clean sample to measure the nearby neutral back-
 2709 ground because they do not deposit energy in the area immediately surround-
 2710 ing them in the EM calorimeter, as shown in Figure 50. So, the energy deposits in the
 2711 region $0.1 < \Delta R < 0.2$ can be attributed to neutral particles alone. To estimate
 2712 the contribution to the whole cone considered for the response measurement,
 2713 that energy is scaled by a geometric factor of $4/3$. This quantity, $\langle E/p \rangle_{BG}$, mea-
 2714 sured in aggregate over a number of particles, gives the contribution to $\langle E/p \rangle$
 2715 from neutral particles in the EM calorimeter. Similar techniques were used in
 2716 the individual layers of the hadronic calorimeters to show that the background
 2717 from neutrals is negligible in those layers [39].

2718 The distribution of this background estimate is shown in Figure 51 for data
 2719 and simulation with the two different physics lists. The contribution from neu-

tral particles falls from 0.1 at low momentum to around 0.03 for particles above 7 GeV. Although the simulation captures the overall trend, it significantly overestimates the neutral contribution for tracks with momentum between 2 and 8 GeV. This effect was also seen in the tails of the E/p distributions in Figure 48. This difference is likely due to modeling of coherent neutral particle radiation in Pythia8 that overestimates the production of π^0 near the production of the charged particles. The discrepancy does not depend on η and thus is unlikely to be a mismodeling of the detector. This difference can be subtracted to form a corrected average of E/p .

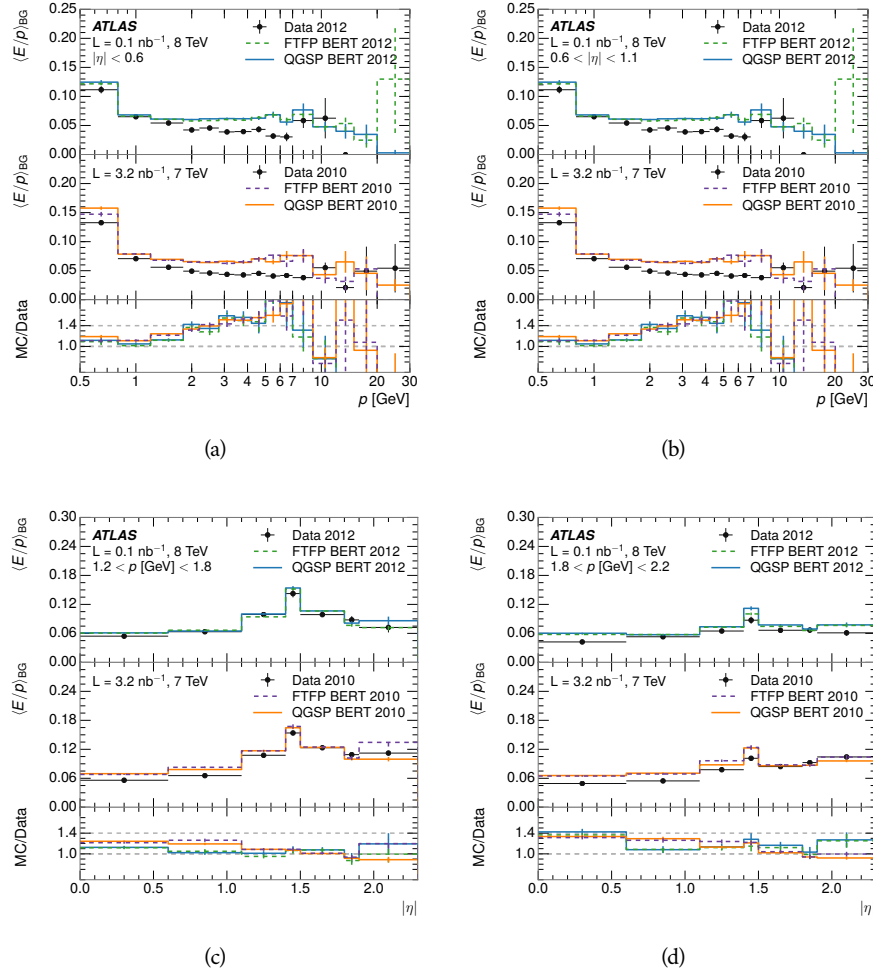


Figure 51: $\langle E/p \rangle_{BG}$ as a function of the track momentum for tracks with (a) $|\eta| < 0.6$, (b) $0.6 < |\eta| < 1.1$, and as a function of the track pseudorapidity for tracks with (c) $1.2 < p/\text{GeV} < 1.8$, (d) $1.8 < p/\text{GeV} < 2.2$.

7.2.4 CORRECTED RESPONSE

Figure 52 shows $\langle E/p \rangle_{COR}$ as a function of momentum for several bins of pseudorapidity. This corrected $\langle E/p \rangle_{COR} \equiv \langle E/p \rangle - \langle E/p \rangle_{BG}$ measures the average calorimeter response without the contamination of neutral particles. It is the

most direct measurement of calorimeter response in that it is the energy measured for fully isolated hadrons. The correction is performed separately in data and simulation, so that the mismodeling of the neutral background in simulation is removed from the comparison of response. The simulation overestimates the response at low momentum by about 5%, an effect that can be mostly attributed to the underestimation of the zero fraction mentioned previously. For $|\eta| < 0.6$, the data-simulation agreement has a larger discrepancy by about 5% for 2010 than 2012, although this is not reproduced in at higher pseudorapidity.

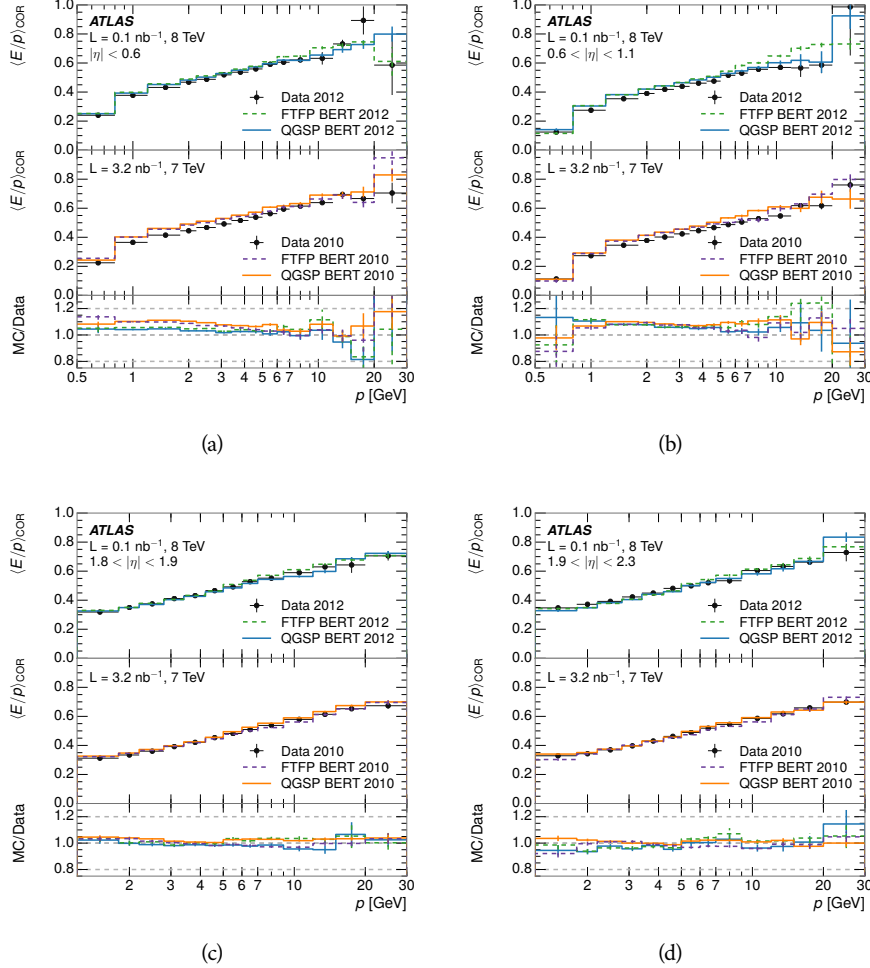


Figure 52: $\langle E/p \rangle_{\text{COR}}$ as a function of track momentum, for tracks with (a) $|\eta| < 0.6$, (b) $0.6 < |\eta| < 1.1$, (c) $1.8 < |\eta| < 1.9$, and (d) $1.9 < |\eta| < 2.3$.

The response measurement above used topological clustering at the EM scale, that is clusters were formed to measure energy but no corrections were applied to correct for expected effects like energy lost outside of the cluster or in uninstrumented material. It is also interesting to measure $\langle E/p \rangle_{\text{COR}}$ using LCW energies, which accounts for those effects by calibrating the energy based on the properties of the cluster such as energy density and depth in the calorimeter. Figure 53 shows these distributions for tracks with zero or more clusters and separately for tracks with one or more clusters. The calibration moves the mean

value of $\langle E/p \rangle_{\text{COR}}$ significantly closer to 1.0 as desired, but the discrepancy between data and simulation remains in the comparison that includes tracks with zero associated clusters. The agreement between data and simulation improves noticeably when at least one cluster is required, as this removes the contribution from the mismodeling of the zero fraction.

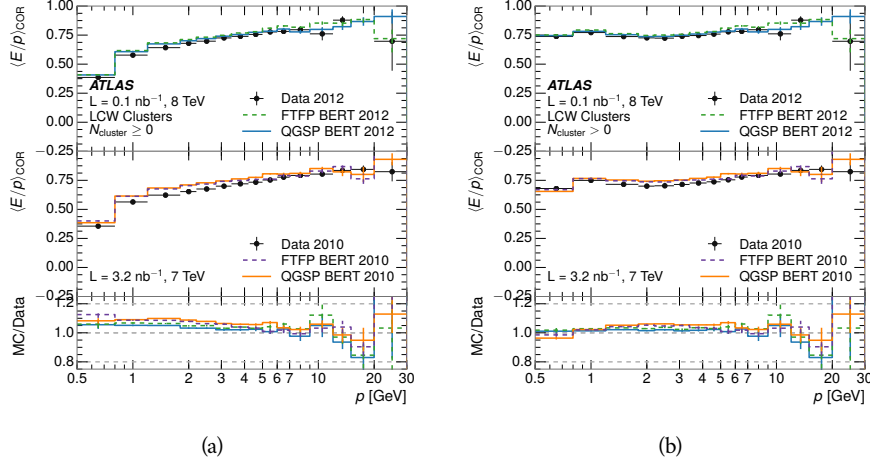


Figure 53: $\langle E/p \rangle_{\text{COR}}$ calculated using LCW-calibrated topological clusters as a function of track momentum for tracks with (a) zero or more associated topological clusters or (b) one or more associated topological clusters.

7.2.5 ADDITIONAL STUDIES

As has been seen in several measurements in previous sections, the simulation does not correctly model the chance of a low momentum hadron to reach the calorimeter. Because of the consistent discrepancy across pseudorapidity and interaction lengths, this can be best explained by incomplete understanding of hadronic interactions with the detector [38]. For example, a hadron that scatters off of a nucleus in the inner detector can be deflected through a significant angle and not reach the expected location in the calorimeter. In addition, these interactions can produce secondary particles that are difficult to model.

The requirement used throughout the previous sections on the number of hits in the TRT reduces these effects by preferentially selecting tracks that do not undergo nuclear interactions. It is interesting to check how well the simulation models tracks with low numbers of TRT hits, which selects tracks that are more likely to have undergone a hadronic interaction. Figure 54 compares the distributions with $N_{\text{TRT}} < 20$ to $N_{\text{TRT}} > 20$ for real and simulated particles¹. As expected, the tracks with fewer hits are poorly modeled in the simulation as $\langle E/p \rangle_{\text{COR}}$ differs by as much as 25% at low momentum. They also have significantly lower $\langle E/p \rangle_{\text{COR}}$ on average, because they are much less likely to have an associated cluster.

¹ The distribution with $N_{\text{TRT}} > 20$ is the same as shown in Figure 52 (a) and is included again here for the comparison.

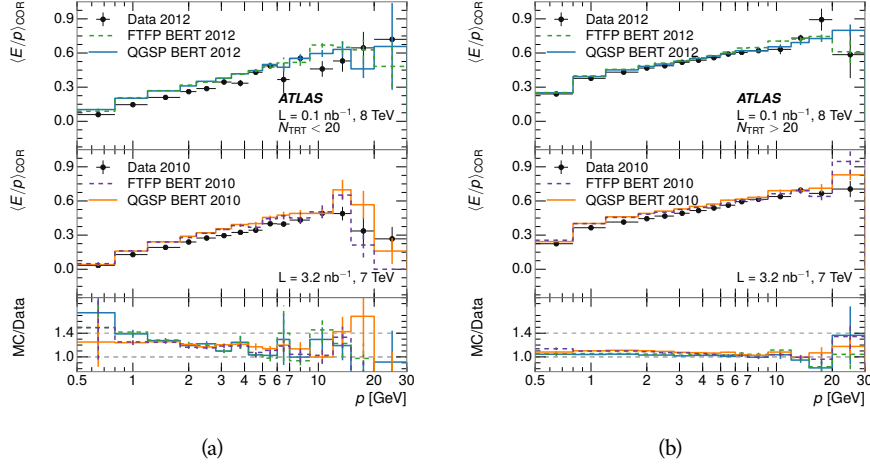


Figure 54: Comparison of the $\langle E/p \rangle_{\text{COR}}$ for tracks with (a) less than and (b) greater than 20 hits in the TRT.

Another interesting aspect of the simulation is the description of antiprotons at low momentum, where QGSP_BERT and FTFP_BERT have significant differences. This can be seen to have an effect in the inclusive response measurement when separated into positive and negative charge. The $\langle E/p \rangle_{\text{COR}}$ distributions for positive and negative particles are shown in Figure 55, where a small difference between QGSP_BERT and FTFP_BERT can be seen in the distribution for negative tracks. The figure also includes data, and the simulation overestimates $\langle E/p \rangle_{\text{COR}}$ mostly due to an underestimation in zero fraction. There is an approximately 5% difference between the 2010 and 2012 simulated events. The difference between positive and negative particles is demonstrated more clearly in Figure 56, which shows the E/p distribution in the two simulations separated by charge. There is a small difference around $E/p > 1.0$, which can be explained by the additional energy deposited by the annihilation of the antiproton in the calorimeter that is modeled well only in FTFP_BERT. This is also explored with data using identified antiprotons in Section 7.3.

The $\langle E/p \rangle$ results in previous sections have considered the electromagnetic and hadronic calorimeters together as a single energy measurement, to emphasize the total energy deposited for a given particle. However, the deposits in each calorimeter are measured separately and $\langle E/p \rangle$ can be constructed for each layer separately. As the layers are composed of different materials and are modeled separately in the detector geometry, confirmation that the simulation matches the data well in each layer adds confidence in both the description of hadronic interactions with the two different materials and also the geometric description of each.

The technique discussed in Section 7.2.3 for selecting MIPs in the electromagnetic calorimeter is also useful in studying deposits in the hadronic calorimeter. The tracks selected with the MIP requirements deposit almost all of their energy exclusively in the hadronic calorimeter. Figure 57 shows $\langle E/p \rangle_{\text{RAW}}^{\text{Had}}$, where RAW indicates that no correction has been applied for neutral backgrounds and

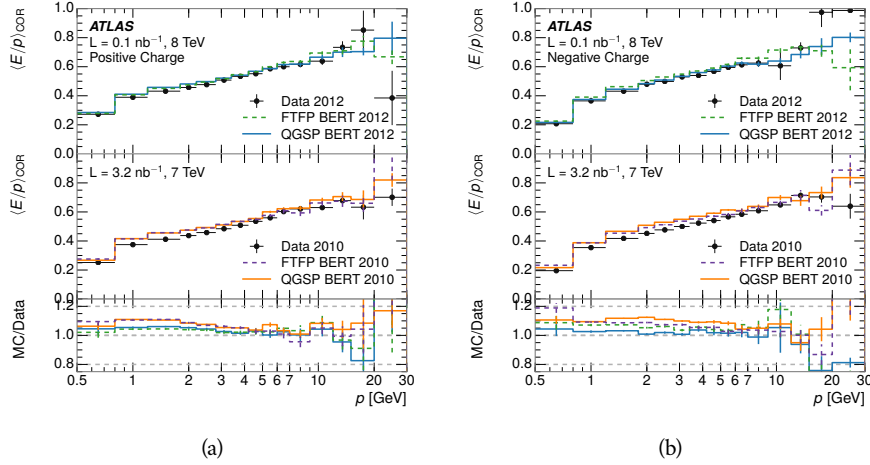


Figure 55: Comparison of the $\langle E/p \rangle_{\text{COR}}$ for (a) positive and (b) negative tracks as a function of track momentum for tracks with $|\eta| < 0.6$.

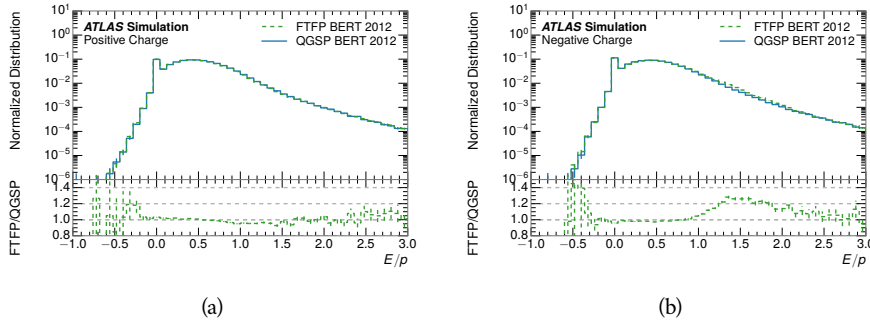


Figure 56: Comparison of the E/p distributions for (a) positive and (b) negative tracks with $0.8 < p/\text{GeV} < 1.2$ and $|\eta| < 0.6$, in simulation with the FTFP_BERT and QGSP_BERT physics lists.

Had indicates that only clusters for the hadronic calorimeter are included². The distributions are shown both for the original EM scale calibration and after LCW calibration. The data and simulation agree very well in this comparison, except in the lowest momentum bin where there is a 5% discrepancy that has already been seen in the measurements in Section 7.2.4.

A similar comparison can be made in the electromagnetic calorimeter by selecting particles which have no associated energy in the hadronic calorimeter. These results are measured in terms of $\langle E/p \rangle_{\text{COR}}^{\text{EM}}$, where EM designates that only clusters in the electromagnetic calorimeter are included and COR designates that the neutral background is subtracted as the neutral background is present in this case. Figure 58 shows the analogous comparisons to Figure 57 in the electromagnetic calorimeter. The $\langle E/p \rangle_{\text{COR}}$ values are lower on average in the EM calorimeter than in the hadronic calorimeter, which is an expected conse-

² The RAW and COR versions of $\langle E/p \rangle$ in this case are the same, as the neutral background is negligible in that calorimeter layer.

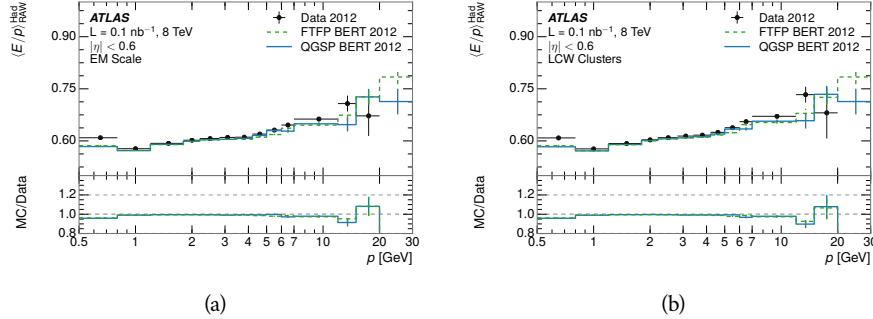


Figure 57: Comparison of the response of the hadronic calorimeter as a function of track momentum (a) at the EM-scale and (b) after the LCW calibration.

quence of their different material types (discussed in Section 5.4). In this case the disagreement between data and simulation is more pronounced, with discrepancies as high as 5% over a larger range of momenta. This level of discrepancy indicates that the description of the electromagnetic calorimeter is actually the dominant source of discrepancy in the combined distributions in Section 7.2.4.

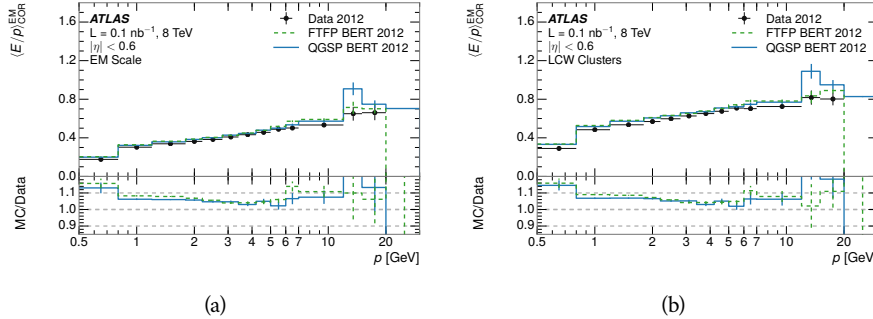


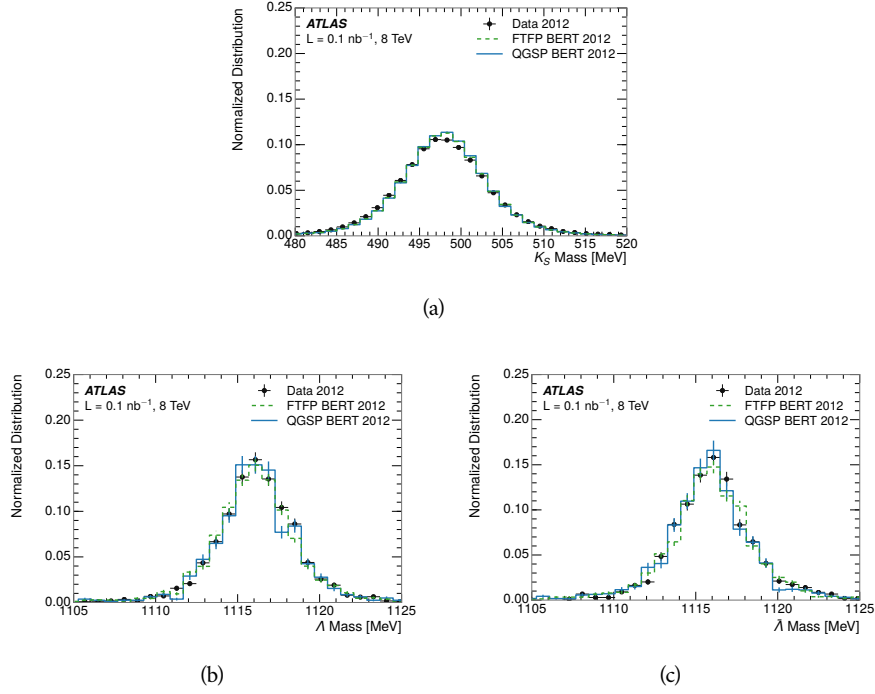
Figure 58: Comparison of the response of the EM calorimeter as a function of track momentum (a) at the EM-scale and (b) with the LCW calibration.

7.3 IDENTIFIED PARTICLE RESPONSE

The inclusive response measurement for hadrons can be augmented by measuring the response for specific particle species. The simulation models each particle type separately, and understanding the properties of each is important in constraining the uncertainty on jets. In order to select and measure specific hadrons, this section relies on the displaced decays of long-lived particles. Such decays can be identified by reconstructing secondary vertices with a requirement on mass. In particular, Λ , $\bar{\Lambda}$, and K_S^0 can be used to select a pure sample of protons, antiprotons, and pions, respectively.

2829 7.3.1 DECAY RECONSTRUCTION

2830 The measurement of the response for identified particles uses the same selection
 2831 as for inclusive particles (Section 7.1.3) with a few additions. Each event used is
 2832 required to have at least one secondary vertex, as described in Section 6.1.3, and
 2833 the tracks are required to match to that vertex rather than the primary vertex.
 2834 Pions are selected from decays of $K_S^0 \rightarrow \pi^+ \pi^-$, which is the dominant decay for
 2835 K_S^0 to charged particles. Protons are selected from decays of $\Lambda \rightarrow \pi^- p$ and an-
 2836 tiprotons from $\bar{\Lambda} \rightarrow \pi^+ \bar{p}$, which are similarly the dominant decays of Λ and $\bar{\Lambda}$
 2837 to charged particles. The species of parent hadron in these decays is determined
 2838 by reconstructing the mass of the tracks associated to the secondary vertex. The
 2839 sign of the higher momentum decay particle can distinguish between Λ and $\bar{\Lambda}$,
 2840 which of course have the same mass, as the proton or antiproton is kinemati-
 2841 cally favored to have higher momentum. The proton or antiproton will carry
 2842 the higher momentum above 95% of the time. Examples of the reconstructed
 2843 masses used to select these decays are shown in Figure 59. The mass peaks in
 2844 data and both simulation models are very similar.



2845 Figure 59: The reconstructed mass peaks of (a) K_S^0 , (b) Λ , and (c) $\bar{\Lambda}$ candidates.

2846 The dominant backgrounds for the identified particle decays are nuclear in-
 2847 teractions and combinatoric sources. These are suppressed by the kinematic re-
 2848 quirements on the tracks as well as an additional veto which removes candidates
 2849 that are consistent with both a Λ or $\bar{\Lambda}$ and a K_S^0 hypothesis, which is possible
 2850 because of the different assumptions on particle mass in each case [39]. After
 2851 these requirements, the backgrounds are found to be negligible compared to the
 2852 statistical errors on these measurements.

2852 7.3.2 IDENTIFIED RESPONSE

2853 With these techniques the E/p distributions are extracted in data and simulation
 2854 for each particle species and shown in Figure 60. These distributions are shown
 2855 for a particular bin of E_a ($2.2 < E_a/\text{GeV} < 2.8$), rather than p . E_a is the energy
 2856 available to be deposited in the calorimeter: for pions $E_a = \sqrt{p^2 + m_\pi^2}$, for pro-
 2857 tons $E_a = \sqrt{p^2 + m_p^2} - m_p$, and for antiprotons $E_a = \sqrt{p^2 + m_p^2} + m_p$. In the
 2858 pion case, the entire energy of the pion is deposited in the calorimeter, so E_a is
 2859 just the usual energy. For protons, the proton remains after depositing its energy
 2860 in the calorimeter, so its mass is not available and must be subtracted from E_a .
 2861 And for antiprotons, the antiproton constituents annihilate with the quarks in
 2862 the protons and neutrons of the calorimeter material, so it deposits its entire en-
 2863 ergy as well as an the additional energy from the annihilation; this extra energy
 2864 is equal to the mass of the antiproton and is added to the available energy. The
 2865 features of the E/p distributions are similar to the inclusive case, with a peak
 2866 around 0.5 at low momentum. The zero fraction is not as pronounced as in the
 2867 inclusive case. There is a small negative tail from noise and a large fraction of
 2868 tracks with zero energy from particles which do not reach the calorimeter. The
 2869 long positive tail is noticeably more pronounced for antiprotons because of the
 2870 additional energy generated by the annihilation of the antiproton with the mate-
 2871 rial of the detector, and the peak of the distribution is also increased for the same
 2872 reason. The simulation correctly captures these features, and the agreement be-
 2873 tween data and simulation is good to within the available statistical limitations.

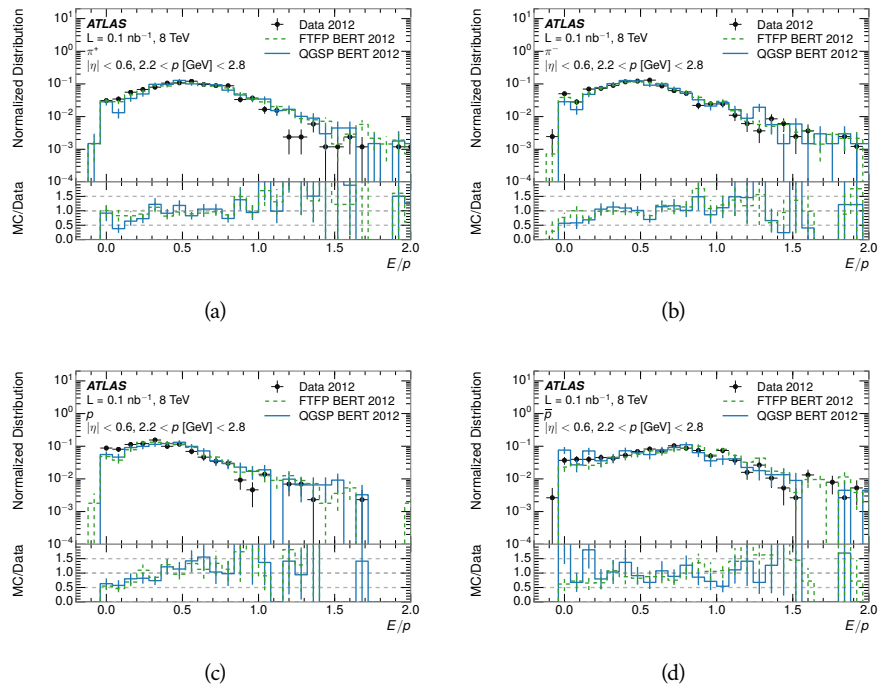


Figure 60: The E/p distribution for isolated (a) π^+ , (b) π^- , (c) proton, and (d) anti-proton tracks.

The zero fraction is further explored in Figure 61 for pions and protons in data and simulation. The simulation consistently underestimates the zero fraction independent of particle species, which implies that this discrepancy is not caused by the model of a particular species but rather a feature common to all. The zero fraction is larger for π^- than π^+ , which is evident in both data and simulation. However there is some suggestion that this increase in zero fraction leads to an even larger discrepancy in the modeling of π^- in simulation.

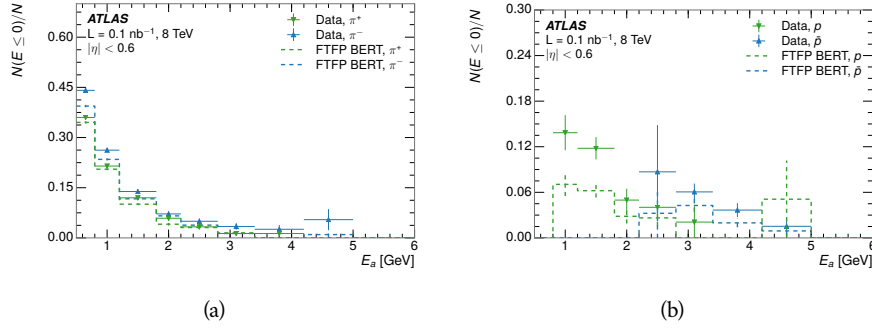


Figure 61: The fraction of tracks with $E \leq 0$ for identified (a) π^+ and π^- , and (b) proton and anti-proton tracks

It is also interesting to compare the response between the different particle species. One approach to do this is to measure the difference in $\langle E/p \rangle$ between two types, which has the advantage of removing the neutral background. These differences are shown in various combinations in Figure 62. The response for π^+ is greater on average than the response to π^- because of a charge-exchange effect which causes the production of additional neutral pions in the showers of π^+ [61]. This effect becomes less significant as the $\langle E/p \rangle$ increases, and the difference approaches zero. Both version of the simulation correctly model this trend. The response for π^+ is also greater on average than the response to p , because a large fraction of the energy of π^+ hadrons is converted to an electromagnetic shower [62, 63]. This effect is again reproduced by both simulations. The \bar{p} response, however, is significantly higher than the response to π^- because of the annihilation of the antiproton, but the difference decreases at higher energies where the additional energy has less relative importance. FTFP_BERT models this effect more accurately than QGSP_BERT because of their different descriptions of \bar{p} interactions with material.

It is also possible to remove the neutral background from these response distributions using the same technique as in Section 7.2.3. The technique is largely independent of the particle species and so can be directly applied to $\langle E/p \rangle$ for pions. The $\langle E/p \rangle_{\text{COR}}$ distributions for pions are shown in Figure 63, which are very similar to the inclusive results. The inclusive hadrons are comprised mostly of pions, so this similarity is not surprising. It is also possible to see the small differences between π^+ and π^- response here, where $\langle E/p \rangle_{\text{COR}}$ is higher on average for π^+ . The agreement between data and simulation is significantly worse for the π^- distributions than for the π^+ , with a discrepancy greater than 10% below 2-3 GeV.

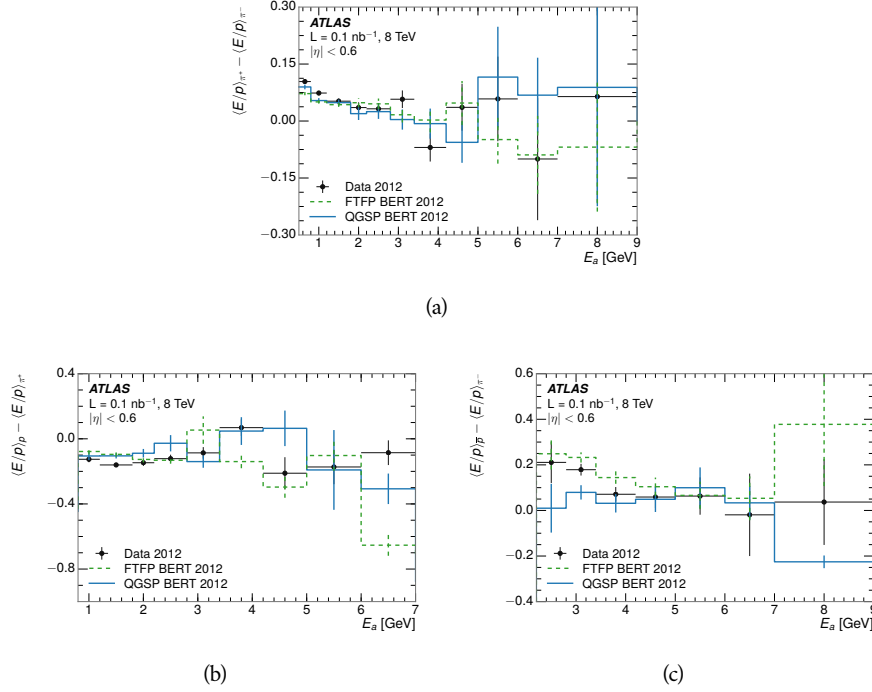


Figure 62: The difference in $\langle E/p \rangle$ between (a) π^+ and π^- (b) p and π^+ , and (c) \bar{p} and π^- .

2907 7.3.3 ADDITIONAL SPECIES IN SIMULATION

2908 The techniques above provide a method to measure the response separately for
 2909 only pions and protons. However the hadrons which forms jets include a number
 2910 of additional species such as kaons and neutrons. The charged kaons are an im-
 2911 portant component of the inclusive charged hadron distribution, which is com-
 2912 prised of roughly 60-70% pions, 15-20% kaons, and 5-15% protons [38]. These
 2913 fractions vary depending on the production mechanism, and the ranges are in-
 2914 dicative of the variations between different events. These are difficult to measure
 2915 in data at the ATLAS detector, as the particles which decay to kaons such as ϕ and
 2916 D mesons have shorter lifetimes and are comparatively rare. These properties
 2917 make it impractical to identify a sufficient number of decays to make statistically
 2918 meaningful measurements. The simulation of these particles includes noticeable
 2919 differences in response between species at low energies, which are shown in Fig-
 2920 ure 64 for FTFP_BERT. The significant differences in response between protons
 2921 and antiprotons below 1 GeV are accounted for above in the definitions of E_a .

2922 7.4 SUMMARY

2923 These various measurements of calorimeter response shown above for data and
 2924 simulation illuminate the accuracy of the simulation of hadronic interactions at
 2925 the ATLAS detector. The results were obtained using 2010 and 2012 data at 7
 2926 and 8 TeV, but reflect the most current understanding of the detector alignment

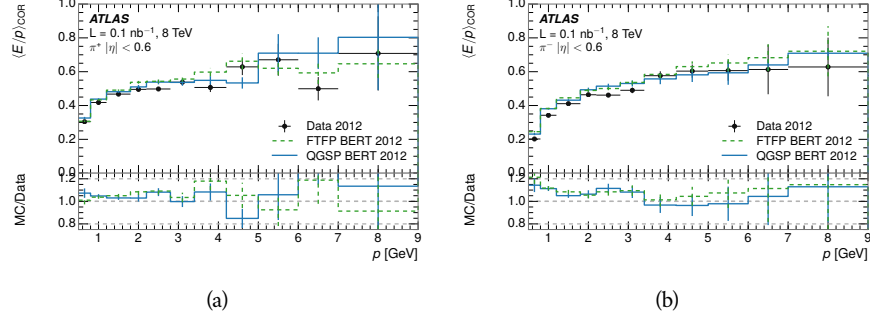


Figure 63: $\langle E/p \rangle_{\text{COR}}$ as a function of track momentum for (a) π^+ tracks and (b) π^- tracks.

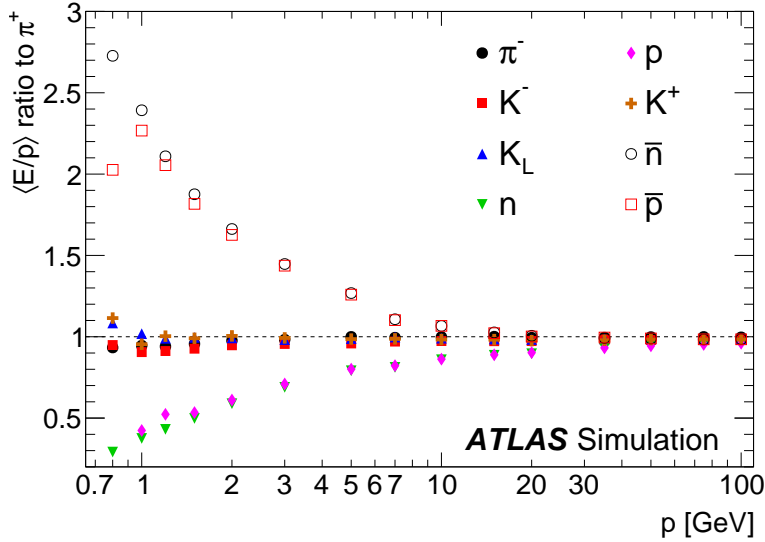


Figure 64: The ratio of the calorimeter response to single particles of various species to the calorimeter response to π^+ with the physics list FTFP_BERT.

and geometry. A number of measurements focusing on a comparison between protons and antiprotons suggest that FTFP_BERT models those interaction more accurately than QGSP_BERT. These measurements, among others, were the motivation to switch the default Geant4 simulation from QGSP_BERT to FTFP_BERT for all ATLAS samples.

Even with these updates, there are a number of approximately 5% discrepancies in response between the data and simulation. The differences result mostly from a difference in the modeling of the zero fraction, which is most significant at low energies. The difference in response without the zero fraction are primarily in the electromagnetic calorimeter, while the modeling of the hadronic calorimeter is accurate. At higher momenta the simulation of hadronic interactions is very consistent with data. Chapter 8 discusses how to use these observed differences to constrain the jet energy scale and its associated uncertainties.

2940

2941 JET ENERGY RESPONSE AND UNCERTAINTY

2942 8.1 MOTIVATION

2943 As jets form a major component of many physics analyses at ATLAS, it is crucial
 2944 to carefully calibrate the measurement of jet energies and to derive an uncer-
 2945 tainty on that measurement. These uncertainties are often the dominant sys-
 2946 tematic uncertainty in high-energy analyses at the LHC. Jet balance techniques,
 2947 as discussed in Section 6.4.3, provide a method to constrain the JES and its uncer-
 2948 tainty in data, and provide the default values used for ATLAS jet measurements at
 2949 most energies [64]. These techniques are limited by their reliance on measuring
 2950 jets in data, so they are statistically limited in estimating the jet energy scale at the
 2951 highest jet energies. This chapter presents another method for estimating the jet
 2952 energy scale and its uncertainty which builds up a jet from its constituents and
 2953 thus can be naturally extended to high jet momentum. Throughout this chapter
 2954 the jets studied are simulated using Pythia8 with the CT10 parton distribution
 2955 set [65] and the AU2 tune [42], and corrections are taken from the studies includ-
 2956 ing data and simulation in Chapter 7.

2957 As described in Section 6.4, jets are formed from topological clusters of energy
 2958 in the calorimeters using the anti- k_t algorithm. These clusters originate from a
 2959 diverse spectrum of particles, in terms of both species and momentum, leading to
 2960 significantly varied jet properties and response between jets of similar produced
 2961 momentum. Figure 65 shows the momentum and particle distributions of sim-
 2962 ultated particles within jets at a few examples energies. Each bin for each distri-
 2963 bution shows the fraction of jet constituents of that particle type and that truth
 2964 energy for a jet of the specified energy. These show that majority of particles in
 2965 jets are charged pions and photons, and the charged pions constituent carry the
 2966 highest energies on average. The figure also demonstrates that the majority of
 2967 the particles in a jet have much lower momentum than the jet itself; for example
 2968 in 90-100 GeV jets less than 1% of particles have energies above 20 GeV. The
 2969 E/p measurements provide a thorough understanding of the dominant particle
 2970 content of jets, the charged hadrons.

2971 8.2 UNCERTAINTY ESTIMATE

2972 A correct modeling of jets in the data by simulation requires that both the parti-
 2973 cle production inside jets as well as the response of the calorimeter to particles
 2974 are correctly modeled. Chapter 7 showed that the simulation does not perfectly
 2975 model the calorimeter response, and provided measurements that can be used
 2976 to correct for discrepancies. To determine the corrections appropriate for jets,
 2977 that is to evaluate a jet energy response, the simulated jet energies are compared

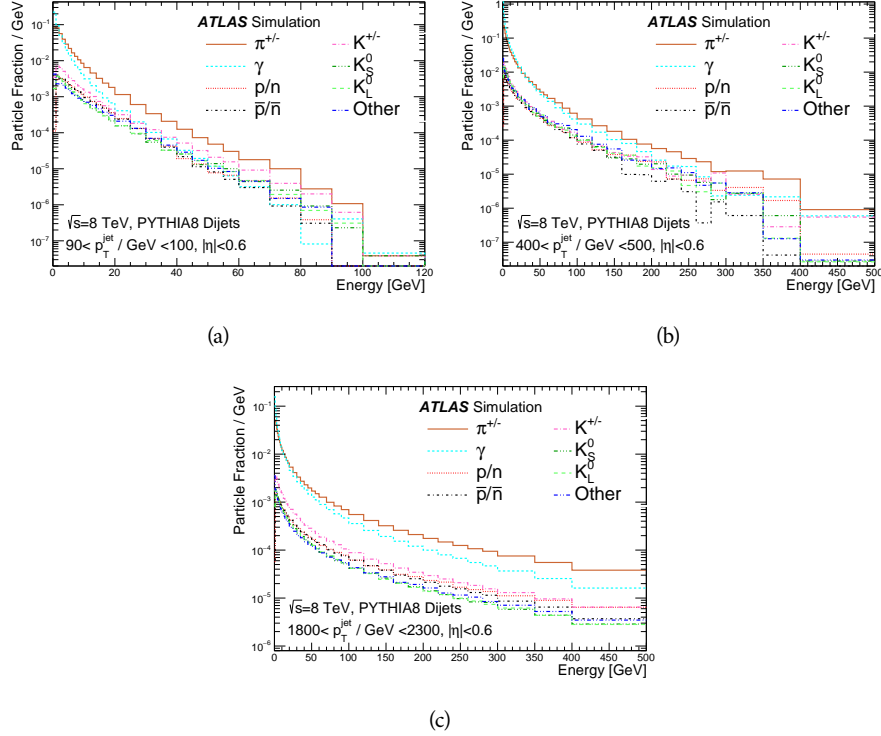


Figure 65: The spectra of true particles inside anti- k_t , $R = 0.4$ jets with (a) $90 < p_T/\text{GeV} < 100$, (b) $400 < p_T/\text{GeV} < 500$, and (c) $1800 < p_T/\text{GeV} < 2300$.

to a corrected jet built up at the particle level. Each cluster in a jet is associated to the truth particle which deposited it, and the energy in that cluster is then corrected for a number of effects based on measurements in data. The primary corrections come from the single hadron response measurements in addition to response measured using the combined test beam which covers higher momentum particles [66]. These corrections include both a shift (Δ), in order to make the simulation match the average response in data, and an uncertainty (σ) associated with the ability to constrain the difference between data and simulation. Some of the dominant sources of uncertainty are itemized in Table 7 with typical values, and the full list considered is described in detail in the associated paper [38]. These uncertainties cover differences between the data and simulation in the modeling of calorimeter response to a given particle. The typical values are listed as ranges to show the variation over momentum and pseudorapidity. For the in situ E/p term, for example, Δ corresponds to the difference between data and simulation for $\langle E/p \rangle_{\text{COR}}$ at the LCW scale (shown in Figure 53 (b)) and σ is the uncertainty on that difference including the statistical uncertainties of both the data and simulated events. No uncertainties are added for the difference between particle composition of jets in data and simulation, as this method focuses on providing a response correction for discrepancies of particle interactions rather than differences in particle composition.

From these terms, the jet energy scale and uncertainty is built up from individual energy deposits in simulation. Each uncertainty term is treated inde-

Abbrev.	Description	Δ (%)	σ (%)
In situ E/p	The comparison of $\langle E/p \rangle_{\text{COR}}$, at the LCW scale, as described in Chapter 7 with statistical uncertainties from 500 MeV to 20 GeV.	0-3	1-5
CTB	The main $\langle E/p \rangle$ comparison uncertainties, binned in p and $ \eta $, as derived from the combined test beam results, from 20 to 350 GeV [66].	0-3	1-5
E/p Zero Fraction	The difference in the zero-fraction between data and MC simulation from 500 MeV to 20 GeV.	5-25	1-5
E/p Threshold	The uncertainty in the EM calorimeter response from the potential mismodeling of threshold effects in topological clustering.	0	0-10
Neutral	The uncertainty in the calorimeter response to neutral hadrons based on studies of physics model variations.	0	5-10
K_L	An additional uncertainty in the response to neutral K_L in the calorimeter based on studies of physics model variations.	0	20
E/p Misalignment	The uncertainty in the p measurement from misalignment of the ID.	0	1
Hadrons, $p > 350$ GeV	An energy independent uncertainty for all particles above the energy range or outside the longitudinal range probed with the combined test beam.	0	10

Table 7: The dominant sources of corrections and systematic uncertainties in the [JES](#) estimation technique, including typical values for the correcting shift (Δ) and the associated uncertainty (σ).

3000 pendently, and is taken to be gaussian distributed. The resulting scale and un-
 3001 certainty is shown in Figure 66, where the mean response is measured relative
 3002 to the calibrated energy reported by simulation. The mean response is slightly
 3003 below one, indicating that the simulation slightly overestimates the calorime-
 3004 ter response on average, and this response is relatively constant as a function
 3005 of the jet p_T . The dominant uncertainties come from the statistical uncertain-
 3006 ties on the E/p measurements at lower energies and the additional uncertainty
 3007 for out of range measurements at higher energies. Combined the resulting un-
 3008 certainty ranges from between 1.5% at low momentum and pseudorapidity to
 3009 as much as 4% at higher momentum and pseudorapidity. The total uncertainty
 3010 from this method at intermediate jet energies is comparable to other simulation-
 3011 based methods [67] and is about twice as large as in-situ methods using data [64].
 3012 This method is the only one which provides an estimation above 1.8 TeV, how-
 3013 ever, and so is still a crucial technique in analyses that search for very energetic
 3014 jets.

3015 These techniques can also be used to measure the correlation between bins of
 3016 average reconstructed jet momentum across a range of p_T and $|\eta|$, where cor-
 3017 relations are expected because of a similarity in particle composition at similar
 3018 energies. Figure 67 shows these correlations, where the uncertainties on jets in
 3019 neighboring bins are typically between 30% and 60% correlated. The uncertainty
 3020 on all jets becomes significantly correlated at high energies and larger pseudora-
 3021 pidities, when the uncertainty becomes dominated by the single term reflecting
 3022 out of range particles.

3023 8.3 SUMMARY

3024 The technique described above provides a jet energy scale and uncertainty by
 3025 building up jet corrections from the energy deposits of constituent particles. The
 3026 E/p measurements are crucial in providing corrections for the majority of parti-
 3027 cles in the jets. The uncertainty derived this way is between 2 and 5% and is about
 3028 twice as large at corresponding momentum than jet balance methods. However
 3029 this is the only uncertainty available for very energetic jets using 2012 data and
 3030 simulation, and repeating this method with Run 2 data and simulation will be
 3031 important in providing an uncertainty for the most energetic jets in 13 TeV col-
 3032 lisions.

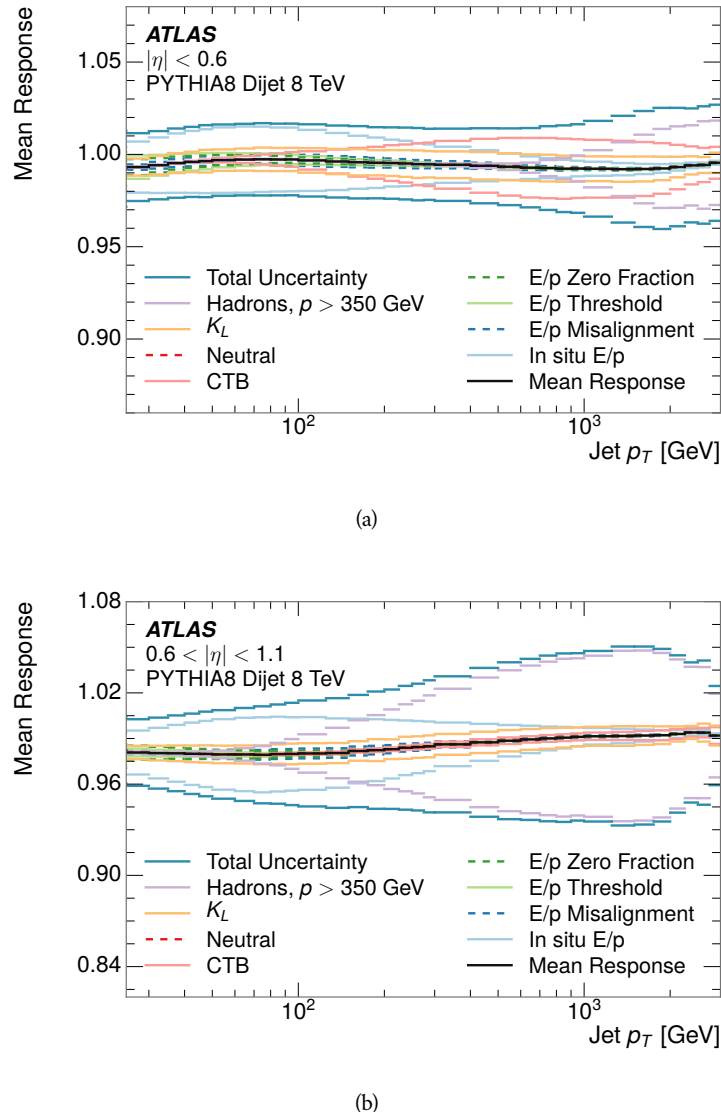


Figure 66: The [JES](#) response uncertainty contributions, as well as the total [JES](#) uncertainty, as a function of jet p_T for (a) $|\eta| < 0.6$ and (b) $0.6 < |\eta| < 1.1$.

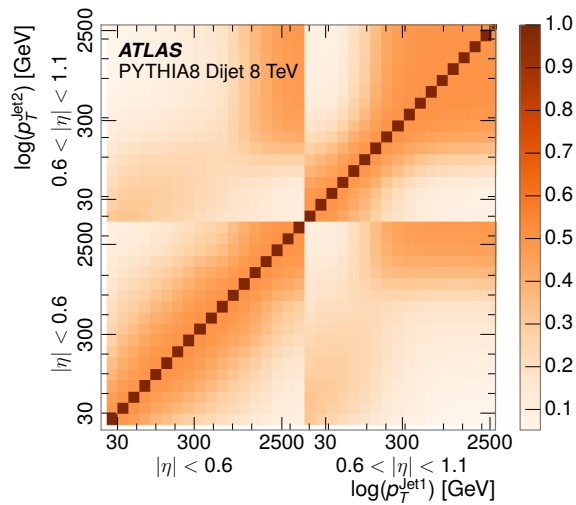


Figure 67: The correlations between bins of average reconstructed jet momentum as a function of jet p_T and $|\eta|$ for jets in the central region of the detector.

3033

PART IV

3034

SEARCH FOR LONG-LIVED PARTICLES

3035

3036

3037 LONG-LIVED PARTICLES IN ATLAS

3038 As discussed in Section 2.6, various limitations in the SM suggest a need for new
 3039 particles at the TeV scale. A wide range of extensions to the Standard Model
 3040 predict that these new particles can have lifetimes greater than approximately
 3041 one-hundredth of a nanosecond. These include theories with universal extra-
 3042 dimensions [68, 69], with new fermions [70], and with leptoquarks [71]. As dis-
 3043 cussed in Section 3.4, many SUSY theories also produce these LLPs, in both R-
 3044 Parity violating [72–74] and R-Parity conserving [75–78] formulations. Split
 3045 supersymmetry [11, 12], for example, predicts long-lived gluinos with O(TeV)
 3046 masses. This search focuses specifically on the SUSY case, but many of the results
 3047 are generic to any model with LLPs.

3048 Long-lived gluinos or squarks carry color-charge and will thus hadronize into
 3049 color neutral bound states called R-Hadrons. These are composit particles like
 3050 the known hadrons but with one supersymmetric constituent, for example $\tilde{g}q\bar{q}$
 3051 and $\tilde{q}\bar{q}$. In this hadronization process, the gluino can acquire an electric charge.
 3052 Gluino pair production, $pp \rightarrow \tilde{g}\tilde{g} + X$, where X denotes the proton remnants,
 3053 has the largest cross sectional increase with the increase in energy to 13 TeV,
 3054 and so this search uses gluino R-Hadrons as its benchmark model. The features,
 3055 techniques, and cross section limits discussed here are all largely independent
 3056 of the model. Planned future updates will extend the case to include additional
 3057 refinements for squark and chargino models, but the current method covers any
 3058 long-lived, charged, massive particle.

3059 9.1 EVENT TOPOLOGY

3060 R-parity conserving SUSY models predict that gluinos will be produced in pairs
 3061 at the LHC, through the processes shown in Figure 68, where the quarks and
 3062 gluons are proton constituents. The gluon-initiated mode dominates for the col-
 3063 lision energy and gluino masses considered for this search. During their produc-
 3064 tion, the long-lived gluinos hadronize into color singlet bound states including
 3065 $\tilde{g}q\bar{q}$ and even $\tilde{g}g$ [79]. The probability to form the gluon-only bound states is
 3066 a free parameter usually taken to be 0.1, and 90% of the remaining R-Hadrons
 3067 form meson states [80]. The charged and neutral states are approximately equally
 3068 likely for mesons, so the R-Hadrons will be charged roughly 50% of the time.

3069 These channels produce R-Hadrons with large p_T , but lower on average than
 3070 their mass, so that they typically propagate with $0.2 < \beta < 0.9$ [80]. Figure 69
 3071 shows the generated p_T and β distributions for a simulated example of R-Hadrons
 3072 with a mass of 1600 GeV. The mean p_T is roughly half of the mass at 800 GeV,
 3073 and so β peaks around 0.5. The fragmentation that produces these hadrons is
 3074 very hard, so the jet structure around the R-Hadron is minimal, with less than 5
 3075 GeV of summed particle momentum expected in a cone of $\Delta R < 0.25$ around

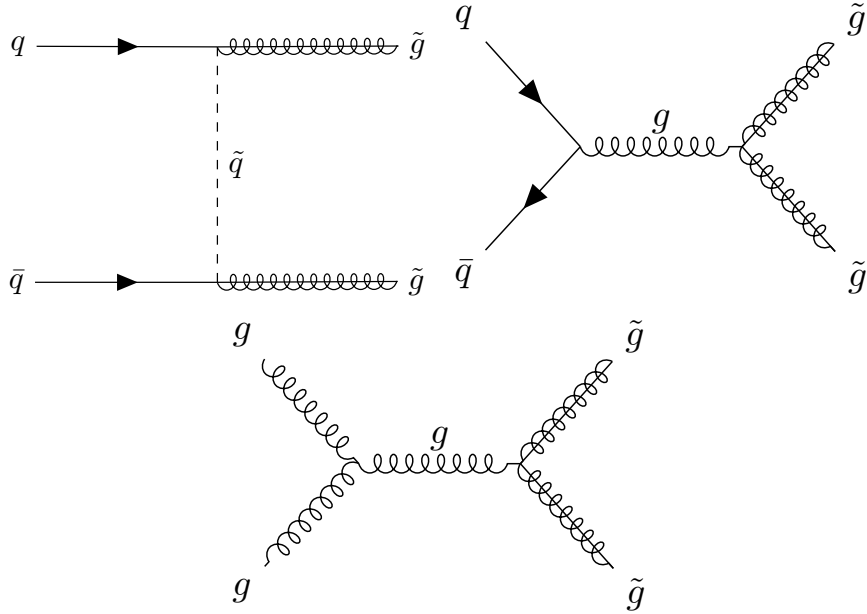


Figure 68: The processes which contribute to gluino pair production in the proton-proton collisions, where the quarks and gluons are proton constituents.

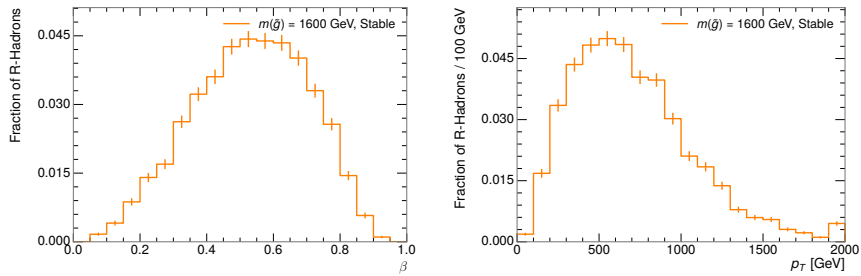


Figure 69: The generated p_T and β distributions for R-Hadrons with $M = 1600$ GeV.

3076 the R-Hadron [80]. After hadronization, depending on the gluino lifetime, the
3077 R-Hadrons then decay into hadrons and a LSP [79].

3078 In summary, the expected event for pair-produced long-lived gluinos is very
3079 simple: two isolated, high-momentum R-Hadrons that propagate through the
3080 detector before decaying to jets. The observable features of such events depend
3081 strongly on the interaction of the R-Hadron with the material of the detector
3082 and also its lifetime. Section 9.1.1 describes the interactions of R-Hadrons which
3083 reach the various detector elements in ATLAS and Section 9.1.2 provides a sum-
3084 mary of the observable event descriptions for R-Hadrons of various lifetimes.

3085 9.1.1 DETECTOR INTERACTIONS

3086 Although the distribution of decay times can be parametrized with a single pa-
3087 rameter, τ , the time before individual R-Hadrons decay follows an exponential
3088 distribution, leading to a range of decay times for any individual lifetime. This is

3089 further confounded by the distribution of β as well as η , so that each R-Hadron
 3090 propagates at a different velocity and travels a different distance before reaching
 3091 each detector element. Therefore, the lifetime-dependent event topologies
 3092 must be discussed as an average, and all times referred to within this section will
 3093 assume $\beta = 0.5$, an $\eta = 0$, and that the particle decays after a time equal to its
 3094 lifetime. Table 8 lists the distances of various subdetectors and the time after
 3095 which a LLP will arrive at that subdetector for a few values of β and with $\eta = 0$.

Subdetector	Distance	τ at $\beta = 0.3$	τ at $\beta = 0.5$	τ at $\beta = 0.7$
Pixel	3.1 cm	0.35 ns	0.20 ns	0.15 ns
Calorimeter	1.5 m	17 ns	10 ns	7.2 ns
Muon System	5 m	56 ns	33 ns	24 ns

Table 8: The radial distances of each of the subdetectors and example arrival times for an R-Hadron with $\eta = 0$ and the specified β .

3096 After approximately 0.2 ns, the R-Hadron reaches the first layer of the pixel
 3097 detector. If charged, it deposits energy into the material through repeated single
 3098 collisions that result in ionization of the silicon substrate [2]. Because of its com-
 3099 paratively low β , the ionization energy can be significantly greater than expected
 3100 for SM particles because the most-probable energy loss grows significantly as β
 3101 decreases [2]. This large ionization can be measured through the ToT read out
 3102 from the pixel detector as described in Section 6.1.2. Large ionization in the
 3103 inner detector is one of the major characteristic features of LLPs. The particle
 3104 propagates through all four layers of the pixel detector, where each provides a
 3105 measurement of ionization, and then exits the pixel detector at 0.8 ns.

3106 Throughout the next few nanoseconds, the R-Hadron propagates through the
 3107 remainder of the inner detector. A charged R-Hadron will provide hits in each
 3108 of these systems as would any other charged particle, and can be reconstructed
 3109 as a track. The track reconstruction provides a measurement of its trajectory
 3110 and thus its p as described in Section 6.1. The large p_T , shown in Figure 69, is
 3111 another characteristic feature of massive particles produced at the LHC.

3112 As of roughly 10 ns, the R-Hadron enters the calorimeter where it interacts
 3113 hadronically with the material. Because of its large mass and p , the R-Hadron
 3114 does not typically stop in the calorimeter, but rather deposits a small fraction of
 3115 its energy through repeated interactions with nucleons. The probability of inter-
 3116 action between the gluino itself and a nucleon is low because the cross section
 3117 drops off with the inverse square of its mass, so the interactions are primarily
 3118 governed by the light constituents [81]. Each of these interactions can poten-
 3119 tially change that quark content and thus change the sign of the R-Hadron, so
 3120 that the charge at exit is typically uncorrelated with the charge at entry [80]. The
 3121 total energy deposited in the calorimeters during the propagation is small com-
 3122 pared to the kinetic energy of the R-Hadron, around 20-40 GeV, so that E/p is
 3123 typically less than 0.1 [80].

3124 Then, 30 ns after the collision, it reaches the muon system, where it again
 3125 ionizes in the material if charged and can be reconstructed as a muon track. Be-
 3126 cause of the charge-flipping interactions in the calorimeter, this track may have

3127 the opposite sign of the track reconstructed in the inner detector, or there may
 3128 be a track present when there was none in the inner detector and vice-versa
 3129 for those which are detected. The propagation time at the typically lower β re-
 3130 sults in a significant delay compared to muons, and a delay over 25 ns causes
 3131 the muon signal to be lost outside the readout window. Between the probabili-
 3132 ty of charge-flip and late arrival, there is a significant chance that an R-Hadron
 3133 which was produced with a charge will not be identified as a muon. When it is
 3134 reconstructed as a muon, that delay can be assessed in terms of a time-of-flight
 3135 measurement, which is another characteristic feature of R-Hadrons.

3136 9.1.2 LIFETIME DEPENDENCE

3137 The above description assumed a lifetime long enough for the R-Hadron to exit
 3138 the detector, which through this search is referred to as **VLL**, as the particle may
 3139 decay after exiting the detector. There are several unique signatures at shorter
 3140 lifetimes where the R-Hadron decays in various parts of the inner detector; these
 3141 lifetimes are referred to as **LL**.

3142 The shortest case where the R-Hadron is considered **LL** is for lifetimes around
 3143 0.01 ns, where the particle decays before reaching any of the detector elements.
 3144 Although the R-Hadrons are produced opposite each other in the transverse
 3145 plane, each R-Hadron decays to a jet and an **LSP**. The two decays are uncorrelated,
 3146 so the two **LSPs** carry different momenta and in different directions. And, since
 3147 the **LSPs** are not measured, the produced jets can be significantly imbalanced in
 3148 the transverse plane which results in large missing energy. That missing energy
 3149 can be used to trigger candidate events, and provides the most efficient trigger
 3150 option for shorter lifetimes. Additionally, the precision of the tracking system
 3151 allows the displaced vertex of the R-Hadron decay to be reconstructed from the
 3152 charged particles in the jet. The distance of that vertex from the interaction point
 3153 can be used to distinguish R-Hadron decays from other processes. Figure 70
 3154 shows a schematic diagram of an example R-Hadron event with such a lifetime.
 3155 The diagram is not to scale, but instead illustrates the detector interactions in the
 3156 pixel detector, calorimeters, and muon system. It includes a representation of a
 3157 charged R-Hadron and a neutral R-Hadron, as well as the **LSPs** and jets (shown as
 3158 charged hadrons) produced in the decay. Neutral hadrons may also be produced
 3159 in the decay but are not depicted. Previous searches on ATLAS have used the
 3160 displaced vertex to target **LLP** decays [82].

3161 The next distinguishable case occurs at lifetimes greater than 0.1 ns but less
 3162 than 10 ns, where the R-Hadron forms a partial track in the inner detector. This
 3163 forms a unique signature of a disappearing track. Two examples of such an event
 3164 are illustrated in Figure 71 and Figure 72, which show the short track in the inner
 3165 detector. The decay distance must be sufficiently long that it reaches the **SCT**, or
 3166 else to track will not be reconstructed at all. Depending on the mass difference
 3167 between the R-Hadron and the **LSP**, the decay products will either be a single, soft
 3168 charged hadron and a **LSP** (Figure 71), or a jet and a **LSP** (Figure 72). A dedicated
 3169 search on ATLAS used the disappearing track signature in the former case to
 3170 search for **LLP** in Run 1 [83].

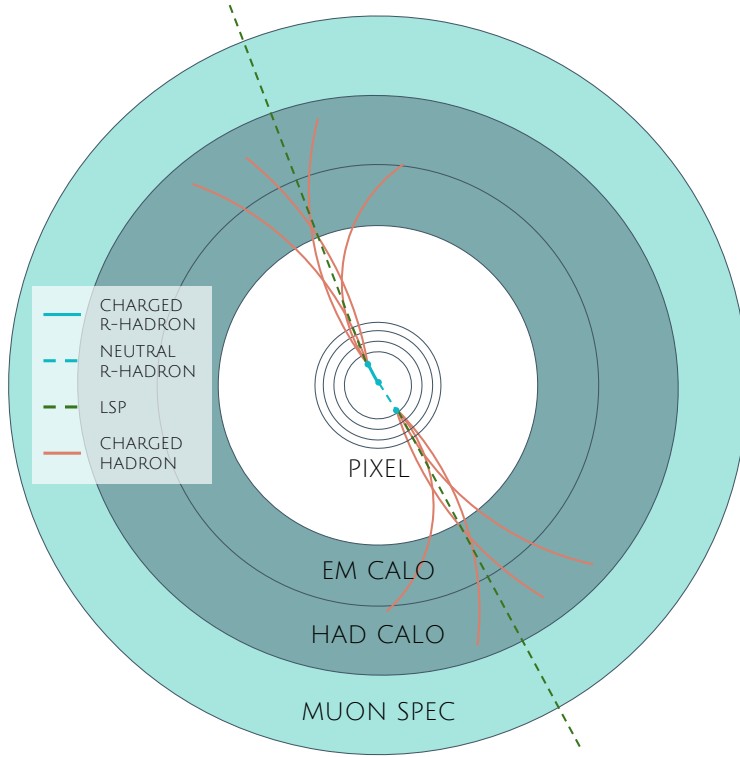


Figure 70: A schematic diagram of an R-Hadron event with a lifetime around 0.01 ns. The diagram includes one charged R-Hadron (solid blue), one neutral R-Hadron (dashed blue), LSPs (dashed green) and charged hadrons (solid orange). The pixel detector, calorimeters, and muon system are illustrated but not to scale.

3171 In the latter case, the decays result in an event-level signature of up to two high-
 3172 p tracks, jets, and significant missing energy. The missing energy has the same
 3173 origin as in the case of 0.01 ns lifetimes, from the decay to unmeasured particles,
 3174 and again can be large. The high- p tracks will also have the characteristically high-
 3175 ionization of massive, long-lived particles in the Pixel detector. Figure 72 shows
 3176 how the jets from the decay can still be reconstructed in the calorimeter. Several
 3177 previous searches on ATLAS from Run 1 have used this signature to search for
 3178 R-Hadrons [84, 85], including a dedicated search for LL particles [86].

3179 If the lifetime is longer than several nanoseconds, in the range of 10–30 ns,
 3180 the R-Hadron decay can occur in or after the calorimeters, but prior to reaching
 3181 the muon system. In the case that the decays occur early enough within the
 3182 calorimeters that the decay can be measured, the event topology is very similar
 3183 to the above with jets originating in the inner detector. If the decay occurs after
 3184 the calorimeter, jets may not be reconstructed at all. The events still often have
 3185 large missing energy, although it is generated through different mechanisms, and
 3186 so the same search strategy can be used. The R-Hadrons do not deposit much
 3187 energy in the calorimeters, so a neutral R-Hadron will not enter into the miss-
 3188 ing energy calculation. A charged R-Hadron opposite a neutral R-Hadron will
 3189 thus generate significant missing energy, and close to 50% of pair-produced R-
 3190 Hadron events fall into this category. If both R-Hadrons are neutral then the

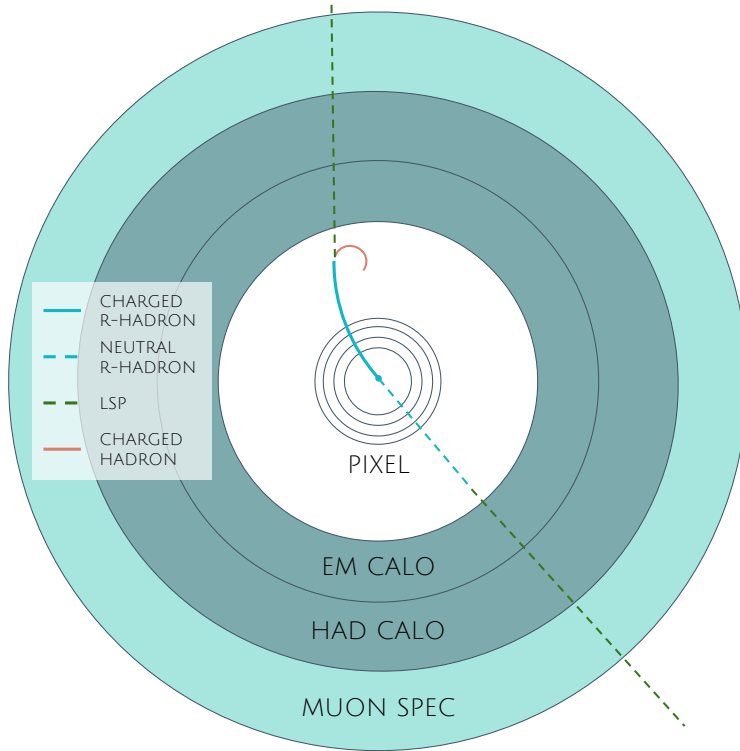


Figure 71: Schematic diagram of an R-Hadron event with a lifetime around 5 ns, where the masses of the R-Hadron and LSP are nearly degenerate. The diagram includes charged R-Hadrons (solid blue), neutral R-Hadrons (dashed blue), LSPs (dashed green) and charged hadrons (solid orange). The pixel detector, calorimeters, and muon system are illustrated but not to scale.

missing energy will be low because neither is detected. Two charged R-Hadrons will also result in low missing energy because both are reconstructed as tracks and will balance each other in the transverse plane. A small fraction of the time, one of the charged R-Hadron tracks may fail quality requirements and thus be excluded from the missing energy calculation and again result in significant missing energy. Figure 73 illustrates another example event with one charged R-Hadron which decays after approximately 20 ns, and shows how the jets from the decay might not be reconstructed.

The longest lifetimes, the VLL case, has all of the features of the 30-50 ns case but with the addition of muon tracks for any R-Hadrons that exit the calorimeter with a charge. That muon track can provide additional information from time-of-flight measurements to help identify LLPs. An example of the event topology for one charged and one neutral VLL R-Hadron is shown in Figure 74. Some searches on ATLAS have included this information to improve the search reach for VLL particles [85, 87].

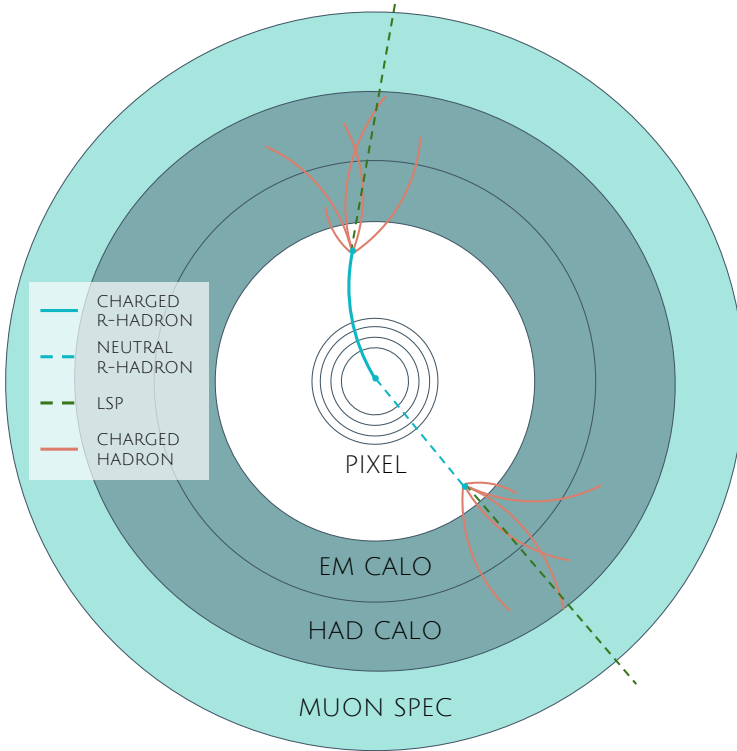


Figure 72: Schematic diagram of an R-Hadron event with a lifetime around 5 ns, where the masses of the R-Hadron and LSP are not degenerate. The diagram includes charged R-Hadrons (solid blue), neutral R-Hadrons (dashed blue), LSPs (dashed green) and charged hadrons (solid orange). The pixel detector, calorimeters, and muon system are illustrated but not to scale.

3206 9.2 SIMULATION

3207 All of the event topologies discussed above are modeled by simulations of R-
 3208 Hadron events in the ATLAS detector. A large number of such samples are
 3209 generated to determine efficiencies, to measure expected yields, and to estimate
 3210 uncertainties. The primary interaction, pair production of gluinos with masses
 3211 between 400 and 3000 GeV, is simulated using Pythia 6.4.27 [4] with the
 3212 AUET2B [88] set of tuned parameters for the underlying event and the CTEQ6L1 [65]
 3213 PDF set. The simulated interactions include a modeling of pileup by adding sec-
 3214 ondary, minimum bias interactions from both the same (in-time pileup) and
 3215 nearby (out-of-time pileup) bunch crossings. This event generation is then aug-
 3216 mented with a dedicated hadronization routine to hadronize the long-lived gluinos
 3217 into final states with R-Hadrons [89], with the probability to form a gluon-gluino
 3218 bound set at 10% [90].

3219 The cross sections used for these processes are calculated at NLO in the strong
 3220 coupling constant with a resummation of soft-gluon emission at next-to-leading
 3221 logarithmic (NLL) [91–95]. The nominal predictions and the uncertainties for
 3222 each mass point are taken from an envelope of cross-section predictions using
 3223 different PDF sets and factorization and renormalization scales [96]. As discussed
 3224 in Section 2.5.4, the PDFs and scales determine the cross section by providing the

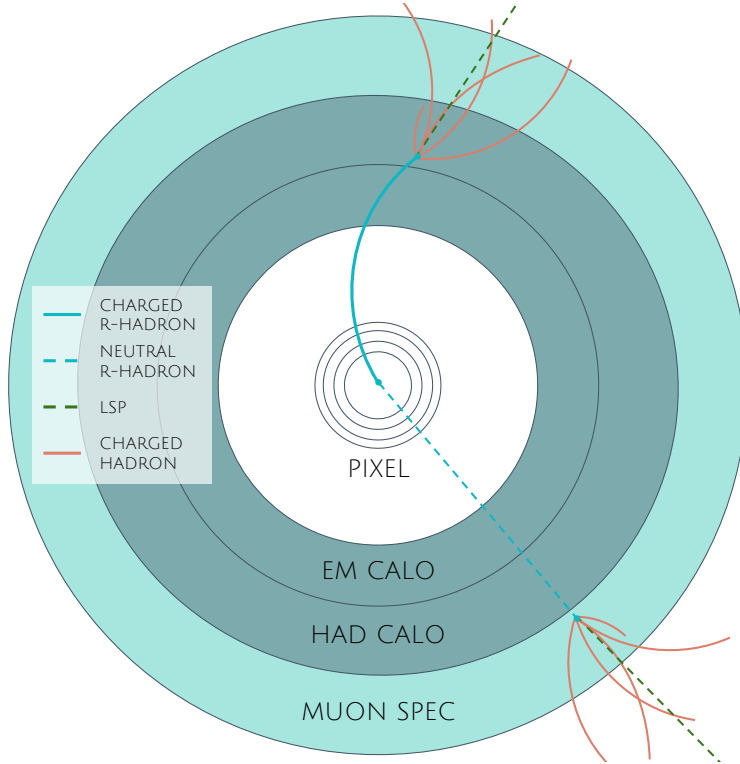


Figure 73: A schematic diagram of an R-Hadron event with a lifetime around 20 ns. The diagram includes one charged R-Hadron (solid blue), one neutral R-Hadron (dashed blue), LSPs (dashed green) and charged hadrons (solid orange). The pixel detector, calorimeters, and muon system are illustrated but not to scale.

probabilities of the proton constituents to interact. Multiple estimates for the PDF and scales at 13 TeV can be used to provide an average cross section calculation and its uncertainty.

The R-Hadrons then undergo a full detector simulation [40], where the interactions of the R-Hadrons with the material of the detector are described by dedicated Geant4 [6] routines. These routines model the interactions described in Section 9.1.1, including the ionizing interactions in the silicon modules of the inner detector and the R-Hadron-nucleon interactions in the calorimeters [97, 98]. The specific routine chosen to describe the interactions of the R-Hadrons with nucleons, the “generic model”, uses a pragmatic approach where the scattering cross section is taken to be a constant 12 mb per light quark. In this model the gluino itself does not interact at all, although it carries most of the kinetic energy of the bound state.

The lifetimes of these R-Hadrons are then simulated at several working points, $\tau = 0.1, 1.0, 3.0, 10, 30, 50$ and $> 50\text{ns}$. The actual decay times follow an exponential distribution, where τ is the characteristic time. Only one decay mode is simulated for these benchmark samples, $\tilde{g} \rightarrow q\bar{q}\tilde{\chi}_1^0$ with the neutralino mass set to 100 GeV. The search discussed here is also efficient for heavier neutralinos, which have very similar topologies but which generate less missing energy.

All of the simulated events are then reconstructed using the same software used for collision data. The fully reconstructed events are then reweighted to

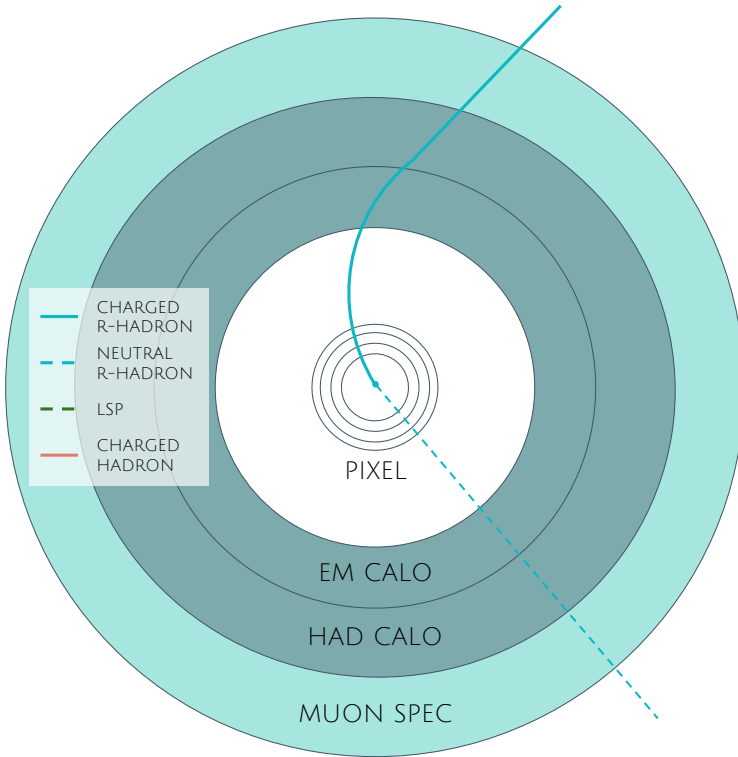


Figure 74: A schematic diagram of a [VLL](#) R-Hadron event. The diagram includes one charged R-Hadron (solid blue) and one neutral R-Hadron (dashed blue). The pixel detector, calorimeters, and muon system are illustrated but not to scale.

3246 match the distribution of initial state radiation in an alternative sample of events,
 3247 generated with MG5_aMC@NLO [5], which has had a more accurate description of
 3248 radiate effects than Pythia6 in previous iterations [86]. MG5_aMC@NLO predicts
 3249 a harder distribution of initial state radiation, where 28% more simulated events
 3250 generate sufficient missing energy to trigger for [VLL](#) R-Hadrons. This reweighting
 3251 provides a more accurate description of the p of the gluino-gluino system
 3252 and is important in modeling the efficiency of triggering and offline event selec-
 3253 tion.

3254

3255 EVENT SELECTION

3256 The **LLPs** targeted by this search differ in their interactions with the detector from
 3257 **SM** particles primarily because of their large mass. When produced at the ener-
 3258 gies available at the **LHC**, that large mass results in a low β (typically $0.2 < \beta < 0.9$
 3259 as shown in Figure 69). Such slow-moving particles heavily ionize in detector
 3260 material. Each layer of the pixel detector provides a measurement of that ion-
 3261 ization, through **ToT**, as discussed in Section 6.1.2. The ionization in the pixel
 3262 detector, quantified in terms of dE/dx , provides the major focus for this search
 3263 technique, along with the momentum measured in the entire inner detector. It is
 3264 effective both for its discriminating power and its use in reconstructing a parti-
 3265 cle's mass, and it can be used for a wide range of masses and lifetimes as discussed
 3266 in Section 9.1.2. However dE/dx needs to be augmented with a few additional
 3267 selection requirements to provide a mechanism for triggering and to further re-
 3268 duce backgrounds.

3269 Ionization itself is not currently accessible for triggering, so this search in-
 3270 stead relies on E_T^{miss} to trigger signal events. Although triggering on E_T^{miss} can
 3271 be inefficient, E_T^{miss} is often large for many production mechanisms of **LLPs**, as
 3272 discussed in Section 9.1.

3273 The use of ionization to reject **SM** backgrounds relies on well-measured, high-
 3274 momentum tracks, so some basic requirements on quality and kinematics are
 3275 placed on the tracks considered in this search. A few additional requirements
 3276 are placed on the tracks considered for **LLP** candidates that increase background
 3277 rejection by targeting specific types of **SM** particles.

The ionization measurement with the Pixel detector can be calibrated to provide an estimator of $\beta\gamma$. That estimate, together with the momentum measurement provided by tracking, can be used to reconstruct a mass for each track which traverses the pixel detector,

$$m = \frac{p}{\beta\gamma} \quad (20)$$

3278 That mass variable will be peaked at the **LLP** mass for any signal, and provides an
 3279 additional tool to search for an excess. In addition to an explicit requirement on
 3280 ionization, this search constructs a mass-window for each targeted signal mass
 3281 in order to search for an excess of events.

3282 The strategy discussed here is optimized for lifetimes of $O(1) - O(10)$ ns.
 3283 The specific values for each requirement in signal region were optimized con-
 3284 sidering the increase in discovery reach for tightening the requirement on each
 3285 discriminating variable. Pixel ionization is especially useful in this regime as
 3286 particles only need to propagate through the first seven layers of the inner de-
 3287 tector, about 37 cm from the beam axis. The search is still competitive with
 3288 other searches for **LLPs** at longer lifetimes, because the primary discriminating

variables are still applicable even for particles that do not decay within the detector [87]. Although the majority of the requirements will be the same for all lifetimes, two signal regions are defined to optimize separately for intermediate and long lifetime particles.

10.1 TRIGGER

Triggering remains a significant difficulty in defining an event selection with high signal efficiency in a search for LLPs. There are no triggers available in the current ATLAS system that can fire directly from a high momentum track with large ionization, as tracking is not available at L1 (Section 5.6). Although in some configurations a charged LLP can fire muon triggers, this requirement introduces significant model dependence on both the allowed lifetimes and the interactions in the calorimeter [80], as discussed in Section 9.1.1.

For a search targeting particles which may decay prior to reaching the muon system, the most efficient available trigger is based on missing energy [80]. As discussed in Section 9.1, signal events can produce significant E_T^{miss} by a few mechanisms. At the trigger level however, the missing energy is only calculated using the calorimeters (Section 5.6) where the R-Hadrons deposit little energy. So, at short lifetimes, E_T^{miss} measured in the calorimeter is generated by an imbalance between the jets and undetected LSPs produced in R-Hadron decays. At longer lifetimes, without the decay products, missing energy is only produced in the calorimeters when the R-Hadrons recoil against an ISR jet.

These features are highlighted in Figure 75, which shows the E_T^{miss} distributions for simulated short lifetime (3 ns) and VLL R-Hadron events. The figure includes both the offline E_T^{miss} , the missing energy calculated with all available information, and Calorimeter E_T^{miss} , the missing energy calculated using only information available at the calorimeter which approximates the missing energy available at the trigger. The short lifetime sample has significantly greater E_T^{miss} and Calorimeter E_T^{miss} than the VLL sample as expected. For the VLL sample, a small fraction of events with very large E_T^{miss} (about 5%) migrate into the bin with very small Calorimeter E_T^{miss} because the E_T^{miss} produced by a charged R-Hadron track opposite a neutral R-Hadron track does not contribute any missing energy in the calorimeters.

So, either case to some extent relies on kinematic degrees of freedom to produce missing energy, as the pair-produced LLPs tend to balance each other in the transverse plain. For long lifetimes in particular, the presence of ISR is important in providing an imbalance in the transverse plane, and is an important aspect of modeling the selection efficiency for R-Hadron events. The missing energy trigger with the lowest threshold available is chosen for this selection in order to maximize the trigger efficiency. The formation of the trigger decision for missing energy was discussed in more detail in Section 5.6. During 2015 data collection this was the HLT_xe70 trigger, which used a 50 GeV threshold on missing energy at L1 and a 70 GeV threshold on missing energy at the HLT which is nearly 100% efficient after the L1 requirement. With these thresholds, the incomplete balance of the LSPs results in a relatively low efficiency for long-

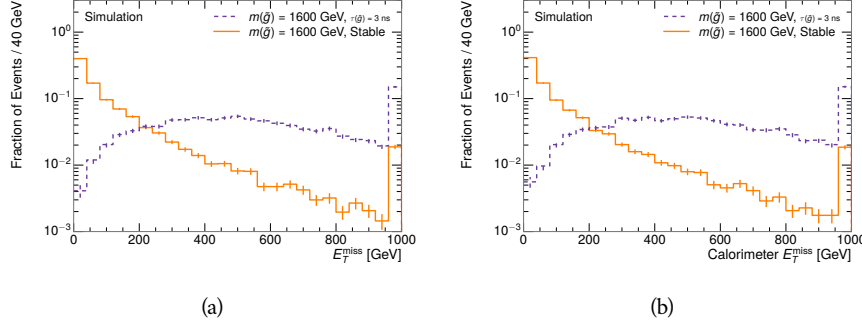


Figure 75: The distribution of (a) E_T^{miss} and (b) Calorimeter E_T^{miss} for simulated signal events before the trigger requirement. The final bin includes all events above the axis range.

3333 lifetime particles, roughly 40%, and efficiencies between 65% and 95% for shorter
 3334 lifetimes depending on both the mass and the lifetime.

3335 10.2 KINEMATICS AND ISOLATION

3336 After the trigger requirement, each event is required to have a primary vertex
 3337 reconstructed from at least two well-measured tracks in the inner detector, each
 3338 with $p_T > 400$ MeV. If more than one such vertex exists, the primary vertex is
 3339 taken to be the one with the largest summed p_T^2 for all tracks associated to that
 3340 vertex. The offline reconstructed E_T^{miss} is required to be above 130 GeV to addi-
 3341 tionally reject SM backgrounds. The transverse missing energy is calculated us-
 3342 ing fully reconstructed and calibrated offline objects, as described in Section 6.5.
 3343 In particular the E_T^{miss} definition in this selection uses jets reconstructed with the
 3344 anti- k_t algorithm with radius $R = 0.4$ from clusters of energy in the calorimeter
 3345 (Section 6.4) and with $p_T > 20$ GeV, as well as reconstructed muons, electrons,
 3346 and tracks not identified as another object type.

3347 The E_T^{miss} distributions are shown for data and a few simulated signals in Fig-
 3348 ure 76, after the trigger requirement. The data contains some events with E_T^{miss}
 3349 below the nominal trigger threshold of 70 GeV, which can occur because E_T^{miss}
 3350 at trigger level uses only calorimeter information while the full offline E_T^{miss}
 3351 additionally includes tracks and muons which can balance the event. The cut
 3352 placed at 130 GeV is 95% efficient for LL and 90% efficient for VLL particles, after
 3353 the trigger requirement, because of the missing energy generating mechanisms
 3354 discussed previously. The distribution of data in this figure and subsequent fig-
 3355 ures in this section can be interpreted as the distribution of backgrounds, as any
 3356 signal contamination would be negligible if present at these early stages of the
 3357 selection (prior to the final requirement on ionization). The background falls
 3358 rapidly with missing energy, motivating the direct requirement on E_T^{miss} for the
 3359 signal region.

3360 It is typically the practice for searches for new physics on ATLAS to place an
 3361 offline requirement on the triggering variable that is sufficiently tight to guar-

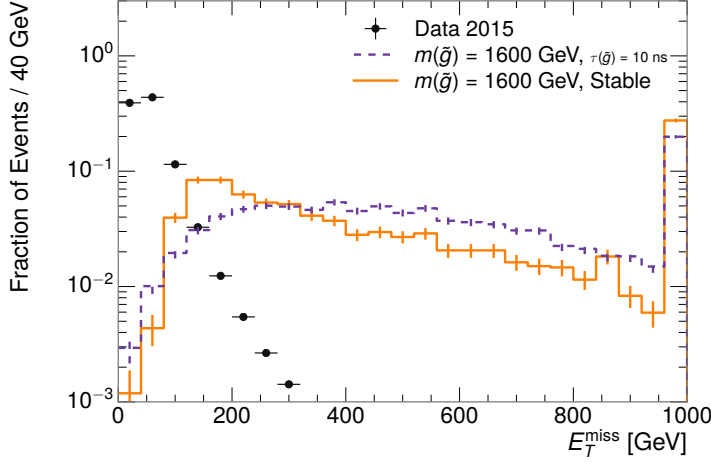


Figure 76: The distribution of E_T^{miss} for data and simulated signal events, after the trigger requirement. The final bin includes all events above the axis range.

3362 antee that the event would pass the trigger. Such a tight requirement makes the
 3363 uncertainty on the trigger efficiency of the simulation negligible, as modeling the
 3364 regime where the trigger is only partially efficient can be difficult. In this analy-
 3365 sis, however, because of the atypical interactions of R-Hadrons with the tracker
 3366 and the calorimeter, the offline requirement on E_T^{miss} is not sufficient to guar-
 3367 antee a 100% trigger efficiency even at large values, as can be seen in Figure 77.
 3368 This figure shows the efficiency for passing the HLT_xe70 trigger as a function
 3369 of the requirement on E_T^{miss} , which plateaus to roughly 85% even at large values.
 3370 This plateau does not reach 100% because events which have large offline miss-
 3371 ing energy from a neutral R-Hadron produced opposite of a charged R-Hadron
 3372 can have low missing energy in the calorimeters. The Calorimeter E_T^{miss} , on the
 3373 other hand, does not have this effect and reaches 100% efficiency at large values
 3374 because it is the quantity that directly corresponds to the trigger threshold. In
 3375 both cases the efficiency of triggering is greater for the short lifetime sample be-
 3376 cause the late decays to hadrons and LSPs produce an imbalance in the calorime-
 3377 ters even though they may not be reconstructed offline as tracks or jets. For this
 3378 reason, the requirement on E_T^{miss} is determined by optimizing the background
 3379 rejection even though it corresponds to a value of trigger efficiency significantly
 3380 below 1.0.

3381 The events are then required to have at least one candidate LLP track. Al-
 3382 though the LLPs are produced in pairs, many models do not consistently yield
 3383 two charged particles, as discussed in Chapter 9. For example, in the R-Hadron
 3384 model highlighted here, only 20% of events have two charged R-Hadrons while
 3385 47% of events have just one. A signal region requiring two charged particle can-
 3386 didates could be a powerful improvement in background rejection for a larger
 3387 dataset, but it is not considered in this version of the analysis as it was found to
 3388 be unnecessary to reject the majority of backgrounds.

3389 For a track to be selected as a candidate, it must have $p_T > 50 \text{ GeV}$ and pass
 3390 basic quality requirements. The track must be associated to the primary vertex.

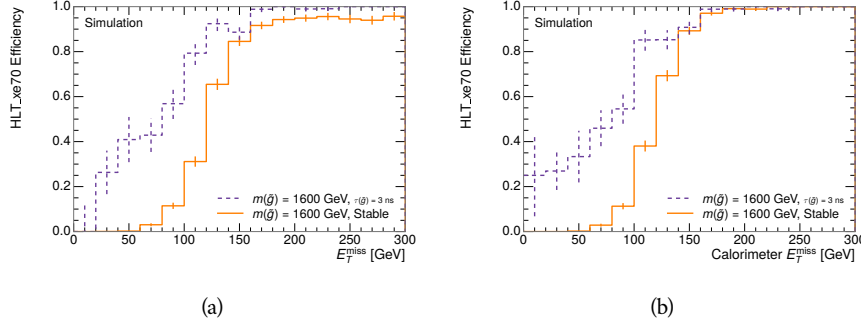


Figure 77: The trigger efficiency for the HLT_xe70 trigger requirement as a function of (a) E_T^{miss} and (b) Calorimeter E_T^{miss} for simulated signal events.

It must also have at least seven clusters in the silicon layers in the inner detector to ensure an accurate measurement of momentum. Those clusters must include one in the innermost layer if the extrapolated track is expected to pass through that layer. And to ensure a reliable measurement of ionization, the track is required to have at least two clusters in the pixel detector that provide a measurement of dE/dx .

At this point in the selection, there is a significant high-ionization background from multiple tracks that significantly overlap in the Pixel detector. Previous versions of this analysis have rejected these overlaps by an explicit overlap rejection between pairs of fully reconstructed tracks, typically by requiring no additional tracks within a cone around the candidate. This technique, however, fails to remove the background from tracks that overlap so precisely that the tracks cannot be separately resolved, which can be produced in very collimated photon conversions.

Another observable, which more directly targets track overlaps, identifies cluster shapes that are likely formed by multiple particles based on a neural network classification algorithm, as discussed in Section 6.1.1. The number of clusters on a given track that are estimated to have contributions from more than one particle is called N_{split} . As the shape of clusters requires significantly less spatial separation to identify overlaps than it does to reconstruct two fully resolved tracks, this variable is more effective at rejecting backgrounds from overlaps. Figure 78 shows the dependence of ionization on N_{split} ; as N_{split} increases the most probable value of dE/dx grows significantly up to twice the expected value when $N_{\text{split}} = 4$.

A requirement of $N_{\text{split}} = 0$ is very successful in reducing the long positive tail of the dE/dx distributions, as can be seen in Figure 79. Comparing the distribution for “baseline tracks”, tracks with only the above requirements on clusters applied and before the requirement on N_{split} , to the distribution with $N_{\text{split}} = 0$, it is clear that the fraction of tracks with large dE/dx is reduced by several orders of magnitude. The tracks without split hits are very close to the dE/dx distribution of identified muons, which are usually well isolated. Figure 79 also includes the distribution of dE/dx in an example signal simulation to demonstrate how effective dE/dx is as a discriminating variable with this isolation applied. The

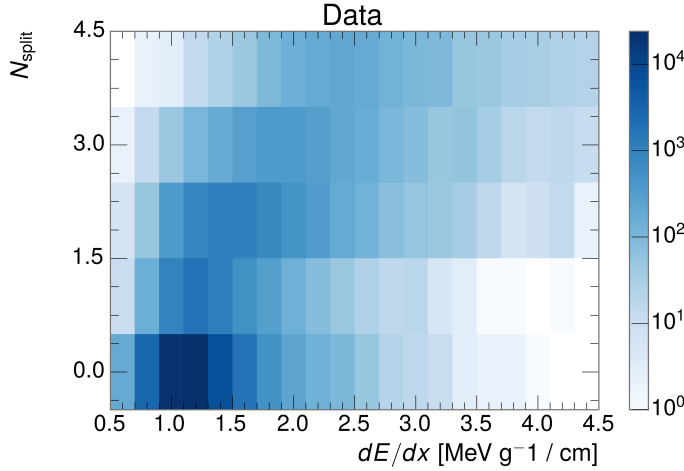


Figure 78: The dependence of dE/dx on N_{split} in data after basic track hit requirements have been applied.

background falls rapidly for $dE/dx > 1.8 \text{ MeV g}^{-1} \text{cm}^2$ while the majority of the signal, approximately 90% depending on the mass, falls above that threshold. Over 90% of LLP tracks in simulated signal events pass the N_{split} -based isolation requirement.

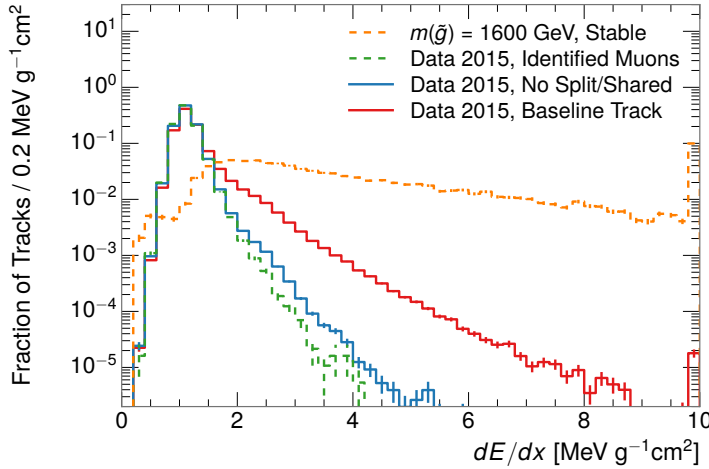


Figure 79: The distribution of dE/dx with various selections applied in data and simulated signal events. The final bin includes all tracks above the axis range.

A few additional kinematic requirements are imposed to help reduce SM backgrounds. The momentum of the candidate track must be at least 150 GeV, and the uncertainty on that measurement must be less than 50%. The distribution of momentum is shown in Figure 80 for tracks in data and simulated signal events after the previously discussed requirements on clusters, transverse momentum, and isolation have been imposed. The signal particles are much harder on av-

verage than their backgrounds as shown in Figure 69. The transverse mass, M_T , defined as

$$M_T = \sqrt{2p_T E_T^{\text{miss}}(1 - \cos(\Delta\phi(E_T^{\text{miss}}, \text{track})))} \quad (21)$$

estimates the mass of a decay of to a single charged particle and an undetected particle and is required to be greater than 130 GeV to reject contributions from the decay of W bosons. Figure 81 shows the distribution of M_T for data and simulated signal events. The signal is distributed over a wide range of M_T , with about 90% above the threshold value of 130 GeV. The data has a large number of contributions below 100 GeV from W boson decays and an additional peak from a kinematic shaping imposed by the requirements on E_T^{miss} and the track p_T in dijet events.

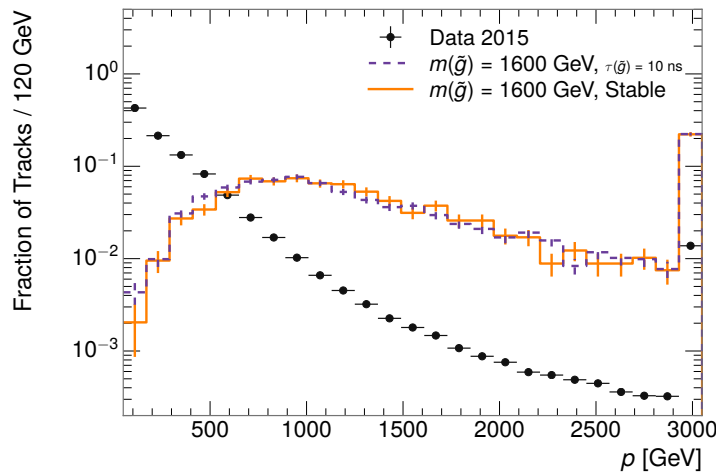


Figure 80: The distribution of track momentum for data and simulated signal events, after previous selection requirements have been applied. The final bin includes all tracks above the axis range.

10.3 PARTICLE SPECIES REJECTION

The amount of ionization deposited by particles with low mass and high momentum has a large positive tail [2], so backgrounds can be formed by a wide variety of SM processes when various charged particles have a few randomly large deposits of energy in the pixel detector. Those backgrounds can be additionally reduced by targeting other interactions with the detector where they are expected to have different behavior than R-Hadrons. The interactions with the detector depend on the types of particles produced rather than the processes which produce them, so this search forms a series of rejections to remove backgrounds from individual particle species. These rejections focus on using additional features of the event, other than the kinematics of the candidate track, as they can provide a powerful source of background rejection with very high signal efficiency. However, the lifetime of an R-Hadron can significantly change

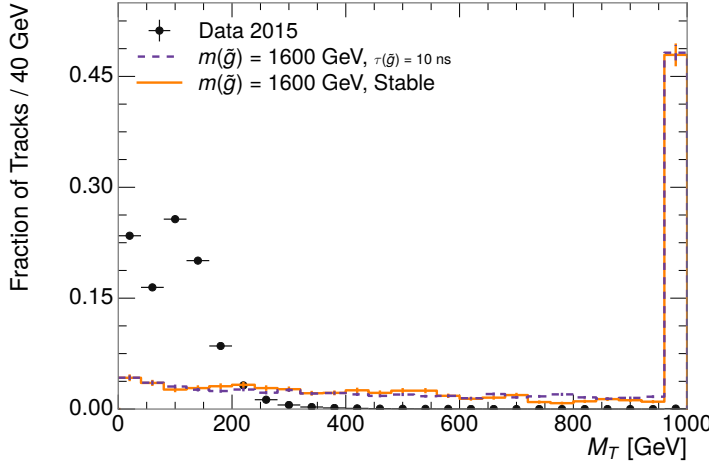


Figure 81: The distribution of M_T for data and simulated signal events, after previous selection requirements have been applied. The final bin includes all tracks above the axis range.

its detector characteristics, as discussed in Section 9.1.2. To accommodate these differences, the **SM** rejections defined in this section are split to form two signal regions, one for long-lifetimes particles, the **VLL** region ($\tau[\text{ns}] \geq 50 \text{ ns}$), and one for intermediate lifetime particles, the **LL** region ($0.4 < \tau[\text{ns}] < 50$).

Jets can contribute high momentum track backgrounds when an individual jet constituent carries large p_T . These tracks can be sufficiently well isolated from the other constituents that they are separately reconstructed and pass the N_{split} requirement. However, jets can be very effectively rejected by considering the larger-scale isolation of the candidate track. In this case the isolation focuses on the production of nearby particles as a jet-veto, rather than the isolation from overlapping tracks based on N_{split} that was used to reduce high-ionization backgrounds. As explained in Section 9.1, the fragmentation process which produces an R-Hadron is very hard and thus is not expected to produce additional particles with a summed momentum of more than 5 GeV. Nearby particles may be produced in the decay of the R-Hadron, but they will be significantly displaced, so the jet-veto only considers tracks associated to the primary vertex. The jet-veto uses the summed momentum of tracks with a cone of $\Delta R < 0.25$, referred to as p_T^{Cone} , which is shown in Figure 82 for data and simulated signal events. In the data this value has a peak at zero from isolated tracks such as leptons, and a long tail from jets which contains as much as 80% of the background above 20 GeV at this stage of the selection. In signal events p_T^{Cone} is strongly peaked at zero and significantly less than 1% of signal events have p_T^{Cone} above 20 GeV. This makes a requirement of $p_T^{\text{Cone}} < 20 \text{ GeV}$ a very effective method to reject background without losing signal efficiency. For the **VLL** signal region, this cut is further tightened to $p_T^{\text{Cone}} < 5 \text{ GeV}$ as it is the most effective variable remaining to extend the search reach for long lifetimes.

Even for fully isolated particles, there are additional methods to reject each type of particle using information in the muon system and calorimeters. Muons

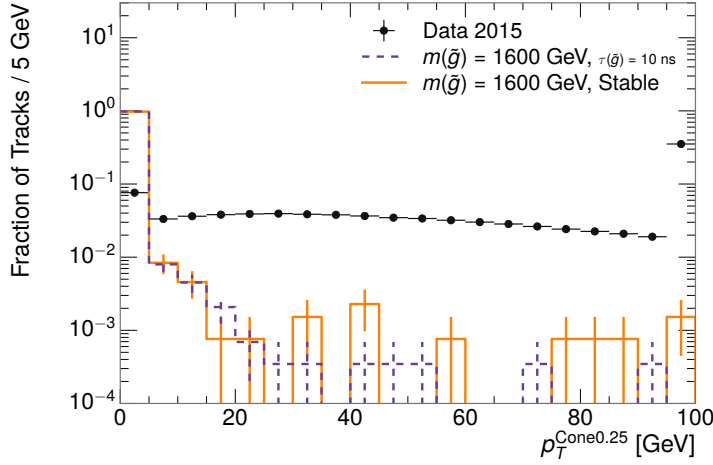


Figure 82: The distribution of summed tracked momentum within a cone of $\Delta R < 0.25$ around the candidate track for data and simulated signal events, after previous selection requirements have been applied. The final bin includes all tracks above the axis range.

3485 can be identified very reliably using the tracks in the muon system, as described
 3486 in Section 6.3. For intermediate lifetimes ($0.4 < \tau[\text{ns}] < 30$), the LLPs do not sur-
 3487 vive long enough to reach the muon system, and so muons are vetoed by rejecting
 3488 tracks that associate to a muon with medium muon identification requirements
 3489 (Section 6.3). For longer lifetimes ($\tau > 30$ ns), this rejection is not applied be-
 3490 cause LLPs which reach the muon system can be identified as muons as often as
 3491 30% of the time in simulated samples.

3492 Calorimeter-based particle rejection relies on the expected small deposits of
 3493 energy from LLPs. When the lifetime is long enough to reach the calorimeter, a
 3494 LLP deposits little of its energy as it traverses the material, as discussed in Sec-
 3495 tion 9.1. Even when the particle does decay before the calorimeter, the majority
 3496 of its energy is carried away by the LSP and not deposited in the calorimeter.
 3497 In both cases the energy is expected to be distributed across the layers of the
 3498 calorimeters and not peaked in just one layer. This can be quantified in terms of
 3499 E/p , the ratio of calorimeter energy of a nearby jet to the track momentum, and
 3500 f_{EM} , the fraction of energy in that jet within the electromagnetic calorimeter.
 3501 When no jets fall within a cone of 0.05 of the particle, E/p and f_{EM} are both de-
 3502 fined as zero. E/p is expected to be above 1.0 for electrons and hadrons because
 3503 of the contributions from other nearby particles. At these momenta there is no
 3504 significant fraction of tracks with no associated clusters due to interactions with
 3505 the detector or insufficient energy deposits (see Section 7.2.2). f_{EM} is peaked
 3506 close to 1.0 for electrons, and distributed between 10% and 90% for hadrons.

3507 These trends can be seen in the two dimensional distribution for signal in
 3508 Figure 83 for VLL and LL (10 ns) signal events. The majority of R-Hadrons in
 3509 both samples fall into the bin for $E/p = 0$ and $f_{\text{EM}} = 0$ because the majority of
 3510 the time there is no associated jet. In the VLL sample, when there is an associated
 3511 jet, E/p is typically still below 0.1, and the f_{EM} is predominantly less than 0.8.

3512 In the LL sample, on the other hand, E/p is larger on average because of the jets
 3513 produced in the R-Hadron decay. It is still typically below 0.1, however, because
 3514 most of the energy of the R-Hadron is carried by the LSP and not the jet. The
 3515 f_{EM} is much lower on average in this case, below 0.1, because the 10 ns lifetime
 3516 particles rarely decay before passing through the electromagnetic calorimeter.
 3517 Figure 83 also includes simulated Z decays to electrons or tau leptons. From the
 3518 decays to electrons it is clear that the majority of electrons have f_{EM} above 0.9.
 3519 The τ decays include a variety of products. Muons can be seen in the bin where
 3520 $E/p = 0$ and $f_{\text{EM}} = 0$ because they do not have an associated jet. Electrons fall
 3521 into the range where $E/p > 1$ and $f_{\text{EM}} > 0.9$. Hadronic tau decays are the most
 3522 common, and fall in the range of $0.1 < f_{\text{EM}} < 0.9$ and $E/p > 1.0$.

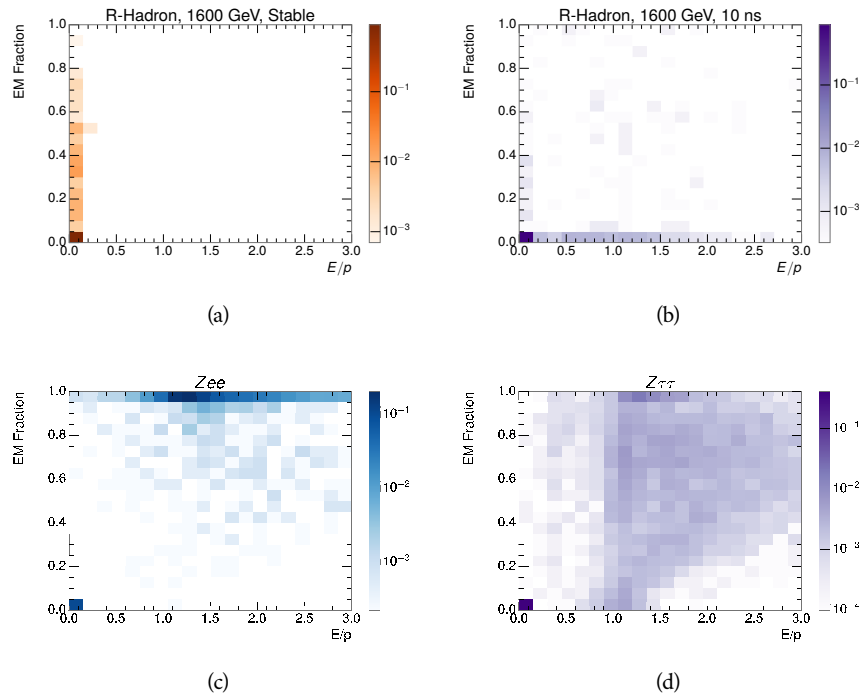


Figure 83: The normalized, two-dimensional distribution of E/p and f_{EM} for simulated
 (a) 1200 GeV VLL R-Hadron, and (b) 1200 GeV, 10 ns R-Hadron, (c) $Z \rightarrow ee$,
 and (d) $Z \rightarrow \tau\tau$ events.

3523 The differences motivate an electron rejection by requiring $f_{\text{EM}} < 0.9$. Simi-
 3524 larly, isolated hadrons are rejected by requiring $E/p < 1.0$. These requirements
 3525 combine to remove the majority of isolated electrons and hadrons but retain over
 3526 95% of the simulated signal across a range of masses and lifetimes. The suite of
 3527 particle species rejection techniques provide a significant analysis improvement
 3528 over previous iterations of ionization-based searches on ATLAS by providing
 3529 additional background rejection with minimal loss in signal efficiency.

3530 10.4 IONIZATION

3531 The final requirement on the candidate track is the primary discriminating vari-
 3532 able, the ionization in the pixel detector. That ionization is measured in terms
 3533 of dE/dx , which was shown for data and simulated signal events in Figure 79.
 3534 dE/dx is dramatically greater for the high mass signal particles than the back-
 3535 grounds, which start to fall immediately after the minimally ionizing peak at 1.1
 3536 MeV g $^{-1}$ cm 2 . The dE/dx for candidate tracks must be greater than a pseudorapidity-
 3537 dependent threshold, specifically $1.80 - 0.11|\eta| + 0.17\eta^2 - 0.05|\eta|^3$ MeV g $^{-1}$ cm $^{-2}$,
 3538 in order to correct for an approximately 5% dependence of the MIP peak position
 3539 on η . The requirement was chosen as part of the signal region optimization, and
 3540 reduces the backgrounds by a factor of 100 while remaining 70-90% efficient for
 3541 simulated signal events depending on the mass.

3542 10.4.1 MASS ESTIMATION

3543 The mean value of ionization in silicon is governed by the Bethe equation and
 3544 the most probable value follows a Landau-Vavilov distribution [2]. Those forms
 3545 inspire a parametric description of dE/dx in terms of $\beta\gamma$,

$$(dE/dx)_{\text{MPV}}(\beta\gamma) = \frac{p_1}{\beta p_3} \ln(1 + [p_2\beta\gamma]^{p_5}) - p_4 \quad (22)$$

3546 which performs well in the range $0.3 < \beta\gamma < 1.5$. This range includes the
 3547 expected range of $\beta\gamma$ for the particles targeted for this search, with $\beta\gamma \approx 2.0$
 3548 for lower mass particles (O(100 GeV)) and $\beta\gamma \approx 0.5$ for higher mass parti-
 3549 cles (O(1000 GeV)). The parameters, p_i , are fit using a 2015 data sample of
 3550 low-momentum pions, kaons, and protons as described in Ref. [99]. Figure 84
 3551 shows the two-dimensional distribution of dE/dx and momentum along with
 3552 the above fitted values for $(dE/dx)_{\text{MPV}}$.

3553 The above equation (22) is then numerically inverted to estimate $\beta\gamma$ and the
 3554 mass for each candidate track. In simulated signal events, the mean of this mass
 3555 value reproduces the generated mass up to around 1800 GeV to within 3%. The
 3556 mass distributions are shown for a few VLL mass points in Figure 85. The large
 3557 widths of these distributions come from the high variability in energy deposits
 3558 in the pixel detector as well as the uncertainty on momentum measurements at
 3559 high momentum, but the means converge to the expected values. A constant
 3560 shift of 3% is observed between the mean of the reconstructed mass distribution
 3561 and the generated mass, which is then corrected by applying a 3% shift in the
 3562 opposite direction.

3563 This analysis evaluates expected yields and the resulting cross sectional limits
 3564 using windows in this mass variable. The windows are formed by fitting mass
 3565 distributions in simulated signal events like those in Figure 85 to Gaussian distri-
 3566 butions and taking all events that fall within $\pm 1.4\sigma$ of the mean. As can be seen
 3567 in Figure 85, typical values for this width are $\sigma \approx 300 - 500$ GeV depending on
 3568 the generated mass.

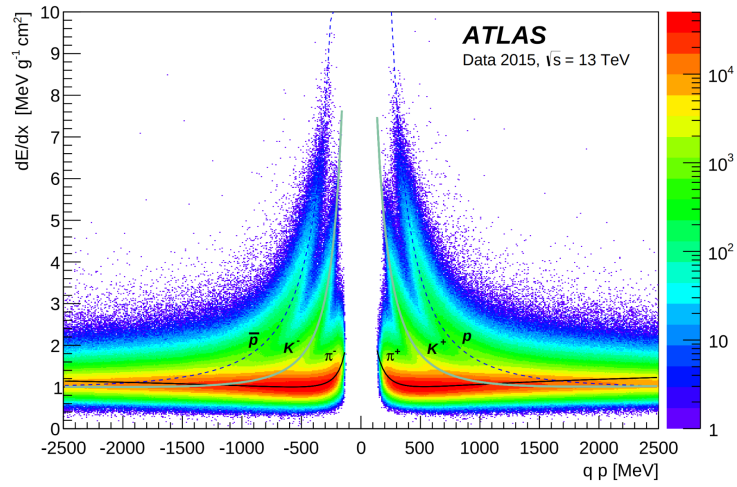


Figure 84: Two-dimensional distribution of dE/dx versus charge signed momentum (qp) for minimum-bias tracks. The fitted distributions of the most probable values for pions, kaons and protons are superimposed.

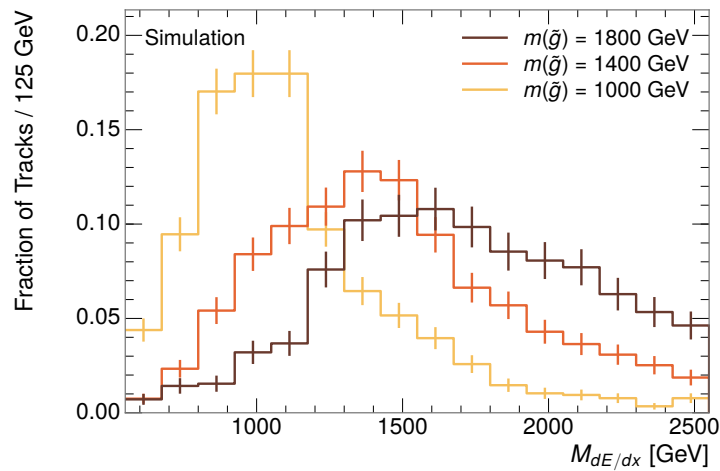


Figure 85: The distribution of mass estimated using dE/dx for simulated VLL R-Hadrons with masses between 1000 and 1600 GeV.

3569 10.5 EVENT SELECTION

3570 The numbers of events passing each requirement are shown in Table 9 for the full
 3571 2015 dataset and a simulated 1600 GeV, 10 ns lifetime R-Hadron sample. The
 3572 table highlights the overall acceptance \times efficiency for signal events, which for
 3573 this example is 19%. Between SM rejection and ionization, the selection require-
 3574 ments reduce the background of tracks which pass the kinematic requirements
 3575 down by an additional factor of almost 2000.

Selection	Signal Events (%)	Data Events	Rejection
Generated	26.0 ± 0.3		
E_T^{miss} Trigger	24.8 ± 0.3 (95%)		
$E_T^{\text{miss}} > 130$ GeV	23.9 ± 0.3 (92%)		
Track Quality and p_T	10.7 ± 0.2 (41%)	368324	1.0
Isolation Requirement	9.0 ± 0.2 (35%)	108079	3.4
Track $p > 150$ GeV	6.6 ± 0.2 (25%)	47463	7.8
$M_T > 130$ GeV	5.8 ± 0.2 (22%)	18746	20
Electron/Hadron Veto	5.5 ± 0.2 (21%)	3612	100
Muon Veto	5.5 ± 0.2 (21%)	1668	220
Ionization Requirement	5.0 ± 0.1 (19%)	11	33000

Table 9: The expected number of events at each level of the selection for LL 1600 GeV, 10 ns R-Hadrons, along with the number of events observed in data, for 3.2 fb^{-1} . The simulated yields are shown with statistical uncertainties only. The total efficiency \times acceptance is also shown for the signal and the rejection factor relative to initial track requirement is shown for data.

3576 There is a strong dependence of this efficiency on lifetime and mass, with effi-
 3577 ciencies dropping to under 1% at low lifetimes. Figure 86 shows the dependence
 3578 on both mass and lifetime for all signal samples considered in this search. The
 3579 dependence on mass is relatively slight and comes predominantly from the in-
 3580 creasing fraction of R-Hadrons which pass the ionization cut with increasing
 3581 mass. The trigger and E_T^{miss} requirements are most efficient for particles that
 3582 decay before reaching the calorimeters. However, the chance of a particle to be
 3583 reconstructed as a high-quality track decreases significantly at low lifetimes as
 3584 the particle does not propagate sufficiently through the inner detector. These
 3585 effects lead to a maximum in the selection efficiency for lifetimes around 10-30
 3586 ns. The lifetimes up to and including 30 ns are shown with the LL selection and
 3587 the 50 ns and stable points are shown with the VLL selection.

3588 The inefficiency of this signal region at short lifetimes comes almost exclu-
 3589 sively from an acceptance effect, in that the particles do not reach the necessary
 3590 layers of the SCT. This can be seen more clearly by defining a fiducial region
 3591 which includes events with at least one R-Hadron that is produced with non-
 3592 zero charge, $p_T > 50$ GeV, $p > 150$ GeV, $|\eta| < 2.5$, and a decay distance greater
 3593 than 30 cm in the transverse plane. At short (1 ns) lifetimes, the acceptance into

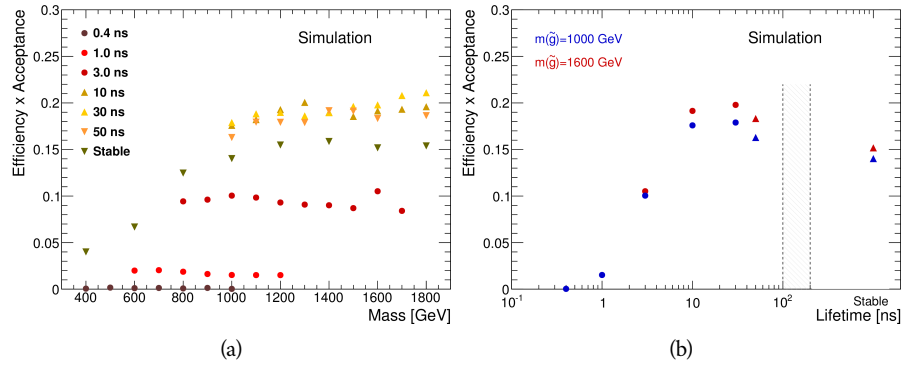


Figure 86: The acceptance \times efficiency as a function of R-Hadron (a) mass and (b) lifetime. (a) shows all of the combinations of mass and lifetime considered in this search, and (b) highlights the lifetime dependence for 1000 GeV and 1600 GeV R-Hadrons.

3594 this region is as low as 4%. Once this acceptance is accounted for, the selection
3595 efficiency ranges from 25% at lifetimes of 1 ns up to 45% at lifetimes of 10 ns.

3596

3597 BACKGROUND ESTIMATION

3598 The event selection discussed in the previous section focuses on detector sig-
 3599 natures, emphasizing a single high-momentum, highly-ionizing track. That track
 3600 is then required to be inconsistent with the expected properties of SM particles,
 3601 with various requirements designed to reject jets, hadrons, electrons, and muons
 3602 (Section 10.3). Therefore the background for this search comes entirely from
 3603 backgrounds that are outliers of various distributions including dE/dx , f_{EM} ,
 3604 and p_T^{Cone} . The simulation can be tuned in various ways to do an excellent job of
 3605 modeling the average properties of each particle type [100], but it is not necessarily
 3606 expected to accurately reproduce outliers. For this reasons, the background
 3607 estimation used for this search is estimated entirely using data.

3608 11.1 BACKGROUND SOURCES

3609 SM charged particles with lifetimes long enough to form tracks in the inner de-
 3610 tector can be grouped into three major categories based on their detector in-
 3611 teractions: hadrons, electrons, and muons. Every particle that contributes to the
 3612 background for this search belongs to one of these types. Relatively pure samples
 3613 of tracks from each of these types can be formed in data by inverting the various
 3614 rejection techniques in Section 10.3. Specifically, muons are selected requiring
 3615 medium muon identification, electrons requiring $E/p > 1.0$ and $f_{EM} > 0.95$,
 3616 and hadrons requiring $E/p > 1.0$ and $f_{EM} < 0.95$.

3617 Figure 87 shows the distributions of momentum and dE/dx for these cate-
 3618 gories in data, after requiring the event level selection as well as the track re-
 3619 quirements on p_T , hits, and N_{split} , as discussed in Section 10.2. Simulated signal
 3620 events are included for reference. These distribution are only illustrative of the
 3621 differences between types, as the rejection requirements could alter their shape.
 3622 This is especially significant for momentum which enters directly into E/p and
 3623 can indirectly affect muon identification. However it is clear that there are some
 3624 differences between types in both distributions, even though the trends are sim-
 3625 ilar. The distributions of momentum are not necessarily expected to match be-
 3626 tween the various types because the production mechanisms for each type result
 3627 in different kinematic distributions. dE/dx is also different between types be-
 3628 cause of incomplete isolation; although the requirement on N_{split} helps to reduce
 3629 the contribution of nearby particles it does not completely remove the effect
 3630 of overlaps. Muons are better isolated because they do not have the additional
 3631 particle from hadronization present for hadrons and they are significantly less
 3632 likely do interact with the detector and produce secondary particles compared to
 3633 hadrons and electrons. Thus muons have the smallest fraction of dE/dx above
 3634 the threshold of $1.8 \text{ MeVg}^{-1}\text{cm}^2$; hadrons and electrons have a larger fraction
 3635 above this threshold.

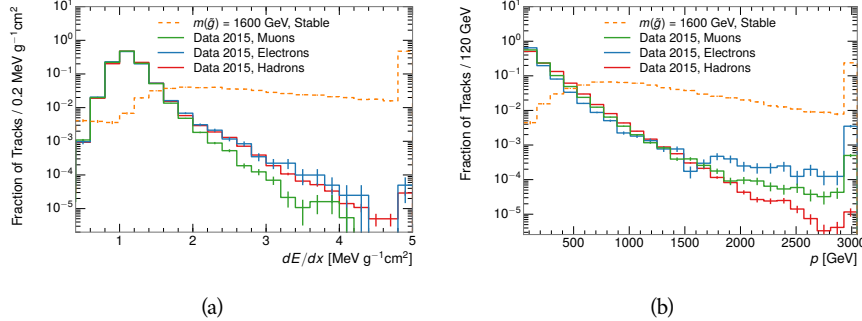


Figure 87: The distribution of (a) dE/dx and (b) momentum for tracks in data and simulated signal after requiring the event level selection and the track selection on p_T , hits, and N_{split} . Each sub-figure shows the normalized distributions for tracks classified as hadrons, electrons, and muons in data and R-Hadrons in the simulated signal.

3636 It is difficult to determine what fraction of each particle type enters into the fi-
3637 nal signal region. The background method will not have significant dependence
3638 on the relative contributions of each species, but it is useful to understand the
3639 differences between each when considering the various tests of the method.

3640 11.2 PREDICTION METHOD

The data-driven background estimation relies on the independence between the ionization measurement and other kinematic variables in the event. For standard model particles with momenta above 50 GeV, dE/dx is not correlated with momentum; though there is a slight relativistic rise as momentum increases, the effect is small compared to the width of the distribution of ionization energy deposits.. So, the proposed method to estimate the mass distribution of the signal region is to use the momentum from a track with low dE/dx (below the threshold value) and to combine it with a random dE/dx value from a dE/dx template. The resulting track is just as likely as the original, so a large set of random generations provide the expected distributions of momentum and ionization. These are then combined using the parametrization described in Section 10.4.1 to estimate $\beta\gamma$ and then form a distribution of mass for the signal region using Equation 20.

Algorithmically this method is implemented by forming two distinct Control Regions (**CRs**). The first **CR**, CR1, is formed by applying the entire event selection from Chapter 10 apart from the dE/dx and mass requirements. The dE/dx requirement is instead inverted for this region. Because of the independence of dE/dx and p , the tracks in this control region have the same kinematic distribution as the tracks in the signal region, and are used to measure a two-dimensional template of p and η . The second **CR**, CR2, is formed from the event selection through the dE/dx requirement, but with an inverted E_T^{miss} requirement. The tracks in this control region are expected to have similar dE/dx distributions as the signal region before the ionization requirement, and so this region is used to measure a two-dimensional template of dE/dx and η .

3664 The contribution of any signal to the control regions is minimized by the in-
 3665 verted selection requirements. Only less than 10% of simulated signal events
 3666 have either dE/dx or E_T^{miss} below the threshold values in the original signal re-
 3667 gion, while the backgrounds are significantly enhanced by inverting those re-
 3668 quirements. The signal contamination is less than 1% in both control regions
 3669 for all of the simulated masses and lifetimes considered in this analysis.

3670 With those measured templates, the shape of the mass estimation is generated
 3671 by first selecting a random (p , η) combination from CR1. This momentum
 3672 value is combined with a dE/dx value taken from the appropriate distribution
 3673 of dE/dx for the selected η from CR2. The use of η in both random samplings
 3674 controls for any correlation between p , dE/dx , and η . Those values are then
 3675 used to calculate a mass in the same way that is done for regular tracks in data,
 3676 see Section 10.4.1. As this procedure includes all dE/dx values, the cut at 1.8
 3677 MeVg $^{-1}$ cm 2 is then enforced to fully model the signal region. The generated
 3678 mass distribution is then normalized by scaling the background estimate to the
 3679 data in the region $M < 160$ GeV, where signals of this type have already been
 3680 excluded [86]. This normalization uses the distributions of mass generated with-
 3681 out the ionization requirement.

3682 The statistical uncertainties on these background distributions are calculated
 3683 by independently fluctuating each bin of the input templates according to their
 3684 Poisson uncertainties. These fluctuations are repeated a large number of times,
 3685 and the uncertainty on the resulting distribution is taken as the root mean square
 3686 (RMS) deviation of the fluctuations from the average. As the procedure uses one
 3687 million random combinations to generate the distributions, The statistical un-
 3688 certainty from the actual random generations is negligible compared to the un-
 3689 certainty from measuring the templates.

3690 11.3 VALIDATION

3691 The validity of the background estimation technique can be evaluated in both
 3692 data and simulation. The underlying assumption that random combinations of
 3693 dE/dx and momentum can predict a mass distribution in an orthogonal region
 3694 can be tested using simulated samples where concerns like multiple particle types
 3695 can be controlled. Using the same technique in another set of signal-depleted
 3696 regions in data then extends this confidence to the more complicated case where
 3697 several particle species are inherently included.

3698 11.3.1 CLOSURE IN SIMULATION

3699 The first test of the procedure is done using a simulated sample of $W \rightarrow \mu\nu$
 3700 decays. These types of events provide the ingredients required to test the back-
 3701 ground estimate, E_T^{miss} and isolated tracks, with high statistics. In this example
 3702 there is no signal, so simulated events in the orthogonal CRs are used to estimate
 3703 the shape of the mass distribution of the simulated events in the signal region. To
 3704 reflect the different topology for W boson decays, the CRs use slightly modified
 3705 definitions. In all CRs, the requirement of $p > 150$ GeV and the SM rejection

3706 requirements are removed. Additionally, for the signal region the requirement
 3707 on E_T^{miss} is relaxed to 30 GeV and the corresponding inverted requirement on
 3708 CR2 is also set at 30 GeV.

3709 With these modified selections, the simulated and randomly generated distri-
 3710 butions of $M_{dE/dx}$ are shown in Figure 88. This figure includes the mass distri-
 3711 butions before and after the requirement on dE/dx , which significantly shapes
 3712 the distributions. In both cases the background estimation technique repro-
 3713 duces the shape of $M_{dE/dx}$ in the signal region. There is a small difference in the pos-
 3714 itive tail of the mass distribution prior to the ionization cut, where the random
 3715 events underestimate the fraction of tracks with mass above 150 GeV by about
 3716 20%. After the ionization requirement, however, this discrepancy is not present
 3717 and the two distributions agree to within statistical uncertainties in the positive
 3718 tail.

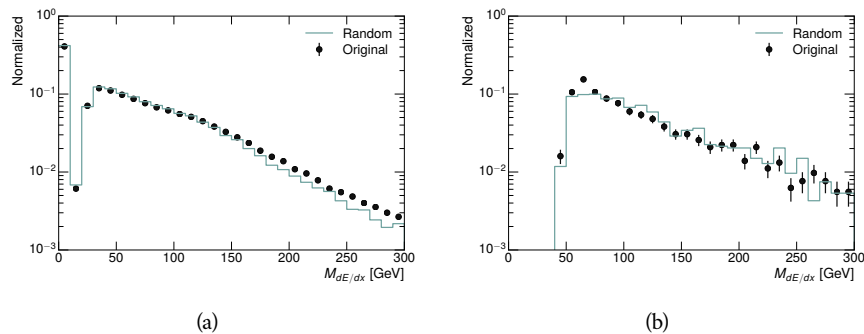


Figure 88: The distribution of $M_{dE/dx}$ (a) before and (b) after the ionization requirement for tracks in simulated W boson decays and for the randomly generated background estimate.

3719 This ability to reproduce the shape of the mass distribution in simulated events
 3720 shows that the technique works as expected. No significant biases are acquired
 3721 in using low dE/dx events to select kinematic templates or in using low E_T^{miss}
 3722 events to select ionization templates, as either would result in a mismodeling of
 3723 the shape of the mass distribution. The simulated events contain only one par-
 3724 ticle type, however, so this test only establishes that the technique works well
 3725 when the the CRs are populated by exactly the same species.

3726 11.3.2 VALIDATION REGION IN DATA

3727 The second test of the background estimate is performed using data in an or-
 3728 thogonal validation region. The validation region, and the corresponding CRs,
 3729 are formed using the same selection requirements as in the nominal method but
 3730 with a modified requirement on momentum, $50 < p[\text{GeV}] < 150$. This allows
 3731 the technique to be checked in a region with very similar properties but where
 3732 the signal is depleted, as the majority of the signal has momentum above 150
 3733 GeV while the backgrounds are enhanced below that threshold. Any biases on
 3734 the particle composition of the CRs for the signal region will be reflected in the
 3735 CRs used to estimate the mass distribution in the validation region.

3736 Figure 89 shows the measured and randomly generated mass distributions for
 3737 data before and after the ionization requirement. The background estimate mod-
 3738 els the actual background before the ionization requirement very well, with good
 3739 agreement to within the statistical uncertainties out to the limit of the mass dis-
 3740 tribution. There are very few events in the validation region after the ionization
 3741 requirement, but the few observed events are consistent with the background
 3742 prediction. The good agreement in this validation region provides a confirma-
 3743 tion that the technique works even in the full-complexity case with multiple par-
 3744 ticle types entering the distributions. Any bias from changes in particle compo-
 3745 sition between regions is small compared to statistical uncertainties.

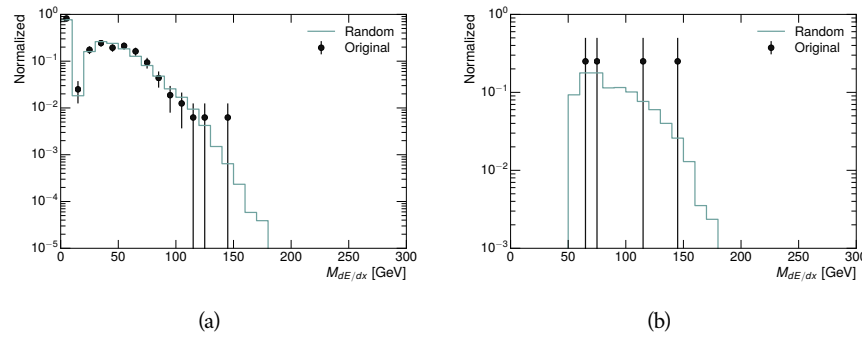


Figure 89: The distribution of $M_{dE/dx}$ (a) before and (b) after the ionization require-
 ment for tracks in the validation region and for the randomly generated back-
 ground estimate.

3746 11.4 EXPECTED BACKGROUND

3747 Using the full technique in the primary regions described in Section 11.2 pro-
 3748 vides a final background estimate for the signal region of this search. It predicts
 3749 a total background of 11.1 ± 1.7 events in the **LL** region and 17.2 ± 2.6 events in
 3750 the **VLL** region. Table 10 shows the number of events predicted in mass windows
 3751 for the grid of mass points, for each of the **LL** and **VLL** signal regions. Only one
 3752 to two events are expected in each mass window, as the background distribution
 3753 falls with increasing mass.

Mass	Expected Background, <code>LL</code>	Expected Background, <code>VLL</code>
1000	1.328 ± 0.063	1.803 ± 0.081
1100	1.255 ± 0.060	1.409 ± 0.069
1200	1.193 ± 0.058	1.310 ± 0.066
1300	0.997 ± 0.051	1.431 ± 0.069
1400	1.131 ± 0.056	1.273 ± 0.065
1500	1.111 ± 0.055	1.115 ± 0.059
1600	1.193 ± 0.058	1.041 ± 0.057
1800	1.138 ± 0.056	0.918 ± 0.053

Table 10: The expected number of background events within each of the mass windows for the stable and metastable signal regions.

3754

3755 SYSTEMATIC UNCERTAINTIES

3756 A number of systematic uncertainties affect the interpretation of the results of
 3757 the search. These uncertainties can be broken down into two major categories,
 3758 those which affect the estimate of the background using data and those which
 3759 affect the measurement of the signal yield estimated with simulated events. The
 3760 total measured systematic uncertainties range between 6-7% for the background
 3761 estimation and 29-33% for the signal yield depending on lifetime. These system-
 3762 atic uncertainties are expected to be small compared to the statistical fluctuations
 3763 of the measured yields so that measured cross-sectional limits will be dominated
 3764 by statistical uncertainties. Only the systematic uncertainties on the background
 3765 estimation are relevant for the search for LLPs, as the systematics on the signal
 3766 yield enter only into the calculation of limits in the absence of a signal. The fol-
 3767 lowing sections describe each source of systematic uncertainty for each of the
 3768 two types.

3769 12.1 BACKGROUND ESTIMATE

3770 The systematic uncertainties on the background estimate come primarily from
 3771 considering alternative methods for generating the background distributions.
 3772 These uncertainties are small compared to the statistical uncertainties on the
 3773 background estimate which come from the limited statistics in measuring the
 3774 template distributions, as described in Section 11.2. They are summarized in
 3775 Table 11.

Source of Uncertainty:	Value [%]
Analytic Description of dE/dx	4.0
Muon Fraction (<a>VLL Region only)	3.0
IBL Ionization Correction	3.8
Normalization	3.0
Total (<a>LL Region):	6.3
Total (<a>VLL Region):	7.0

Table 11: A summary of the sources of systematic uncertainty for the data-driven back-
 ground in the signal region. If the uncertainty depends on the mass, the maxi-
 mum values are reported.

3776 12.1.1 ANALYTIC DESCRIPTION OF dE/dX

3777 The background estimate uses a binned template distribution to estimate the
 3778 dE/dx of tracks in the signal region, as described in Section 11.2. It is also possi-
 3779 ble to fit that measured distribution to a functional form to help smooth the dis-
 3780 tribution in the tails of dE/dx where the template is driven by a small number
 3781 of tracks. Both Landau convolved with a Gaussian and Crystal Ball functions
 3782 are considered as the functional form and used to re-estimate the background
 3783 distribution. The deviations compared to the nominal method are found to be
 3784 4%, and this is taken as a systematic uncertainty to cover the inability to care-
 3785 fully predict the contribution from the long tail of dE/dx where there are few
 3786 measurements available in data.

3787 12.1.2 MUON FRACTION

3788 The signal region for **VLL** R-Hadrons explicitly includes tracks identified as muons,
 3789 which have a known difference in their dE/dx distributions compared to non-
 3790 muon tracks (Section 11.1). To account for a difference in muon fraction be-
 3791 tween the background region and the signal region for this selection, the dE/dx
 3792 templates for muons and non-muons are measured separately and then the rel-
 3793 ative fraction of each is varied in the random generation. The muon fraction
 3794 is varied by its statistical uncertainty and the resulting difference of 3% in back-
 3795 ground yield is taken as the systematic uncertainty.

3796 12.1.3 **IBL** CORRECTIONS

3797 The **IBL**, described in Section 5.3.1, received a significant dose of radiation during
 3798 the data collection in 2015. The irradiation can cause a drift in the **ToT** calibra-
 3799 tion of the frontend electronics and thus alter the dE/dx measurement which
 3800 includes the **ToT** output by the **IBL**. These effects are corrected for in the nomi-
 3801 nal analysis by scaling the dE/dx measurements by a constant factor derived for
 3802 each run to match the average dE/dx value to a reference run. However, this
 3803 corrective factor does not account for inter-run variations. To account for the
 3804 potential drift of dE/dx within a single run, the correction procedure is repeated
 3805 by varying the corrections up and down by the maximal run-to-run variation
 3806 from the full data-taking period, which results in an uncertainty of 3.8%.

3807 12.1.4 NORMALIZATION

3808 As described in Section 11.2, the generated distribution of masses is normalized
 3809 in a shoulder region ($M < 160$ GeV) where signals have been excluded by pre-
 3810 vious analyses. That normalization factor is varied by its statistical uncertainty
 3811 and the resulting fluctuation in the mass distribution of 3% is taken as a system-
 3812 atic uncertainty on the background estimate.

3813 12.2 SIGNAL YIELD

3814 The systematic uncertainties on the signal yield can be divided into three cate-
 3815 gories; those on the simulation process, those on the modeling of the detector
 3816 efficiency or calibration, and those affecting the overall signal yield. They are
 3817 summarized in Table 11. The largest uncertainty comes from the uncertainty on
 3818 the production cross section for gluinos.

Source of Uncertainty	-[%]	+[%]
ISR Modeling (LL Region)	1.5	1.5
ISR Modeling (VLL Region)	14	14
Pile-up Reweighting	1.1	1.1
Trigger Efficiency Reweighting	0.9	0.9
E_T^{miss} Scale	1.1	2.2
Ionization Parametrization	7.1	0
μ Identification	4.3	4.3
Luminosity	5	5
Signal size uncertainty	28	28
Total (LL Region)	30	29
Total (VLL Region)	33	32

Table 12: A summary of the sources of systematic uncertainty for the simulated signal yield. The uncertainty depends on the mass and lifetime, and the maximum negative and positive values are reported in the table.

3819 12.2.1 ISR MODELING

3820 As discussed in Section 9.2, MadGraph is expected to reproduce the distribution
 3821 of ISR in signal events more accurately than the nominal Pythia samples [86].
 3822 The analysis reweights the distribution of ISR in the simulated signal events to
 3823 match the distribution found in generated MadGraph samples. This has an effect
 3824 on the selection efficiency in the signal samples, where ISR contributes to the
 3825 generation of E_T^{miss} . To account for the potential inaccuracy on the simulation
 3826 of ISR at high energies, half of the difference between the signal efficiency with
 3827 the reweighted distribution and the original distribution is taken as a systematic
 3828 uncertainty.

3829 12.2.2 PILEUP REWEIGHTING

3830 The simulated events were generated prior to data collection with an estimate of
 3831 the average number of interactions per bunch crossing. This estimate does not
 3832 match the value of pileup during actual data collection, but a large fraction of the

3833 simulated events would be discarded in order to match the distribution in data.
 3834 Therefore the simulated signal events are not reweighted for pileup by default
 3835 in the analysis. The effect of the pileup on signal efficiency is not expected to
 3836 depend on the mass or lifetime of the generated signal events, which allows all
 3837 of the generated signal events to be used together to assess the pileup dependence.
 3838 To account for the potential effect of the difference in the number of interactions
 3839 per bunch crossing between data and simulation, the difference in yield between
 3840 the nominal signal events and the reweighted events averaged over all masses
 3841 and lifetimes is taken as a systematic uncertainty on the yield for each mass and
 3842 lifetime (1.1%).

3843 12.2.3 TRIGGER EFFICIENCY REWEIGHTING

3844 As described in Section 10.2, the selection for this analysis does not require a suf-
 3845 ficiently large value of E_T^{miss} to be above the plateau of trigger efficiency. There-
 3846 fore, some signal events which would otherwise pass the event selection can be
 3847 excluded because of the trigger requirement. These effects can be difficult to es-
 3848 timate in simulation, and thus are constrained by comparing data and simulated
 3849 events in an alternative W boson region which uses decays to muons to find a rel-
 3850 atively pure sample of events with missing energy. The trigger efficiencies for
 3851 data and simulated W events are shown in Figure 90. The comparison between
 3852 data and MC in this region constrains the simulation of the trigger efficiency.
 3853 The simulated signal events are reweighted by the ratio of data to simulation in
 3854 the W boson decays, while the difference between the data and simulation in
 3855 those decays is taken as a systematic uncertainty. This results in an uncertainty
 3856 of only 0.9% as the majority of events are well above the plateau and the dis-
 3857 agreement between data and simulation is small even below that plateau.

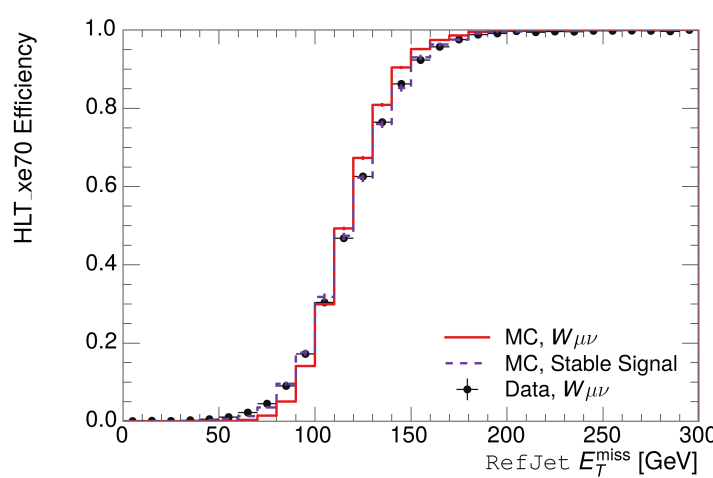


Figure 90: The trigger efficiency for the HLT_xe70 trigger requirement as a function of Calorimeter E_T^{miss} for simulated data events with a W boson selection. Simulated signal events and simulated W boson events are also included.

Systematic Variation	-[%]	+[%]
JET_GroupedNP_1	-0.7	1.3
JET_GroupedNP_2	-0.7	1.2
JET_GroupedNP_3	-0.5	1.3

Table 13: Example of the contributing systematic variations to the total systematic for the E_T^{miss} Scale, as measured in a 1200 GeV, VLL R-Hadron signal sample.

3858 12.2.4 MISSING TRANSVERSE MOMENTUM SCALE

3859 Variations on the JES enter into this analysis only in the requirement on E_T^{miss} ,
 3860 as variations on individual jets can alter the reconstructed E_T^{miss} in signal events.
 3861 The effect of the measured E_T^{miss} is evaluated by varying the E_T^{miss} scale according
 3862 to the one sigma variations on objects affecting event kinematics in simu-
 3863 lated signal events. Missing energy is reconstructed from fully reconstructed
 3864 objects so any systematic uncertainties affecting jets, muons, electrons, or the
 3865 E_T^{miss} soft terms are included. The variations on these objects are taken from
 3866 measurements in data using balance techniques as discussed in Section 6.4.3.
 3867 The resulting difference in selection efficiency is expected to be small, because
 3868 the jet variations only alter energies by a few percent. The only non-negligible
 3869 contributions found using this method are itemized in Table 13 for an example
 3870 signal sample (1200 GeV, VLL R-Hadron), where the systematic is measured as
 3871 the relative difference in the final signal efficiency after applying the associated
 3872 variation through the CP tools. The only variations that are significant are the
 3873 grouped jet systematic variations, which combine recommended jet systematic
 3874 uncertainties into linearly independent variations.

3875 As the peak of the reconstructed E_T^{miss} distribution in the signal is significantly
 3876 above the current threshold for events which pass the trigger requirement, the
 3877 effect of scale variation is expected to be small, which is consistent with the mea-
 3878 sured systematic error of approximately 2%. Events which do not pass the trigger
 3879 requirement usually fail because there are no ISR jets in the event to balance the
 3880 R -hadrons' transverse momentum, so the reconstructed E_T^{miss} is low and there-
 3881 fore also expected to be not very sensitive to scale changes.

3882 12.2.5 MOMENTUM PARAMETRIZATION

3883 The uncertainty on the signal efficiency from track momentum is calculated us-
 3884 ing the sagitta bias for q/P_{trk} , the only systematic variation of tracking that effects
 3885 track momentum. The systematic is only important for tracks that are near the
 3886 150 GeV momentum threshold, as the variation may push these tracks above
 3887 or below the selection requirement. Because the majority of R-Hadron tracks
 3888 are well above this value (Figure 80), the resulting uncertainty is expected to be
 3889 small. This uncertainty is propagated to the final selection efficiency by varying

3890 the track momentum by the measured one sigma variations from tracking mea-
 3891 surements [24], and the associated uncertainty is found to be negligible (0.3%).

3892 12.2.6 IONIZATION REQUIREMENT

3893 The dE/dx distributions in data and simulated events have different most prob-
 3894 able values, which is due in part to radiation effects in the detector that are not
 3895 fully accounted for in the simulation. The difference does not affect the mass
 3896 measurement used in this analysis, as independent calibrations are done in sim-
 3897 ulation and in data. However, it does affect the efficiency of the high dE/dx
 3898 selection requirement. To calculate the size of the effect on the signal efficiency,
 3899 the dE/dx distribution in signal simulation is scaled by a factor obtained from
 3900 comparing the dE/dx distribution of inclusive tracks in data and in simulation.
 3901 The difference in efficiency for this sample with a scaled dE/dx distribution, rel-
 3902 ative to the nominal case, is taken as a systematic uncertainty on signal efficiency.
 3903 The uncertainty is as large as 7% for low masses and falls to a negligible effect for
 3904 large masses.

3905 12.2.7 ELECTRON AND JET REJECTION

3906 The systematic uncertainty on the electron rejection is measured by varying the
 3907 EM fraction requirement significantly, from 0.95 to 0.9. This is found to have
 3908 a less than 0.04% effect on signal acceptance, on average, and so is completely
 3909 negligible. Similarly, the uncertainty on jet rejection is measured by tightening
 3910 the E/p requirement from 0.5 to 0.4. This is found to have no effect on signal
 3911 acceptance, so again the systematic is again negligible.

3912 12.2.8 MUON VETO

3913 The signal region for [LL](#) particles has a requirement that the candidate tracks are
 3914 not identified as medium muons because the majority of R-Hadrons in the life-
 3915 time range included in that region do not reach the muon spectrometers before
 3916 they decay. However, the exponential tail of the R-Hadron lifetime distribution
 3917 results in some R-Hadrons traversing the muon spectrometer. Even these R-
 3918 Hadrons can still fail the muon medium identification some of the time, because
 3919 they may arrive late to the muon spectrometer as discussed in Section 9.1.1. The
 3920 hits generated by a R-Hadron will not be readout if it arrives 25 ns after the
 3921 bunch crossing, causing it to fail the loose muon selection (Section 6.3.1). This
 3922 can be seen in Figure 91, which shows the efficiency of the muon veto as a func-
 3923 tion of $1/\beta$, for two simulated [VLL](#) R-Hadron samples.

3924 Thus, the efficiency of the muon veto depends on the timing resolution of
 3925 the spectrometer, so an uncertainty is applied to the signal efficiency to cover
 3926 differences in timing resolution between data and simulation. First, a sample of
 3927 $Z \rightarrow \mu\mu$ events is selected in data in which one of the muons has a late arrival
 3928 time measured in the [MDT](#). Then the reconstructed β distribution is compared
 3929 to the distribution in simulated $Z \rightarrow \mu\mu$ events; the difference between these

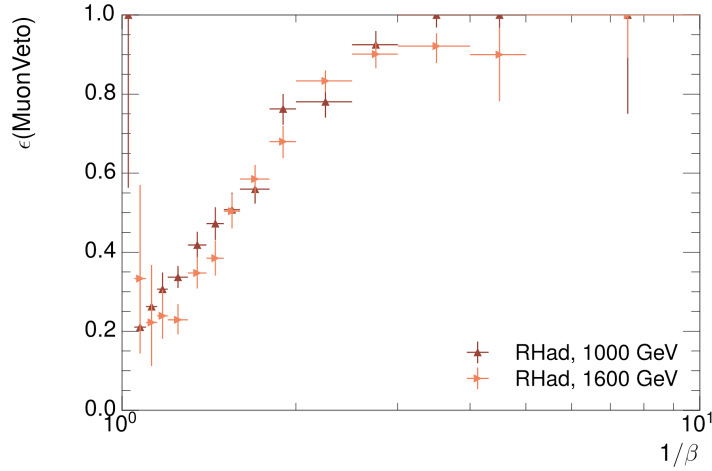


Figure 91: The efficiency of the muon veto for R -hadrons of two different masses, as a function of $\frac{1}{\beta}$ for simulated R-Hadron tracks.

3930 two distributions reflects the difference in timing resolution between data and
 3931 simulation. To emulate this difference in simulated signal events, the magnitude
 3932 of the difference is used to scale and shift the true β distribution of R-Hadrons in
 3933 simulation. Signal events are then reweighted based on this varied β distribution,
 3934 and the difference in the efficiency of the muon veto selection is compared with
 3935 the nominal and reweighted true β distributions. The difference in muon veto
 3936 efficiency is taken as a systematic uncertainty of the muon veto.

3937 The comparison of reconstructed β between data and simulation is performed
 3938 separately in the barrel, transition, and endcap regions of the spectrometer, and
 3939 the reweighting of the true β distribution in signal is done per region. The com-
 3940 parison of average reconstructed MDT β between data and simulation for the
 3941 barrel region is shown in Figure 92 for $Z \rightarrow \mu\mu$ events. As expected, The uncer-
 3942 tainty is found to be negligible for R -hadrons with short lifetimes, and is only
 3943 significant for lifetimes above 30 ns.

3944 12.2.9 LUMINOSITY

3945 The luminosity uncertainty is provided by a luminosity measurement on ATLAS
 3946 and was measured to be 5% at the time of the publication of this analysis. The
 3947 uncertainty is estimated by comparing luminosity measurements using several
 3948 independent luminometers [101].

3949 12.2.10 SIGNAL CROSS SECTION

3950 As discussed in Section 9.2, the signal cross sections are calculated at NLO in the
 3951 strong coupling constant with a resummation of soft-gluon emission at NLL. The
 3952 nominal predictions and the uncertainties for each mass point are taken from an
 3953 envelope of cross-section predictions using different PDF sets and factorization

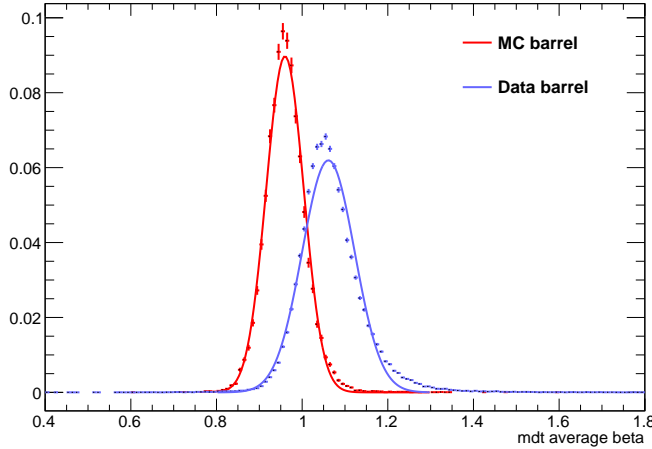


Figure 92: The average reconstructed MDT β distribution for $Z \rightarrow \mu\mu$ events in which one of the muons has a late arrival time in the MDT, for both data and simulation. A gaussian fit is superimposed.

3954 and renormalization scales [96], as discussed in Section 9.2. The uncertainties
 3955 on those cross sections range between 14% and 28% for R-Hadrons in the range
 3956 of 400 to 1800 GeV [97, 98]. The uncertainty increases with the mass.

3957

3958 RESULTS

3959 Sixteen events were observed in the **VLL** signal region and eleven events were
 3960 observed in the **LL** signal region, prior to requirements on the candidate track
 3961 mass. The background estimate predicts $17 \pm 2.6(\text{stat}) \pm 1.2(\text{syst})$ events for
 3962 the **VLL** region and $11.1 \pm 1.7(\text{stat}) \pm 0.7(\text{syst})$ events for the **LL** region. These
 3963 counts are summarized in Table 14.

3964 The mass estimated using dE/dx (Section 10.4.1) provides the final discrimi-
 3965 nating variable, where the signal would be expected as an excess in the falling ex-
 3966 ponential tail of the expected background. The observed distribution of masses
 3967 is shown in Figure 93, along with the predicted distribution from the background
 3968 estimate for each signal region. Both include a few example simulated signal dis-
 3969 tributions, which show the scale of an excess were the R-Hadron signals present.
 3970 Their is no statistically significant evidence of an excess in the data over the back-
 3971 ground estimation. From this distribution it is clearly possible to rule out signals
 3972 with lower masses, around 1200 GeV, which have larger cross sections.

3973 13.1 CROSS SECTION LIMITS

3974 Because there is no significant excess of events observed in the signal region, this
 3975 analysis sets upper limits on the allowed cross section for R-Hadron production.
 3976 These limits are set for each mass point by counting the observed events in data,
 3977 along with the expected background and simulated signal events, in windows of
 3978 mass. The mass windows are formed by fitting the distribution of signal events to
 3979 a Gaussian distribution, and the window is then $\pm 1.4\sigma$ around the center of that
 3980 Gaussian. Two examples of the windows formed by this procedure are shown in
 3981 Tables 15-16, for the **VLL** and 10 ns working points. The corresponding counts of
 3982 observed data, expected background, and simulated signal for those same work-
 3983 ing points are shown in Tables 17-18. Appendix A includes the mass windows
 3984 and counts for all of the considered signal points.

3985 The 95% confidence level upper limits on the cross sections for a large grid
 3986 of masses (between 800 and 1800 GeV) and lifetimes (between 0.4 and **VLL**) are

Selection Region	Expected Background	Data
VLL	$17.2 \pm 2.6 \pm 1.2$	16
LL	$11.1 \pm 1.7 \pm 0.7$	11

Table 14: The estimated number of background events and the number of observed events in data for the specified selection regions prior to the requirement on mass. The background estimates show statistical and systematic uncertainties.

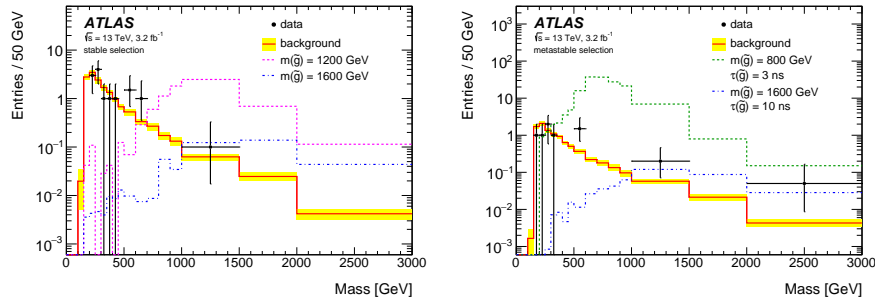


Figure 93: The observed mass distribution of events in data and the generated background distribution in (a) the **VLL** and (b) the **LL** signal region. A few example simulated signal distributions are superimposed.

$m(\tilde{g})$ [GeV]	Left Extremum [GeV]	Right Extremum [GeV]
1000	655	1349
1100	734	1455
1200	712	1631
1300	792	1737
1400	717	1926
1500	815	2117
1600	824	2122
1700	900	2274
1800	919	2344

Table 15: The left and right extremum of the mass window for each generated mass point with a 10 ns lifetime.

$m(\tilde{g})$ [GeV]	Left Extremum [GeV]	Right Extremum [GeV]
800	627	1053
1000	726	1277
1200	857	1584
1400	924	1937
1600	993	2308
1800	1004	2554

Table 16: The left and right extremum of the mass window used for each generated **VLL** mass point.

$m(\tilde{g})$ [GeV]	Expected Signal	Expected Background	Observed Data
800	462.83 ± 14.86	1.764 ± 0.080	2
1000	108.73 ± 3.38	1.458 ± 0.070	1
1200	31.74 ± 0.95	1.137 ± 0.060	1
1400	10.22 ± 0.29	1.058 ± 0.058	1
1600	3.07 ± 0.09	0.947 ± 0.054	1
1800	1.08 ± 0.05	0.940 ± 0.054	1

Table 17: The expected number of signal events, the expected number of background events, and the observed number of events in data with their respective statistical errors within the respective mass window for each generated `VLL` mass point

$m(\tilde{g})$ [GeV]	Expected Signal	Expected Background	Observed Data
1000	144.48 ± 5.14	1.499 ± 0.069	2
1100	73.19 ± 2.61	1.260 ± 0.060	2
1200	41.54 ± 1.41	1.456 ± 0.067	2
1300	22.58 ± 0.77	1.201 ± 0.058	2
1400	12.70 ± 0.42	1.558 ± 0.071	2
1500	6.73 ± 0.24	1.237 ± 0.060	2
1600	3.90 ± 0.13	1.201 ± 0.058	2
1700	2.27 ± 0.07	1.027 ± 0.052	2
1800	1.34 ± 0.04	1.019 ± 0.052	2

Table 18: The expected number of signal events, the expected number of background events, and the observed number of events in data with their respective statistical errors within the respective mass window for each generated mass point with a lifetime of 10 ns.

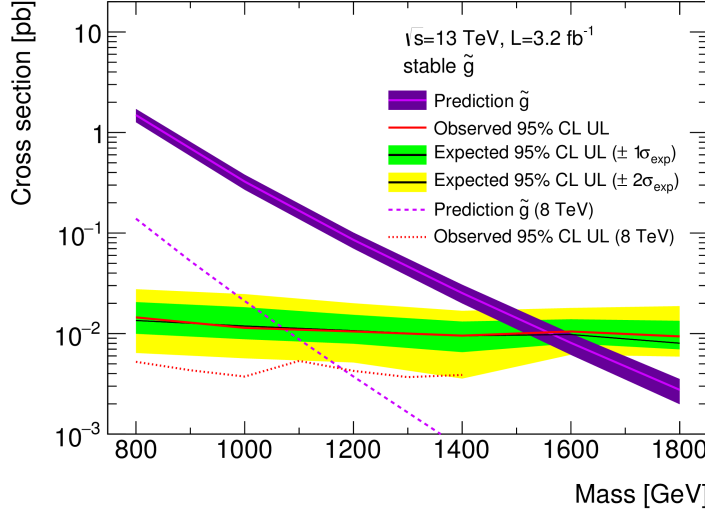


Figure 94: The observed and expected cross section limits as a function of mass for the [VLL](#) simulated signal. The predicted cross section values for the corresponding signals are also shown.

3987 extracted from these counts with the CL_S method using the profile likelihood
 3988 ratio as a test statistic [102]. For this procedure, the systematic uncertainties esti-
 3989 mated for the signal and background yields are treated as Gaussian-distributed
 3990 nuisance parameters. The uncertainty on the normalization of the expected
 3991 background distribution is included in the expected background events. At this
 3992 point the expected cross section limit is calculated for both the [LL](#) and [VLL](#) signal
 3993 region for each lifetime point, and the region with the best expected limit is se-
 3994 lected for each lifetime. Using that procedure, the [LL](#) region is used for lifetimes
 3995 up to and including 30 ns, and the [VLL](#) region for lifetimes above it.

3996 The resulting upper limits on the cross sections are shown as a function of
 3997 mass in Figure 94 and Figure 95 for each lifetime considered. The limits are
 3998 interpolated linearly between each mass point, and the dependence of the limit
 3999 on the mass is small as the efficiency is relatively constant for large R-Hadron
 4000 masses. There is however a strong dependence on lifetime, as discussed in Sec-
 4001 tion 10.5, where the probability to form a fully reconstructed track and the kine-
 4002 matic freedom to produce E_T^{miss} result in a local maximum in the limit at 10-30
 4003 ns. The figures also include the expected cross section for pair-produced gluino
 4004 R-Hadrons for reference. For the 10 ns and [VLL](#) cross section limits, both the
 4005 observed limit and expected cross section for the Run 1, 8 TeV version of this
 4006 analysis are also shown. There the cross section limits are lower because of the
 4007 larger available luminosity. The signal cross sections are also much lower be-
 4008 cause of the lower collision energy.

4009 13.2 MASS LIMITS

4010 The cross section limits can then be used to derive a lower mass limit for gluino
 4011 R-Hadrons by comparing them to the theoretically predicted production cross

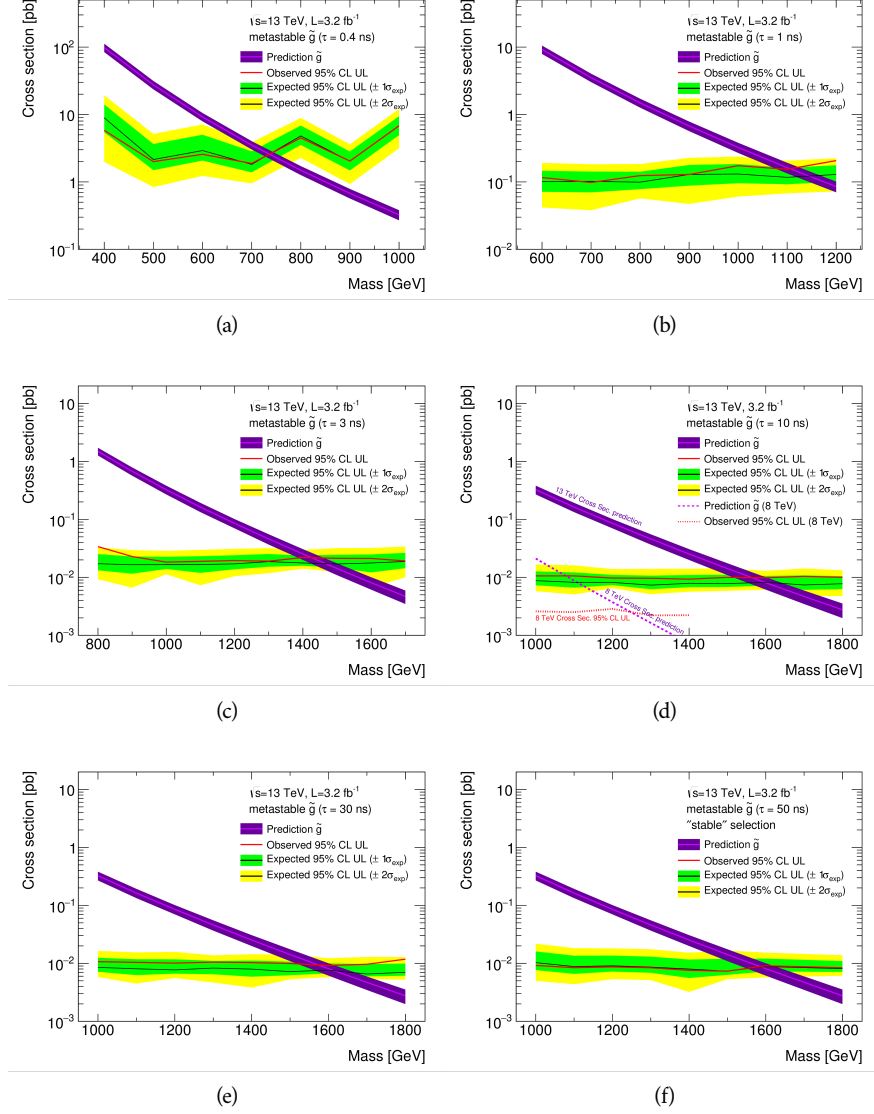


Figure 95: The observed and expected cross section limits as a function of mass for each generated lifetime. The predicted cross section values for the corresponding signals are also shown. An example of Run 1 cross section limits and predicted cross sections are shown in (d) for comparison.

sections. These mass limits range from only 740 GeV at the lowest lifetimes considered, where the selection efficiency is very low, to up to 1580 GeV at 30 ns where the selection efficiency is maximized. The observed and expected mass limits for each lifetime point are detailed in Table 19, which also lists which selection region was used for each lifetime. These excluded range of masses as a function of lifetime is also shown in Figure 96. The Run 1 limits are included for comparison; the limits have increased by about 200 GeV on average. The search has also improved since the previous incarnation from Run 1 in optimizing the region between 30 GeV and detector-stable lifetimes by introducing the second signal region. The definition of the VLL region prevents the significant drop in mass limit that occurred above 30 GeV in the Run 1 analysis.

Selection	τ [ns]	$M_{\text{obs}} > [\text{GeV}]$	$M_{\text{exp}} > [\text{GeV}]$
LL	0.4	740	730
"	1.0	1110	1150
"	3.0	1430	1470
"	10	1570	1600
"	30	1580	1620
VLL	50	1590	1590
"	VLL	1570	1580

Table 19: The observed and expected 95% CL lower limit on mass for gluino R-Hadrons for each considered lifetime.

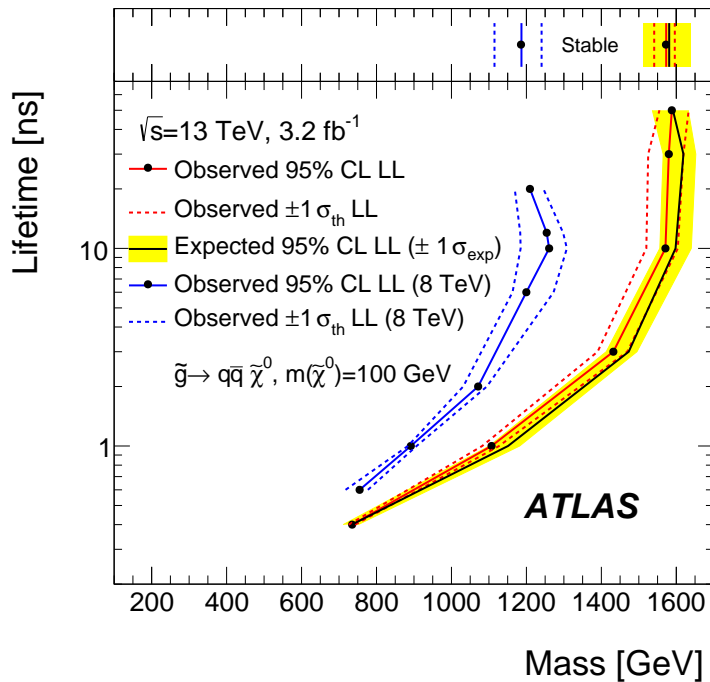


Figure 96: The excluded range of masses as a function of gluino lifetime. The expected lower limit (LL), with its experimental $\pm 1\sigma$ band, is given with respect to the nominal theoretical cross section. The observed 95% LL obtained at $\sqrt{s} = 8 \text{ TeV}$ [86] is also shown for comparison.

4023

4024 SUMMARY AND OUTLOOK

4025 The search described herein targetted the unique signature of TeV-scale, charged
4026 **LLPs**, which are predicted in a variety of extensions to the **SM** including some
4027 versions of **SUSY**. The dataset of 13 TeV proton-proton collisions was collected
4028 during 2015 by the ATLAS detector at the **LHC**, with an integrated luminosity
4029 of 3.2 fb^{-1} . The specific search strategy focused on identifying massive, charged
4030 particles which propagate through the Pixel detector in ATLAS by their characteristically large ionization.
4031 Recent updates to the strategy also include a number of rejection techniques that significantly reduce **SM** backgrounds compared
4032 to previous iterations. The analysis also provided a data-driven background estimation method that was shown to be effective with validation tests in both
4033 simulation and actual data.

4036 No significant excesses above the background prediction were found in the
4037 data, and so limits were placed on the production of massive, charged, **LLPs**. Using
4038 a benchmark model of simulated R-Hadrons, cross sections above 10-100
4039 fb were excluded at 95% confidence level, depending on the lifetime of the R-
4040 Hadron. Together with the predicted gluino pair-production cross sections, these
4041 lead to mass limits on R-Hadrons up to 1600 GeV where the search is most sensitive.
4042 Though these specific values assume an R-Hadron **LLP**, the search strategy accommodates a number of other species and the limits can be interpreted for
4043 other models.

4045 This search plays an important role in the current, combined ATLAS search
4046 for long lived particles. The mass limits provided by various ATLAS searches for
4047 long-lived gluino R-Hadrons can be seen in Figure 97. This search provides the
4048 most competitive limit for lifetimes between 3 ns up through very long lifetimes,
4049 where it is still competitive with dedicated searches for **VLL** particles. The limits
4050 placed on gluino production are very similar to the limits on promptly decaying
4051 models.

4052 These results are expected to be significantly improved in the following years,
4053 primarily because of continuing data collection at 13 TeV at the **LHC**. During
4054 2016, but after the release of this analysis, ATLAS recorded an additional 35.5
4055 fb^{-1} of collisions, and analysis of this data would significantly extend the limits
4056 presented here. The next iteration of the analysis can also provide additional
4057 interpretations of the search, by explicitly including other models like stop R-
4058 Hadrons and charginos in the limit calculations, as has been done in previous
4059 searches [86]. This strategy will continue to provide a competitive approach to
4060 discovering new **LLPs** throughout the lifetime of the **LHC**.

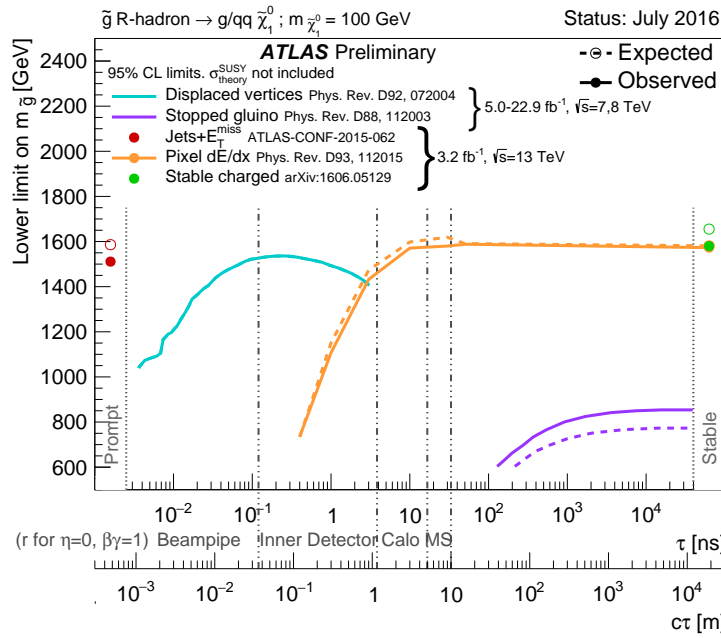


Figure 97: The constraints on the gluino mass as a function of lifetime for a split-supersymmetry model with the gluino R-Hadrons decaying into a gluon or light quarks and a neutralino with mass of 100 GeV. The solid lines indicate the observed limits, while the dashed lines indicate the expected limits. The area below the curves is excluded. The dots represent results for which the particle is assumed to be prompt or VLL. This curve representing this analysis is shown in orange.

4061

PART V

4062

APPENDIX

4063

$m(\tilde{g})$ [GeV]	Left Extremum [GeV]	Right Extremum [GeV]
1000	682	1387
1100	763	1478
1200	801	1606
1300	809	1841
1400	861	2011
1500	920	2032
1600	952	2173
1800	1017	2422

Table 20: The left and right extremum of the mass window for each generated mass point with a 50 ns lifetime.

$m(\tilde{g})$ [GeV]	Left Extremum [GeV]	Right Extremum [GeV]
1000	689	1321
1100	746	1513
1200	788	1670
1300	860	1734
1400	833	1925
1500	852	2048
1600	833	2283
1700	946	2379
1800	869	2505

Table 21: The left and right extremum of the mass window for each generated mass point with a 30 ns lifetime.

$m(\tilde{g})$ [GeV]	Left Extremum [GeV]	Right Extremum [GeV]
1000	655	1349
1100	734	1455
1200	712	1631
1300	792	1737
1400	717	1926
1500	815	2117
1600	824	2122
1700	900	2274
1800	919	2344

Table 22: The left and right extremum of the mass window for each generated mass point with a 10 ns lifetime.

$m(\tilde{g})$ [GeV]	Left Extremum [GeV]	Right Extremum [GeV]
800	531	1065
900	576	1165
1000	610	1345
1100	635	1432
1200	663	1563
1300	620	1667
1400	742	1727
1500	761	1937
1600	573	2000
1700	621	2182

Table 23: The left and right extremum of the mass window used for each generated mass point with a lifetime of 3 ns.

$m(\tilde{g})$ [GeV]	Left Extremum [GeV]	Right Extremum [GeV]
600	411	758
700	385	876
800	486	970
900	406	987
1000	408	1136
1100	555	1196
1200	516	1378

Table 24: The left and right extremum of the mass window used for each mass point with a lifetime of 1 ns.

$m(\tilde{g})$ [GeV]	Left Extremum [GeV]	Right Extremum [GeV]
400	204	510
500	295	639
600	288	702
700	323	701
800	190	771
900	277	677
1000	249	688

Table 25: The left and right extremum of the mass window for each generated mass point with a lifetime of 0.4 ns.

$m(\tilde{g})$ [GeV]	Left Extremum [GeV]	Right Extremum [GeV]
800	627	1053
1000	726	1277
1200	857	1584
1400	924	1937
1600	993	2308
1800	1004	2554

Table 26: The left and right extremum of the mass window used for each generated stable mass point.

$m(\tilde{g})$ [GeV]	Expected Signal	Expected Background	Observed Data
1000	131.18 ± 6.35	1.803 ± 0.081	1.0 ± 1.0
1100	71.11 ± 3.35	1.409 ± 0.069	1.0 ± 1.0
1200	37.18 ± 1.75	1.310 ± 0.066	1.0 ± 1.0
1300	20.76 ± 0.95	1.431 ± 0.069	1.0 ± 1.0
1400	12.63 ± 0.57	1.273 ± 0.065	1.0 ± 1.0
1500	6.57 ± 0.29	1.115 ± 0.059	1.0 ± 1.0
1600	3.56 ± 0.16	1.041 ± 0.057	1.0 ± 1.0
1800	1.27 ± 0.05	0.918 ± 0.053	1.0 ± 1.0

Table 27: The expected number of signal events, the expected number of background events, and the observed number of events in data with their respective statistical errors within the respective mass window for each generated mass point with a lifetime of 50 ns.

$m(\tilde{g})$ [GeV]	Expected Signal	Expected Background	Observed Data
1000	144.65 ± 6.34	1.328 ± 0.063	2.0 ± 1.4
1100	75.28 ± 3.27	1.255 ± 0.060	2.0 ± 1.4
1200	40.51 ± 1.75	1.193 ± 0.058	2.0 ± 1.4
1300	20.91 ± 0.93	0.997 ± 0.051	2.0 ± 1.4
1400	11.97 ± 0.51	1.131 ± 0.056	2.0 ± 1.4
1500	6.81 ± 0.28	1.111 ± 0.055	2.0 ± 1.4
1600	4.19 ± 0.16	1.193 ± 0.058	2.0 ± 1.4
1700	2.42 ± 0.09	0.963 ± 0.050	2.0 ± 1.4
1800	1.46 ± 0.05	1.138 ± 0.056	3.0 ± 1.7

Table 28: The expected number of signal events, the expected number of background events, and the observed number of events in data with their respective statistical errors within the respective mass window for each generated mass point with a lifetime of 30 ns.

$m(\tilde{g})$ [GeV]	Expected Signal	Expected Background	Observed Data
1000	144.48 ± 5.14	1.499 ± 0.069	2.0 ± 1.4
1100	73.19 ± 2.61	1.260 ± 0.060	2.0 ± 1.4
1200	41.54 ± 1.41	1.456 ± 0.067	2.0 ± 1.4
1300	22.58 ± 0.77	1.201 ± 0.058	2.0 ± 1.4
1400	12.70 ± 0.42	1.558 ± 0.071	2.0 ± 1.4
1500	6.73 ± 0.24	1.237 ± 0.060	2.0 ± 1.4
1600	3.90 ± 0.13	1.201 ± 0.058	2.0 ± 1.4
1700	2.27 ± 0.07	1.027 ± 0.052	2.0 ± 1.4
1800	1.34 ± 0.04	1.019 ± 0.052	2.0 ± 1.4

Table 29: The expected number of signal events, the expected number of background events, and the observed number of events in data with their respective statistical errors within the respective mass window for each generated mass point with a lifetime of 10 ns.

$m(\tilde{g})$ [GeV]	Expected Signal	Expected Background	Observed Data
800	362.97 ± 14.68	1.841 ± 0.080	5.0 ± 2.2
900	169.20 ± 6.69	1.710 ± 0.076	3.0 ± 1.7
1000	84.78 ± 3.23	1.727 ± 0.076	2.0 ± 1.4
1100	40.06 ± 1.60	1.679 ± 0.075	2.0 ± 1.4
1200	20.06 ± 0.81	1.598 ± 0.072	2.0 ± 1.4
1300	10.76 ± 0.43	1.851 ± 0.080	2.0 ± 1.4
1400	5.52 ± 0.22	1.374 ± 0.064	2.0 ± 1.4
1500	3.16 ± 0.13	1.355 ± 0.064	2.0 ± 1.4
1600	2.13 ± 0.11	2.235 ± 0.093	3.0 ± 1.7
1700	1.10 ± 0.06	1.995 ± 0.085	2.0 ± 1.4

Table 30: The expected number of signal events, the expected number of background events, and the observed number of events in data with their respective statistical errors within the respective mass window for each generated mass point with a lifetime of 3 ns.

$m(\tilde{g})$ [GeV]	Expected Signal	Expected Background	Observed Data
600	431.80 ± 36.60	2.418 ± 0.099	3.0 ± 1.7
700	192.77 ± 15.28	3.267 ± 0.126	3.0 ± 1.7
800	69.63 ± 5.90	2.125 ± 0.089	3.0 ± 1.7
900	28.91 ± 2.59	3.114 ± 0.121	3.0 ± 1.7
1000	13.64 ± 1.22	3.359 ± 0.129	5.0 ± 2.2
1100	6.13 ± 0.57	1.879 ± 0.081	3.0 ± 1.7
1200	3.24 ± 0.30	2.387 ± 0.098	5.0 ± 2.2

Table 31: The expected number of signal events, the expected number of background events, and the observed number of events in data with their respective statistical errors within the respective mass window for each generated mass point with a lifetime of 1 ns.

$m(\tilde{g})$ [GeV]	Expected Signal	Expected Background	Observed Data
400	181.71 ± 75.59	6.780 ± 0.238	4.0 ± 2.0
500	103.88 ± 30.05	4.310 ± 0.160	4.0 ± 2.0
600	28.34 ± 9.34	4.868 ± 0.177	4.0 ± 2.0
700	13.62 ± 4.00	3.908 ± 0.147	4.0 ± 2.0
800	2.75 ± 1.15	9.001 ± 0.308	8.0 ± 2.8
900	2.25 ± 0.71	5.045 ± 0.183	5.0 ± 2.2
1000	0.34 ± 0.19	6.026 ± 0.214	6.0 ± 2.4

Table 32: The expected number of signal events, the expected number of background events, and the observed number of events in data with their respective statistical errors within the respective mass window for each generated mass point with a lifetime of p4 ns.

$m(\tilde{g})$ [GeV]	Expected Signal	Expected Background	Observed Data
800	462.83 ± 14.86	1.764 ± 0.080	2.0 ± 1.4
1000	108.73 ± 3.38	1.458 ± 0.070	1.0 ± 1.0
1200	31.74 ± 0.95	1.137 ± 0.060	1.0 ± 1.0
1400	10.22 ± 0.29	1.058 ± 0.058	1.0 ± 1.0
1600	3.07 ± 0.09	0.947 ± 0.054	1.0 ± 1.0
1800	1.08 ± 0.05	0.940 ± 0.054	1.0 ± 1.0

Table 33: The expected number of signal events, the expected number of background events, and the observed number of events in data with their respective statistical errors within the respective mass window for each generated stable mass point

- 4067 [1] Nobelprize.org. "The 2004 Nobel Prize in Physics - Popular Information". 2014. URL: <https://cds.cern.ch/record/1165534>.
- 4068
- 4069 [2] K. A. Olive et al. "Review of Particle Physics". In: *Chin. Phys. C* 38 (2014),
4070 p. 090001. doi: [10.1088/1674-1137/38/9/090001](https://doi.org/10.1088/1674-1137/38/9/090001).
- 4071 [3] A. D. Martin, W. J. Stirling, R. S. Thorne, and G. Watt. "Parton distributions for the LHC". In: *Eur. Phys. J. C* 63 (2009), pp. 189–285. doi: [10.1140/epjc/s10052-009-1072-5](https://doi.org/10.1140/epjc/s10052-009-1072-5). arXiv: [0901.0002 \[hep-ph\]](https://arxiv.org/abs/0901.0002).
- 4072
- 4073
- 4074 [4] Torbjorn Sjöstrand, Stephen Mrenna, and Peter Skands. "PYTHIA 6.4 Physics and Manual". In: *JHEP* 0605 (2006), p. 026. doi: [10.1088/1126-6708/2006/05/026](https://doi.org/10.1088/1126-6708/2006/05/026). arXiv: [hep-ph/0603175](https://arxiv.org/abs/hep-ph/0603175).
- 4075
- 4076
- 4077 [5] J. Alwall, R. Frederix, S. Frixione, V. Hirschi, F. Maltoni, O. Mattelaer, H.
4078 S. Shao, T. Stelzer, P. Torrielli, and M. Zaro. "The automated computation
4079 of tree-level and next-to-leading order differential cross sections, and
4080 their matching to parton shower simulations". In: *JHEP* 07 (2014), p. 079.
4081 doi: [10.1007/JHEP07\(2014\)079](https://doi.org/10.1007/JHEP07(2014)079). arXiv: [1405.0301 \[hep-ph\]](https://arxiv.org/abs/1405.0301).
- 4082
- 4083 [6] S. Agostinelli et al. "GEANT4: A simulation toolkit". In: *Nucl. Instrum.*
4084 *Meth. A* 506 (2003), pp. 250–303. doi: [10.1016/S0168-9002\(03\)01368-8](https://doi.org/10.1016/S0168-9002(03)01368-8).
- 4085
- 4086 [7] Prajwal Raj Kafle, Sanjib Sharma, Geraint F. Lewis, and Joss Bland-Hawthorn.
4087 "On the Shoulders of Giants: Properties of the Stellar Halo and the Milky
4088 Way Mass Distribution". In: *Astrophys. J.* 794.1 (2014), p. 59. doi: [10.1088/0004-637X/794/1/59](https://doi.org/10.1088/0004-637X/794/1/59). arXiv: [1408.1787 \[astro-ph.GA\]](https://arxiv.org/abs/1408.1787).
- 4089
- 4090 [8] Savas Dimopoulos and Howard Georgi. "Softly broken supersymmetry
4091 and SU(5)". In: *Nuclear Physics B* 193.1 (1981), pp. 150 –162. ISSN: 0550-
4092 3213. doi: [http://dx.doi.org/10.1016/0550-3213\(81\)90522-8](http://dx.doi.org/10.1016/0550-3213(81)90522-8).
- 4093
- 4094 [9] A. Djouadi et al. "The Minimal supersymmetric standard model: Group
4095 summary report". In: *GDR (Groupement De Recherche) - Supersymetrie Mont-*
4096 *pellier, France, April 15-17, 1998*. 1998. arXiv: [hep-ph/9901246 \[hep-ph\]](https://arxiv.org/abs/hep-ph/9901246).
4097 URL: https://inspirehep.net/record/481987/files/arXiv-hep-ph_9901246.pdf.
- 4098
- 4099 [10] Lawrence J. Hall, Yasunori Nomura, and Satoshi Shirai. "Spread Super-
- 4100 symmetry with Wino LSP: Gluino and Dark Matter Signals". In: *JHEP* 01
4101 (2013), p. 036. doi: [10.1007/JHEP01\(2013\)036](https://doi.org/10.1007/JHEP01(2013)036). arXiv: [1210.2395 \[hep-ph\]](https://arxiv.org/abs/1210.2395).
- 4102
- 4103 [11] G. F. Giudice and A. Romanino. "Split supersymmetry". In: *Nucl. Phys. B*
4104 699 (2004), p. 65. doi: [10.1016/j.nuclphysb.2004.11.048](https://doi.org/10.1016/j.nuclphysb.2004.11.048). arXiv:
[hep-ph/0406088](https://arxiv.org/abs/hep-ph/0406088).

- 4105 [12] N. Arkani-Hamed, S. Dimopoulos, G. F. Giudice, and A. Romanino. “Aspects of split supersymmetry”. In: *Nucl. Phys. B* 709 (2005), p. 3. doi: [10.1016/j.nuclphysb.2004.12.026](https://doi.org/10.1016/j.nuclphysb.2004.12.026). arXiv: [hep-ph/0409232](https://arxiv.org/abs/hep-ph/0409232).
- 4106
- 4107
- 4108 [13] Lyndon Evans and Philip Bryant. “LHC Machine”. In: *JINST* 3 (2008), S08001. doi: [10.1088/1748-0221/3/08/S08001](https://doi.org/10.1088/1748-0221/3/08/S08001).
- 4109
- 4110 [14] C Lefevre. “LHC: the guide (English version). Guide du LHC (version anglaise)”. 2009. URL: <https://cds.cern.ch/record/1165534>.
- 4111
- 4112 [15] “LEP Design Report Vol.1”. In: (1983).
- 4113 [16] ATLAS Collaboration. “The ATLAS Experiment at the CERN Large Hadron Collider”. In: *JINST* 3 (2008), S08003. doi: [10.1088/1748-0221/3/08/S08003](https://doi.org/10.1088/1748-0221/3/08/S08003).
- 4114
- 4115
- 4116 [17] S. Chatrchyan et al. “The CMS experiment at the CERN LHC”. In: *JINST* 3 (2008), S08004. doi: [10.1088/1748-0221/3/08/S08004](https://doi.org/10.1088/1748-0221/3/08/S08004).
- 4117
- 4118 [18] A. Augusto Alves Jr. et al. “The LHCb Detector at the LHC”. In: *JINST* 3 (2008), S08005. doi: [10.1088/1748-0221/3/08/S08005](https://doi.org/10.1088/1748-0221/3/08/S08005).
- 4119
- 4120 [19] K. Aamodt et al. “The ALICE experiment at the CERN LHC”. In: *JINST* 3 (2008), S08002. doi: [10.1088/1748-0221/3/08/S08002](https://doi.org/10.1088/1748-0221/3/08/S08002).
- 4121
- 4122 [20] M Capeans, G Darbo, K Einsweiller, M Elsing, T Flick, M Garcia-Sciveres, C Gemme, H Pernegger, O Rohne, and R Vuillermet. *ATLAS Insertable B-Layer Technical Design Report*. Tech. rep. CERN-LHCC-2010-013. ATLAS-TDR-19. 2010. URL: <https://cds.cern.ch/record/1291633>.
- 4123
- 4124
- 4125
- 4126 [21] T. Cornelissen, M. Elsing, S. Fleischmann, W. Liebig, and E. Moyse. “Concepts, Design and Implementation of the ATLAS New Tracking (NEWT)”. In: (2007). Ed. by A. Salzburger.
- 4127
- 4128
- 4129 [22] “Performance of the ATLAS Inner Detector Track and Vertex Reconstruction in the High Pile-Up LHC Environment”. In: (2012).
- 4130
- 4131 [23] A. Salzburger. “The ATLAS Track Extrapolation Package”. In: (2007).
- 4132
- 4133 [24] ATLAS Collaboration. *Early Inner Detector Tracking Performance in the 2015 Data at $\sqrt{s} = 13$ TeV*. ATL-PHYS-PUB-2015-051. 2015. URL: <https://cds.cern.ch/record/2110140>.
- 4134
- 4135 [25] ATLAS Collaboration. “A neural network clustering algorithm for the ATLAS silicon pixel detector”. In: *JINST* 9 (2014), P09009. doi: [10.1088/1748-0221/9/09/P09009](https://doi.org/10.1088/1748-0221/9/09/P09009). arXiv: [1406.7690 \[hep-ex\]](https://arxiv.org/abs/1406.7690).
- 4136
- 4137
- 4138 [26] ATLAS Collaboration. *Performance of primary vertex reconstruction in proton-proton collisions at $\sqrt{s} = 7$ TeV in the ATLAS experiment*. ATLAS-CONF-2010-069. 2010. URL: <https://cds.cern.ch/record/1281344>.
- 4139
- 4140
- 4141 [27] ATLAS Collaboration. *Vertex Reconstruction Performance of the ATLAS Detector at $\sqrt{s} = 13$ TeV*. ATL-PHYS-PUB-2015-026. 2015. URL: <https://cds.cern.ch/record/2037717>.
- 4142
- 4143

- 4144 [28] ATLAS Collaboration. “Electron reconstruction and identification effi-
 4145 ciency measurements with the ATLAS detector using the 2011 LHC proton-
 4146 proton collision data”. In: *Eur. Phys. J. C* 74 (2014), p. 2941. doi: [10.1140/epjc/s10052-014-2941-0](https://doi.org/10.1140/epjc/s10052-014-2941-0). arXiv: [1404.2240](https://arxiv.org/abs/1404.2240) [hep-ex].
 4147
 4148 PERF-2013-03.
- 4149 [29] ATLAS Collaboration. *Electron efficiency measurements with the ATLAS*
 4150 *detector using the 2012 LHC proton–proton collision data*. ATLAS-CONF-
 4151 2014-032. 2014. URL: <https://cds.cern.ch/record/1706245>.
- 4152 [30] ATLAS Collaboration. *Measurements of the photon identification efficiency*
 4153 *with the ATLAS detector using 4.9 fb^{-1} of pp collision data collected in 2011*.
 4154 ATLAS-CONF-2012-123. 2012. URL: <https://cds.cern.ch/record/1473426>.
- 4155
 4156 [31] ATLAS Collaboration. “Muon reconstruction performance of the AT-
 4157 LAS detector in proton–proton collision data at $\sqrt{s} = 13 \text{ TeV}$ ”. In: (2016).
 4158 arXiv: [1603.05598](https://arxiv.org/abs/1603.05598) [hep-ex]. PERF-2015-10.
- 4159 [32] ATLAS Collaboration. “Topological cell clustering in the ATLAS calorime-
 4160 ters and its performance in LHC Run 1”. In: (2016). arXiv: [1603.02934](https://arxiv.org/abs/1603.02934)
 4161 [hep-ex]. PERF-2014-07.
- 4162 [33] ATLAS Collaboration. *Properties of jets and inputs to jet reconstruction and*
 4163 *calibration with the ATLAS detector using proton–proton collisions at $\sqrt{s} =$*
 4164 *13 TeV* . ATL-PHYS-PUB-2015-036. 2015. URL: <https://cds.cern.ch/record/2044564>.
- 4165
 4166 [34] Matteo Cacciari, Gavin P. Salam, and Gregory Soyez. “The anti- k_t jet
 4167 clustering algorithm”. In: *JHEP* 04 (2008), p. 063. doi: [10.1088/1126-6708/2008/04/063](https://doi.org/10.1088/1126-6708/2008/04/063). arXiv: [0802.1189](https://arxiv.org/abs/0802.1189) [hep-ph].
- 4168
 4169 [35] ATLAS Collaboration. *Jet global sequential corrections with the ATLAS de-*
 4170 *tector in proton–proton collisions at $\sqrt{s} = 8 \text{ TeV}$* . ATLAS-CONF-2015-002.
 4171 2015. URL: <https://cds.cern.ch/record/2001682>.
- 4172 [36] ATLAS Collaboration. “A study of the material in the ATLAS inner detec-
 4173 tor using secondary hadronic interactions”. In: *JINST* 7 (2012), P01013.
 4174 doi: [10.1088/1748-0221/7/01/P01013](https://doi.org/10.1088/1748-0221/7/01/P01013). arXiv: [1110.6191](https://arxiv.org/abs/1110.6191)
 4175 [hep-ex]. PERF-2011-08.
- 4176 [37] ATLAS Collaboration. “Electron and photon energy calibration with the
 4177 ATLAS detector using LHC Run 1 data”. In: *Eur. Phys. J. C* 74 (2014),
 4178 p. 3071. doi: [10.1140/epjc/s10052-014-3071-4](https://doi.org/10.1140/epjc/s10052-014-3071-4). arXiv: [1407.5063](https://arxiv.org/abs/1407.5063) [hep-ex].
 4179 PERF-2013-05.
- 4180 [38] ATLAS Collaboration. “A measurement of the calorimeter response to
 4181 single hadrons and determination of the jet energy scale uncertainty us-
 4182 ing LHC Run-1 pp -collision data with the ATLAS detector”. In: (2016).
 4183 arXiv: [1607.08842](https://arxiv.org/abs/1607.08842) [hep-ex]. PERF-2015-05.
- 4184 [39] ATLAS Collaboration. “Single hadron response measurement and calorime-
 4185 ter jet energy scale uncertainty with the ATLAS detector at the LHC”. In:
 4186 *Eur. Phys. J. C* 73 (2013), p. 2305. doi: [10.1140/epjc/s10052-013-2305-1](https://doi.org/10.1140/epjc/s10052-013-2305-1). arXiv: [1203.1302](https://arxiv.org/abs/1203.1302) [hep-ex].
 4187 PERF-2011-05.

- 4188 [40] ATLAS Collaboration. “The ATLAS Simulation Infrastructure”. In: *Eur.*
 4189 *Phys. J. C* 70 (2010), p. 823. doi: [10.1140/epjc/s10052-010-1429-9](https://doi.org/10.1140/epjc/s10052-010-1429-9). arXiv: [1005.4568 \[hep-ex\]](https://arxiv.org/abs/1005.4568). SOFT-2010-01.
- 4191 [41] T. Sjöstrand, S. Mrenna, and P. Skands. “A Brief Introduction to PYTHIA
 4192 8.1”. In: *Comput. Phys. Commun.* 178 (2008), pp. 852–867. doi: [10.1016/j.cpc.2008.01.036](https://doi.org/10.1016/j.cpc.2008.01.036). arXiv: [0710.3820](https://arxiv.org/abs/0710.3820).
- 4194 [42] ATLAS Collaboration. *Summary of ATLAS Pythia 8 tunes*. ATL-PHYS-PUB-
 4195 2012-003. 2012. url: <http://cds.cern.ch/record/1474107>.
- 4196 [43] A.D. Martin, W.J. Stirling, R.S. Thorne, and G. Watt. “Parton distribu-
 4197 tions for the LHC”. In: *Eur. Phys. J. C* 63 (2009). Figures from the [MSTW](#)
 4198 [Website](#), pp. 189–285. doi: [10.1140/epjc/s10052-009-1072-5](https://doi.org/10.1140/epjc/s10052-009-1072-5).
 4199 arXiv: [0901.0002](https://arxiv.org/abs/0901.0002).
- 4200 [44] A. Sherstnev and R.S. Thorne. “Parton Distributions for LO Generators”.
 4201 In: *Eur. Phys. J. C* 55 (2008), pp. 553–575. doi: [10.1140/epjc/s10052-008-0610-x](https://doi.org/10.1140/epjc/s10052-008-0610-x). arXiv: [0711.2473](https://arxiv.org/abs/0711.2473).
- 4203 [45] A. Ribon et al. *Status of Geant4 hadronic physics for the simulation of LHC*
 4204 *experiments at the start of LHC physics program*. CERN-LCGAPP-2010-02.
 4205 2010. url: <http://lcgapp.cern.ch/project/docs/noteStatusHadronic2010.pdf>.
- 4207 [46] M. P. Guthrie, R. G. Alsmiller, and H. W. Bertini. “Calculation of the
 4208 capture of negative pions in light elements and comparison with exper-
 4209 iments pertaining to cancer radiotherapy”. In: *Nucl. Instrum. Meth.* 66
 4210 (1968), pp. 29–36. doi: [10.1016/0029-554X\(68\)90054-2](https://doi.org/10.1016/0029-554X(68)90054-2).
- 4211 [47] H. W. Bertini and P. Guthrie. “News item results from medium-energy
 4212 intranuclear-cascade calculation”. In: *Nucl. Instr. and Meth. A* 169 (1971),
 4213 p. 670. doi: [10.1016/0375-9474\(71\)90710-X](https://doi.org/10.1016/0375-9474(71)90710-X).
- 4214 [48] V.A. Karmanov. “Light Front Wave Function of Relativistic Composite
 4215 System in Explicitly Solvable Model”. In: *Nucl. Phys. B* 166 (1980), p. 378.
 4216 doi: [10.1016/0550-3213\(80\)90204-7](https://doi.org/10.1016/0550-3213(80)90204-7).
- 4217 [49] H. S. Fesefeldt. *GHEISHA program*. Pitha-85-02, Aachen. 1985.
- 4218 [50] G. Folger and J.P. Wellisch. “String parton models in Geant4”. In: (2003).
 4219 arXiv: [nucl-th/0306007](https://arxiv.org/abs/nucl-th/0306007).
- 4220 [51] N. S. Amelin et al. “Transverse flow and collectivity in ultrarelativistic
 4221 heavy-ion collisions”. In: *Phys. Rev. Lett.* 67 (1991), p. 1523. doi: [10.1103/PhysRevLett.67.1523](https://doi.org/10.1103/PhysRevLett.67.1523).
- 4223 [52] N. S. Amelin et al. “Collectivity in ultrarelativistic heavy ion collisions”.
 4224 In: *Nucl. Phys. A* 544 (1992), p. 463. doi: [10.1016/0375-9474\(92\)90598-E](https://doi.org/10.1016/0375-9474(92)90598-E).
- 4226 [53] L. V. Bravina et al. “Fluid dynamics and Quark Gluon string model - What
 4227 we can expect for Au+Au collisions at 11.6 AGeV/c”. In: *Nucl. Phys. A* 566
 4228 (1994), p. 461. doi: [10.1016/0375-9474\(94\)90669-6](https://doi.org/10.1016/0375-9474(94)90669-6).

- 4229 [54] L. V. Bravin et al. “Scaling violation of transverse flow in heavy ion colli-
 4230 sions at AGS energies”. In: *Phys. Lett. B* 344 (1995), p. 49. doi: [10.1016/0370-2693\(94\)01560-Y](https://doi.org/10.1016/0370-2693(94)01560-Y).
- 4232 [55] B. Andersson et al. “A model for low-pT hadronic reactions with gen-
 4233 eralizations to hadron-nucleus and nucleus-nucleus collisions”. In: *Nucl.*
 4234 *Phys. B* 281 (1987), p. 289. doi: [10.1016/0550-3213\(87\)90257-4](https://doi.org/10.1016/0550-3213(87)90257-4).
- 4235 [56] B. Andersson, A. Tai, and B.-H. Sa. “Final state interactions in the (nu-
 4236 clear) FRITIOF string interaction scenario”. In: *Z. Phys. C* 70 (1996), pp. 499–
 4237 506. doi: [10.1007/s002880050127](https://doi.org/10.1007/s002880050127).
- 4238 [57] B. Nilsson-Almqvist and E. Stenlund. “Interactions Between Hadrons
 4239 and Nuclei: The Lund Monte Carlo, Fritiof Version 1.6”. In: *Comput. Phys.*
 4240 *Commun.* 43 (1987), p. 387. doi: [10.1016/0010-4655\(87\)90056-7](https://doi.org/10.1016/0010-4655(87)90056-7).
- 4241 [58] B. Ganhuyag and V. Uzhinsky. “Modified FRITIOF code: Negative charged
 4242 particle production in high energy nucleus nucleus interactions”. In: *Czech.*
 4243 *J. Phys.* 47 (1997), pp. 913–918. doi: [10.1023/A:1021296114786](https://doi.org/10.1023/A:1021296114786).
- 4244 [59] ATLAS Collaboration. “Topological cell clustering in the ATLAS calorime-
 4245 ters and its performance in LHC Run 1”. In: (2016). arXiv: [1603.02934](https://arxiv.org/abs/1603.02934)
 4246 [[hep-ex](#)].
- 4247 [60] Peter Speckmayer. “Energy Measurement of Hadrons with the CERN
 4248 ATLAS Calorimeter”. Presented on 18 Jun 2008. PhD thesis. Vienna: Vi-
 4249 enna, Tech. U., 2008. URL: <http://cds.cern.ch/record/1112036>.
- 4250 [61] CMS Collaboration. “The CMS barrel calorimeter response to particle
 4251 beams from 2 to 350 GeV/c”. In: *Eur. Phys. J. C* 60.3 (2009). doi: [10.1140/epjc/s10052-009-0959-5](https://doi.org/10.1140/epjc/s10052-009-0959-5).
- 4252 [62] J. Beringer et al. (Particle Data Group). “Review of Particle Physics”. In:
 4254 *Chin. Phys. C* 38 (2014), p. 090001. URL: <http://pdg.lbl.gov>.
- 4255 [63] P. Adragna et al. “Measurement of Pion and Proton Response and Lon-
 4256 gitudinal Shower Profiles up to 20 Nuclear Interaction Lengths with the
 4257 ATLAS Tile Calorimeter”. In: *Nucl. Instrum. Meth. A* 615 (2010), pp. 158–
 4258 181. doi: [10.1016/j.nima.2010.01.037](https://doi.org/10.1016/j.nima.2010.01.037).
- 4259 [64] ATLAS Collaboration. “Jet energy measurement and its systematic un-
 4260 certainty in proton–proton collisions at $\sqrt{s} = 7$ TeV with the ATLAS de-
 4261 tector”. In: *Eur. Phys. J. C* 75 (2015), p. 17. doi: [10.1140/epjc/s10052-014-3190-y](https://doi.org/10.1140/epjc/s10052-014-3190-y). arXiv: [1406.0076](https://arxiv.org/abs/1406.0076) [[hep-ex](#)]. PERF-2012-01.
- 4263 [65] Hung-Liang Lai, Marco Guzzi, Joey Huston, Zhao Li, Pavel M. Nadolsky,
 4264 et al. “New parton distributions for collider physics”. In: *Phys. Rev. D* 82
 4265 (2010), p. 074024. doi: [10.1103/PhysRevD.82.074024](https://doi.org/10.1103/PhysRevD.82.074024). arXiv: [1007.2241](https://arxiv.org/abs/1007.2241) [[hep-ph](#)].
- 4267 [66] E. Abat et al. “Study of energy response and resolution of the ATLAS
 4268 barrel calorimeter to hadrons of energies from 20 to 350 GeV”. In: *Nucl.*
 4269 *Instrum. Meth. A* 621.1–3 (2010), pp. 134 –150. doi: <http://dx.doi.org/10.1016/j.nima.2010.04.054>.

- [67] ATLAS Collaboration. “Jet energy measurement with the ATLAS detector in proton–proton collisions at $\sqrt{s} = 7$ TeV”. In: *Eur. Phys. J. C* 73 (2013), p. 2304. doi: [10.1140/epjc/s10052-013-2304-2](https://doi.org/10.1140/epjc/s10052-013-2304-2). arXiv: [1112.6426 \[hep-ex\]](https://arxiv.org/abs/1112.6426). PERF-2011-03.
- [68] Nausheen R. Shah and Carlos E. M. Wagner. “Gravitons and dark matter in universal extra dimensions”. In: *Phys. Rev. D* 74 (2006), p. 104008. doi: [10.1103/PhysRevD.74.104008](https://doi.org/10.1103/PhysRevD.74.104008). arXiv: [hep-ph/0608140 \[hep-ph\]](https://arxiv.org/abs/hep-ph/0608140).
- [69] Jonathan L. Feng, Arvind Rajaraman, and Fumihiro Takayama. “Graviton cosmology in universal extra dimensions”. In: *Phys. Rev. D* 68 (2003), p. 085018. doi: [10.1103/PhysRevD.68.085018](https://doi.org/10.1103/PhysRevD.68.085018). arXiv: [hep-ph/0307375 \[hep-ph\]](https://arxiv.org/abs/hep-ph/0307375).
- [70] Paul H. Frampton and Pham Quang Hung. “Long-lived quarks?” In: *Phys. Rev. D* 58 (5 1998), p. 057704. doi: [10.1103/PhysRevD.58.057704](https://doi.org/10.1103/PhysRevD.58.057704). URL: <http://link.aps.org/doi/10.1103/PhysRevD.58.057704>.
- [71] C. Friberg, E. Norrbin, and T. Sjostrand. “QCD aspects of leptoquark production at HERA”. In: *Phys. Lett. B* 403 (1997), pp. 329–334. doi: [10.1016/S0370-2693\(97\)00543-1](https://doi.org/10.1016/S0370-2693(97)00543-1). arXiv: [hep-ph/9704214 \[hep-ph\]](https://arxiv.org/abs/hep-ph/9704214).
- [72] Herbert K. Dreiner. “An introduction to explicit R-parity violation”. In: (1997). arXiv: [hep-ph/9707435](https://arxiv.org/abs/hep-ph/9707435).
- [73] Edmond L. Berger and Zack Sullivan. “Lower limits on R-parity-violating couplings in supersymmetry”. In: *Phys. Rev. Lett.* 92 (2004), p. 201801. doi: [10.1103/PhysRevLett.92.201801](https://doi.org/10.1103/PhysRevLett.92.201801). arXiv: [hep-ph/0310001](https://arxiv.org/abs/hep-ph/0310001).
- [74] R. Barbieri, C. Berat, M. Besancon, M. Chemtob, A. Deandrea, et al. “R-parity violating supersymmetry”. In: *Phys. Rept.* 420 (2005), p. 1. doi: [10.1016/j.physrep.2005.08.006](https://doi.org/10.1016/j.physrep.2005.08.006). arXiv: [hep-ph/0406039](https://arxiv.org/abs/hep-ph/0406039).
- [75] M. Fairbairn et al. “Stable massive particles at colliders”. In: *Phys. Rept.* 438 (2007), p. 1. doi: [10.1016/j.physrep.2006.10.002](https://doi.org/10.1016/j.physrep.2006.10.002). arXiv: [hep-ph/0611040](https://arxiv.org/abs/hep-ph/0611040).
- [76] Christopher F. Kolda. “Gauge-mediated supersymmetry breaking: Introduction, review and update”. In: *Nucl. Phys. Proc. Suppl.* 62 (1998), p. 266. doi: [10.1016/S0920-5632\(97\)00667-1](https://doi.org/10.1016/S0920-5632(97)00667-1). arXiv: [hep-ph/9707450](https://arxiv.org/abs/hep-ph/9707450).
- [77] Howard Baer, Kingman Cheung, and John F. Gunion. “A Heavy gluino as the lightest supersymmetric particle”. In: *Phys. Rev. D* 59 (1999), p. 075002. doi: [10.1103/PhysRevD.59.075002](https://doi.org/10.1103/PhysRevD.59.075002). arXiv: [hep-ph/9806361](https://arxiv.org/abs/hep-ph/9806361).
- [78] S. James Gates Jr. and Oleg Lebedev. “Searching for supersymmetry in hadrons”. In: *Phys. Lett. B* 477 (2000), p. 216. doi: [10.1016/S0370-2693\(00\)00172-6](https://doi.org/10.1016/S0370-2693(00)00172-6). arXiv: [hep-ph/9912362](https://arxiv.org/abs/hep-ph/9912362).
- [79] Glennys R. Farrar and Pierre Fayet. “Phenomenology of the Production, Decay, and Detection of New Hadronic States Associated with Supersymmetry”. In: *Phys. Lett. B* 76 (1978), pp. 575–579. doi: [10.1016/0370-2693\(78\)90858-4](https://doi.org/10.1016/0370-2693(78)90858-4).

- 4314 [80] A. C. Kraan, J. B. Hansen, and P. Nevski. “Discovery potential of R-hadrons
 4315 with the ATLAS detector”. In: *Eur. Phys. J.* C49 (2007), pp. 623–640. doi:
 4316 [10.1140/epjc/s10052-006-0162-x](https://doi.org/10.1140/epjc/s10052-006-0162-x). arXiv: [hep-ex/0511014](https://arxiv.org/abs/hep-ex/0511014)
 4317 [[hep-ex](#)].
- 4318 [81] Rasmus Mackeprang and David Milstead. “An Updated Description of
 4319 Heavy-Hadron Interactions in GEANT-4”. In: *Eur. Phys. J.* C66 (2010),
 4320 pp. 493–501. doi: [10.1140/epjc/s10052-010-1262-1](https://doi.org/10.1140/epjc/s10052-010-1262-1). arXiv:
 4321 [0908.1868](https://arxiv.org/abs/0908.1868) [[hep-ph](#)].
- 4322 [82] ATLAS Collaboration. “Search for massive, long-lived particles using mul-
 4323 titrack displaced vertices or displaced lepton pairs in pp collisions at
 4324 $\sqrt{s} = 8$ TeV with the ATLAS detector”. In: *Phys. Rev. D* 92 (2015), p. 072004.
 4325 doi: [10.1103/PhysRevD.92.072004](https://doi.org/10.1103/PhysRevD.92.072004). arXiv: [1504.05162](https://arxiv.org/abs/1504.05162) [[hep-ex](#)].
 4326 SUSY-2014-02.
- 4327 [83] ATLAS Collaboration. “Search for charginos nearly mass degenerate with
 4328 the lightest neutralino based on a disappearing-track signature in pp
 4329 collisions at $\sqrt{s} = 8$ TeV with the ATLAS detector”. In: *Phys. Rev. D*
 4330 88 (2013), p. 112006. doi: [10.1103/PhysRevD.88.112006](https://doi.org/10.1103/PhysRevD.88.112006). arXiv:
 4331 [1310.3675](https://arxiv.org/abs/1310.3675) [[hep-ex](#)]. SUSY-2013-01.
- 4332 [84] ATLAS Collaboration. “Searches for heavy long-lived sleptons and R-
 4333 Hadrons with the ATLAS detector in pp collisions at $\sqrt{s} = 7$ TeV”. In:
 4334 *Phys. Lett. B* 720 (2013), p. 277. doi: [10.1016/j.physletb.2013.02.015](https://doi.org/10.1016/j.physletb.2013.02.015). arXiv: [1211.1597](https://arxiv.org/abs/1211.1597) [[hep-ex](#)]. SUSY-2012-01.
- 4336 [85] ATLAS Collaboration. “Searches for heavy long-lived charged particles
 4337 with the ATLAS detector in proton–proton collisions at $\sqrt{s} = 8$ TeV”. In:
 4338 *JHEP* 01 (2015), p. 068. doi: [10.1007/JHEP01\(2015\)068](https://doi.org/10.1007/JHEP01(2015)068). arXiv:
 4339 [1411.6795](https://arxiv.org/abs/1411.6795) [[hep-ex](#)]. SUSY-2013-22.
- 4340 [86] ATLAS Collaboration. “Search for metastable heavy charged particles
 4341 with large ionisation energy loss in pp collisions at $\sqrt{s} = 8$ TeV using the
 4342 ATLAS experiment”. In: *Eur. Phys. J.* C 75 (2015), p. 407. doi: [10.1140/epjc/s10052-015-3609-0](https://doi.org/10.1140/epjc/s10052-015-3609-0). arXiv: [1506.05332](https://arxiv.org/abs/1506.05332) [[hep-ex](#)]. SUSY-
 4344 2014-09.
- 4345 [87] ATLAS Collaboration. “Search for heavy long-lived charged R-hadrons
 4346 with the ATLAS detector in 3.2 fb^{-1} of proton–proton collision data at
 4347 $\sqrt{s} = 13$ TeV”. In: *Phys. Lett.* B760 (2016), pp. 647–665. doi: [10.1016/j.physletb.2016.07.042](https://doi.org/10.1016/j.physletb.2016.07.042). arXiv: [1606.05129](https://arxiv.org/abs/1606.05129) [[hep-ex](#)].
- 4349 [88] ATLAS Collaboration. *Further ATLAS tunes of PYTHIA 6 and Pythia 8*. ATL-
 4350 PHYS-PUB-2011-014. 2011. url: <https://cds.cern.ch/record/1400677>.
- 4352 [89] Aafke Christine Kraan. “Interactions of heavy stable hadronizing parti-
 4353 cles”. In: *Eur. Phys. J.* C37 (2004), pp. 91–104. doi: [10.1140/epjc/s2004-01946-6](https://doi.org/10.1140/epjc/s2004-01946-6). arXiv: [hep-ex/0404001](https://arxiv.org/abs/hep-ex/0404001) [[hep-ex](#)].
- 4355 [90] M. Fairbairn et al. “Stable massive particles at colliders”. In: *Phys. Rept.*
 4356 438 (2007), p. 1. doi: [10.1016/j.physrep.2006.10.002](https://doi.org/10.1016/j.physrep.2006.10.002). arXiv:
 4357 [hep-ph/0611040](https://arxiv.org/abs/hep-ph/0611040).

- 4358 [91] W. Beenakker, R. Hopker, M. Spira, and P. M. Zerwas. “Squark and gluino
 4359 production at hadron colliders”. In: *Nucl. Phys. B* 492 (1997), p. 51. doi:
 4360 [10.1016/S0550-3213\(97\)00084-9](https://doi.org/10.1016/S0550-3213(97)00084-9). arXiv: [hep-ph/9610490](https://arxiv.org/abs/hep-ph/9610490).
- 4361 [92] A. Kulesza and L. Motyka. “Threshold resummation for squark-antisquark
 4362 and gluino-pair production at the LHC”. In: *Phys. Rev. Lett.* 102 (2009),
 4363 p. 111802. doi: [10.1103/PhysRevLett.102.111802](https://doi.org/10.1103/PhysRevLett.102.111802). arXiv: [0807.2405 \[hep-ph\]](https://arxiv.org/abs/0807.2405).
- 4365 [93] A. Kulesza and L. Motyka. “Soft gluon resummation for the production
 4366 of gluino-gluino and squark-antisquark pairs at the LHC”. In: *Phys. Rev.*
 4367 *D* 80 (2009), p. 095004. doi: [10.1103/PhysRevD.80.095004](https://doi.org/10.1103/PhysRevD.80.095004). arXiv:
 4368 [0905.4749 \[hep-ph\]](https://arxiv.org/abs/0905.4749).
- 4369 [94] Wim Beenakker, Silja Brensing, Michael Kramer, Anna Kulesza, Eric Lae-
 4370 nen, et al. “Soft-gluon resummation for squark and gluino hadroproduc-
 4371 tion”. In: *JHEP* 0912 (2009), p. 041. doi: [10.1088/1126-6708/2009/12/041](https://doi.org/10.1088/1126-6708/2009/12/041). arXiv: [0909.4418 \[hep-ph\]](https://arxiv.org/abs/0909.4418).
- 4373 [95] W. Beenakker, S. Brensing, M.n Kramer, A. Kulesza, E. Laenen, et al. “Squark
 4374 and Gluino Hadroproduction”. In: *Int. J. Mod. Phys. A* 26 (2011), p. 2637.
 4375 doi: [10.1142/S0217751X11053560](https://doi.org/10.1142/S0217751X11053560). arXiv: [1105.1110 \[hep-ph\]](https://arxiv.org/abs/1105.1110).
- 4376 [96] Michael Krämer et al. *Supersymmetry production cross sections in pp colli-*
 4377 *sions at $\sqrt{s} = 7 \text{ TeV}$* . 2012. arXiv: [1206.2892 \[hep-ph\]](https://arxiv.org/abs/1206.2892).
- 4378 [97] Rasmus Mackeprang and Andrea Rizzi. “Interactions of Coloured Heavy
 4379 Stable Particles in Matter”. In: *Eur. Phys. J.* C50 (2007), pp. 353–362. doi:
 4380 [10.1140/epjc/s10052-007-0252-4](https://doi.org/10.1140/epjc/s10052-007-0252-4). arXiv: [hep-ph/0612161](https://arxiv.org/abs/hep-ph/0612161)
 4381 [hep-ph].
- 4382 [98] Rasmus Mackeprang and David Milstead. “An Updated Description of
 4383 Heavy-Hadron Interactions in GEANT-4”. In: *Eur. Phys. J.* C66 (2010),
 4384 pp. 493–501. doi: [10.1140/epjc/s10052-010-1262-1](https://doi.org/10.1140/epjc/s10052-010-1262-1). arXiv:
 4385 [0908.1868 \[hep-ph\]](https://arxiv.org/abs/0908.1868).
- 4386 [99] “dE/dx measurement in the ATLAS Pixel Detector and its use for particle
 4387 identification”. In: (2011).
- 4388 [100] ATLAS Collaboration. “The ATLAS Simulation Infrastructure”. In: *Eur.*
 4389 *Phys. J.* C70 (2010), pp. 823–874. doi: [10.1140/epjc/s10052-010-1429-9](https://doi.org/10.1140/epjc/s10052-010-1429-9). arXiv: [1005.4568 \[physics.ins-det\]](https://arxiv.org/abs/1005.4568).
- 4391 [101] ATLAS Collaboration. “Luminosity determination in pp collisions at \sqrt{s}
 4392 = 8 TeV using the ATLAS detector at the LHC”. In: (2016). arXiv: [1608.03953 \[hep-ex\]](https://arxiv.org/abs/1608.03953).
- 4394 [102] Alexander L. Read. “Presentation of search results: The CL(s) technique”.
 4395 In: *J. Phys.* G28 (2002), [,11(2002)], pp. 2693–2704. doi: [10.1088/0954-3899/28/10/313](https://doi.org/10.1088/0954-3899/28/10/313).